ANNÉE 2021

UNIVERSITÉ DE RENNES 1

UNIVERSITE BRETAGNE LOIRE

THÈSE / UNIVERSITÉ DE RENNES 1
sous le sceau de l'Université Bretagne Loire

pour le grade de

DOCTEUR DE L'UNIVERSITÉ DE RENNES 1

Mention : Physique

Ecole doctorale « Matière, Molécules et Matériaux »

présentée par

Théo Guillaume

préparée à l'unité de recherche UMR 6251 IPR

Institut de Physique de Rennes
UFR Sciences et Propriété de la matière

Construction of an E-band chirped-pulse spectrometer and application to the measurement of low temperature collisional processes of astrochemical interest.

Thèse soutenue à Rennes le 25 octobre
devant le jury composé de :

Arthur Suits
Professeur University of Missouri USA/rapporteur

Olivier Pirali
Directeur de recherche Université de Paris Saclay/rapporteur

Samir Kassi
Ingenieur de recherche Université de Grenoble Alpes/examinateur

Lucile Rutkowski
Chargée de recherche Université de Rennes 1/examinatrice

Sébastien Le Picard
Professeur Université de Rennes 1/examinateur

Brian Hays
Ingenieur de recherche Université de Rennes 1/invité

Ian Sims
Professeur Université de Rennes 1/directeur de thèse

Résumé

Cette thèse présente la construction et le développement d'un nouvel instrument et son utilisation via la technique CPUF technique (Chirped Pulse in Uniform Flow) pour étudier des phénomènes collisionnels à basse température d'intérêt astrophysique.

La thèse détaille les caractéristique de l'intrument CRESUCHIRP aisi que les dévellopement technique lié a son utilisation pour la technique CPUF. Le nouveau reactaur CRESU (Cinétique de Réaction en Ecoulement supersonique Uniforme) ainsi que les instruments qui y sont liés son presentés. La caracterisation du nouveau spectrometre CP-FTmmW (Chirped Pulse-Fourier Transform millimeter Wave) en bande E (60-90 GHz) est détaillé ainsi que le couplage avec le reacteur CRESU

Les performances du spectrometre en tant qu'instrument spectrocopique sont presentées avec la mesure de l'élargissement collisionnel à température ambiante pour le système OCS + He.

Les experiences utilisant la technique CPUF sont presentées avec la mesure de l'évolution de l'élargissement collisionnel des systèmes HCN + He et HNC + He en fonction de la température (10-70 K).

Une étude du potentiel de l'instrument pour son application sur des mesures de cinétique à basse temperature est présentée pour les reactions entre le radical CN et l' éthane à 10 K et l'acétylène à 30 K. Une tentative de calibration des produits est détaillée.

Les forces et faiblesses du nouvel instrument sont discutés ainsi que de potentielles améliorations à la technique.

mots clefs **–** Cinétique chimique, astrochimie, réaction en phase gazeuse, CRESU, spectroscopie rotationnelle, rapport de branchement

Abstract

This thesis presents research work on the construction and development of a new instrument and its utilization in the framework of the CPUF technique (Chirped Pulse in Uniform Flow) to study low-temperature collisional processes of astrochemical interest.

The thesis details the characteristics of the CRESUCHIRP apparatus and the technical development related to its utilization as a CPUF instrument. The new CRESU (Cinétique de Réaction en Ecoulement supersonique Uniforme) apparatus and the supporting instrumentation are described. The characterization of an E-band (60-90 GHz) CP-FTmmW spectrometer (Chirped Pulse-Fourier Transform millimeter Wave) is presented with its coupling to the rest of the instrument.

The capability of the spectrometer as a spectroscopic tool is presented with the measurement of pressure broadening coefficients at room temperature for the system OCS + He.

Experiments using the CPUF technique are presented with the measurement of the difference in collisional interaction of isomers at low temperatures: HCN and HNC with He.

Studies of the potential of the instrument for application to kinetics measurement at low temperature are presented for the reactions CN + ethane at 10 K and CN + acetylene at 30 K. Tentative calibrations of these two reactions are presented.

The strengths and weaknesses of the new instrument are discussed, as well as potential improvements to the technique.

Keywords – Chemical Kinetics, Astrochemistry, Gas-phase reactions, CRESU (Reaction Kinetics in Uniform Flow), Chirped pulse microwave spectroscopy, Branching ratio

Remerciements

Je voudrais tout d'abord remercier mon directeur de thèse Ian Sims pour m'avoir donné l'occasion de participer au développement du projet CRESUCHIRP et notamment à la construction de cette belle experience.

Then I want to thank the amazing team working on the project with me which made it such an incredible journey Ilsa, Brian, Divita, Omar, Myriam, and Tom. We went through the rollercoaster of building that monster together and had such great moments. I want to add a special note for Ilsa, thank you for being my partner in crime for all the delightful mischief we came out with.

Je veux remercier toutes les personnes avec qui j'ai pu échanger et tisser des liens à l'IPR pendant ces trois années et demies. Les membres du département de Physique moléculaire pour leur soutien, discussions scientifiques et conversations endiablées au repas. La fine équipe de l'atelier de mécanique ainsi que les gestionnaires et l'équipe de direction pour leur aide et disponibilité sans laquelle ce travail n'aurait pas pu être. Une note spéciale pour Lucile et Jean-Charles pour m'avoir soutenu, bouger les fesses et fini les bouteilles avec moi.

J'aimerai particulièrement remercier Laurence Chérigier-Kovacic et Caroline Mossé pour leur incroyable soutien lors de mon arrivé à l'université sans lequel je ne serai jamais allé aussi loin.

Je voudrais remercier ma famille et mes amis particulierement mes parents et mon frère, pour leur soutien permanent, le chemin fut déjà très très long et cette nouvelle étape aurait été impossible à franchir sans votre soutien.

Pour finir je voudrais remercier Patrick Cornet pour m'avoir, sans que je m'en rende compte, inculqué les notions de base de l'ingénierie et à qui j'aurais tellement aimé montrer ce que j'ai aidé à construire. Merci

This work presents the results of the development of the CPUF technique in Rennes in the frame of the ERC project CRESUCHIRP proposed by Ian R. Sims. The project involved multiple people, especially a group of six post-doc/Ph.D. students; Brian M. Hays (post-doc), Ilsa R. Cooke (post-doc), Thomas S. Hearne (post-doc), Divita Gupta (Ph.D. student), Omar Abdelkader Khedaoui (Ph.D. student), Myriam Drissi (Ph.D. student), with which the work presented here was carried out.

Contents

Chapter 1

Introduction

1.1 Chemistry in space

Chemistry in space is not as dead as one might think on the first approach. Even at really cold temperatures and low densities, chemistry in space is diverse, with today more than 200 molecules discovered in a wide variety of environments [1]. This richness has merited its own field, astrochemistry, arising from the interconnections between chemistry, astronomy, and physics. Astrochemistry is a field advancing on multiple fronts supporting each other observations, models and laboratory experiments. Astronomical observations provide information on the nature of chemical species in space and the conditions in which they are found. Modeling aims to understand what is observed by creating a model of what is happening under the observed conditions, trying to make it match observations by including physical and chemical parameters. And laboratory experiments that try to break the problem into elementary phenomena and to experimentally determine the parameters to be supplied to the models under the conditions observed. One category of parameters required to increase the accuracy models is directly related to the chemistry occurring in the different environments where molecules are detected. The kinetics of reactions at low temperature especially those which form and transform the molecules detected in space is still largely unknown and can be hard to predict theoretically and thus requires experimental measurements.

As a result of this lack of data, research on the determination of rate coefficients for elementary reactions at low temperatures has seen a strong interest in recent decades. Most reactions see their rates coefficient becoming negligible at lower temperatures as they possess energetic barriers on their potential energy surfaces. But some reactions, many including radicals, do not possess such barriers along their minimum energy path

and thus see their rate coefficient increase at low temperatures. These barrierless reactions remain efficient or even become faster as the temperature drops [2, 3] all the way to the low temperatures found in extraterrestrial atmospheres such as that of Titan (ca. 70-150 K [4]) or interstellar clouds (ca. 10—100 K [5, 6]).

For a simple bimolecular reaction such as F + $H_2 \longrightarrow$ HF + H, the measurement of the total rate coefficient $k(T)$ is sufficient as an input for models of low-temperature astrochemical environments [7]. More complex reactions may have more than one set of products, for example, the reaction 1.1 of CN radicals with ethene.

1.2 Branching ratios for elementary reactions

While measuring the overall rate coefficient $k(T)$ provides significant insight, more complex chemical environments require a deeper understanding of the reactions, notably the product channel-specific rate coefficients (here, k_{1a} and k_{1b} in equation 1.1 as a function of temperature or as an equivalent, the product branching ratio (in this case for 1a: $k_{1a}/(k_{1a}+k_{1b})$).

$$\begin{aligned} CN + C_2H_4 \longrightarrow\ & C_3H_3N + H \qquad (1a) \\ & C_2H_3 + HCN \qquad (1b) \end{aligned} \tag{1.1}$$

The measurement of overall rate coefficients at low temperatures has seen a constant output of scientific results for the last few decades, especially with the help of well-established techniques like Pulsed Laser Photolysis-Laser Induced Fluorescence (PLP-LIF), but branching ratio measurements have been lagging far behind especially at low-temperature [2, 8, 9]. This is mostly due to the lack of an established universal technique for these measurements. Direct measurement of branching ratios requires to be able to detect quantitatively very low concentrations of different products. This lack of an optimum technique is what drove the work and the technical developments presented in this thesis. The determination of absolute radical concentration is challenging [10]. Mass spectrometric and fluorescence methods are good, sensitive techniques but require difficult calibration to determine absolute concentrations. Direct absorption measurements can in theory provide absolute measurements but require physical parameters (absorption cross-sections for example) which have not always already been measured, especially at cold temperatures.

Despite these challenges instruments and techniques have been developed in the last two decades. Leading to the measurements of reaction products and of branching ratios

for elementary reactions [8].

1.3 Brief review of techniques for measurement of branching ratios

Among promising candidates for measuring branching fraction, the Cavity Ring-Down Spectroscopy (CRDS) technique is a sensitive tool that allows the measurement of absolute concentrations by comparing the change in the ring-down time of an optical cavity when the cavity is without the molecule of interest and when it is present. It has provided experimental measurements such as the spectroscopic measurements of the hydroxy-methyl-peroxy radical formed by the reaction between the hydroperoxy radical and formaldehyde in a flow reactor at room temperature [11]. Brown *et al.* [12] developed the Simultaneous Kinetics and Ring-down technique (SKAR) and presented its capabilities with the room temperature study of the reactions NO + $NO_3 \longrightarrow 2NO_2$ and OH + $HNO_3 \rightarrow H_2O + NO_3$ Fig. 1.1 present the schematic of their instrument.

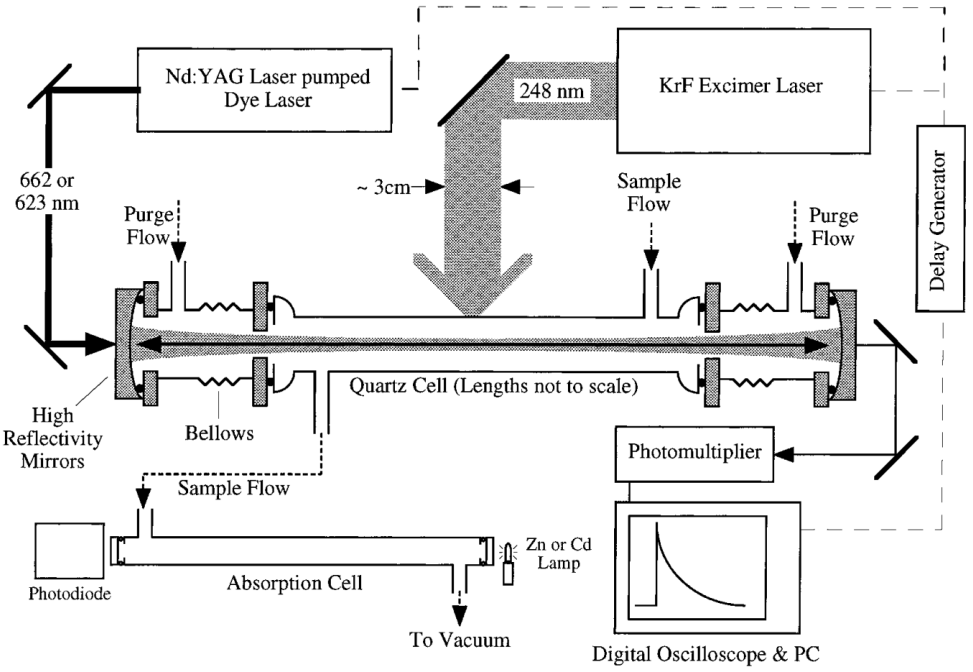

Figure 1.1: Figure and caption taken from Brown *et al.* [12] to present their experimental setup. "Schematic of the experimental apparatus used to measure the temporal profile of a reactant or a product on the time scale of the ring-down signal."

LIF techniques are very sensitive but struggle to yield absolute measurements. Some groups have used H-atom detection in the vacuum ultraviolet (VUV) and calibration reac-

tions to lead to measurement of products yield [10] for example for the reaction between the methylidyne radical CH ($X^2\Pi$) with ethane, ethene, propyne, allene, propene and *trans*-butene at room temperature [13]. Fig. 1.2 presents an example of a PLP-LIF instrument used to study reaction kinetics at low temperature from the work of Taylor *et al.* [14]. This instrument uses a pulsed Laval nozzle apparatus using solenoid valves to generate cold supersonic expansion. Pump-probe techniques using PLP-LIF allow for the radical generation to occur in the cold expansion and to measure the time-dependent fluorescence signal of species involved in the reaction using a photomultiplier tube. It benefits from a good sensitivity (one laser pulse can it usually enough to detect the fluorescent signal) but does not allow for the quantitative comparison of the signal of different species necessary to measure branching ratios. This makes it a technique more suited to the measurement of rate coefficients than branching ratios.

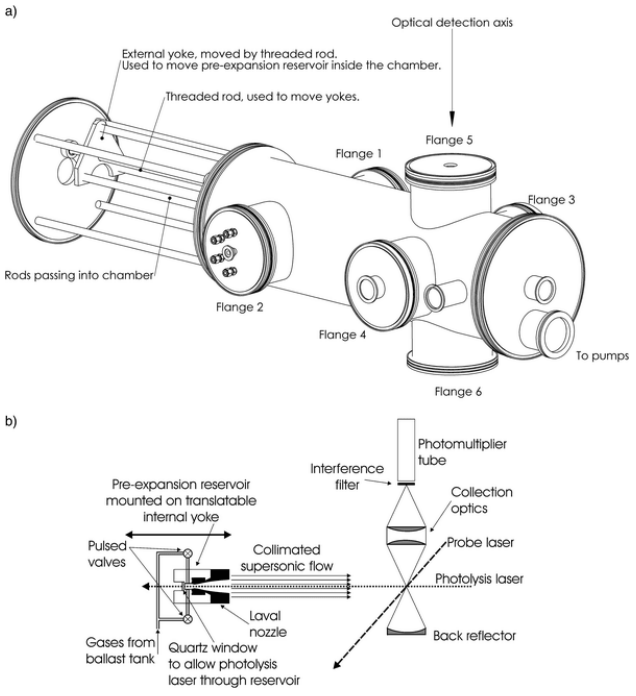

Figure 1.2: Figure and caption taken from Taylor *et al.* [14] to present their experimental setup. "(a) Three-dimensional image of the pulsed Laval nozzle apparatus. Flanges 1 and 2 enable gas to be provided to the two pulsed valves as well passing electrical feedthroughs for control of stepper-motors and monitoring of pressures. The probe-laser beam enters and leaves the cell through Brewster angled windows mounted on Flanges 3 and 4. The fluorescence collection optics are mounted on rails held between Flanges 5 and 6. (b) Schematic showing the details of the reservoir, Laval nozzle, supersonic flow and fluorescence collection system."

To push forward the measurements more efficient techniques are required, sensitive

enough to detect the products of reactions and with broadband capability to be able to compare them. Four techniques with potential have seen development toward measurement of branching ratios.

Mass spectrometry provides in principle a universal method of detection and has shown promises. It has been employed recently with great success in combination with threshold VUV single-photon ionization using synchrotron light from the Advanced Light Source (ALS) in Berkeley. The synchrotron was first coupled to magnetic-sector mass spectrometer by Osborn *et al.* [15] and then a multiplexed photoionization mass spectrometer was added and used by Lockyear *et al.* [16] for the study of fulvene in the reaction of C_2H with 1,3-butadiene at room temperature. Fig. 1.3 presents the schematic of the apparatus developed by Osborn *et al.*. A quadrupole mass spectrometer was coupled by Soorkia *et al.* [17] with a pulsed Laval nozzle apparatus and the synchrotron light of the ALS and was used by Bouwman *et al.* [18] for the measurement of reaction rate and isomer-specific product branching ratios of $C_2H + C_4H_4$: 1-butene, *cis*-2-butene, *trans*-2-butene, and isobutene at 79 K. Fig. 1.4 presents the schematic of the apparatus developed by Soorkia *et al.*. A similar apparatus has been recently built in Rennes to explore the capability of such an instrument to lower temperatures in a continuous Laval apparatus with the study of the reaction between the radical C_2H and acetylene to form $C_4H_2 + H$ at 75 and 52 K [19] Fig. 1.5 presents a schematic of the apparatus.

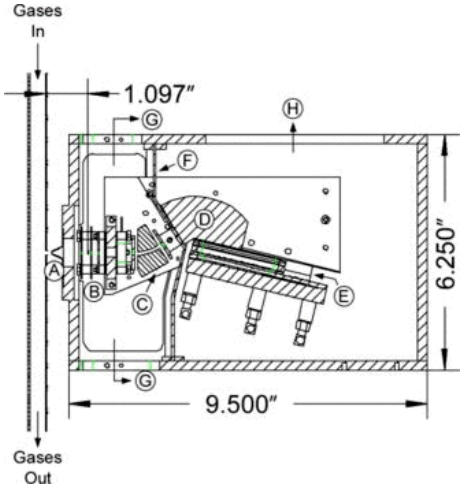

Figure 1.3: Figure and caption taken from Osborn *et al.* [15] to present their experimental setup. "Cross section view of the reactor tube, mass spectrometer, and detector region. (A) pinhole, (B) ion optics, (C) electrostatic sector, (D) magnetic sector, (E) 2D time- and position-sensitive detector, (F) partition wall dividing the ionization region from the detection region for the purposes of differential pumping, (G) pumping ports for the ionization region, and (h) pumping port for the detector region."

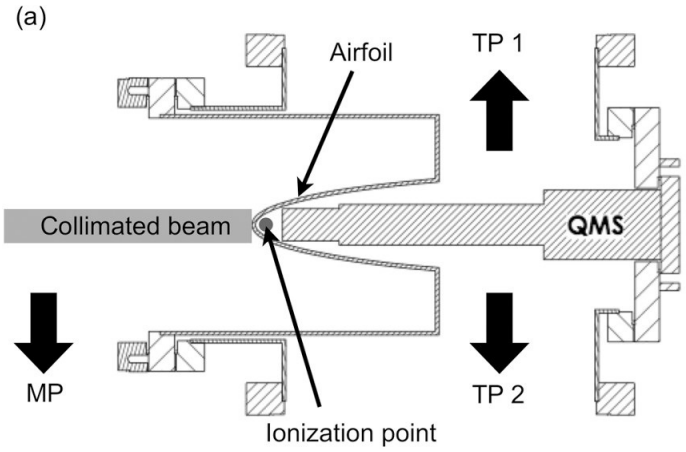

Figure 1.4: Figure and caption taken from Soorkia *et al.* [17] to present their experimental setup. "The pump-out ports in the source and detection regions are indicated: TP for turbomolecular pump, MP for mechanical pump, and DP for diffusion pump."

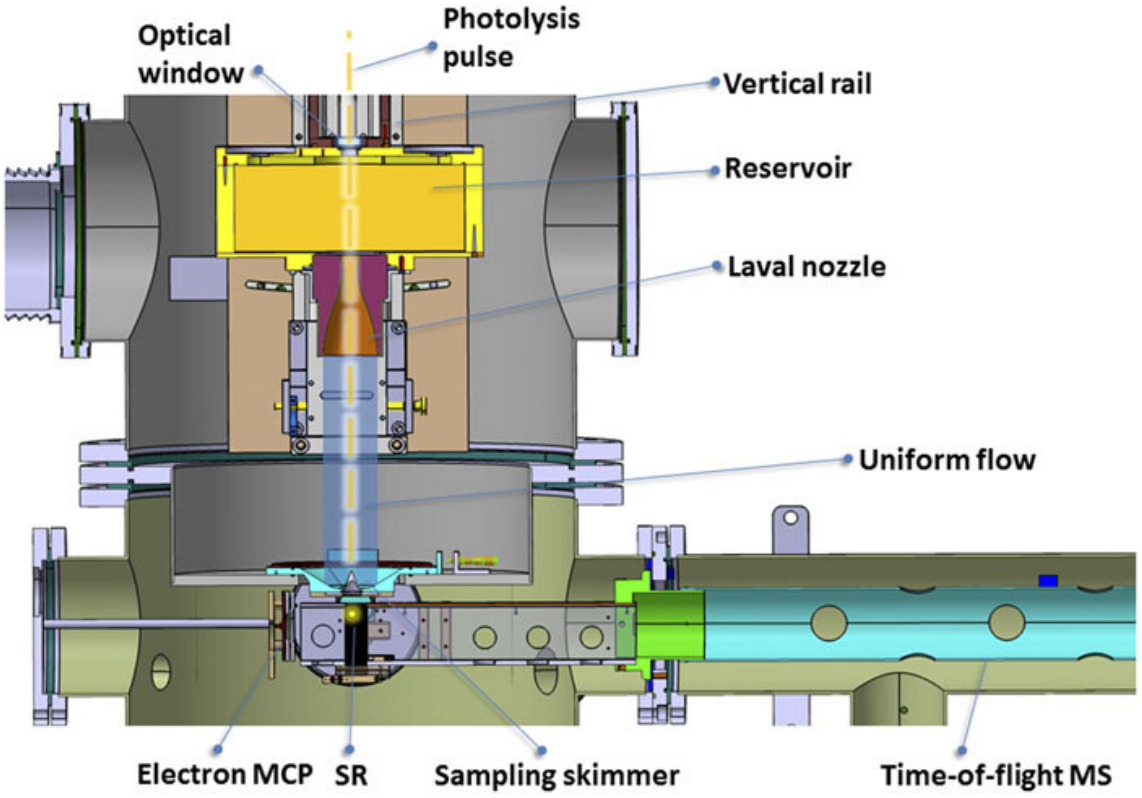

Figure 1.5: Figure and caption taken from Durif *et al.* [19] to present their experimental setup. "Inside view of the reaction and detection chambers. The ion micro-channel plate detector, implemented at the end of the drift tube, is out of view."

Frequency comb spectroscopy has also seen some development towards application to chemical kinetics with the development of the Time-Resolved Frequency Comb Spec-

troscopy technique (TRFCS) by Fleisher *et al.* [20] which is presented in Fig. 1.6. This technique benefits from the broadband capabilities and high sensitivity of a frequency comb coupled to a cavity. They presented the use of a Virtually Image Phased Array (VIPA) coupled to a diffraction grating which allows separating spatially the comb teeth in function of their frequencies. The resulting light is then captured by an IR camera, leading to 2-D images containing thousands of individual comb teeth in one image. This technique was recently used in the study of OD + CO at room temperature by Bjork *et al.* [21] who were able to detect the *trans*-DOCO reaction intermediate. Other promising developments are on the way to use frequency comb as a broadband sensitive technique to study reaction kinetics [22].

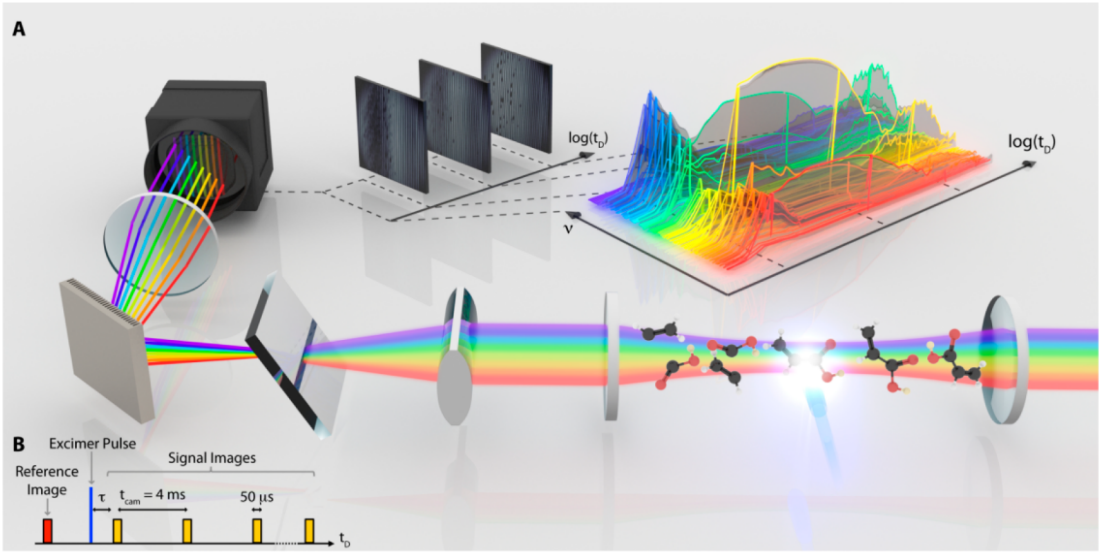

Figure 1.6: Figure and caption taken from Fleisher *et al.* [20] to present their experimental setup. "(A) Illustration of time-resolved frequency comb spectroscopy (TRFCS) performed with a high-finesse optical cavity coupled to a reaction flow cell. The time delay between photolysis and spectral acquisition provides microsecond time resolution over a broad spectral bandwidth of 65 cm^{-1} in the mid-infrared (mid-IR). (B) Block diagram of the data acquisition scheme, where time zero (tD = 0 µs) is defined by the photolysis pulse (blue)."

A recent application of the SKAR technique in a supersonic expansion was recently published by Suas-David *et al.* [23] presenting the measurements of the reaction between the radical CN both in the vibrational level $v = 0$ and $v = 1$ and propene at 70 K Fig. 1.7 presents the schematic of the instrument described in the article. The CRDS technique was coupled to a pulsed Laval nozzle apparatus using a piezoelectric stack valve. This allows them to compare the evolution of the ring-down time of the cavity while the reac-

tion is taking place in the cold supersonic expansion. This instrument could potentially be used to detect reaction products at low temperature, using the absolute concentration measurement provided by the CRDS could then allow measuring branching ratios.

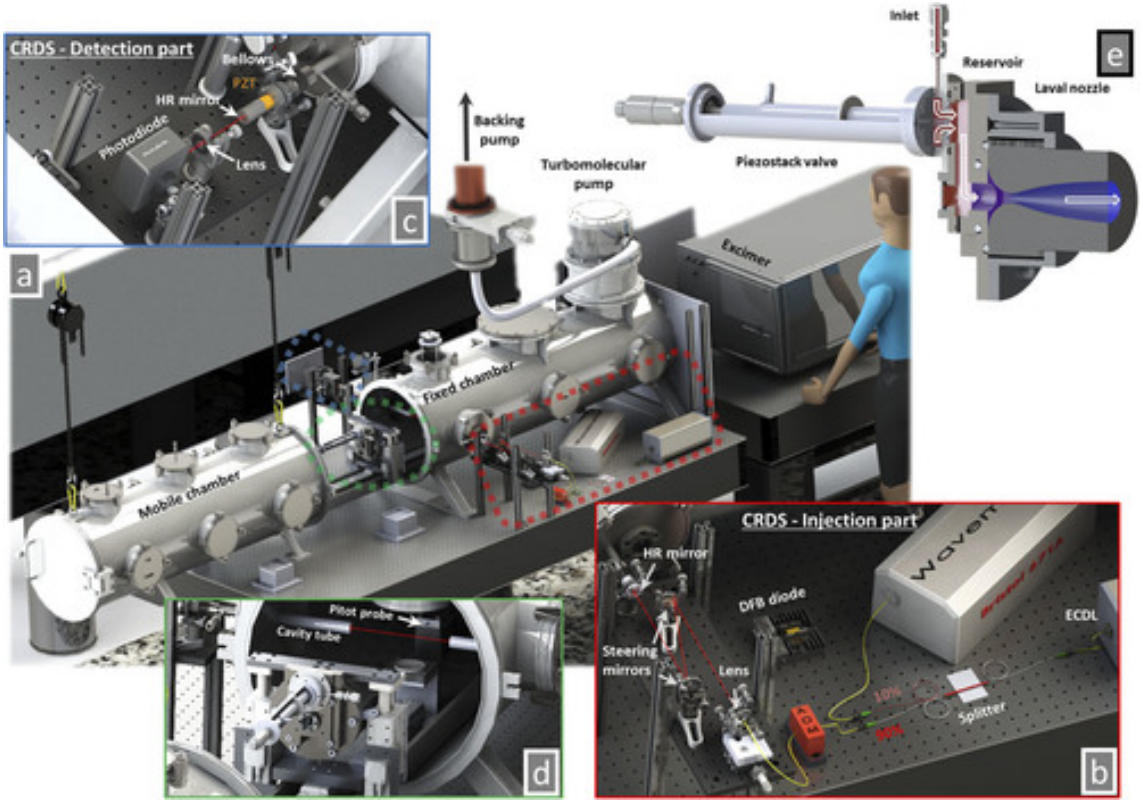

Figure 1.7: Figure and caption taken from Suas-David *et al.* [23] to present their experimental setup. "Overview of the setup modeled with SolidWorks. The mobile and fixed chambers along with the continuous wave (cw)-CRD spectrometer are lying on a massive optical table associated with passive isolator legs (a). On both sides of the fixed chamber, the injection (b) and detection (c) parts of the CRDS are set. The mobile chamber is hung on a rail and then can be lifted and translated to access the interior of the vacuum chamber and the pulsed uniform flow setup [(d) rearview]. It is composed of three parts (e): the piezoelectric stack valve (PSV), the reservoir, and the Laval nozzle. These are mounted on actuators allowing for an accurate 2D displacement in regard to the fixed pitot probe (d) and cw-CRDS."

A lot of progress has been made and instruments capable of measuring branching ratios at low temperature have been developed but the field is still struggling to detect products at low temperature with enough sensitivity or broadband capabilities to be established as a universal technique qualified for these measurements.

A recently developed technique, Chirped Pulse Fourier Transform millimeter Wave spectroscopy (CP-FTmmW, described in more detail later) [24], is showing promise to be used as a tool for measuring branching ratios at low temperature. Rotational spectroscopy

has the advantage of being highly specific and almost universal, potentially allowing for simultaneous detection of all the products of a reaction. Rotational spectroscopy as a kinetics tool greatly benefits from a direct link to astronomical observations as most of the searches for new molecules in space are carried by radio telescopes. Already existing collaborations between observers and spectroscopists would greatly benefit kinetics study with rotational spectroscopy as it would complete the path to understanding astrochemistry. Observers need spectroscopic data on molecules to search for them which can also be used by kineticists studying elementary processes leading to the formation of these molecules. For example, the recent discovery of CN-bearing molecules in space [25, 26], benefited from the spectroscopic work on similar molecules [27], which then is used to look for the formation route of these molecules.

The first application of CP-FTmmW to study low-temperature kinetics has been presented by a collaboration between the groups of Arthur Suits (then Wayne State, Detroit), Robert Field (MIT) and Ian Sims (Rennes) [28–30]. This led to the development of a new technique, Chirped-Pulse in Uniform Flow (CPUF), taking the advantage of the CP-FTmmW technique to allow broadband detection of molecules and coupling it with the well established CRESU technique (a French acronym: cinétique de réaction en écoulement supersonique uniform or reaction kinetics in uniform supersonic flow, the technique will be described later) capable of generating large volumes of rotationally cooled products. The cooling aspect brings two advantages, the first one is to allow measurements at temperatures relevant for astrochemistry. The second advantage is that cooling molecules increase the intensity of the rotational transitions overlapping with the instrument's bandwidth because of the Boltzmann distribution of populations. Fig. 1.8 presents the effect of the cooling on the line intensity of acrylonitrile at 300 and 10 K. It is clearly shown that at 10 K the peak of the Boltzmann distribution perfectly overlaps with the band of the spectrometer used in this work which contributes in matching the two techniques. Fig. 1.9 presents the schematic of the first CPUF apparatus designed by Oldham *et al.* [28]. They used a piezoelectric stack valve similar to Suas-David *et al.* [23] and coupled the pulsed Laval nozzle apparatus to a Ka-band (26-40 GHz) CP-FTmmW spectrometer.

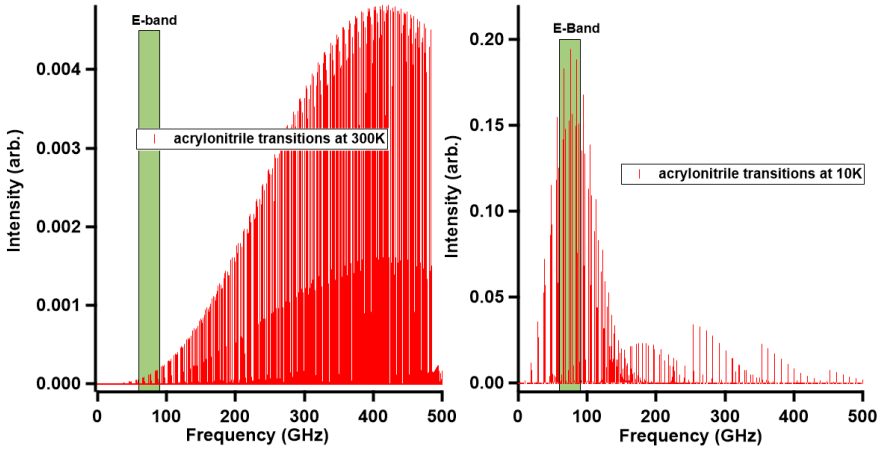

Figure 1.8: Pure rotational spectra of acrylonitrile computed from Cologne Database for Molecular Spectroscopy catalog. Intensity are scaled to the Boltzmann distribution at 300 K on the right and 10 K on the left

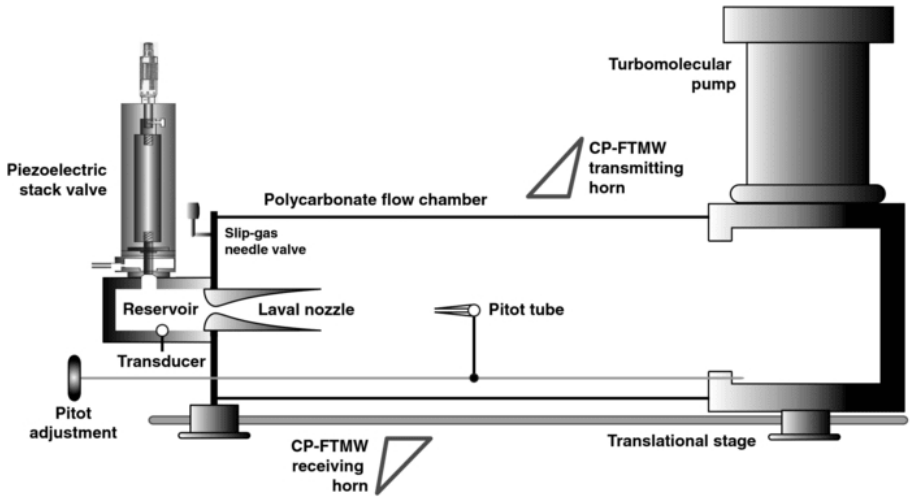

Figure 1.9: Figure and caption taken from Oldham *et al.* [28] to present their experimental setup. "The pulsed uniform supersonic flow system. The stacked piezoelectric valve is mounted on a reservoir outside of the vacuum chamber. Pressures in the reservoir and main chambers are monitored by pressure transducers mounted on the reservoir and inside of a Pitot tube, respectively. The vacuum chamber consists of a polycarbonate tube of outside diameter ∼30 cm which is transparent in the microwave spectral region. The figure is not to scale."

Abeysekera *et al.* demonstrated the possibility of the technique by studying the distribution of SO in the photodissociation of SO_2 at 193 nm using their CP-FTmmW spectrometer in the Ka-band (26-40 GHz) in a Laval expansion at 22 K [29]. They demonstrate in the same paper the potential of the technique for reaction kinetics study at low temper-

ature by presenting the time evolution of the product HC_3N from the reaction between the radical CN and acetylene Fig. 1.10 is taken from the paper to present their results.

They extended their work on the study of the reaction between the radical CN and propyne which present the branching fraction of the detected products at 22 K [30]. Using a new CP-FTmmW spectrometer in the E-band (60-90 GHz) they reported the detection of three products, HC_3N, CH_3C_3N and HCN

1.4 Aims of this thesis

This work presents the results of the development of the CPUF technique in Rennes with the design and construction of the CRESUCHIRP apparatus which will be presented in chapter 2 with the technical development related to the application of the CPUF technique. A room-temperature pressure broadening study is presented in chapter 3 to qualify the performance of the new E-band chirped-pulse spectrometer and of the modeling of the signal on the OCS + He system. Chapter 4 presents the use of the new experimental apparatus for CPUF experiments, first focusing on the photodissociation of acrylonitrile at 193 nm as a benchmarking system, then as a tool to study collisional processes in conditions relevant for astrochemistry with the study of the HCN + He and HNC + He systems at low temperatures. Finally, the performance of the apparatus as a tool for low-temperature kinetics is presented with the study of the reactions between the radical CN and C_2H_2 and C_2H_6. Chapter 5 presents the conclusions of this work with future perspectives and developments of the instrument to possibly overcome the limitations identified in this study.

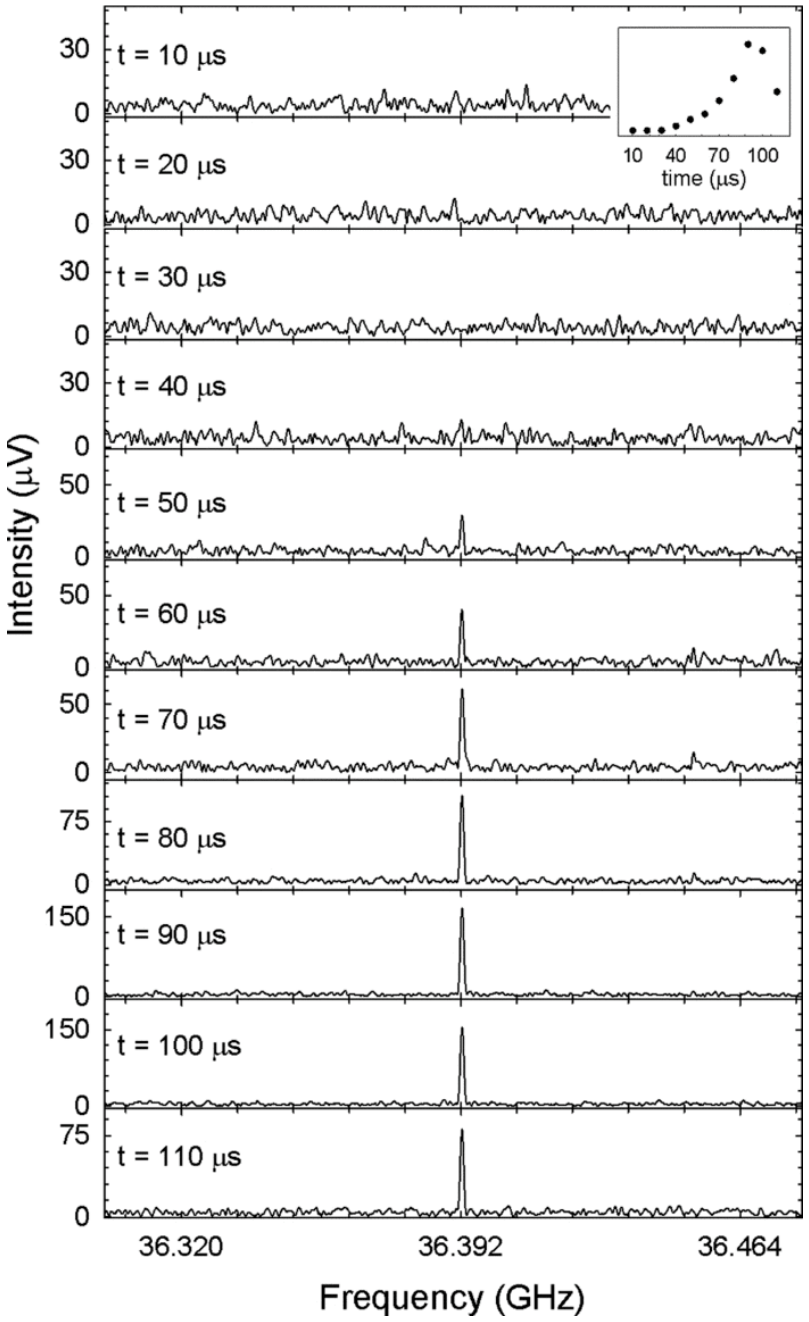

Figure 1.10: Figure and caption taken from Abeysekera *et al.* [29] to present the first CPUF results. "Spectra illustrating the time evolution of the J = 4-3 rotational transition of HCCCN ($\tilde{X}^1\Sigma^+1$), generated via the bimolecular reaction of the CN ($X^2\Sigma^+$) radical and C_2H_2 ($\tilde{X}^1\Sigma^+1$), are displayed. The CN radical was produced by irradiation of BrCN with a 193 nm laser. HCCCN appears approximately 40-50 μs after the laser is fired. The inset shows the integrated intensity of the HCCCN line at each time point, with the peak intensity occurring at ∼90 μs. Each spectrum is an average of 22000 acquisitions obtained over the frequency range 35.25-36.45 GHz using a 1 μs duration upchirp."

Chapter 2

Experimental techniques

This chapter presents the experimental and theoretical methods used in this work. The first section describes the basics of the CRESU technique followed by a short introduction to rotational spectroscopy and the CP-FTmmW technique. A description of the model used to characterize the evolution of the polarization of a molecular sample is presented. The CRESU components of the experiment are presented with a description of the spectrometer used in this work. Details about the acquisition and data analysis procedure used for the experiments are shown with examples.

2.1 The CRESU technique

Generating a cold gas-phase environment with frequent enough collisions to preserve local thermodynamic equilibrium and allow for a sufficient extent of chemical reaction to take place to follow the kinetics is not a straightforward thing to accomplish. To date, only one experimental technique really achieves this without too many downsides, the CRESU technique.

Similar to a free jet expansion, the CRESU technique relies on an adiabatic expansion between a reservoir and a vacuum chamber with orders of magnitudes of difference in pressure in order to cool the gas. The difference from a free jet expansion is that instead of expanding through a simple hole or slit, the gas expands in a specially designed nozzle. The Laval nozzle is a convergent-divergent nozzle in which the gas accelerates from rest at the entrance to the convergent part of the nozzle up to the speed of sound at the throat, and then to supersonic speeds in the divergent part of the nozzle. As the gas expands it cools down and can reach temperatures as low as 10 K, but can go even lower using a liquid nitrogen precooled nozzle [31]. The particularity of these nozzles is not only that

the gas is cooled to low temperature which can be obtained also by a free jet expansion and to even cooler temperatures, but the flow generated by the CRESU technique at the exit of the nozzle is shaped by the nozzle profile in an axisymmetric tube of cold gas where the density and temperature are uniforms along the whole flow. This is one of the really important advantages of this technique, the physical conditions along the whole flow are determined by design and uniform and accurately known. This means that experiments can be performed with total control and knowledge of the thermodynamic parameters and with the possibility to vary these parameters. Another advantage of the CRESU technique is the density of the flows, typically between 10^{16}-10^{17} cm^{-3}. This high density allows for the conservation of local thermodynamic equilibrium by frequent collisions which rapidly cool down any products generated from exothermic processes (chemical reaction, photolysis product, etc.).

The temperature of the CRESU flow generated by a Laval nozzle can be calculated by applying a compressible version of Bernoulli's equation. Neglecting gravitational effects because of the relatively small size of the nozzle and taking into account enthalpy and potential energy in an isentropic flow we can apply the following equation with the Laplace law:

$$C_p T_{flow} + \frac{v_{flow}^2}{2} = C_p T_0 + \frac{v_0^2}{2} \tag{2.1}$$

$$PV^{\gamma} = constant \tag{2.2}$$

Where C_p is the specific heat capacity at constant pressure, T the fluid temperature, v the fluid velocity and γ the ratio of specific heat capacities: $\gamma = \frac{C_p}{C_v}$ with C_v is the specific heat capacity at constant volume. The indices refer to reservoir values "0" and flow value "$flow$". We introduce the Mach number (2.3), the ratio of the fluid speed compared to the speed of sound (c_s).

$$M = \frac{v}{c_s} = \frac{v\sqrt{M_m}}{\sqrt{\gamma RT}} \tag{2.3}$$

With R the ideal gas constant (R = 8.314 J K^{-1} mol^{-1}), T the fluid temperature, and M_m its molar mass. By assuming a large static reservoir $v_0 = 0$ and an ideal gas $C_p - C_v = R$ we can write:

$$T_{flow} = T_0 \left(1 + \frac{\gamma - 1}{2} M^2\right)^{-1} \tag{2.4}$$

Laval nozzles are designed to generate uniform flows using a buffer gas (helium, argon, nitrogen and sometimes hydrogen) and a set of pressures for the reservoir and the chamber. This leads to a defined Mach number in the jet and following equation 2.4 a

temperature. The conditions are simulated using computational fluid dynamics software to determine the expected temperature and density of the nozzle. The nozzles are then characterized experimentally using impact pressure measurements using a Pitot tube [32]. This consists of a hollow tube (1 mm in diameter typically) mounted parallel to the flow propagation on a computer-controlled table that allows for the movement of the probe in a 2D plane centered on the axis of the nozzle. The passage of the tip of the probe in the flow creates a shockwave in front of the tube, the resulting impact pressure is then measured by a pressure gauge connected to the tube. The pressure in the flow (P_f) and the impact pressure (P_i) are related by the equation (2.5). As the core of the flow is isentropic the impact pressure (P_i) can be expressed as a function of the reservoir pressure (P_r) relation (2.6). Measuring the reservoir and impact pressure then allows the calculation of the Mach number and from there the determination of temperature and density.

$$P_i = P_f \left(\frac{\gamma+1}{2} \right)^{\frac{\gamma+1}{\gamma-1}} M^{\frac{2\gamma}{\gamma-1}} \left(\gamma M^2 - \frac{\gamma-1}{2} \right)^{\frac{1}{1-\gamma}} \tag{2.5}$$

$$P_i = P_r \left(\frac{(\gamma+1)M^2}{(\gamma-1)M^2+2} \right)^{\frac{\gamma}{\gamma-1}} \left(\frac{\gamma+1}{2\gamma M^2-\gamma+1} \right)^{\frac{1}{\gamma-1}} \tag{2.6}$$

These measurements allow for the characterization of the flow density and temperature as presented in Fig. 2.1 for an argon flow at 30 K. The 1-D profiles are used to determine the average density and temperature of the flow over the duration of the flow. From these measurements the average Mach number of the flow is known and can be used to convert the distance from the nozzle to the time it takes for the gas to go from the end of the nozzle to a position in the flow. This allows the determination of the "hydrodynamic time" of the nozzle i.e the time available with this nozzle to study time-dependent processes.

2-D maps such as that presented in Fig. 2.2 are used to determine the size of the isentropic core of the flow and its variation along the flow. They are also a way to present the boundary layer of the flow which is the region in between the cold-core and the residual warm gas in the chamber. In the boundary layer, the temperature increases rapidly from the temperature of the core to room temperature while the density drop. This layer can add warm gas contribution when using a perpendicular measuring technique.

The CRESU technique is a great tool to study chemical kinetics [9, 33] or more exotic spectroscopy [34] but still has some limitations. First, the gas being supersonic and the uniformity of the flow being limited in length leads to a hydrodynamic time ranging from 90 to 1300 µs being available to study kinetics. The reactant must be diluted to less than 1% of the flow for hydrodynamic considerations, so only relatively fast reactions can be

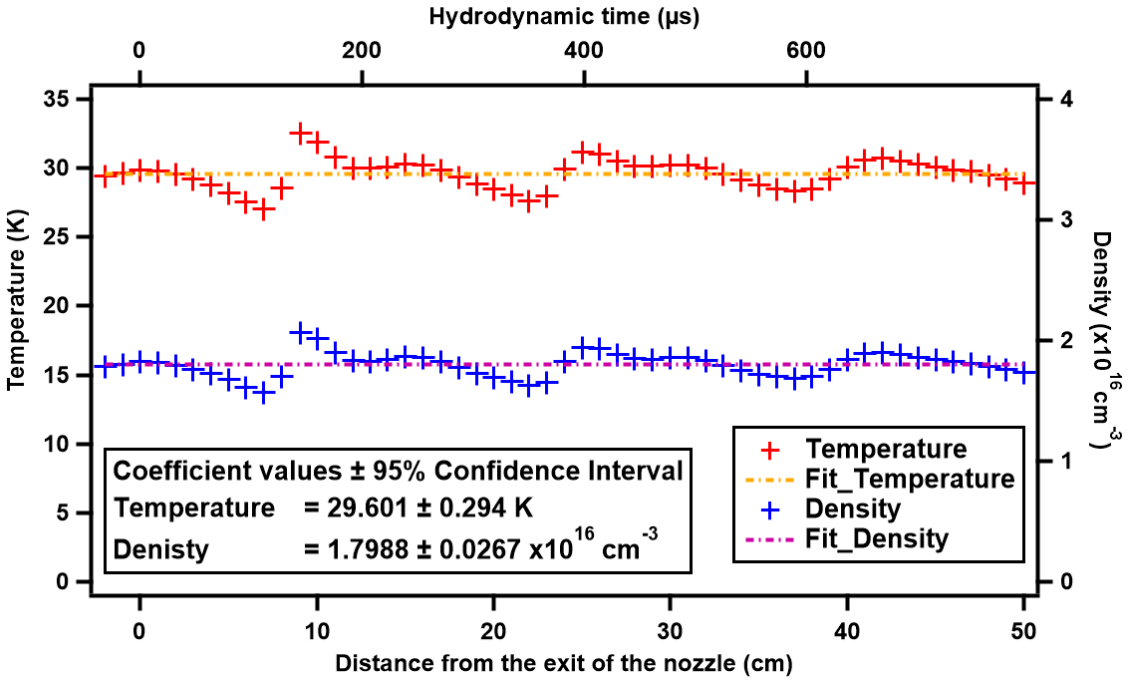

Figure 2.1: Pitot 1D profile of the Ar 30 K nozzle flow. In red the temperature and in blue the density. Dashed lines show the constant fit used to determine the average of the temperature and density along the flow.

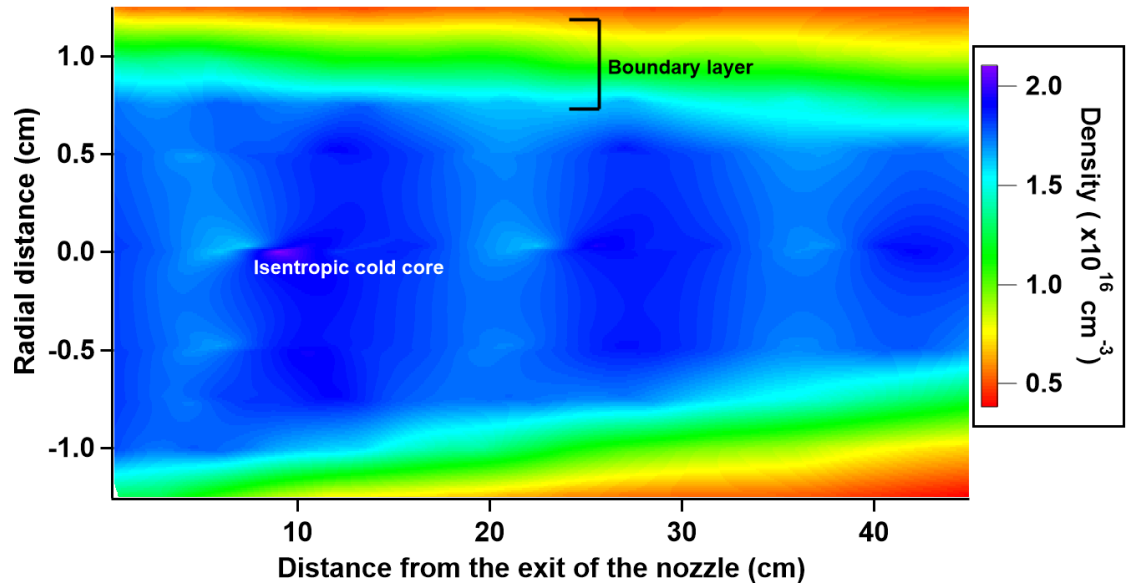

Figure 2.2: Pitot 2D map of the density of the Ar 30 K nozzle flow.

studied using this technique, typically involving radicals or ions. The rate coefficient of the reaction has to be on the order of 10^{-11} cm^{-3} s^{-1} or greater to be studied. In certain cases, it is possible to extend this limit down to 10^{-13} cm^{-3} s^{-1} when one of the reactants

can be used as the buffer as in the study of H_2 + F by Tizniti *et al.* [7]. The high density and cold temperature of the CRESU flow are favorable conditions for the formation of molecular clusters, which in certain experiments can also limit the amount of reagent or precursor that can be injected into the flows. Typically the CRESU technique is mostly used to study phenomena independent of the pressure (bimolecular reaction for example). It is possible to design a Laval nozzle with the same temperature and different pressure but the range of pressure accessible does not always allow to study in detail pressure dependant phenomena. A practical limitation is that in order to generate CRESU flows, a large quantity of gas is required (20 to 100 standard liters per minute) and industrial level pumping capacity is needed to keep the pressure in the chamber low enough (32000 m^3 h^{-1}). This leads to continuous CRESU apparatuses only being used in France at the Institut de Physique de Rennes and in Bordeaux [35] with a miniaturized version of the technique. The large pumping capacities required for these experiments render it impractical to transfer the technique to other laboratories. This is why a big emphasis has been put on developing pulsed CRESU apparatuses requiring less gas and smaller pumping capacity, which today are in use in laboratories throughout the world in Spain [36], the USA [28] and in the UK [14].

2.2 Quick introduction to rotational spectroscopy

Rotational spectroscopy is a powerful tool for the determination of molecular structure in physical chemistry [37–39]. In the work presented here, it is used as an analytical tool to identify and quantify molecules. This section presents the basic formalism used to describe rotational transitions.

Molecules are classified using the characteristic of their moment of inertia I. Three conventional axes a, b and c are used to determine the moment of inertia of molecules, conventionally c is the axis which has the maximum moment of inertia, a is perpendicular to c and is the axis with the minimum moment of inertia and b is the remaining perpendicular axis. Then according to convention we have:

$$I_c \geq I_b \geq I_a \tag{2.7}$$

Different classes of molecules can be distinguished from the relation between their moments of inertia:

The linear molecules such as HCN for which $I_c = I_b$,$I_a = 0$

The symmetric top molecules separate in prolate such as H_3CCN with $I_c > I_b = I_a$ and

oblate BCl_3 with $I_c = I_b > I_a$

The spherical to molecules such as CH_4 with $I_c = I_b = I_a$

The asymmetric top molecules such as formaldehyde with $I_c \neq I_b \neq I_a$

For linear molecules in the rigid rotor approximation the rotational term $F(J)$ can be expressed:

$$F(J) = \frac{h}{8\pi^2 cI} J(J+1) = BJ(J+1) \tag{2.8}$$

Where J is the rotational quantum number, c the speed of light and h Planck's constant. The rotational selection rule $\Delta J = \pm 1$ leads to pure rotational spectra presented in Fig. 2.3. Where the transitions are separated by $2B$ and the relative intensities of the lines follow the Boltzmann distribution:

$$\frac{N_{J''}}{N_{J'}} = \frac{g_{J''}}{g_{J'}} exp\left(-\frac{\Delta E}{k_B T}\right) \tag{2.9}$$

Where J'' refers to the upper state and J' the lower state. N is the population of the level, g is the degeneracy of the level and ΔE is the difference in energy between the two levels.

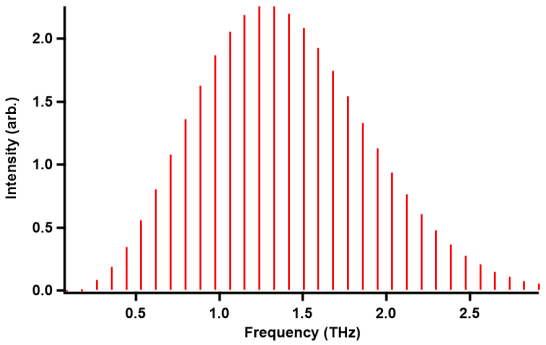

Figure 2.3: Pure rotational spectrum of HCN at 300 K generated using SPFIT/SPCAT (explained later).

On top of the simple model of the rigid rotor, multiple perturbations can be applied to represent more accurately experimental spectra. One of these perturbations is a centrifugal distortion which corrects for the fact that the rotor is not rigid but more accurately represented by a spring connecting the nuclei. This lead to the transition spacing decreasing with increasing J and $F(J)$ becoming:

$$F(J) = BJ(J+1) - DJ^2(J+1) \tag{2.10}$$

For symmetric tops two moments of inertia leads to two rotational constants: for example for a prolate top molecule:

$$A = \frac{h}{8\pi^2 c I_a} \qquad B = \frac{h}{8\pi^2 c I_b} \tag{2.11}$$

This lead to the introduction of the quantum number K which correspond to the projection of the rotational angular momentum along the a axis and the energy for a rotational level $F(J)$ (without centrifugal distortion) become:

$$F(J,K) = BJ(J+1) + (A-B)K^2 \tag{2.12}$$

The rotation states are labeled as J_K. And the centrifugal distortion, in this case, is now modeled by three constants D_J, D_{JK} and D_K which leads to $F(J)$ becoming:

$$F(J,K) = BJ(J+1) + (A-B)K^2 - D_J J^2(J+1) - D_{JK}J(J+1)K^2 - D_K K^4 \tag{2.13}$$

For asymmetric tops three moments of inertia lead to three rotational constants:

$$A = \frac{h}{8\pi^2 c I_a} \qquad B = \frac{h}{8\pi^2 c I_b} \qquad C = \frac{h}{8\pi^2 c I_c} \tag{2.14}$$

But in this case, the Hamiltonian can not be factored which means no simple expression can be written for the energy. The symmetric top molecules' energy levels are described by three quantum numbers J, K_a and K_c where K_a and K_c are the K values that the molecule would have in the limiting oblate and prolate cases, respectively. The rotation states are labeled as $J_{K_aK_c}$. Perturbation like centrifugal distortion also takes a more complicated form with more rotational constant needed to describe each phenomenon.

Using this formalism and more realistic Hamiltonian (adding more perturbations) allows for the calculation of the frequency of the transitions of molecules.

The transitions and information associated (quantum number, transition dipole moment, degeneracy...) are compiled in catalogs which can be found in online databases (for example The Cologne Database for Molecular Spectroscopy CDMS [40–42] or The Molecular Spectroscopy database of the Jet Propulsion Laboratory (JPL)). The system used by the community to generate these catalogs of lines is called SPFIT/SPCAT designed by Pickett *et al.* [43]. These two programs allow the generation of a catalog file for molecules using literature values for the input parameters (dipole moment, rotational constant...) or to fit these parameters from lists of measured transitions. These are power-

ful tools that in this work are used only to find the frequency of transitions and to rescale the relatives' intensities between transitions at different temperatures.

Time-domain pulsed rotational spectroscopy is similar to pulsed nuclear magnetic resonance (NMR). In a simplified way, when a sample of molecules with a dipole moment is excited by a pulse of resonant millimeter-wave the precessing molecules align their dipole moment with the electric field thus generating a macroscopic polarization of the sample. When the excitation is stopped the sample polarisation diminish as the system relaxes through light emission and non-radiative broadening phenomena (lifetime, Doppler, pressure...) decrease the coherent precession of the sample. The radiation emitted is called the Free Induction Decay (FID), as in NMR. It corresponds in the time domain to a decaying sine wave at the frequency of the excited rotational transition. The decay of the FID is dictated by broadening phenomena, a detailed presentation of the modeling is presented in section 2.4.

2.3 Chirped Pulse Fourier Transform millimeter Wave spectroscopy (CP-FTmmW)

Broadband chirped-pulse Fourier transform rotational spectroscopy was developed by Brooks Pate and coworkers [24] around 2008. This new technique benefited from the advancement in telecommunications technology which made it possible to develop a broadband instrument capable of recording a full spectrum in one acquisition thus greatly reducing the time it takes to measure rotational spectra. The technique differs for more classical microwave spectrometers by the way excitation pulses are generated. In classical instruments, excitation is mostly single frequency and in order to acquire a spectrum, the frequency and configuration of the instrument (cavity) have to be changed for each acquisition [44]. This is where chirped-pulse spectroscopy brings its big advantage, by relying on the development in telecommunications technology, especially in arbitrary waveform generators and broadband signal digitizers. The key of the technique is the generation of phase-coherent chirped-pulse microwaves pulses. Advanced arbitrary waveform generators allow adjusting pulse duration and sweep rate to be short compare to Free Induction decay (FID) dephasing, thus optimizing the polarisation of the sample.

The description of a sample macroscopic polarisation using fast frequency sweep has been previously described by McGurk *et al.* [45]. They showed that this type of excitation is an efficient way to polarize a sample. They derived from the optical Bloch equations that the signal from a chirped pulse excitation has the form:

$$S \propto \omega\mu^2 E_{pulse}\Delta N_0 \left(\frac{\pi}{\alpha}\right)^{1/2} \tag{2.15}$$

Where ω is the frequency, μ the transition dipole moment, E_{pulse} the electric field magnitude, ΔN_0 the population difference at equilibrium and α the sweep rate. This $\alpha^{-1/2}$ scaling is key as it means that for defined pulse duration, the signal decreases with the square root of the bandwidth, which differs from transform-limited pulses, where the decrease is linear. That difference comes from the fact that for linear swept chirp the amount of energy delivered to the sample is not dependent on the bandwidth because the bandwidth can be modified without changing the pulse length in contrast to transform-limited pulses.

The technique quickly flourished with multiple instruments being built around the world [46–50] and represents a major advance, allowing the structural specificity of rotational spectroscopy to be used in the field of reaction dynamics and kinetics.

2.4 Modeling of the FID dephasing

The signal recorded in a CP-FTmmW spectrometer is the Free Induction Decay (FID), which is the characteristic decay back to equilibrium of a sample polarized by an external electric field. This polarization is described by the optical Bloch equations [51]. For the linear fast passage regime, in which most microwave or millimeter-wave chirped-pulse spectrometers aim to operate, the polarization magnitude has been solved before for chirped excitation pulse [45, 52–54]. The model was also solved for situations using only $\pi/2$ single-frequency pulses [52, 55], which most CP-FTmmW spectrometers are capable of producing. We focus here on the shape of the FID after the polarizing pulse is turned off and the dipoles are freely precessing.

The simplest description of the shape of the FID is given only in terms of homogeneous decay, dictated by the phenomenological decay constant T_2 in the optical Bloch equations [52]. This describes the decay of coherence within a polarized system, which includes the rate of decay by collisional rotational inelastic energy transfer, as well as elastic or phase changing collisions [56]. The decay constant T_2 is related to the pressure broadening rate by $T_2 = 1/(2\pi\gamma_{Pres}p)$, where γ_{Pres} is the pressure broadening coefficient and p is the gas pressure. The linewidth of a pressure broadened signal in the frequency domain is thereby related to the decay time of the polarized sample in the time domain. Microwave spectroscopy is frequently performed in the limit where Doppler broadening or decay is the dominant dephasing mechanism. The shape of the FID is no longer dom-

inated by the pressure decay rate and must include the Doppler decay rate. Within this limit, a simple form of the exponential decay function fails to describe the system and it is necessary to include a Gaussian type function as well [57].

Experiments to monitor pressure broadening in FIDs were among the first performed using FTmmW techniques. The first experiments often measured self-broadening rates, using OCS [58] and NH_3 [59], where pressure broadening decay rates are high enough that the Doppler decay could be ignored. Collisions with foreign colliders, at first, did not include Doppler broadening in their fitting of experimental data [60]. Later, Mäder and coworkers studied pressure broadening rates between different molecules and various rare and diatomic gas colliders, where accurately accounting for Doppler decay was important for disentangling the pressure decay rates [61–66] specifically using the time domain Voigt profile. The decay profile was used for both line position and pressure broadening determination, as it yielded quite accurate results for both [67]. Eventually, this profile was superseded with the inclusion of the speed dependence of collisions [68, 69], but this additional rate of relaxation was found to have minimal effect on He collisions with other molecules [70].

The time-domain Voigt profile is the Fourier transform of the commonly used Voigt function, which is a convolution of the Gaussian and Lorentzian functions, representing the Doppler and pressure broadened components of a transition profile. Eq. 2.16 shows the time domain Voigt function taken from the derivation of the Fourier transform of a Voigt function for use in spectroscopy [71]:

$$f(t) = A.exp\left(-2\pi\Delta\nu_{Pres}t - \frac{\pi^2\Delta\nu_{Dopp}^2 t^2}{ln(2)}\right) cos(2\pi\nu_0 t + \theta) \tag{2.16}$$

where $f(t)$ is the signal intensity as a function of time, A is the initial amplitude of the FID, $\Delta\nu_{Pres}$ is the pressure broadening rate, $\Delta\nu_{Dopp}$ is the Doppler broadening rate, ν_0 is the center frequency of the transition, and θ is the phase of the signal. The phase and amplitude fitting parameters were included in Eq. 2.16 from comparison with the equation used by Haekel and Mäder, where these parameters were found to have assisted in the fitting of experimental data [67]. The measured pressure broadening rate $\Delta\nu_{Pres}$ is related to the temperature-dependent pressure broadening coefficient $\gamma_{Pres}(T)$ by $\Delta\nu_{Pres} = \gamma_{Pres}(T) \times p$. By plotting $\Delta\nu_{Pres}$ vs. p, the pressure broadening coefficient can be found at a specific temperature. The Doppler decay rate is the Doppler half-width at half max (HWHM) of the frequency domain signal. The fitting model used by Haekel and Mäder constrained the Doppler component to its theoretical value [67], but in the

experiment described in the next chapters, it was found that the Doppler component could be fit along with the other fitting parameters in the model using a non-linear least-squares fitting algorithm [72].

2.5 Quick introduction to reaction kinetics

This section presents the concepts of reactions kinetics relevant to the work of this thesis, focusing only on bimolecular reactions. For example, using the chemical equation:

$$\mathrm{A} + \mathrm{B} \longrightarrow \mathrm{C} + \mathrm{D} \tag{2.17}$$

The rate at which the reactant A is consumed is expressed:

$$-\frac{d[\mathrm{A}]}{dt} = k[\mathrm{A}][\mathrm{B}] \tag{2.18}$$

Where k is the bimolecular rate coefficient expressed in cm^3 $\mathrm{molecule}^{-1}$ s^{-1}. This rate corresponds to the efficiency of the reaction and is one of the parameters inputted into the reaction networks used to model the observed astrochemical environments. In order to measure this rate laboratory experiments are usually conducted under pseudo-first-order conditions, where the concentration of one reactant (B in this case) is present in excess compare to the other. In these conditions, the variation of the concentration of B is neglected and equation 2.18 becomes:

$$-\frac{d[\mathrm{A}]}{dt} = k'[\mathrm{A}] \tag{2.19}$$

Where $k' = k[\mathrm{B}]$, this implies that under pseudo-first-order conditions the rat coefficient of a reaction can be measure by measuring the variation in concentration of only one of the reactants. This makes PLP-LIF a perfect technique to measure rate coefficient especially of radial-neutral reaction as it is sensitive enough to detect the variation of the concentration of the radical. One important aspect for astrochemistry is that the rate coefficient can vary over temperature $k(T)$ which means that measurement needs to be carried varying the temperature and low enough that it is relevant to astrochemical environments. The variation of the rate in function of the temperature is often expressed by the Arrhenius equation:

$$k(T) = A\ exp(-E_A/T) \tag{2.20}$$

Where A is a pre-exponential factor, E_a the activation energy and T the temperature.

The measured and computed rates are compiled in astrochemical databases such as the KInetic Database for Astrochemistry (KIDA) [73] which can then be used in reaction networks to simulated chemistry in astrochemical environments.

The second parameter important for this study and for modeling already discussed in the introduction is the branching fraction between multiple channels of a reaction. If this time the reaction possess multiple channels:

$$\begin{aligned} \mathrm{A}+\mathrm{B} \longrightarrow\ & \mathrm{C}+\mathrm{D} && (a) \\ & \mathrm{E}+\mathrm{F} && (b) \\ & \mathrm{G}+\mathrm{H} && (c) \end{aligned} \tag{2.21}$$

In this case for each channel, a specific rate can be defined $k = k_a + k_b + k_c$. In order to further improve the understanding of such reactions these specific rates, or their relative importance: the branching fractions need to be measured and such as the overall rate the measure has to be performed in function of the temperature as potentially the fraction could change with the temperature.

2.6 Room temperature flow cell

As a first tool for characterization of the new spectrometer on molecular samples, a room temperature flow cell was designed and built. A schematic of the cell is presented in Fig. 2.4. It is a 16 cm diameter, 1.5 m long cell separated into three parts. ISO 160 flanges connect the different parts and terminate each end. The cell is fitted with 8 ISO KF 40 half nipples to accommodate gas inputs, pressure gauges and vacuum pumps. The ends of the cell are closed with 1 cm thick 10 cm diameter wedged Teflon windows. The interior of the cell is lined with 2 cm millimeter-wave absorptive foam (Eccosorb HR-10 Laird). The wedge on the window and the absorptive covering is required to reduce reflections of the polarising microwave pulse. The effect of reflections on the system will be presented later. This cell was used for the first characterization of the spectrometer on molecular samples and in the measurement of room temperature pressure broadening rate between OCS and He, which are presented in chapter 3.

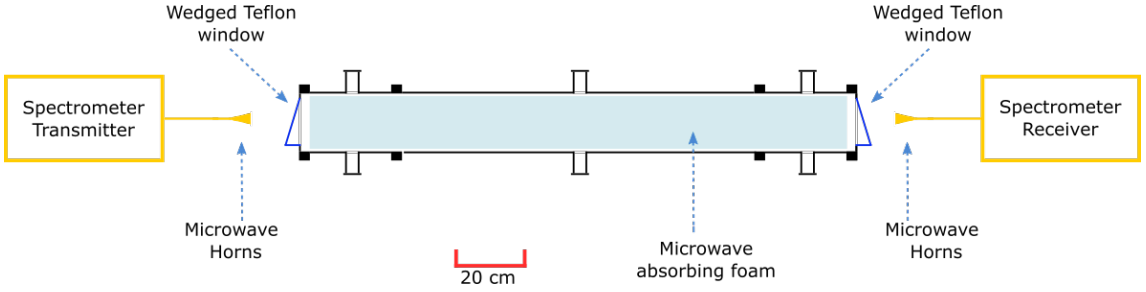

Figure 2.4: Schematic of the room temperature flow cell used for the experiments presented in chapter 3

.

2.7 The CRESU apparatus

This section focuses on the CRESU aspect of the experimental setup. The first section presents the new CRESU chamber followed by a description of the instruments associated with the generation of radicals in the chamber. The last section briefly presents the LabVIEW interface of the experiment.

2.7.1 CRESU chamber

A new CRESU chamber dedicated to CPUF measurements has been designed and built. A scaled schematic is presented in Fig.2.5. It is constructed from 0.5 m diameter stainless steel tube and is ∼3 m long. Its design combines aspects of existing CRESU chambers that have been built in Rennes [19, 74] and Birmingham [75] over the last few decades. It was constructed in four separate sections, each of them mounted on chassis fitted with vertical adjustments to allow careful alignment of the sections. Almost all the components of the chamber were constructed in-house at the university workshop. A four-way cross (MDC Vacuum products) at the end connects the chamber to a Roots blower 32000 m^3 h^{-1} pumping group (Pfeiffer Vacuum) via a motorized butterfly valve (Pro-axiss). The valve enables isolation from the pumps and throttling to adjust the pumping capacity and thus the pressure in the chamber. The cross is also connected to a second CRESU chamber used for Pulsed-Laser Photolysis Laser-Induced Fluorescence (PLP-LIF) studies that was designed and built previously and is described by James *et al.* [75]. The other two ports of the cross are connected to Brewster windows mounted on ISO KF 40 flanges that allow the photolysis laser beam to pass through either the CPUF or LIF chambers (region E in Fig. 2.5).

The three other sections of the CPUF chamber (regions A, C and D in 2.5) were

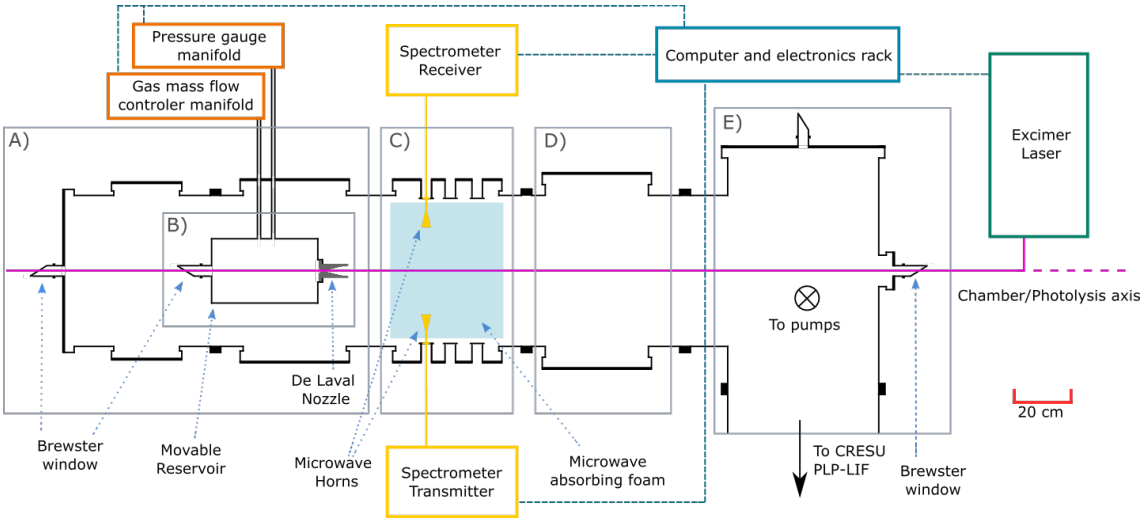

Figure 2.5: Scale schematic of the CRESUCHIRP chamber with representation of the supporting instrumentation. Five regions are distinguished to facilitate their description in the text. A) is the "CRESU" section, B) the reservoir, C) the probing region, D) the skimmer section and E) the "coupling" section.

all designed in order to be accessible for future adaptations of the experiment and for maintenance with ISO 320 flanges on the sides and ISO 200 flanges on the top and bottom. Multiple ISO KF 40 ports are mounted on these flanges, allowing for the coupling of various feed-throughs required for the experiment as well as extra ports for the future development of the chamber.

The CRESU reservoir is installed on a translation table inside the vacuum chamber. The table is mounted on the chamber using adjustable connections that allow a careful alignment of the reservoir on the chamber axis along the whole length of the chamber. The table is fitted with a motorized translation system driven by a linear displacement stage with 1 meter of travel (model TBVI 20UUOPB from ECMU-CSR) coupled to a braked stepper motor (Stogra SM88.1.18ML8 V Z385) driven by an in-house controller fitted with a step controller (Parker XLi 80) allowing movement of the reservoir along the chamber axis in order to vary the position between the exit of the Laval nozzle (in region B in 2.5) and the probing region (region C in 2.5) with a travel range of 60 cm. It is possible to choose the region of the flow in which the molecules are being probed by the CP-FTmmW spectrometer and the hydrodynamic time available for kinetic measurements by moving the position of the reservoir relative to the position of the spectrometer. The position of the reservoir is measured in real-time using a potentiometric ruler (model PTX 101-0050-112-1110 from ARM).

The reservoir itself (region B in 2.5) is a tube (300 mm long, 215mm inner diameter)

$\sim$11 L in volume closed on one end by a flange supporting the Laval nozzle and on the other end by a flange fitted with the gas inputs that include an independent input for the buffer, precursor as well as a Brewster window (fitted with gas input for purging). The reservoir is entirely Teflon coated in order to minimize wall reactions due to collisions with the metallic walls. A diffusing plate in Teflon (170 mm in diameter and 3 mm thick fitted with hundreds of 6 mm diameter holes spread as a grid, one larger hole 30 mm diameter allowing for the laser beam to pass through the reservoir) is mounted in the middle of the reservoir to facilitate gas mixing and generate a laminar flow at the entry into the convergent part of the Laval nozzle.

Figure 2.6: Picture of the two CRESU chambers on the left the CRESUCHIRP apparatus and on the right the PLP-LIF apparatus.

Flexible bellows run from the reservoir to outside of the chamber to connect to a gas manifold from which the gases are delivered to the reservoir. Other bellows lead to a pressure manifold equipped with capacitance gauges (Brooks XacTorr CMX0) which allow for absolute measurement of the reservoir and chamber pressures essential to the establishment of reproducible CRESU flows.

The gases are introduced from the gas manifold which is equipped with multiple mass

flow controllers covering different flow ranges. The main buffer gases used to generate the CRESU flow (Air Liquide He,$\geq$ 99.995% N_2,$\geq$ 99.995% Ar,$\geq$ 99.998%) are delivered using a (Brooks SLA5800 series) 100 slm flow controller. Flow controllers ranging from 20 sccm to 5 slm (Brooks GF series) are used to introduce the reactants. Reactant precursor molecules can be introduced from a separate line via sublimation (if solid at room temperature) by passing a controlled flow of buffer gas through a glass vessel fitted with a porous glass frit (the vessel is equipped with a pressure gauge (MKS Baratron Gauge, Type 626). Vaporized liquids are introduced in a quantitative manner through a controlled evaporation and mixing system (CEM) (described in Gupta *et al.* [76]) that mixes the gas stream with the output of the mass flow controllers.

Chronologically, the chamber was first built without the region C of Fig. 2.5. As the project evolved, this section was added to the chamber to incorporate a section with a secondary expansion through a skimmer. The reason behind this addition will be discussed in the perspective section of this thesis. The main results presented here did not require this addition but some of the measurements that are used to represent technical development on acquisition and data analysis were taken using this system (indicated in the caption of the figures). The details of the addition will appear in the thesis of Omar Abdelkader Khedaoui. Briefly, this addition incorporates a secondary expansion chamber installed inside the CRESU chamber and aligned on the chamber axis. This chamber is differentially pumped by a turbomolecular pump and is arranged on the chamber axis with a Brewster window on one side and a skimmer on the other side. Fig. 2.6 presents a picture of the two CRESU apparatus.

2.7.2 Photolysis set up and radical precursor concentration

The CRESU technique as implemented in Rennes is by design a continuous and stable system where gas flow is the same at all times (excluding the pulsed CRESU technique, not being installed yet on our experimental apparatus). In order to study dynamic processes, this steady-state needs to be perturbed. In our experiments, the perturbation arises from a laser pulse being fired along the axis of the flow. For the experiment presented in this work, the photolysis source is an excimer laser (Coherent LPX pro 210) which can operate at 351, 248 or 193 nm. The laser beam is aligned along the chamber/flow axis and is transmitted through the chamber via three vacuum windows mounted at the Brewster angle (mounted on ISO KF 40 port at each extremity of the chamber and at the back of the reservoir) in UV grade fused silica (Crystran). The Brewster windows were designed taking into account the size of the laser beam in order to allow a maximum of laser light

through the chamber. An iris placed at the entrance of the chamber is then used to control the size of the beam inside the chamber, to match it to the size of the isentropic core of the nozzle in use. The laser beam propagates from the laser head to the chamber through PVC pipes and boxes which can be purged with nitrogen when using 193 nm wavelength to avoid the generation of ozone in the air along the beam path, which would drastically lower the power transmitted inside the chamber. The laser beam is used to photodissociate precursor species within the flow. When used for kinetics experiments, it is used to generate radicals in the flow which then initiate the reaction. The fluence of the laser can be measured using a laser power meter (Molectron) attached at the end of the chamber on the ISO KF 40 port in place of the Brewster window or placed directly in the chamber when not under vacuum.

A UV/Vis spectrometer coupled to an absorption cell and a deuterated lamp enables the measurement of precursor (more details about it can be found in Divitas Gupta's thesis). The UV-Vis cell is 63 cm long and has quartz windows at its two ends, followed by lenses. The light source (oceaninsight DH2000-DUV) has two options, a deuterium lamp and a halogen lamp to cover a complete range of 190-2500 nm transmitted via an optic fiber (QP600-2-XSR). On the other end, another optic fiber is used to transmit the light, after the absorption by the compound (BrCN in this case) in the cell, to a Maya2000-Pro spectrometer fitted with an Ocean Optics H5 grating to provide a resolution of 0.16 nm. This system provides an absolute measurement of the precursor injected into the CRESU flow. In this work the precursor used is BrCN which when photolyzed at 193 nm generates the radical CN with which reactions are studied. BrCN is a solid compound and was placed on a glass frit in a 30 cm long glass vessel traversed a controlled buffer gas flow the pressure was adjusted within the glass vessel by means of a valve downstream. The returning vapor flow was passed through the UV/Vis absorption cell before being injected into the CRESU flow. Measurement with this setup showed different results than simple calculations using the vapor pressure of BrCN and the pressure of the precursor cell. These differences probably come from the cooling of the BrCN due to its sublimation.

The intensity (I_o) of the deuterium lamp source over the wavelength range 200-250 nm and the background/stray intensity (I_{off}) with the lamp off was measured using the Ocean View software. The intensity measurement (I) when BrCN is flowing through the UV-Vis cell was then input into the Beer Lambert's law $ln((I - I_{off}/(I_0 - I_{off})) = \sigma N d$ where σ is the BrCN absorption cross-section measured by Felps *et al.* [77], d is the length of UV-Vis cell and N is the number density of the species. The number density calculated was averaged over the measured wavelength range of 200-250 nm, which was then used to

calculate the BrCN number density in the main CRESU flow. Using this number density, the laser fluence at 193 nm and the absorption cross-section of BrCN, the number density of CN radicals generated can be estimated.

2.7.3 LabVIEW interface and control of the apparatus

The whole experiment can be controlled from the main computer which communicates with every instrument through a LabVIEW (National Instruments, version 2014) interface designed with the help of Luc Briand, an L3 intern under my supervision at the time. The program is designed to keep experimental parameters accessible and updated at all times. It is built using asynchronous running of Virtual Instruments (VIs) dedicated to each part of the experiment. Using this type of programming, the different sub-VIs are updated independently. Performing an action on one instrument leaves all of the other instruments to maintain communication to the computer at any time. The program is designed to be able to follow at any time the pressures and gas flows related to the experiment which are the most critical experimental parameters. The presentation of the program structure and front panel of the program can be found in the appendix. The bottom part of the screen allows for switching between different panels that control different parts of the experiment that are used less frequently. They include the panel where the parameters for the generation of the input file for the arbitrary waveform generation (AWG) controlling the excitation pulse characteristics can be modified and the panels which control the AWG and the digitizer. The program controls the acquisition of the data from the digitizer panel and for each acquisition generates a summary file logging all the parameters and measurements of the program at the time the acquisition is started. It automatically organizes and names all of the files on a by-date basis. The program is designed to be easy to expand with new features or instruments. A standardized method of designing sub-VIs, a versioning scheme and a log file allow keeping track of modification over time. The program controls the spectrometer through the AWG and the digitizer. The generation of the waveforms generated by the AWG broadcast and by the spectrometer is also handled by the program. The CRESU part of the experiment is controlled through the interface with the mass flow controllers (10 of them from two different manufacturers) and the pressure gauges (8 of them from two different manufacturers) with the possibility to easily add more for dedicated set up on the side (such as the UV/Vis cell). The reservoir position and displacement are handled by the program which also stores the Laval nozzles conditions and parameters.

2.8 Spectrometer description and characterization

A new chirped-pulse Fourier transform millimeter-wave (CP-FTmmW) spectrometer operating in the E-band (60-90 GHz) has been constructed, incorporating numerous advances in millimeter wave technology that had not been available to previous spectrometers operating in this frequency range [30, 54, 78, 79], but were available to spectrometers operating at lower frequencies [24]. In particular, a PIN diode switch and a low noise amplifier (LNA) operating at E-band frequencies were purchased from commercial vendors. Furthermore, relatively high-power amplifiers for this frequency range were used to maximize the polarizing signal. The design of the millimeter chain was done by Brian Hays. Schematics of the spectrometer in two configurations using different acquisition devices are presented in Fig. 2.7 and 2.8.

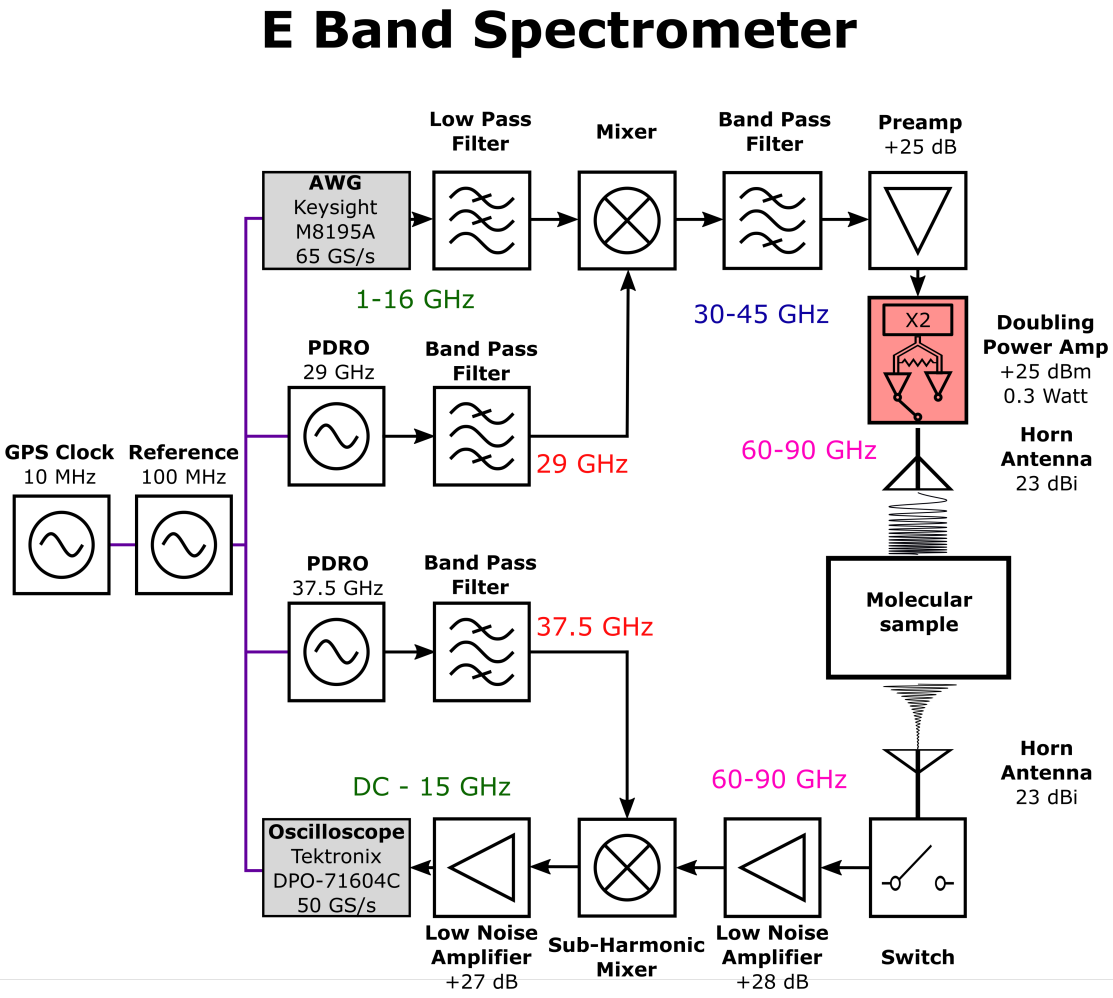

Figure 2.7: Schematic of the E-band spectrometer using the oscilloscope as the acquisition device

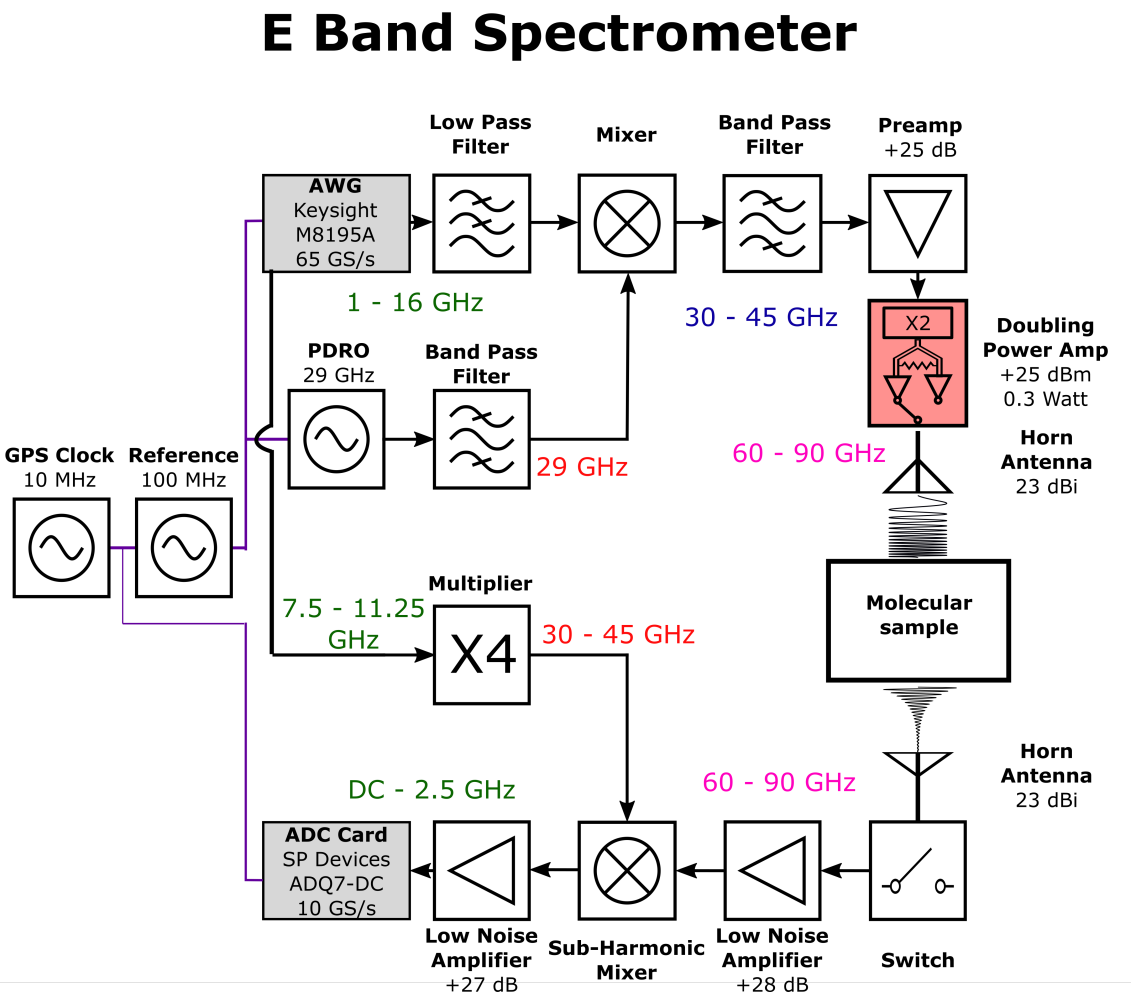

Figure 2.8: Schematic of the E-band spectrometer using the digitizer as the acquisition device

The spectrometer is mounted on two independent 1.15 m high tables (receiver and transmitter) built-in 60×60 aluminum profile for sturdiness and easy mounting of equipment. On top of each, an optical breadboard allows for optical post assembly to permit fine alignment of the waveguide for coupling with the fixed element of the experiment. The mountings for all of the microwave components are installed on the table. Some of them are mounted on heat-sink blocks to be maintained at a constant temperature of 25°C by a water chiller (ACCEL series 250 PHP) in order to maintain the stability of the components through long experiments. The water circulation circuit of each table is fitted at the end with quick-connect connection that allows to easily disconnect the water without spilling it. The chiller runs the water through the two tables in a loop, stabilizing any connected component at 0.1°C. In-house power supply systems standardize and make easy

the powering of any microwave component and make it impossible to power a component with the wrong voltages (the individual power supply modules come from Acopian).

The up-conversion side of the spectrometer is similar to the design of Zaleski *et al.*, but accomplished at a higher frequency range [48]. An arbitrary waveform generator (AWG, Keysight M8195A, 64 GS/s 18 GHz hardware bandwidth) was used to produce frequencies in the range of 1–16 GHz. The signal from the AWG was up-converted in a mixer (Marki M11850H) using a phase-locked dielectric resonator oscillator (PDRO, Microwave Dynamics PLO-2070–29.00) operating at 29 GHz as the local oscillator (LO) source. The upper sideband is selected using a broadband high-pass filter (Reactel 9HS-X30/45G- K11R) before entering the preamplifier (Quinstar QPW-205020525-J0). This signal is then input into a Quinstar integrated system (QBM-609025E0U0R) that includes a passive frequency doubler to bring the frequency range to 60–90 GHz (Quinstar QPM-75002E), a waveguide splitter (Quinstar QJH-EUFBZIL), two millimeter-wave power amplifiers (Quinstar QPW-60752530-C2W0 and Quinstar QPW-75902530-C2W0), and a waveguide switch (Quinstar QWZ-ET2800). One amplifier operates between 60–75 GHz while the other operates between 75–90 GHz. Both amplifiers output about 300 mW of RF power over each band, with significant power up to 94 GHz for the higher frequency amplifier. The amplifiers are controlled via TTL signals for fast turn-on and turn-off times of less than 20 ns. The waveguide switch is a low-loss (0.7 dB) but slow (50 ms) electro-mechanical switch which selects the amplifier to be used. The radiation is output through a 23 dBi gain horn antenna (Quinstar QWH-EPRR00). Fig.2.9 presents a picture of the Quinstar integrated system.

The receiver system incorporates many advances in commercial millimeter wave technology, especially high-frequency LNAs and switches that were mentioned but unavailable when Park *et al.* made their first high-frequency spectrometer in 2011 [54]. The start of the receiver system is an identical horn antenna (Quinstar QWH-EPRR00) followed by a variable attenuator that attenuates signals by up to 30 dB (Quinstar QAL-E00000), for monitoring pulse power while running experiments. The signal then enters a fast single pole-single throw PIN switch operating in the 60–90 GHz range (Millimeter Wave Products 911E/387TTL). The switch has a 10 ns 10% -90% rise time to either transmission or isolation, with around 3 dB insertion loss across the band, and over 30 dB of isolation. This switch protects the next element, the millimeter-wave LNA, from the initial polarizing pulse. The LNA (Millitech LNA-12–02,350) has (28 ±4) dB of gain across the 60–90 GHz range. It has a 3 dB noise figure, rising to 4.5 dB below 67 GHz. After the low-noise amplifier is a subharmonic mixer (Virginia Diodes WR12SHM), which has a dual side-

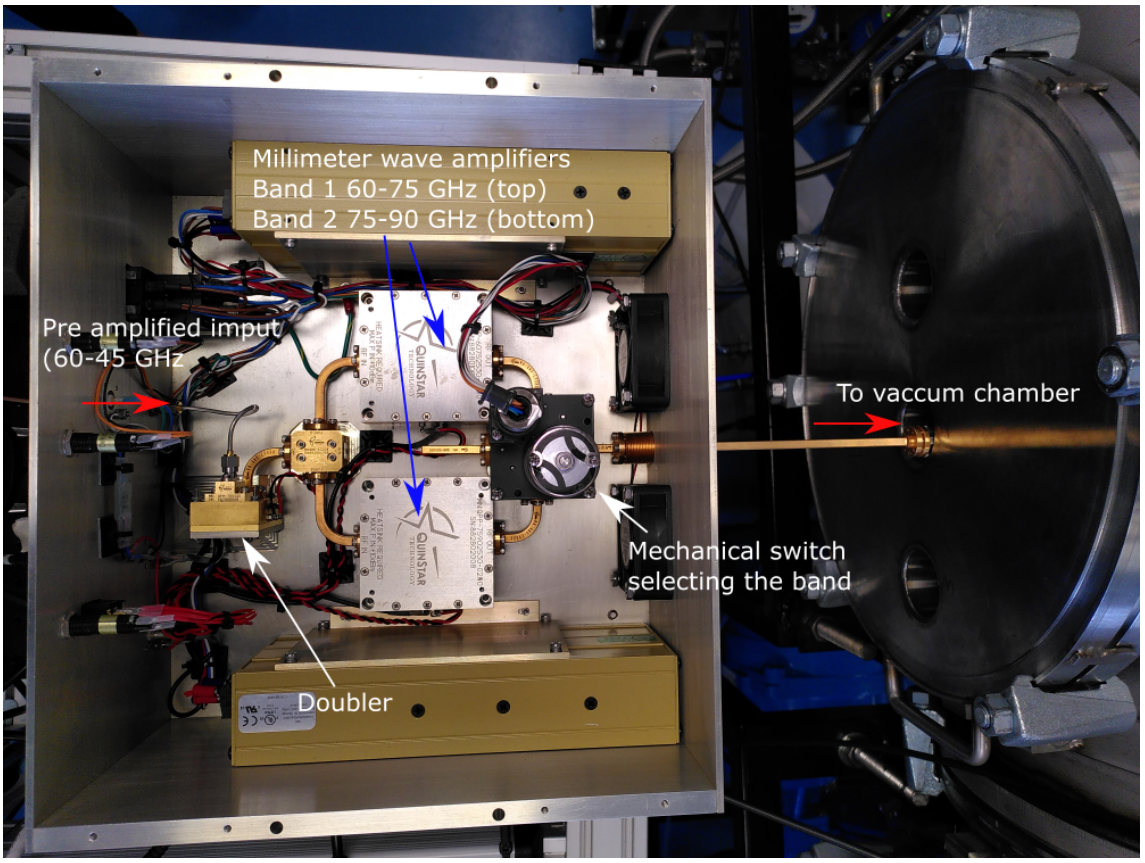

Figure 2.9: Picture of the inside of the Quinstar integrated system with the millimeter wave components involved in the last up-conversion stage.

band conversion loss of 6 dB with a 3 dB bandwidth of DC-15 GHz at the intermediate frequency (IF) port. The output from the IF is further amplified using a LNA with 25 dB of gain and a 2.5 dB noise figure (Miteq AFS4-0 0,101,800–25-S-4). The choice of the LO source is determined by whether an oscilloscope or a digitizer card is used to record the heterodyned signal. The LO can come from one of two sources: a PDRO operating at 37.5 GHz (Microwave Dynamics PLO-2070–37.50) or the second channel of the AWG sent through a quadrupler (Quinstar QMM-38,150,504 J) providing an LO between 30–45 GHz. Fig. 2.10 presents a picture of the receiver.

The oscilloscope is a Tektronix DPO 71604C with 16 GHz of analog bandwidth and is capable of running at 100 GS/s; however, it is normally used at 50 GS/s for faster data processing. The oscilloscope provides broadband capabilities as well as flexible modes of operation, particularly FastFrame (a proprietary software from Tektronix). However, the oscilloscope cannot operate multiplexed acquisition schemes at the processing speeds needed for high data throughput experiments, so a digitizer is used instead for the experiment and the oscilloscope is used for troubleshooting and characterization of the instru-

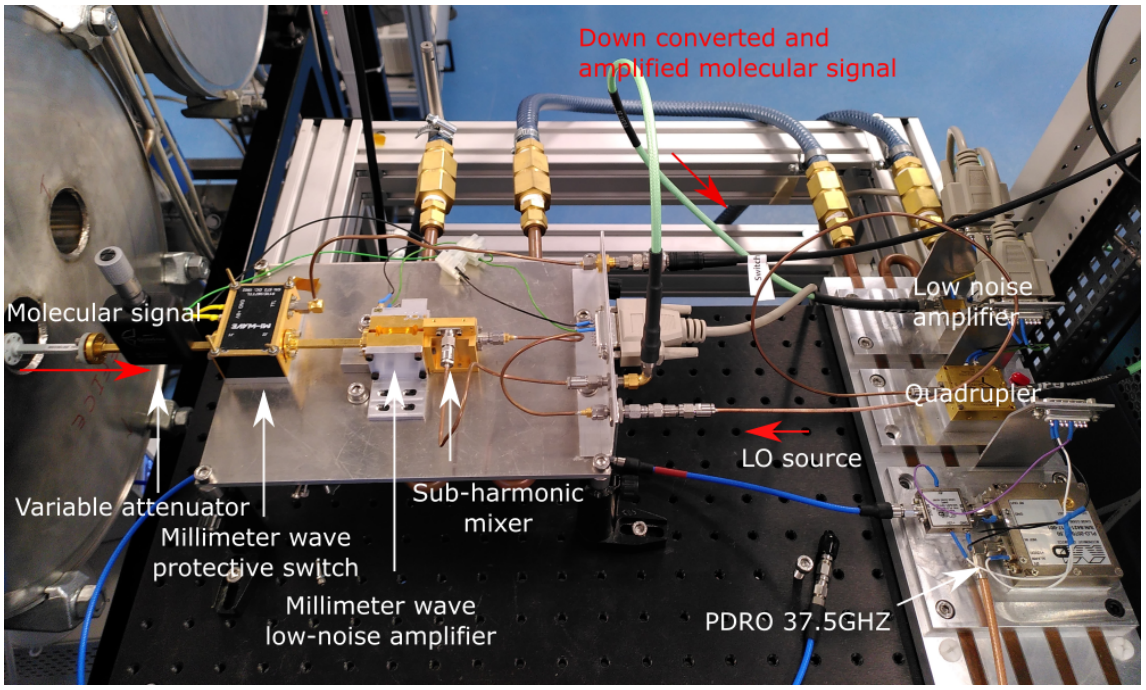

Figure 2.10: Picture of the E-band spectrometer receiver with each component involved in the down conversion and amplification of the molecular signal

ment. The digitizer is a Teledyne SP Devices ADQ7DC-PCIE card running at 10 GS/s with a 2.5 GHz 3 dB bandwidth.

The oscilloscope and digitizer are triggered by pulses from an AWG marker channel. The switch and pulsed amplifiers are controlled by a BNC 577 digital pulse/delay generator (DDG), which is triggered by another marker channel on the AWG. Each cycle of the experiment is conducted in a manner to protect the low noise receiver from the intense polarizing pulse so that the polarizing pulse does not damage the LNA. Most of the system, particularly the AWG, the PDRO's, and the oscilloscope, is synchronized to a 100 MHz oven-controlled crystal oscillator (Precision Test Systems GPS10-eR-50) which is locked to a GPS-disciplined Rb clock (Stanford Research Systems FS740) operating at 10 MHz. The higher-frequency 100 MHz signal is used to improve phase stability compared to the lower-frequency 10 MHz standard [80]. The digitizer and the DDG are synchronized to the 10 MHz clock.

The spectral purity of a chirp across each band was measured using the oscilloscope with the PDRO as the LO source and without the LNAs or the switch in the signal path. An attenuator was used before the mixer to ensure that the high-powered chirped-pulse signal would not exceed the linear response regime. The PDRO provides a pure and filtered LO source for down-conversion, while the oscilloscope provides a wide bandwidth of 16

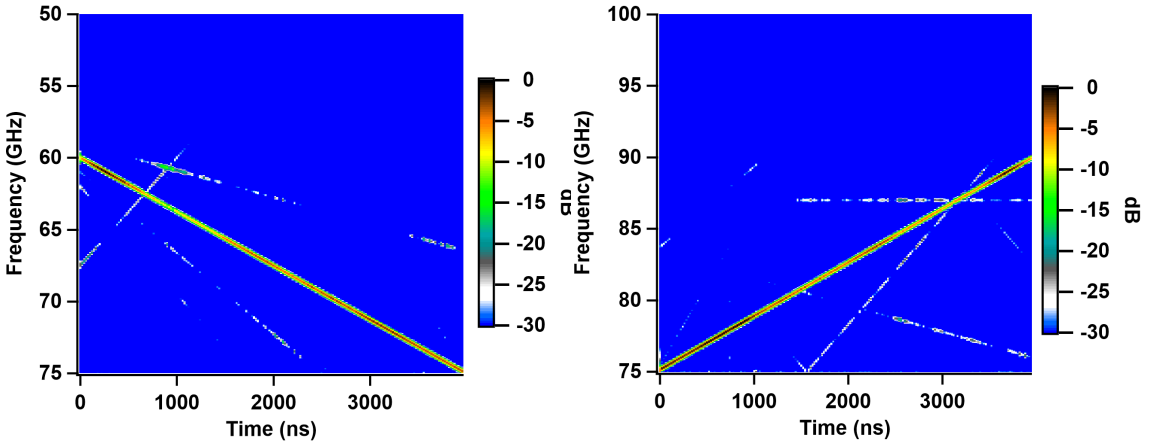

(a) (b)

Figure 2.11: Spectrograms of a) 60—75 GHz (15 GHz—DC at IF) and b) 75—90 (DC—15 GHz at IF) are shown. The dynamic range is 30 dB. The spectrograms in plot a) are 2 dB higher in total intensity.

GHz with a flat frequency response of ± 0.5 dB using digital signal processing within the oscilloscope. Frequency chirps lasting 5 µs, extending across the full bandwidth of each amplifier, were used to test the frequency response of the transmitter. Spectrograms were constructed using 1000 time points per spectrum with 198 spectra, and are shown in Fig. 2.11a (60—75 GHz) and Fig. 2.11b (75—90 GHz). The spectral response of the system was found to vary by about 5 dB across the bandwidth with major spurs recorded at less than 20 dBc, as can be seen in Fig. 2.11a and 2.11b. The major exception to this is around 64 GHz, where there was a significant reduction in the intensity of the main signal as well as an increase in the spurious content. This spur can be reduced by providing more power directly into the doubler, but this compresses the signal at other frequencies and introduces unwanted, sharp intensity variations. The up-conversion scheme produces some harmonic spurs, but these were not the dominant spurs in the spectrum. However, a third harmonic of the up-conversion PDRO did bleed through into the chirp in the higher frequency band. Higher input power into the integrated system increases harmonic content without increasing the overall spectral intensity, indicating that the overall system was operating near compression or saturation. The switches currently available in the E-band are not as high performance as those in lower frequency spectrometers; the isolation is often below 40 dB. However, with short chirps, the electronics do not seem to have reached the damage threshold, especially in the high-frequency LNA and sub-harmonic mixer. There is, however, some recovery time observed that appears to be purely electronic due to the high power of the polarizing pulse bleeding through the switch.

When using the digitizer, the PDRO is replaced with the quadrupled output of the

Table 2.1: Presentation of the different configurations of the digitizer tested and used for the work of this thesis. The analog bandwidth is not affected by this change in digital bandwidth and is around 3GHz for this model of digitizer.

Sampleskip factor	Sample rate (GS/s)	maximum recording time (µs)
1	10	200
2	5	400
4	2.5	800
8	1.25	1600

AWG as the LO. Using the same reference source as the pulse production in the receiver helps reduce phase fluctuations [49]. This provided a LO source that allows the digitizer to cover the entire range of the spectrometer in segments [50]. The digitizer is capable of fast averaging, recording up to 200 µs of 14-bit data at 10 GS/s up to 262 144 times in an FPGA accumulator with a 20 ns rearm time. High duty cycle experiments can be performed in this mode of operation, as well as experiments using a wide variety of pulse sequences over the recording time. The digitizer can complete a 200 µs collection cycle 100k times in less than a minute, running at a rate higher than 4.5 kHz with a duty cycle higher than 90%. The digitizer also has the capability to lower its sampling rate. This is performed by having the card skip the recording of a predetermined number of samples within the sampling cycle. For example, skipping 7 samples reduces the sampling rate to 1.25 GS/s and thus allows 1600 µs of kinetic time to be recorded. By adjusting this "sampleskip" factor it is possible to adjust the recording time, the relation between this factor, the sample rate and the maximum recording time is simple as this digitizer only interleaves two ADCs to records the data. Table 2.1 summarises the different configurations tested and used with this system. This reduction of the sample rate does not really come at the cost of the bandwidth as it is still possible to observed transition over the Nyquist frequency at their aliased frequency. This is not a limitation for the type of experiment realized with this system as the frequencies of the transitions detected are always known which makes identifying aliased frequencies an easy problem.

The combination of the digitizer with the quadrupled AWG output as the LO introduced some issues. The quadrupler is not as pure a source for the LO as the PDRO and introduced spurious content into the spectrum. The digitizer also introduces strong spurs, particularly at 5 GHz, 2.5 GHz, 100 MHz, and 10 MHz. These mostly come from clock inputs whereas the 5 GHz spur likely occurs from the slight DC offset produced from the interleaving of the two analogs to digital converters (ADCs) within the digitizer. The 5

GHz spur was easily filtered during post-processing. However, the interaction between the LO source, the mixer, and the digitizer appears to have produced several spurious frequencies that were always present in recorded spectra. These may have been due to spurious LO signals mixing together within the mixer [81]. Post-treatment methods were developed to remove this spurious content from the signals. They will be presented in section 2.9.

The new E-band spectrometer presented here has taken advantage of several recent technological advances in millimeter-wave electronics that were unavailable to previous spectrometer designs but help to compensate for the reduced signal-to-noise ratios in pressure-broadened data. The power amplifiers use here can produce more powerful polarizing pulses than current active multiplier technology. To reduce the noise level of the receiver, the power amplifiers are pulsed to decrease the level of white noise from entering the receiver and a LNA has been added before the down-conversion mixer. The advantages of placing a LNA before a mixer in a receiver were recently discussed for emission spectrometers [82, 83]. However, a blanking switch has to be employed to protect the LNA, which raised the noise temperature compared to the emission receivers. This is unavoidable when using high power amplifiers in the transmitter, to protect the high sensitivity electronics. Even with the blanking switch included, this design should result in a lower noise temperature in the receiver than designs that input directly into a mixer first before amplification. While the spectrometer performs very well when searching for weak signals, the optical path of the polarizing pulse presents a major issue. Reflections within the experiment persisted well into the record time, distorting the FID at early times. Reflections present a larger concern as the pressure rises. Since the FIDs become both shorter and weaker, the loss of signal can be significant compared to those obtained at low pressures. Acquisition schemes and post-processing routines were developed to mitigate the reflection problem and will be presented in section 2.9.

The spectrometer can be coupled to the room temperature flow cell by positioning the table at each end of the cell with the microwave horns facing the wedged Teflon windows of the cell.

The spectrometer can be coupled to the CRESU chamber positioning the table on each side of the chamber aligned with a pair of specially design ISO 320 flange equipped with three ISO KF 40 ports on each of the flange. These multiple ports were designed with in mind a future development of the chamber using a secondary expansion chamber with a skimmer (briefly described at the end of section 2.1), they allow for coupling of the spectrometer at different positions in the skimmer chamber. For the results presented in

this thesis only two of them are used which have been adapted to mount vacuum leak tight waveguide bulkheads (Pasternack, PEWAD5001) connected to the spectrometer through waveguides. The transmitter and receiver tables can be moved independently from the chamber to allow access for maintenance or installation of the in-chamber microwave components (microwave waveguides and horn antennas and microwave absorbing foam).

Inside the chamber, the waveguide bulkheads are connected to 50 mm long waveguides, at their ends the horn antennas are mounted. The vacuum seal between the chamber and air through the waveguide is accomplished at this connection by the use of homemade windows consisting of 100 micron thick Teflon sheets clamped between the two waveguide flanges. Gaskets shaped for waveguide flanges (SAS Industries Inc., 1056-7407) are used to create vacuum seals between individual waveguide elements. Fig. 2.12 presents a picture of the assembly allowing the horn antenna to be installed inside the vacuum chamber. In this configuration, the distance between each horn and the isentropic core of the uniform supersonic flow is about 15 cm. This distance was chosen for CPUF experiments as a compromise between reflections of the exiting pulse and signal strength after testing different configurations. This design of vacuum feedthrough for the horn was inspired by windows designed for use on the ALMA radio telescope [84].

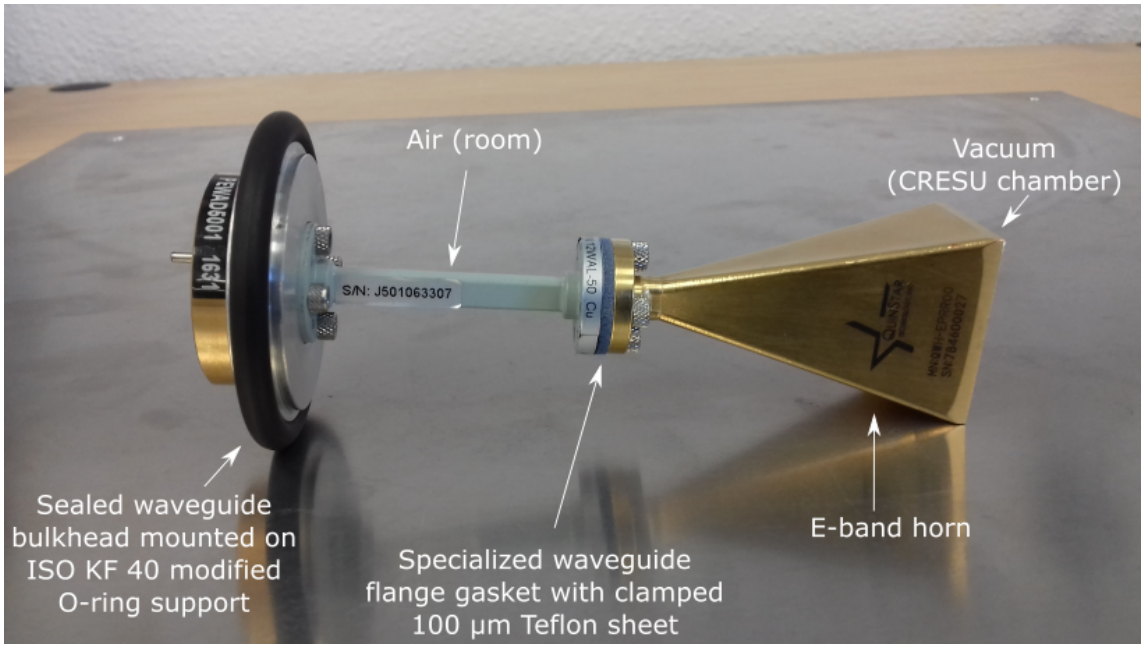

Figure 2.12: Picture of the assembly of waveguide components allowing the horn antenna to be installed inside the vacuum chamber.

Inside the chamber, the section around the probing region (C in Fig. 2.5) is covered by a layer of 25 mm thick microwave absorbing foam (Eccosorb HR 25, Laird), with a

reflectivity around -25dB for the E-band. A conical structure of this foam is also mounted around the waveguides and the horns. Fig. 2.13 presents a picture of the installation of the microwave absorbing foam inside the vacuum chamber. The Eccosorb foam significantly reduces the reflections of the spectrometer excitation pulse inside the chamber; without this absorbing layer, it would be impossible to perform CPUF experiments because any signal would be obscured by the reflections on the short timescale imposed by the relatively high-pressure CRESU environment.

Figure 2.13: Picture of the microwave absorbing form layout inside the vacuum chamber.

2.8.1 The first spectrum recorded with the instrument

The first-ever recorded spectrum with the instrument is presented in Fig. 2.14. It was taken in the flow cell described in 2.6 leaving a liquid sample of methyl cyanide (Sigma Aldrich $\geq$99.9%) evaporate from a glass container (7 µbar). The FID can be clearly seen in the inset, the shape an indicator of the beating between multiple frequencies. The Fourier transform show the spectrum with the catalog frequencies and intensity from CDMS. The rotational transitions are clearly resolved and present an SNR over 1000. It is

also possible to see some vibrationally excited transitions and even some transitions from the isotopologue $CH_3{}^{13}CN$. This first test only had for goal to test the spectrometer with a molecular signal. It proved that the spectrometer was running as expected and that it could be used for experiments in the flow cell which lead to the experiment presented in chapter 3.

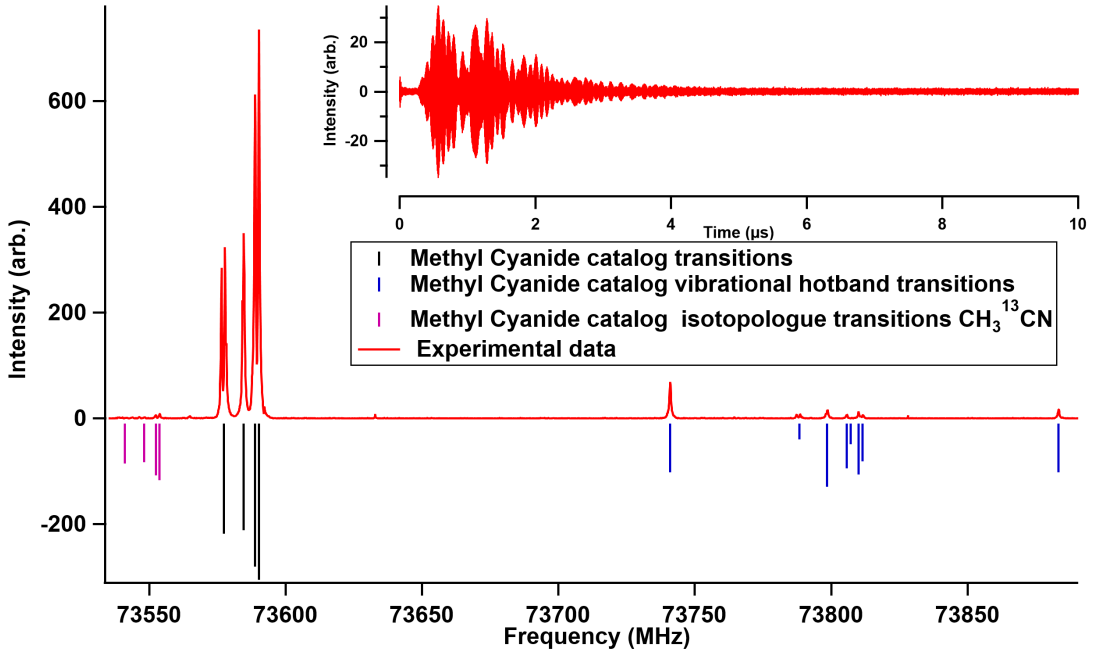

Figure 2.14: First recorded spectrum taken with the E-band spectrometer in the room temperature flow cell (7µbar of methyl cyanide). Transitions between 73500 and 73900 MHz. FID in the time domain in the inset.

2.9 Acquisition protocol and post-processing

As a newly developed technique, with only one similar apparatus in the world [29], CPUF still was at the start of the project a new method for studying kinetics in a CRESU apparatus. An effort was made to design a standardized procedure for running these experiments, leading to the development of particular acquisition schemes and methods of processing the data. The development of these tools was planned to ensure versatility in the running of experiments and in the analysis of the data. Special care was taken in order to keep all the elements compatible and with an open architecture to be able to keep improving and developing the CPUF technique in Rennes. The next section presents these developments.

2.9.1 Standardization of acquisition

The spectrometer acquisition protocol was standardized in order to run CPUF experiments with optimized duty cycles while reducing the risk of mistakes, particularly resulting from different timings which could expose the sensitive receiver to the powerful excitation pulse. "Frames" were developed as a standard, inspired by the FastFrame™ technology from Tektronix, employed in preceding CP-FTmmW studies [29, 49, 85], where a frame is the smallest unit of signal and trigger needed to perform a CP-FTmmW experiment. It contains all the signals that the spectrometer requires to function, output by the AWG (4 channels with each two differential outputs) and an associated digital delay generator (DDG) triggered by the AWG and controlling the timings of the spectrometer. An example of such a frame recorded on the oscilloscope with all the involved triggers is presented in Fig. 2.15. The size of a frame, i.e. time for a cycle of excitation/FID recording, is also standardized. The size used is determined by the environment of the sample. Each size of frame allows for a maximum duration for the polarization pulse, which depending on the geometries between the horn can be adjusted based on the electric field magnitude in the probing region. A lower electric field means that the duration of the pulse needs to be increased in order to reach the $\pi/2$ pulse for maximum polarization of the sample. The size of the frame also allows for a maximum recording time after the polarization pulse. The determination of the optimal time depends on the condition affecting the dephasing of the sample. For example, in the CRESU environment FIDs decay in a few hundreds of nanoseconds so frames of 2.5 µs are optimum allowing for an excitation pulse varying between 0–500 ns and a recording time of 1.7 µs, needed in post-processing even if the FID only lasts a few hundreds of nanoseconds, leaving 300 ns for any timing error. These frames are adequately sized to excite and record FIDs with the minimum of downtime possible. Fig. 2.16 presents a 2.5 µs frame recorded on the digitizer, with distinction between the pulse and signal portions. Frames can then be repeated one-after-another in sequence to optimize the experimental duty cycle and increase the averaging depth. They can also be arranged in particular sequences, hereafter referred to as acquisition schemes, providing different benefits to the signal or to access more information about the experiment (reflection rejection, time dependence...).

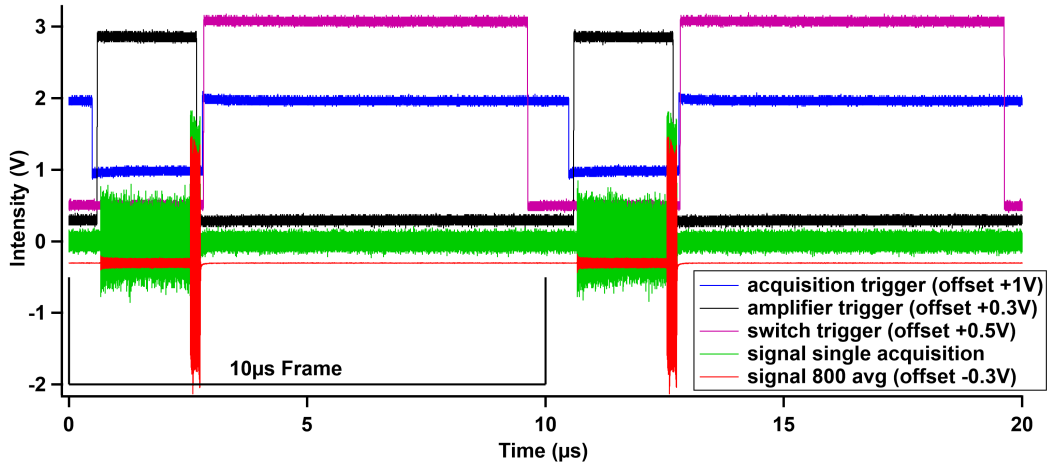

Figure 2.15: A frame and all the related triggers recorded on the oscilloscope at 25 GS/s. Each curve is offset on the figure to allow for visualisation of overlapping signals at this high a sample rate.

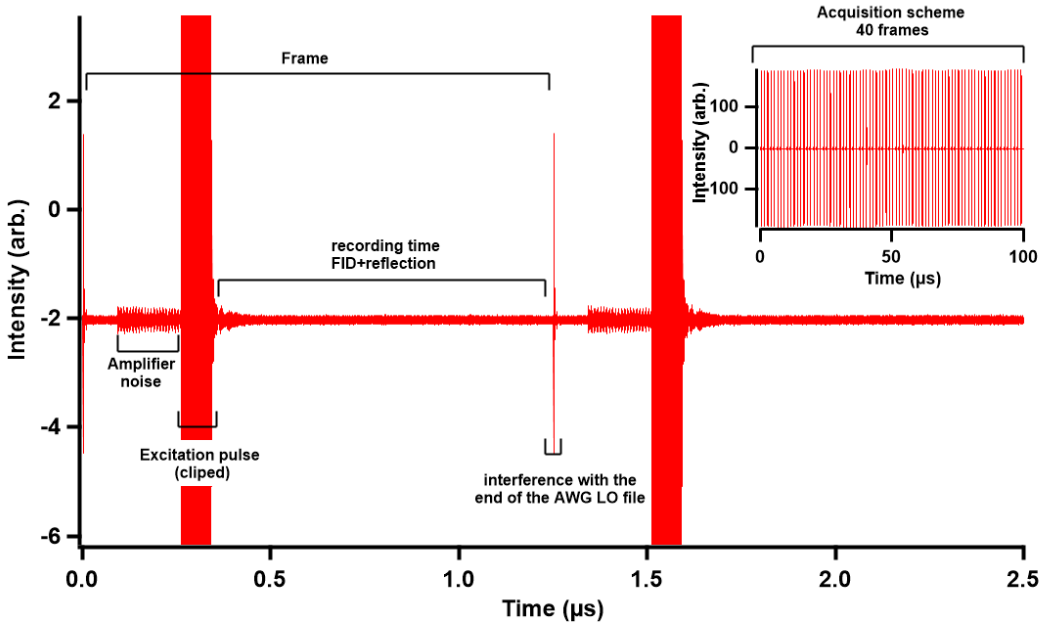

Figure 2.16: A frame recorded on the digitizer detailing the different regions.

2.9.2 Acquisition scheme

During the project, acquisition schemes were developed to improve the quality of the data and increase the amount of information taken from each acquisition. The first part of these schemes is to match the number of frames generated by the spectrometer with the capability of the digitizer by filling the record length of the card with as many frames repeated after each other as possible. For example, the acquisition card used to capture the

molecular signal is capable of recording up to 2 million points, at 10 GS/s its maximum sample rate this lead to 200 µs of record time. By filling these 200 µs with 80 frames of 2.5 µs and then analyzing independently the 80 FIDs, it is possible to extract the time evolution of the signal over 200 µs, thus giving information about the time evolution of the probed species. In addition to the possibility of "vertical" averaging of these 80 FIDs by repetition of the scheme and averaging on board on the card, the frames can also be averaged together "horizontally" in post-processing to increase the SNR at the cost of reducing the time resolution. This increases the averaging depth without having to acquire for a longer time by averaging frames that are next to each other. The time resolution of the instrument is inherently limited by the size of the frame used in the experiment and by an integer multiple of the size of the frame if horizontal averaging is used. To represent these limits, the time-dependent results presented later are presented as horizontal bar of the size of the frame (or multiple of the size of the frame if horizontal averaging is used). The sample rate of the card can be reduced to increase the record time at the cost of reducing the Nyquist frequency instead. This is used for the data collected with argon nozzle, which has a longer hydrodynamic time compare to the helium nozzles (around 1 ms compared to around 100 µs).

When the CRESU flow is established, the gas which moves in front of the horns always has the same characteristics. In order to observe a time-dependent signal, the conditions in the uniform flow have to be perturbed. This perturbation has to be done by a source external to the flow, in our case from the laser pulse. The microwave horns are fixed on the side of the chamber and cannot be moved during an experiment. The reservoir can move but the displacement is only used to adjust the distance between the horn and the nozzle to the hydrodynamic time available for the particular nozzle used. The acquisition of the time dependence of the signal is possible because the gas is moving through the stationary detection region. The principle is to have a delay between the laser pulse and the microwave frame. As this delay corresponds to the time it takes for the molecule to come from a point upstream of the flow to the probing region in front of the horn. During this time, kinetic processes can happen and their time dependence can be measured. Fig. 2.17 illustrates this. Four imaginary molecular samples in the flow are considered (S1, S2, S3 and S4). At the time t_0 (A) the excimer laser fires and the spectrometer starts emitting a train of four frames, the four samples are situated along the flow, S1 is situated in the probing region at this time and the first frame has been broadcast, leading to the molecule in S1 been probed by the spectrometer. At the time $t_0+\Delta t$ (B), all samples have moved with S2 now in the probing region and are excited by the second frame. At the time $t_0+2\Delta t$

(C), the gas has moved again and S3 is now being probed. At the time t_0 + hydrodynamic time (D), S4, which was in the nozzle throat at t_0, is now in the probing region and is excited by the last frame. Analyzing the four frames independently allows one to obtain the time evolution of the signal. Each sample had a time equal to the delay between the laser and the corresponding frame to interact in the flow.

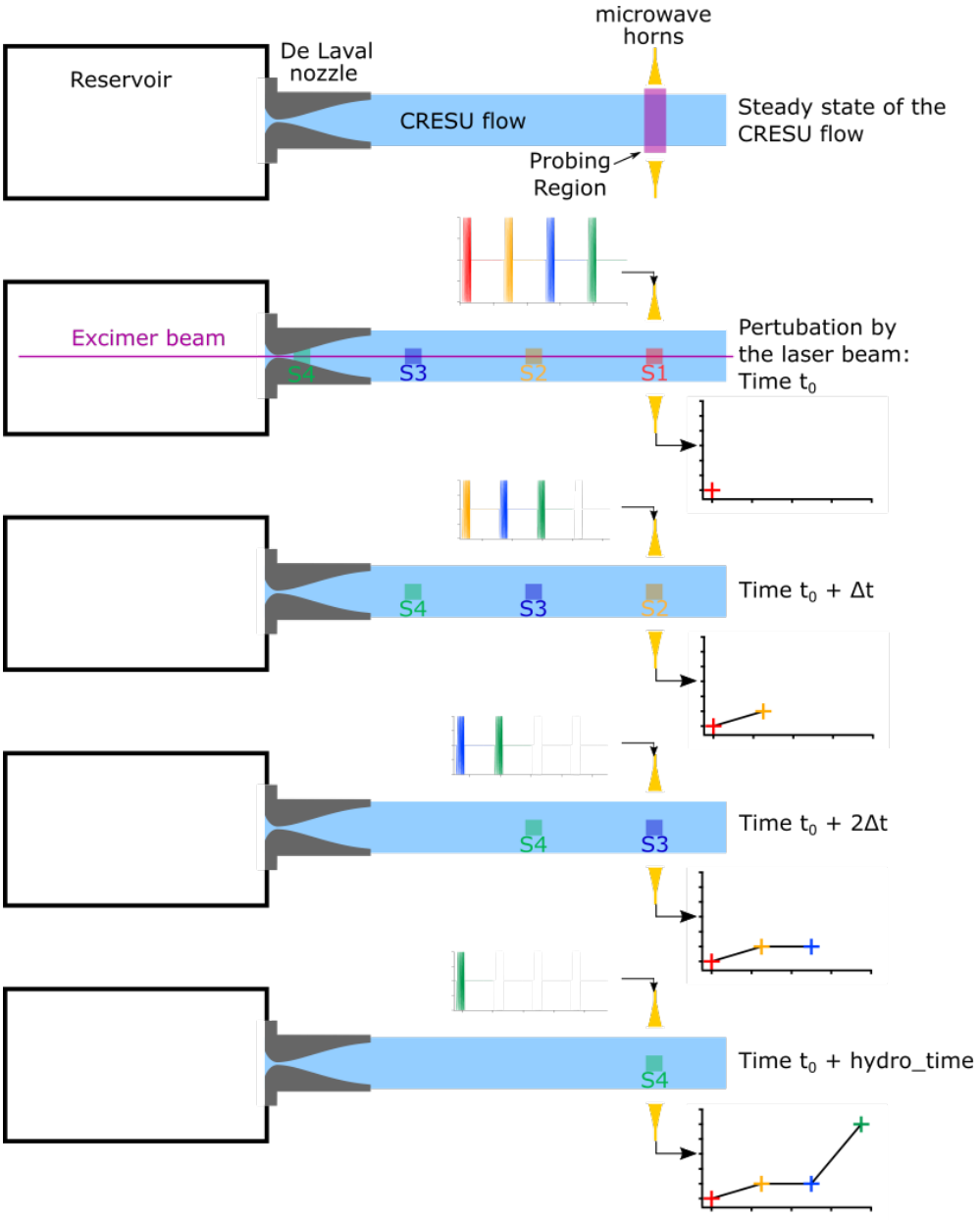

Figure 2.17: Schematic presenting how the time dependence of a signal can be measured using an immobile detector but relying on the movement of the flow.

As described previously, microwave reflections within the chamber are a limiting factor that must be addressed in order to extract weak molecular signals. Two approaches

are used in order to reduce the impact of the reflections. The first one is a "passive" approach and consists in covering the metallic surfaces inside the chamber with microwave absorbing foam (eccosorb) as described above. Fig. 2.18 presents the effect of adding the foam in the chamber. This method can reduce the intensity of the reflections by orders of magnitude but does not allow for complete removal of the reflections as seen in the red curve of Fig. 2.18, the baseline in the frequency domain present in the excitation pulse still retains some structure and shape differing from a random noise floor.

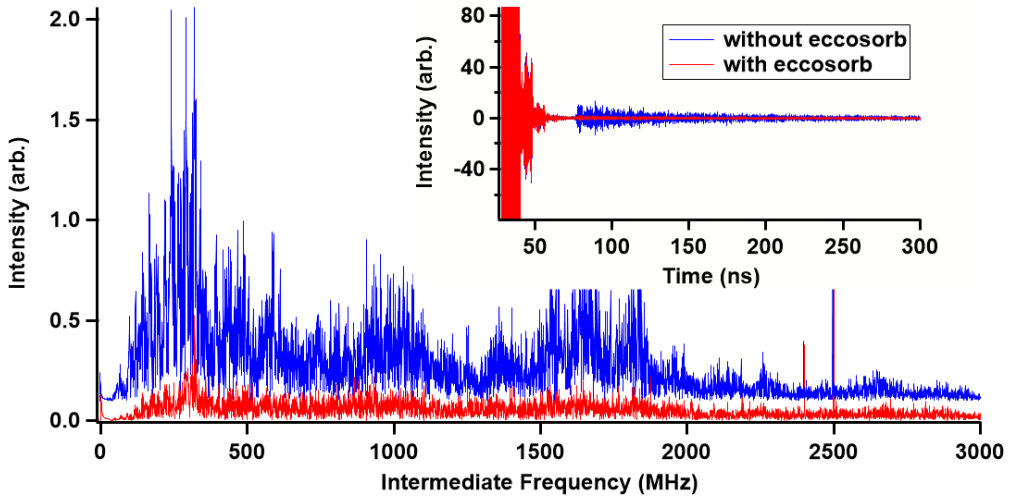

Figure 2.18: Presentation of the effect of coating the chamber with eccosorb on the reflections using a 2 GHz wide chirped excitation pulse. The main graph present the effect in the frequency domain and the inset in the time domain. In blue the signal without eccosorb and in red with it.

In order to fully remove reflections from the signals, a more "active" method needs to be employed. For this, a special acquisition scheme was developed for observing molecular signals initiated by laser photolysis. Working on the principle of subtracting background coherent noise from the signal (hereafter referred to as background subtraction), that is comparing what is present in the signal before the laser fires, where no molecules of interest are present in the flow, and what is present after when the molecules are generated. Two versions of this scheme were designed chronologically, the second method is an improvement on the first method.

The first scheme is referred to as "active background subtraction" (ABGS). It uses the fixed phase relationship between excitation pulses and their reflections; i.e., if the excitation pulse's phase is rotated, its reflection's phase will be rotated by the same amount. When two excitation pulses of the same phase are subtracted from each other, the pulses coherently cancel as well as their reflections. In order to accomplish the same effect with

the digitizer which is programed to only accumulate onboard the excitation pulse needs to have opposite phases to be canceled out in the accumulation operation. Two trains of frames with the excitation pulse phase turned by 180°between the two trains have to be emitted and the acquisition triggered for each train. The addition of these two pulse trains in the digitizer's accumulation circuit leads to a cancellation of the out-of-phase components, allowing for background subtraction of reflections. Fig. 2.19 illustrates this method of background subtraction using a 500 MHz single frequency excitation pulse recorded through the CRESU chamber with the oscilloscope. The frame in blue is the sum of the two first frames which are made with opposite phase excitation pulses. In the time domain, it is already clear that the reflections are subtracted. The inset focuses on the excitation pulse itself as the subtraction of the main frequency component is clearly seen, a higher frequency can be seen on top of the 500 MHz sine wave which has not been subtracted when the two frames are summed. Fig 2.20 presents the same frame and the corresponding spectrum. In this figure in the frequency domain, it is even clearer that the reflections having a frequency close to the excitation pulse are completely removed. Only one frequency around 3.75 GHz still remains after the subtraction in the recording zone. This is the same frequency that can be seen on top of the excitation pulse in Fig. 2.19. This frequency is far enough from the excitation pulse to not obscure a potential molecular line. It probably comes from harmonic content that was amplified in the multiplication chain and has a different phase relationship to the excitation pulse.

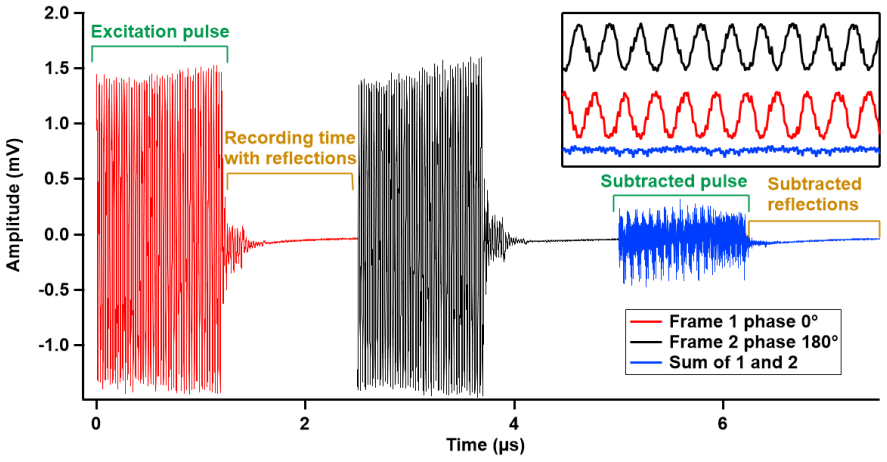

Figure 2.19: Presentation of the principle of background subtraction using out-of-phase pulses in the time domain. In red a single frequency excitation pulse IF at 500 MHz with 0° phase. In black the same pulse but with 180° phase rotation. In blue is the sum of these two pulses. The inset focuses on a few cycles of the pulse. Regions of the pulse and recording time are labeled.

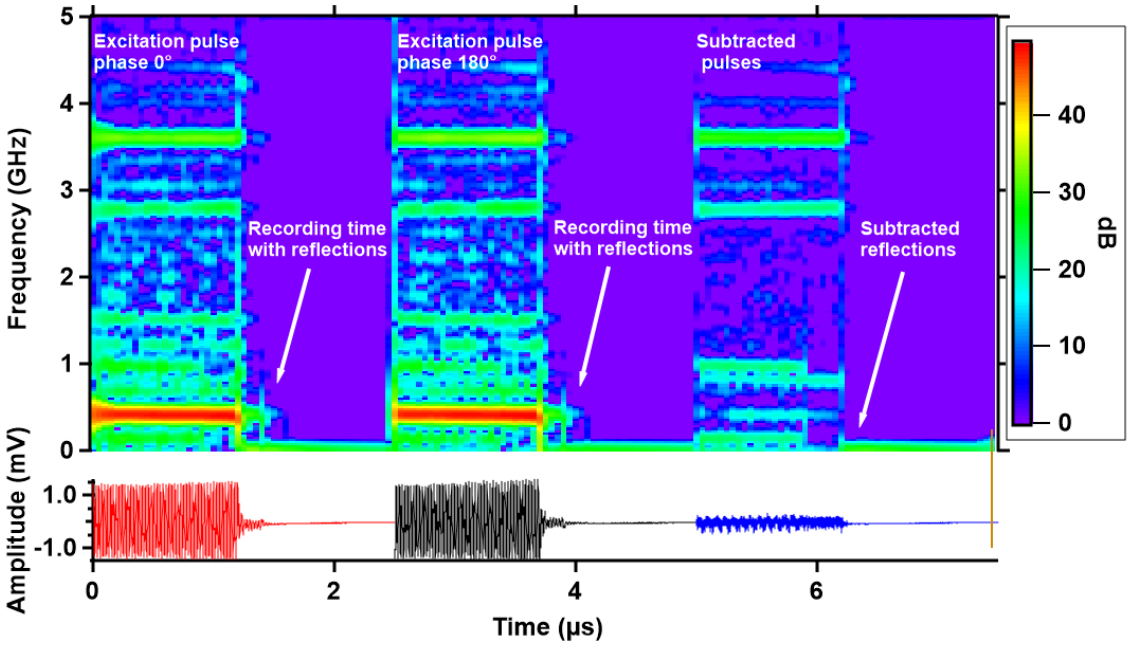

Figure 2.20: Presentation of the principle of background subtraction using out of phase pulses in the frequency domain with the use of a spectrogram. The same pulses are used as for fig 2.19.

The active background subtraction routine was used during the first set of experiments before the possibility of lowering the sampling rate of the card was explored. At this stage, the 200 µs maximum recording time of the card was required to run photolysis experiments in helium flows and be able to record the whole hydrodynamic time. It was then decided to perform the subtraction directly using the onboard averaging of the card to conserve these 200 µs of dynamic time. The spectrometer was configured to send two trains of 80 frames of 2.5µs each train set with opposite phase for the excitation pulse. The laser was triggered within the second train as presented by Fig. 2.21. The resulting signal would be free of reflections as any frame before the laser contains only the excitation pulse and reflections. The frame after the laser would contain the excitation and reflections in the opposite phase and the FIDs of any molecular signal arising from the photolysis in the flow. The output signal of the card being the sum of these two trains of frame the only coherent signals remaining would be the FIDs because they would be the only signals without an out-of-phase equivalent in the first train of frames.

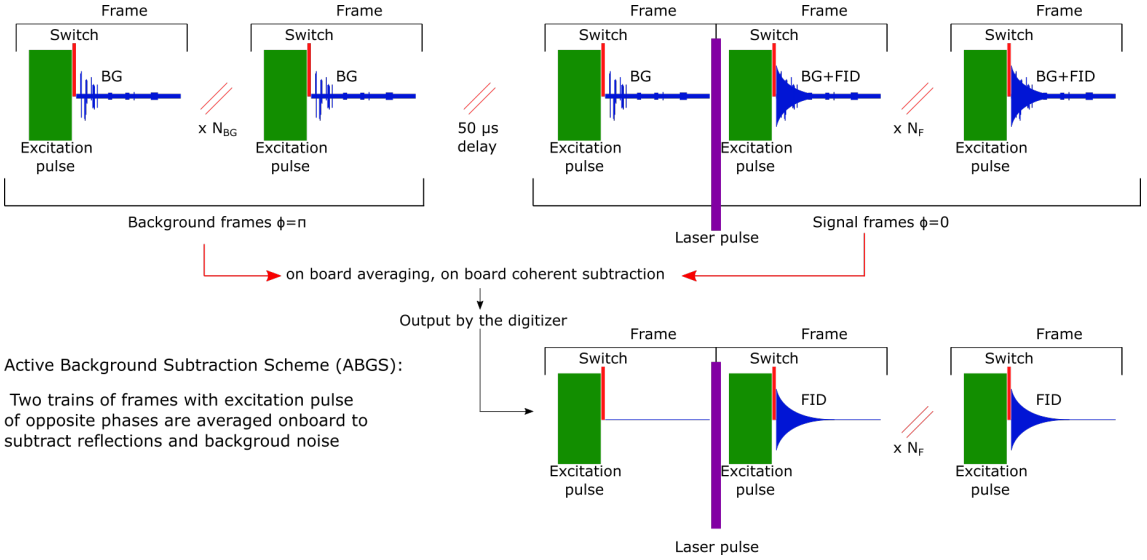

Figure 2.21: Schematic of the active background subtraction scheme

This scheme performed well enough to allow for the first tentative detection of signals in the CPUF experiment but there were limitations to its continued implementation. An issue in the spectrometer, the source of which is still unknown today, generates a phase variation (up to 1/10th of a radian) between 50 and 100 µs of the recording time, independent of any of the parameters tested (sample rate of the cards, size of frame, frequency of the excitation pulse...). This phase variation hindered the applicability of this scheme. This slight phase shift can be corrected using a procedure described in the next section but requires postprocessing instead of the on-the-fly subtraction achieved in the active background subtraction routine. In order to apply this correction, both trains of frames needed to be recorded. To accomplish this while keeping the same dynamic time, the sampling rate of the card was reduced to 5 GS/s, thus allowing for 400 µs of time to be recorded. A similar scheme to the ABGS was then used (and called the "sample skip scheme"). 160 identical 2.5 µs frames were generated by the spectrometer and recorded on the card. The photolysis laser is triggered at some point during this sequence. The recorded signal is then composed of frames acquired before the laser pulse, containing the reflections of the excitation pulse in the chamber and no molecular signal, as well as frames that were acquired after the laser pulse, containing both the reflections and the molecular signal. The former can then be subtracted from the latter to effectively remove the reflections, allowing for the observation of weak molecular signals that would be otherwise hidden under the reflections, illustrated in Fig. 2.22. In this scheme, it is not necessary to change the phase of the pulse as the subtraction is done in post-processing. This scheme allows

access to all the data being recorded at all times and permits some post-processing treatments that were not possible to apply using the ABGS scheme (notably a phase shift correction). It is also more flexible as in this case the number of background frames can be adjusted by the user, increasing the length of the dynamic time in the recording.

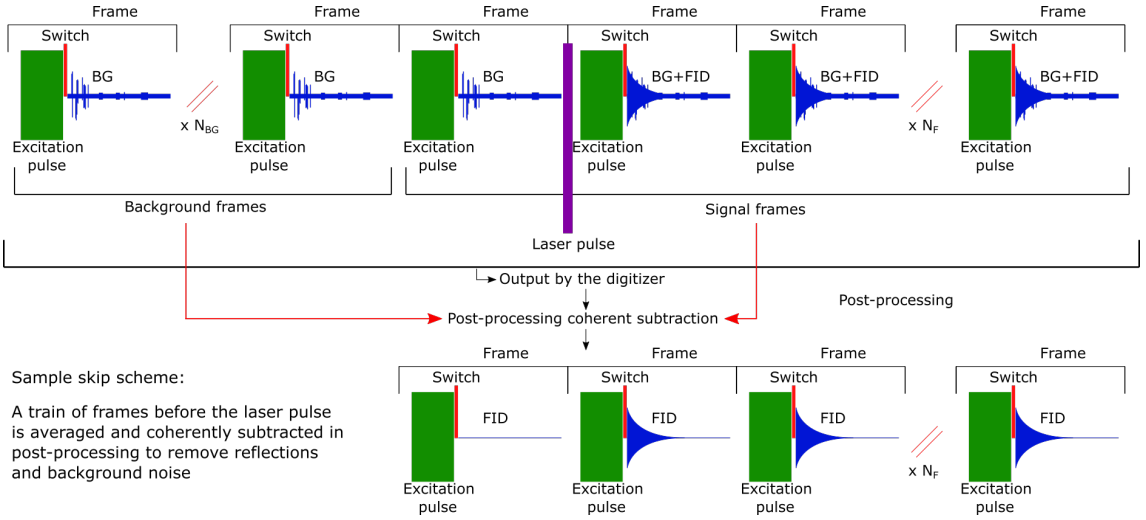

Figure 2.22: Schematic of the "sample skip" acquisition scheme

The two routines also have the benefit of removing any potential molecular signals independent of the reaction of interest. When running the experiment at high repetition rates, it is possible that the time between each laser shot is too short to allow for all the target molecules generated in the reservoir to be fully evacuated. This would lead to the presence in the data of a non-zero and constant molecular signal on top of the molecular signal generated by each iteration of the reaction. The scheme just described allows for the removal of this parasitic signal while not affecting the laser-triggered reaction signal.

2.9.3 Post-processing of data

To extract information from raw data, post-processing routines were developed. The analysis is done using Igor Pro (version 8, Wavemetrics) where numerical functions are written in a programming language similar to C. The post-processing routine almost always applies mathematical functions to the time domain signals and before a Fast Fourier Transform (FFT) is applied to the data (only the phase correction described in the next paragraph uses the frequency domain to treat the data before time-domain manipulation). Reflections can be mitigated by the use of particular acquisition schemes as described above. Electronic noise and spurs, resulting, for example from clocks and LO bleed-through, can pollute the spectra and complicate the interpretation of the results. In order to clean the

spectra, an analysis routine using a "pattern filter" based on the recording and subtraction of the coherent noise was developed, similar to the way the effect of mismatched ADCs was removed from spectra taken with another digitizer [86]. The electronic spurs are inherent to the spectrometer and present at all times in the recorded signal. The sum of these parasitic sine waves forms a repeating pattern in the noise which can be collected multiple times during the downtime between frames and averaged in order to remove random fluctuations from the electronic spur signal. The resulting pattern can then be subtracted in phase from all of the frames to remove this electronic noise from the signal and therefore clearing the spectra after the FFT is taken. The size of the pattern can be adjusted to include different ranges of frequency spurs. It was found empirically that a pattern of 800 points at 10 GS/s is optimized for reducing spurious content in the E band spectrometer. Implementation of this filtering routine on acrylonitrile transitions measured in a 30 K argon CRESU flow is shown in Fig. 2.23. The two sets of data demonstrate the high degree of rejection of electronics spurs delivered in different regions of the spectrometer frequency range, one with a regular density of spurs A) and one in the worst configuration of the spectrometer B) (higher harmonic content in the quadrupler output at low frequency as can be seen in the first spectrogram of Fig. 2.11a). This pattern filter allows even in this worst-case scenario the removal of almost all the electronics spurs. It is also capable of removing electronics spurs that are present on a line profile without affecting the shape of the line as shown in the inset of Fig. 2.23 C).

This filter is effective for removing electronic spurs but not for intermodulation spurs [48] which are molecular signals mixed with the impurity of the LO source. But these are only seen in our acquisition in the case of a really strong signal when flowing stable product and reaching SNR of more than 1000. These intermodulation spurs are also in these cases one or two orders of magnitude lower in intensity than the molecular line, which makes them a negligible contribution in the spectra as presented in fig. 2.24. In this figure, it can also be noted that even if the waveform used to excite the acrylonitrile $J_{Ka,Kc}$ = $7_{1,7}$-$6_{1,6}$ is constructed as a single frequency sine wave the other nearby transitions of acrylonitrile are also excited but at much lower intensities. In the experiments presented here, the "paternfilter" is especially useful when spurs are situated at a frequency very close to the transition and affecting the line shape as shown in Fig. 2.23 C). When the spurs are far from the transitions they are less of an issue as typical experiments run with this setup look for transitions whose frequencies are already known and cannot be confused with electronics spurs. This filter would be really efficient for a spectroscopic study where the determination of spectroscopic quantity is the main objective or when

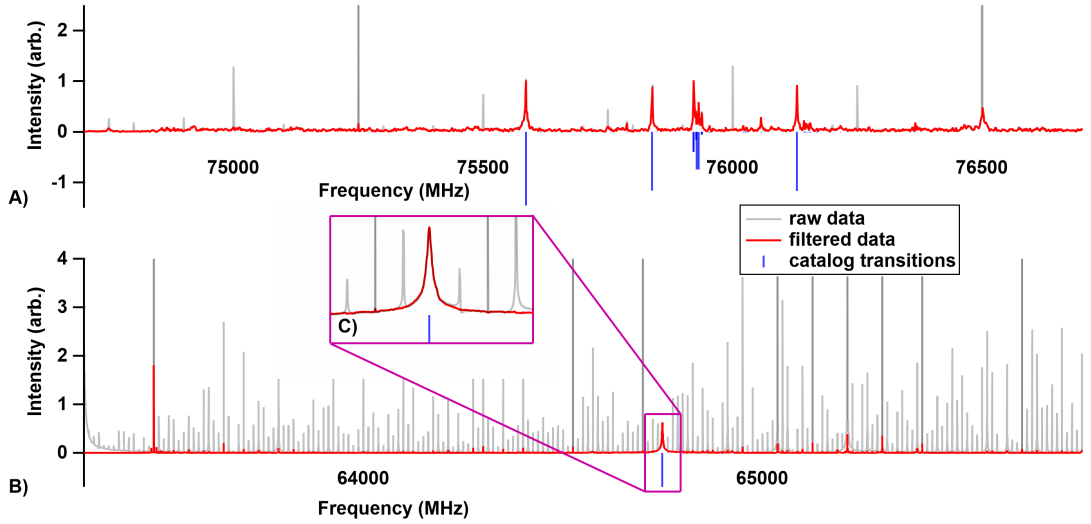

Figure 2.23: Demonstration of the spurious rejection of the pattern filter. In transparent black the magnitude of the Fourier transform of the signal before the filtering, in red the magnitude of the Fourier transform of the signal after the filtering. In blue the catalog line frequencies, with intensities scaled to 30 K. A) acrylonitrile spectrum between 75 and 76.5 GHz in Helium 16 K flow (acrylonitrile density: 5.2×10^{13} cm^{-3} 8×10^5 avg) LO 74 GHz B) acrylonitrile $J_{Ka,Kc}$ = $7_{1,7}$-$6_{1,6}$ transition in Ar 30 K flow (acrylonitrile density: 1.8×10^{12} cm^{-3} 4×10^5 avg) LO 63.3 GHz. (probed in the secondary expansion chamber) C) Inset zoomed on rejection of spurs on the same acrylonitrile transition as B)

looking for molecules with unstudied spectroscopic constants.

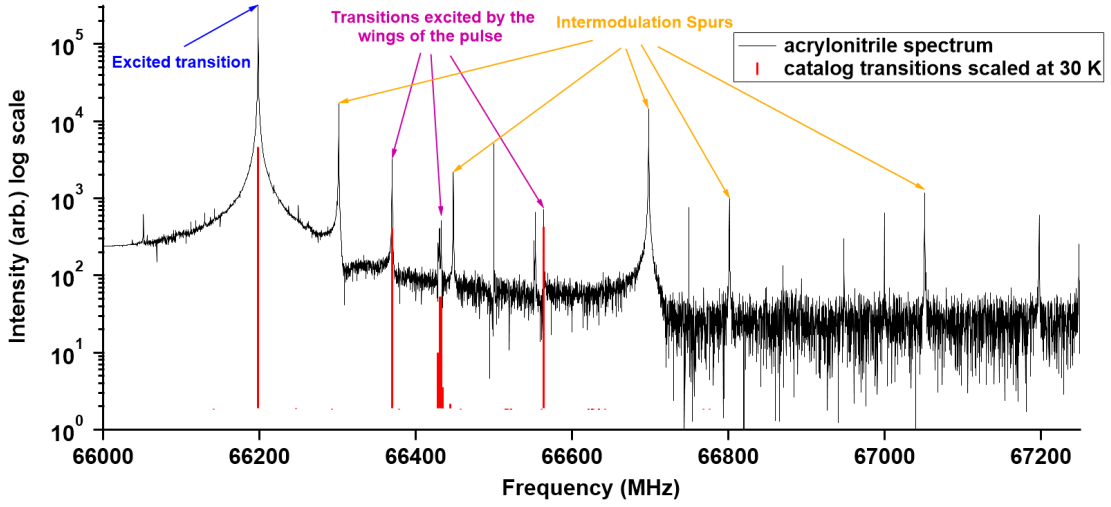

Figure 2.24: Demontration of the intermodulation spurious content on acrylonitrile $J_{Ka,Kc}$ = $7_{1,7}$-$6_{1,6}$ transition in Ar 30 K flow (acrylonitrile density: 1.8×10^{12} cm^{-3} 4×10^5 avg) LO 63.3 GHz. (probed in the secondary expansion chamber)

In some experiments, a certain degree of phase drift was observed between successive frames, the cause of this phase shift is still unknown. To correct for this phase drift which was affecting the quality of the background subtraction a modification of the analysis procedure was implemented rotating the phases of the affected frames using their complex Fourier transforms via the equation:

$$\begin{pmatrix} \mathbb{R}\mathrm{e}\{F'(\omega)\} \\ \mathbb{I}\mathrm{m}\{F'(\omega)\} \end{pmatrix} = \begin{pmatrix} \cos\Delta\phi & \sin\Delta\phi \\ -\sin\Delta\phi & \cos\Delta\phi \end{pmatrix} \begin{pmatrix} \mathbb{R}\mathrm{e}\{F(\omega)\} \\ \mathbb{I}\mathrm{m}\{F(\omega)\} \end{pmatrix}$$

as described in Park *et al.* [54] where $\mathbb{R}\mathrm{e}\{F'(\omega)\}$ and $\mathbb{I}\mathrm{m}\{F'(\omega)\}$ refer to the real and imaginary parts of the Fourier transform, respectively and $\Delta\phi$ is the phase angle by which the data is rotated. $\Delta\phi$ is calculated for each scan as the difference between the phase at the point of maximum intensity in the excitation pulse and that of the first "background frame". This correction ensures that the background subtraction is done coherently and leads to the rejection of reflections.

2.9.4 The streamlined post-treatment of data

All of the above-described procedures were designed to streamline the analysis of the data in order to ensure that data are analyzed the same way and can be compared, and so that analysis can be done while running experiments in between each acquisition. For this purpose, analysis functions were written and the typical functions are presented in the next paragraph with examples.

The whole on-the-fly analysis package is compacted into two functions. The first one is there to take the raw data and depending on the scheme used, to allow the visualization of the data frame by frame. The function also takes care of all the filtering and different variations of the function are used depending on the type of experiment. In the laser experiment, the function performs the background subtraction (according to the "sampleskip scheme"), for experiments without background subtraction the function only filters the data. If a phase drift between the frame that was mentioned in section 2.9.2 is detected then the last version adds a stage that corrects for this. Here the first version will be presented as it is the one which is the most frequently used. The code for these functions can be found in the appendix.

The function is called *cutavgfilpieceLaser* and the function parameters are:

- *rawData* = name of the wave in Igor Pro
- *sizeofframe* = size in samples of the frame used, depending on the sampleskip factor

and the file loaded in the AWG, it can be calculated =2000000/numoframetot

- *sampleskip* = sample skip factor used in the scan (parameter of the digitizer which allow for lowering the sampling rate)
- *numoffframetot* = total number of frames in the scan
- *numofcut* = number of cust for horizontal averaging
  numofcut=numofframe/horizontalaveraging
- *BGendframe* = number of frames to use to generate the background
- *A* = starting index of the FFT
- *B* = ending index of the FFT
- *startpattern* = starting index of the pattern for the pattern filter
- *switchoffset* = ending index of the pattern for the pattern filter
- *patternsize* = size in samples of the pattern for the pattern filter typically 800 points at 10 GS/s

Using these parameters, it is possible to adjust each step of the analysis. The function first starts by generating the "background frame". In order to do this, the first frames are arithmetically averaged (the number depending on the scheme and the parameter *BGendframe*). The resulting frame is then filtered using a "soft" finite impulse response filter (FIR) which corrects for the DC offset and low-frequency recovery. Then the pattern filter is applied to the "background frame" to remove electronics spurs (the pattern filter is controlled by the last three parameters *startpattern*, *switchoffset*, *patternsize* which allow to control where in the frame the pattern is taken). The remaining portions of the "signal frame" are then individually isolated, they can be arithmetically averaged by packets to add horizontal averaging using the parameter *numofcut* which increases the averaging depth without having to do more acquisitions, each of these resulting packets is then filtered using the same FIR and pattern filter as for the "background frame". The "background frame" is then subtracted from each of the "signal frames" in order to achieve background subtraction and remove reflections. The FFT of each of the "signal frames" is then calculated between the two user-defined points *A* and *B*. The function then plots two graphs. One with all the "signal frames" in the time domain and the other with their FFTs. Fig. 2.25 presents the different steps of filtering on the time domain and frequency

domain of the data at each step. The effects are most clearly presented in the frequency domain. In the bottom panel, it can be seen in the black curve that the raw data contain a few spurs (in this case they are quite far from the line and not really an issue), a DC offset and the recovery in one of the microwave component of the receiver chain are affecting quite drastically the baseline on the whole spectrum. The major problem is the "reflection floor" around the spectral line which completely obscures the baseline around the line and modifies the line shape. The application of the FIR filter allows removal of the DC offset and the recovery which flattens the baseline on the whole spectrum except around the reflection where the reflections are still the major disturbance (blue curve). The application of the pattern filter then corrects for all the few remaining spurs except one (red curve). Finally, the background subtraction removes all the reflection floor around the line which allows for a clear analysis of the signal (purple curve). Fig. 2.26 presents the difference between the magnitude of the FFT of a raw signal and a post-process signal. It proves that the post-processing of the data does not affect the line shape or intensity. Only a small asymmetric residual (two orders of magnitudes less) can be seen when looking at the difference between the two signals. This experiment is performed in the skimmer chamber presented above as it is the only possible way to show this due to the major reflections of the main chamber which are not present in the skimmer chamber.

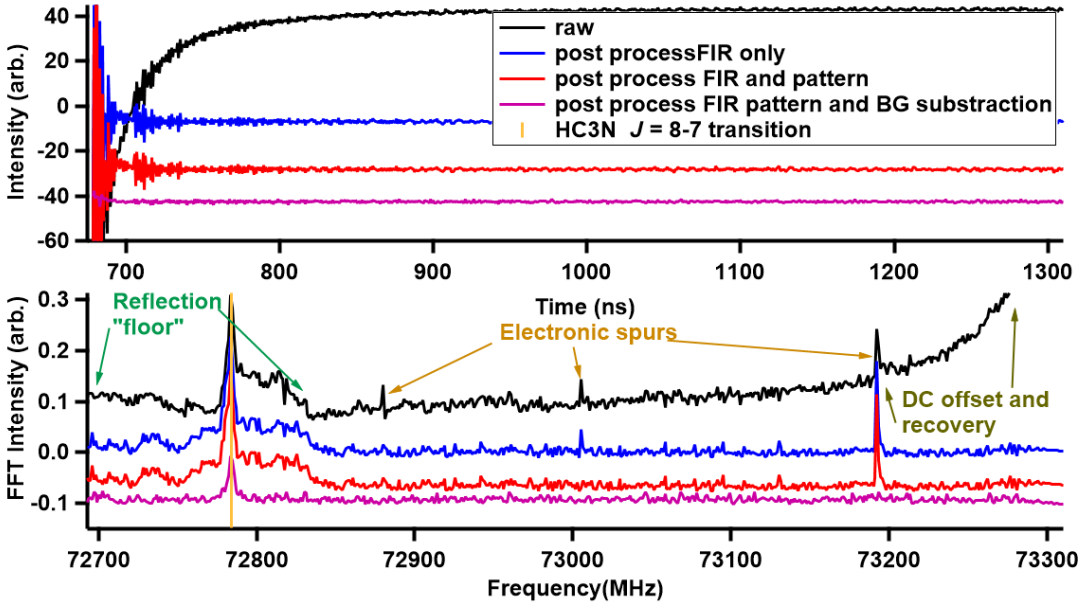

Figure 2.25: Presentation of each step of the post processing on time domain data (top graph) and frequency domain data (bottom panel) using the signal from HC_3N J = 8-7 transition from the photolysis of acrylonitrile in an Ar 30 K CRESU flow 1.8×10^{12} cm^{-3} 4×10^5 avg

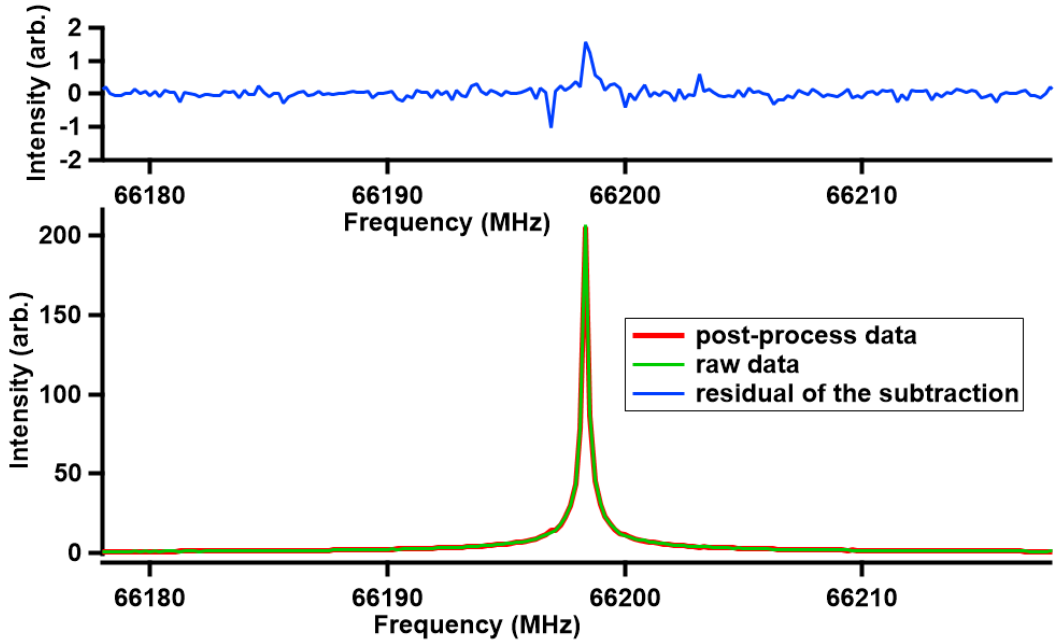

Figure 2.26: Comparison of the magnitude of the FFT of the raw data and the magnitude of the FFT of the post process data on an acrylotnirile transitions $J_{Ka,Kc} = 7_{0,7}$-$6_{0,6}$ in the skimmer chamber from a 30 K argon flow. density of acrylotnirile 1.8×10^{12}cm^{-3}. The top graph shows the difference between the to FFTs 4×10^{5} avg.

A second function is then usually used which allows the presentation of the time evolution of a spectral line. This function is called *timedepsig* and the function parameters are:

- *rawData* = name of the wave in Igor Pro
- *numofcut*: *numofcut* used in the cutavgfilpiecelaser function used with this dataset
- *frequency*: frequency of the line to integrate in sample
- *width*: number of point to integrate around the line.
- *tottime*: total time in µs. use to generate the time wave associated with the intensity tottime = (numofframe-numofbackground) x sizeofframe
- *cutwithlaser*: cut in which there is the laser frame. to mark it on the graph if set to zero no marker will be put

This function calculates a simple integration of the point around the line then plots the result as a function of the time the frame was acquired relative to the time the laser fired. From this, the time dependence of the laser-induced process can be extracted and studied. Fig. 2.27 show the different stages of this data analysis. A variation of this function can be used on strong enough signals to fit individual FIDs using the model presented in section 2.4, this allows the extraction of more information (pressure and Doppler broadening rates).

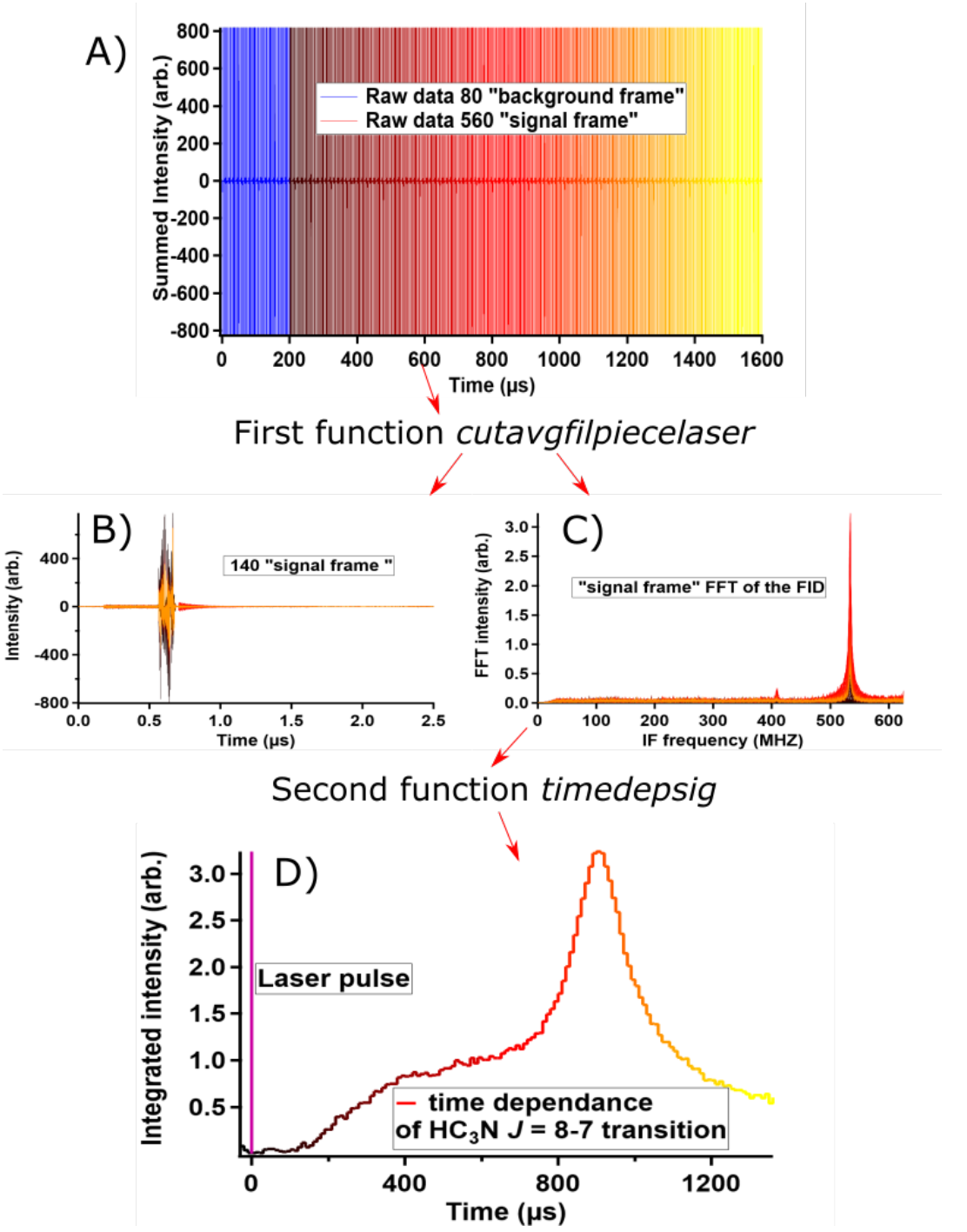

Figure 2.27: Post-treatment step: A) raw data 640 frame in one acquisition averaged 10^5 times. B) 140 "signal frame" after post-treatment. C) FFT of the 140 FID. D) Time evolution of the HC_3N J = 8-7 transition from the photolysis of acrylonitrile at 193 nm in an Ar 30 K CRESU flow (1.8×10^{12} cm^{-3} acrylonitrile, fluence 1.7×10^{16} cm^{-2} photons per pulse, 1.2×10^5 avg per point).

2.9.5 Generation of the waveform

One of the big advantages of CP-FTmmW spectroscopy is its broadband capability. In the case of the spectrometer developed for this work, the microwave components were chosen to allow for detection of rotational transitions between 60-90 GHz and in fact a little more as the high-frequency power amplifier can extend a few GHz around this range. But the components are only one part of the spectrometer, and while running experiments they don't require control from the user. On the other end, the determination of the waveform to be broadcast by the spectrometer is the step that requires input from the user. For this, the E-band spectrometer benefits from the capacity of the arbitrary waveform generator (Keysight M8195A) which with 64 GS/s allows for absolute control over all parameters of the generation of any possible waveform under 18 GHz. This level of control on the waveform allows the selection of all the parameters of the excitation pulse broadcast by the spectrometer. A part of the LabVIEW program is dedicated to the generation of waveforms to generate the file that is used for the AWG. Two types of excitation pulses are typically used with the spectrometer, chirped waves and single-frequency pulses. For both types of pulse, the user can decide on the frequency of the pulse (starting and ending in the case of the chirped pulse), the duration of the excitation, the phase of the wave, the frequency of the second channel sine wave which is used as an LO when running with the digitizer and the timing of the two marker channels used to trigger the rest of the experiment. The waveforms are generated with the size of frame defined by the user. The sizes are chosen from a set of standardized maximum wave sizes to match specific situations, such as whether spectra are Doppler or pressure broadened or to allow for a variety of pulse lengths to be used to match the transition dipole moment for a particular situation. It is at this stage that safeties are implemented to protect the receiver part of the spectrometer from the powerful excitation pulse. The safety consists of an arbitrarily defined sample (different for each frame size) from which the pulse is constructed backward. The marker channel which controls the triggering of the delay generator (which then controls the critical timing of the millimeter-wave switch) is also bound to this arbitrarily defined sample. These two precautions ensure that in generating a waveform it is impossible to make a mistake that would lead to damaging the spectrometer's sensitive receiver components.

The decision between using a chirped excitation or a single frequency pulse depends on the species studied and the environment in which the study is done. In a highly collisional environment (CRESU conditions) the effects of pressure limit the performance of the spectrometer. In this case, the fast passage excitation regime cannot polarize the

sample sufficiently (because of the collisions) to reliably detect the species with low concentration (typically six orders of magnitude less than the buffer gas). In this case, the waveforms are generated with single-frequency pulses i.e the mathematical function used to make the waveform is a sine wave containing only one frequency, the pulse is in reality not a δ function in frequency but is broadened both according to the time-bandwidth product of the pulse and by the components of the spectrometer. When looking for a stable product that can be injected at a higher concentration (typically three orders of magnitude less than the buffer gas) then the spectrometer is sensitive enough to be used with chirped excitation, thus allowing the detection of multiple spectral lines in an acquisition. For both types of pulse, the signal can be optimized by choosing the local oscillator frequency that would down-convert the high-frequency FIDs with the most efficiency and adjusting the duration of the excitation pulse for the collisional environment.

The collisional environment limits the sensitivity of the spectrometer but the broadband capability of the microwave components still allows the detection of multiple species but not at the same time. In order to do this, the same experiment is repeated changing the frequency of the excitation pulse for each species that needs to be studied. Another type of waveform combining both aspects could be used as presented by Broderick *et al.*, [87] where instead of using chirped excitation they stack multiple single frequency pulses after each other in order to generate a "multicolor" pulse. This allows keeping the high polarisation resulting from single-frequency pulses while being able to detect multiple transitions at the same time. But this type of pulse is also ineffective in a highly collisional environment like a CRESU flow. As the molecules polarised by the first part of the pulse may have, in these conditions, already completely relaxed before the whole multicolor pulse has been fully broadcast thus making them impossible to detect. A way around this limitation could be to stack the pulse on each other and not after each other. Simply generating a waveform being the sum of multiple sine waves at different frequencies thus generating a "multifrequency" pulse. Measurements using three acrylonitrile transitions, presented in Fig. 2.28, show that this type of pulse leads to reduced signal comparing to excitation pulse containing only one frequency. In this figure, the left panel presents the FFT of acrylonitrile FIDs showing that when using the "multifrequency" pulse the signal is reduced by a factor of five for the strongest line. The right panel presents the FFT of the pulses. It can be seen that in the case of the multicolor pulse (blue) the pulse contains the three frequencies with about the same intensity compare to the multifrequency pulse which displays more than three frequencies and a low and uneven intensity for the three frequencies of interest. The difference between the two pulses FFTs which mathematically should be

the same is a good indication that at the up-converting stage some component is reacting to the multifrequency pulse in an undesirable way, leading to a reduction in the molecular signal. This probably occurs or at the mixing stage or at the doubling stage. Leading to unwanted mixing between the multiple frequencies of the pulse spreading the power of the pulse at other frequencies. Thus leading to a weaker excitation electric field. This could maybe be tested by running Rabi cycle experiments (described in the next section).

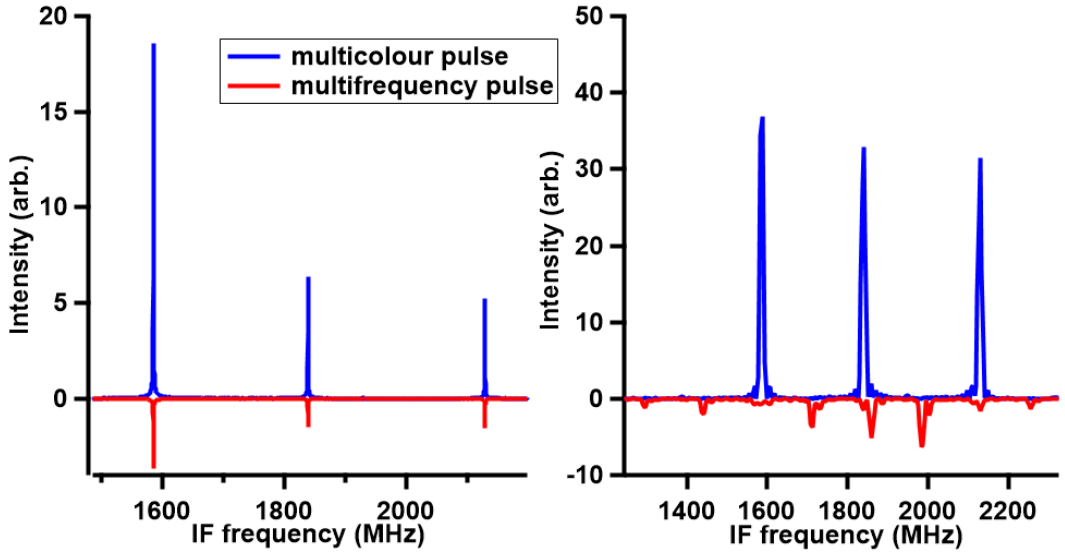

Figure 2.28: Comparison between multicolor pulse and multifrequency pulse. On acrylonitrile transitions between 75500 and 77000 MHz in the skimmer chamber from an Ar 30 K flow. density of acrylonitrile 1.8×10^{12}cm^{-3} 10^4 avg

2.10 Characterization of the frequency response of the instrument

As presented in the introduction the main goal of the CRESUCHIRP project is to measure branching ratios of reactions at low temperatures. In order to do this, it is necessary to be able to compare signals from different molecules to be able to obtain a ratio from the intensities of rotational transitions of these molecules. This required multiple effects to be taken into account which would be discussed later but one of these effects is directly linked to the instrument and will be discussed in this section. When measuring any physical property with an instrument the instrument itself affects the measurement and the response of the instrument needs to be characterized in order to remove the bias it inherently applies to a measurement. In the case of this study, the important effect that needs

to be characterized is the frequency response of the instrument which is an inherently difficult problem for a broadband instrument as every component in the chain adds its own frequency response to form the overall frequency response of the instrument. Also, it is important that every component of the chain operates in a linear regime to be able to compare different signals.

A way to determine this frequency response would be to divide the task in two, first the characterization of the excitation of the molecular sample then the characterization of the receiver.

The characterization of the frequency response of the broadcast can be done independently of the characterization of the receiver even while using this one to record the signal. Doing this relies on using a molecular sample to characterize the electric field in the probing region using a Rabi cycle experiment as presented by Park *et al.* [54]. The principle is to introduce a molecule in the probing region and then using single-frequency pulse excitation of varying duration and comparing the intensity of the line resulting from these excitations. The result of this experiment can be compared to an exponentially-damped Rabi oscillator. The intensity of the signal S can then be described by equation 2.22. Where t_p is the duration of the pulse, $1/\tau$ the decay rate of the coherence and $\omega_r = \mu\varepsilon/\hbar$ the on-resonance Rabi frequency with μ the transition dipole moment and ε the amplitude of the E-field. Fig. 2.29 presents an example of this type of experiment inside the CRESU chamber using an acrylonitrile transition as a probe of the E-field in a pinhole expansion. The data were fit to equation 2.22 to obtain the value of ω_r which in turn allow for the determination of the electric field. For this frequency and this configuration of the spectrometer, the average amplitude of the E-field over the probing region was found to be 136 $\pm$ 14 V/m ($\pm 1\sigma$).

$$S \propto exp\left(\frac{-t_p}{\tau}\right)|sin(\omega_r t_p)| \tag{2.22}$$

These Rabi cycle experiments could be a way of determining the frequency response of the broadcast independently of the characteristic of the receiver which is a major advantage. They still have some limitations as the electric field is determined using molecular transition it is going to be by definition a discrete measurement. But it is possible to use multiple molecules in order to map the frequency response of the transmitter in its whole range at discrete points. Then it could be assumed that over a short frequency range the frequency response of the transmitter does not vary significantly, which it was designed for, the only issue with this assumption comes from the fact that the microwave pulses are broadcast inside a chamber and not free space. It would be possible that some resonance

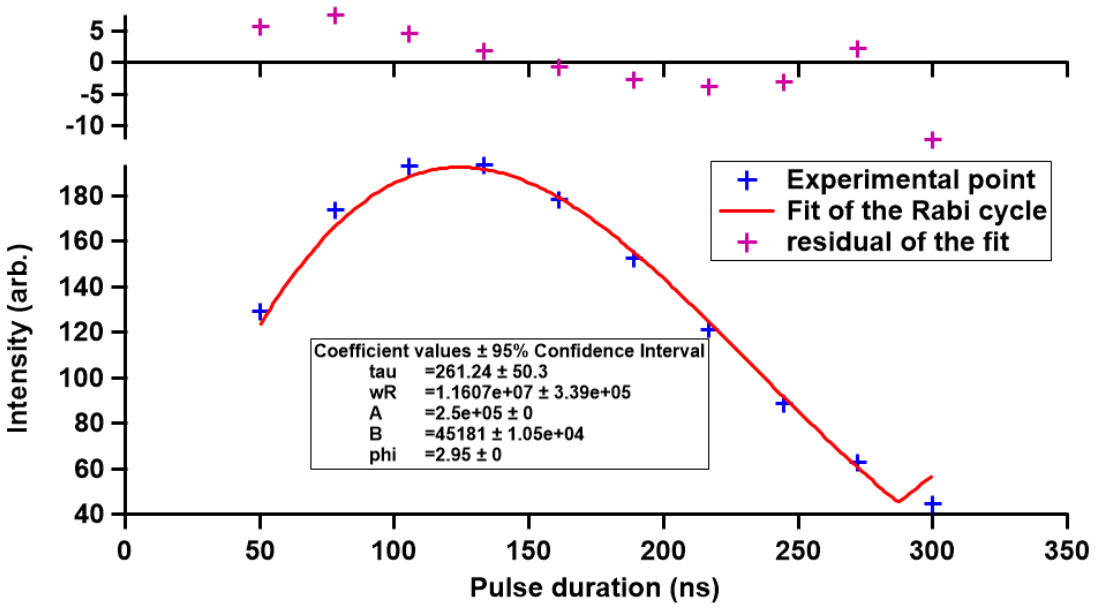

Figure 2.29: Rabi cycle experiment from a pin-hole expansion inside the CRESU chamber using the acrylonitrile $J_{Ka,Kc} = 7_{0,7}$-$6_{0,6}$ transition.

effect linked with the geometry of the chamber affects the propagation of waves through the chamber adding a frequency response from the chamber which could be missed by the discrete mapping of the E-field. Two ways to go around this potential problem are possible. The first would be to always try to look at a transition from a stable molecule close to the transition of a potential product. The second would be to run a numerical simulation of the propagation of radiofrequency waves in the geometry of the chamber but this is a really complex and tedious process, beyond the scope of the present work.

After a determination of the frequency response of the broadcast using Rabi cycle experiments, it would be possible to use the result of such measurements to calibrate the frequency response of the receiver. In order to do this a molecule such as acrylonitrile could be photolyzed in a CRESU flow and multiple transitions could be excited using single-frequency pulses. By subtracting the signal after the laser pulse to the signal before it could be possible to obtain the spectrum of the acrylonitrile which was photolyzed. From this spectrum, a rotational diagram could be calculated to determine the temperature of the photolyzed acrylonitrile. The relative intensities of the line could be compared to the relative intensity of a simulated spectrum at the flow temperature (determined by the Pitot probe measurements) the difference between the relative intensities of the two spectra, after correcting for the response of the transmitter determined like presented in the preceding paragraph, would lead to the determination of the frequency response of

the receiver. This assumed that each pulse polarizes the sample with the same efficiency, since $\pi/2$ pulse can not be attained in CRESU conditions the duration of the pulses would need to be adjusted according to the transitions dipole moments.

While the characterization of the frequency response of the spectrometer using Rabi cycle experiments seems like a straightforward enough task it actually is quite a long and tedious process. The configuration using the digitizer as the acquisition device is the one usually used to run experiments. This process of characterizing the receiver response needs to be done for each of the configurations of the receiver i.e. for each local oscillator frequency used for the upper and the lower side-band. This corresponds to hundreds of scans to be acquired and analyzed to exhaustively characterize the spectrometer. And as this frequency response arises from the interaction between each of the components of the instrument this exhaustive characterization is only done for one configuration of the whole instrument i.e. every time a change in the spectrometer chain or in the geometry of the chamber is changed the whole characterization needs to be redone. Because of the complexity of the task and the limitations of CPUF experiment which does not allow, in the result presented in this work, the measurement of multi-channel reactions. This exhaustive calibration of the frequency response of the spectrometer has yet never been done.

Chapter 3

OCS in He

Work extracted and expanded from *Brian M.Hays,* ***Théo Guillaume****, Thomas S.Hearne, Ilsa R.Cooke, Divita Gupta, Omar Abdelkader Khedaoui, Sébastien D. Le Picard, Ian R.Sims: Design and performance of an E-band chirped pulse spectrometer for kinetics applications: OCS – He pressure broadening jqrst (July 2020)* [88].

Contribution in the work in Methodology, Software, Validation, Formal analysis, Investigation, Resources, Writing - review and editing, Visualization.

Microwave spectroscopy has typically been performed in the cold, collision-free environment of a molecular beam or free jet expansion, which is ideal for spectroscopic studies [24, 89]. These environments are unsuitable for directly studying bimolecular reactions and dynamics, where collisions are essential. Gas-phase bimolecular reaction kinetics is usually studied in the presence of a buffer gas so that excess energy from reactant preparation or product formation can be thermally equilibrated. Some studies using CP-FTmmW spectrometers have been performed in environments where collisions are relevant [81, 90–93], but the effect of collisions on these spectra has received little attention using new instrumental techniques. Given the importance of collisional environments to the study of reaction kinetics, the effect of collisions on CP-FTmmW spectra was of great interest as it was a first step in the development and characterization of the spectrometer of the CRESUCHIRP instrument. This step was necessary to prepare the coupling of the spectrometer and the CRESU apparatus.

Pressure broadening is a well-known phenomenon where spectral transitions are broadened to a width proportional to the pressure in the environment. In time-domain experiments, pressure broadening contributes to the dephasing rate of the FID. The effects of pressure dephasing have been examined in cold buffer gas cells using a CP-FTmmW spec-

trometer, where pressure broadening coefficients of transitions from a few molecules were measured at very low temperatures, and very large pressure broadening coefficients were found [90]. Using a CP-FTmmW spectrometer, the Doppler effect was directly fit to a single transition FID to measure the mass of different molecular species after the pressure component of a Voigt profile was found using Hahn echo experiments [81, 91]. Recently, self-broadening pressure coefficients of OCS and ammonia were fit at room temperature [92, 93] but without a buffer gas, reducing the relevance of these experiments to the CPUF technique. To simulate these conditions, we investigated OCS pressure broadening in excess He up to pressures comparable to CRESU experiments.

OCS is a favorable molecule for microwave and millimeter-wave experiments as it has quite intense transitions, and He was expected to be the principal buffer gas for the CPUF experiments. The pressure broadening coefficients for the OCS + He system have been studied for many years, usually using microwave spectroscopy [60, 94–98] but also with infrared spectroscopy [99]. Measuring new pressure broadening coefficient for this system enables the validation of the E-band spectrometer as a scientific tool and helps pave the way to CPUF experiments.

3.1 Experimental methods

The experiments were performed in the room temperature flow cell described in section 2.6. The partial pressure of OCS (Sigma Aldrich 97.5% purity) was maintained at a constant level by maintaining a constant flow rate in the cell using a mass flow controller (Brooks GF series 20 sccm N_2 full range). The pressure in the cell was then adjusted by adding a separate flow of helium (Air Liquide 99.995%) also regulated by a mass flow controller (Brooks GF series 100 sccm N_2 full range). The measurements were performed in the pressure range between 2 and 350 µbar. The range was divided in two as the pumping system used for the low pressure (Edwards nXDS6i scroll pump and Edwards EXT75DX turbomolecular pumps) was not able to keep a constant pumping speed at higher pressure. For these higher pressure points, the flow cell was connected to the roots blower group (32000 m^3/h Pfeiffer Vacuum) use to pump the CRESU chamber. Three pure rotational transitions of OCS within the range of the E-band were examined: J = 5–4, J = 6–5, and J =7–6 (60814.270 MHz, 72976.779 MHz, 85139.121 MHz (JPL catalog)). These transitions were pumped using resonant single-frequency pulses that were 1 µs long, with the FID being recorded up to 20 µs. 10^5 averages were taken in less than 1 min for each transition using the digitizer setup described in section 2.8. The resulting FID were fitted using the methods described in section 2.4.

3.2 Results

We examined three transitions of OCS broadened by He. Figs. 3.1 and 3.2 show a low-pressure FID and a high-pressure FID respectively along with their fast Fourier transforms (FFT), as well as the residuals resulting from the subtraction of the data from a fit to the time domain Voigt model (Eq. 2.16), all for the J = 5–4 transition. The high degree of averaging allowed for extremely high signal-to-noise in the low-pressure regime, in both time and frequency domain data, as shown in Fig. 3.1 a and b. A rectangular window was applied to the time domain signal before the FFT in order to retain the decay characteristics of the line profile in the frequency domain, which differs from many other chirped-pulse experiments where different windowing functions were applied [24]. A 20 µs long window was used with the FFT on the low-pressure data to maximize frequency accuracy, resulting in a full width at half maximum (FWHM) of ∼0.2 MHz for the measured OCS transition. The high-pressure data of OCS in He is shown in Fig. 3.2 a and b. The signal-to-noise is significantly reduced compared to the low-pressure data, despite the same partial pressure of OCS being used. Only a 2 µs long window was used for the FFT of the high-pressure data due to this extremely fast dephasing. Extending the window of the FFT for pressure broadened FIDs was found to be unnecessary after twice the decay time [92]. The resulting transition had a FWHM of ∼2.5 MHz, due to the extremely short FID.

The FID for OCS in He was fit in the time domain using the time domain Voigt model (Eq. 2.16). All of the parameters for the fitting model, in particular, the Doppler decay, were fit for the model shown in Fig. 3.1. At high pressures, the Doppler decay term was constrained while the other parameters were allowed to vary. The time-domain Voigt model accurately reproduced the experimental signal, as shown in the Fourier transform of the residuals. The peak of the residuals is below 1% of the transition intensity, which indicates a high-quality fit of the experimental data.

The data taken at high pressures (Fig. 3.2 a) was well fit by the model, producing a well-constrained pressure broadening coefficient for OCS and He even from low SNR data. The down-converted frequency placed the IF for this transition/LO combination close to the main clock spur of the digitizer at 2.5 GHz, present at the left of Fig. 3.2 b. The pattern filter reduces the intensity of this spur, but cannot remove all of it, even after high amounts of averaging. The time-domain fit only includes the desired transition without any effect from the close-lying spur. While no residuals are above the noise level, there may be additional components to the FID that are below the noise level at this pressure which are not taken into account in the fit.

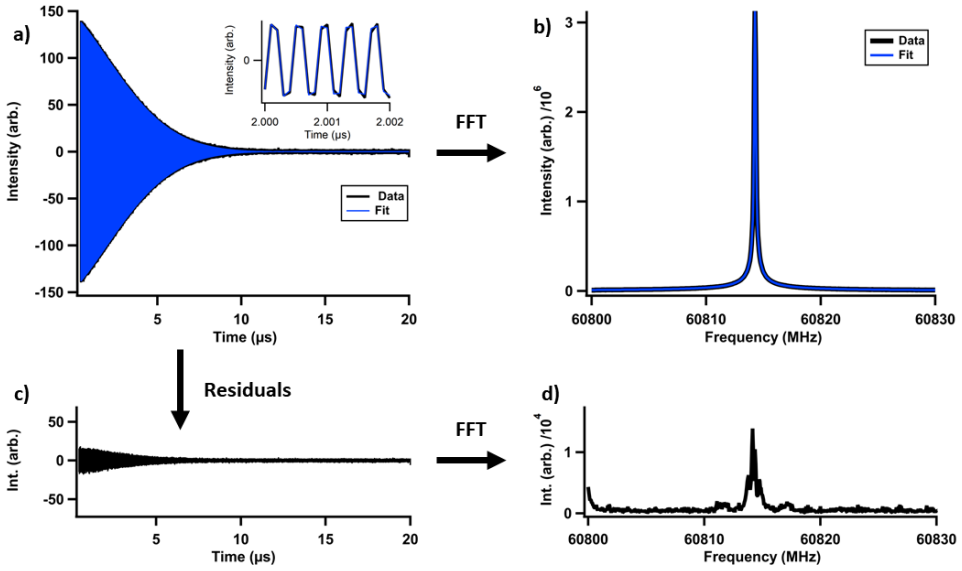

Figure 3.1: The J = 5–4 transition of $\sim 5 \times 10^{-5}$ mbar OCS in 5×10^{-3} mbar of He. a) The FID (black) fit to the time domain Voigt model (blue). An inset shows the quality of the fit over 2 ns. b) The FFT of the data (black) and the fit (blue). c) The residuals between the data and the fit in the time domain, with the same (arbitrary) intensity units as in a), spurs being the largest decaying signal. d) The FFT of the time domain residuals around the transition frequency, with the same (arbitrary) intensity units as in b) but displayed at 200 times magnified scale.

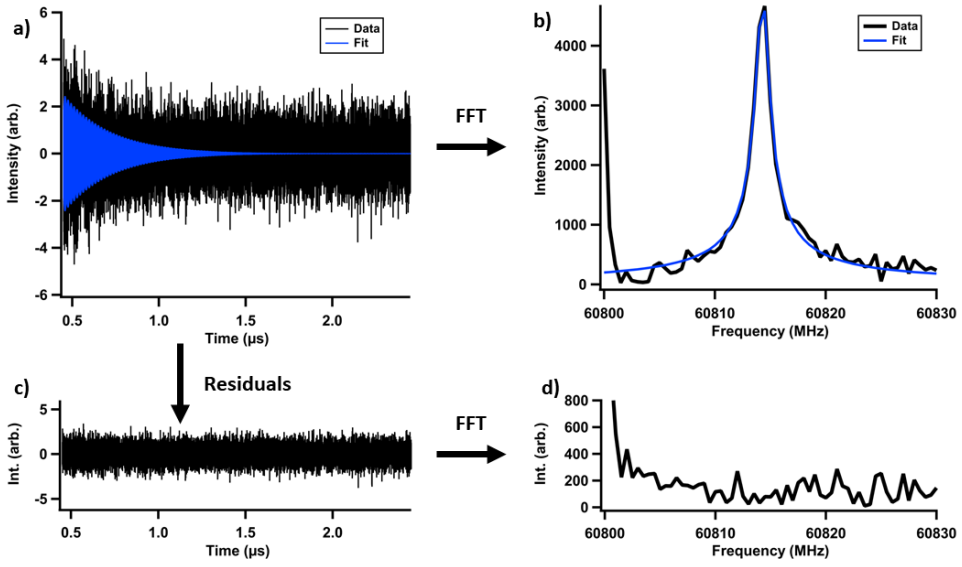

Figure 3.2: The J = 5–4 transition of $\sim 5 \times 10^{-5}$ mbar OCS in 0.239 mbar of He. a) The time domain FID (black) fit to the time domain Voigt model (blue). b) The FFT of the data (black) and the fit (blue). c) The residuals between the data and the fit in the time domain, a) and c) have the same (arbitrary) intensity units. d) The FFT of the time domain residuals around the transition frequency, with the same (arbitrary) intensity units as in b).

Two experiments were performed to measure the pressure broadening coefficients of the OCS + He system using different pumping systems. First, a low-pressure experiment was performed at pressures well below the crossover point between the Doppler and pressure broadening, so as to experimentally constrain Doppler broadening. The pressure and Doppler broadening rates obtained from the fits for the J = 5–4, J = 6–5, and J = 7–6 transition are shown in Fig. 3.3,3.4 and 3.5. The Doppler broadening fit was constrained to zero slope, effectively providing an average across the measured range of pressures. Error bars are represented on the graph but are typically a few orders of magnitude smaller than the magnitude of the constant that was fit, as the quality of the fits was quite high at low pressures. The Doppler rate was found to be within 1% of the expected value at 295 K for these OCS transitions.

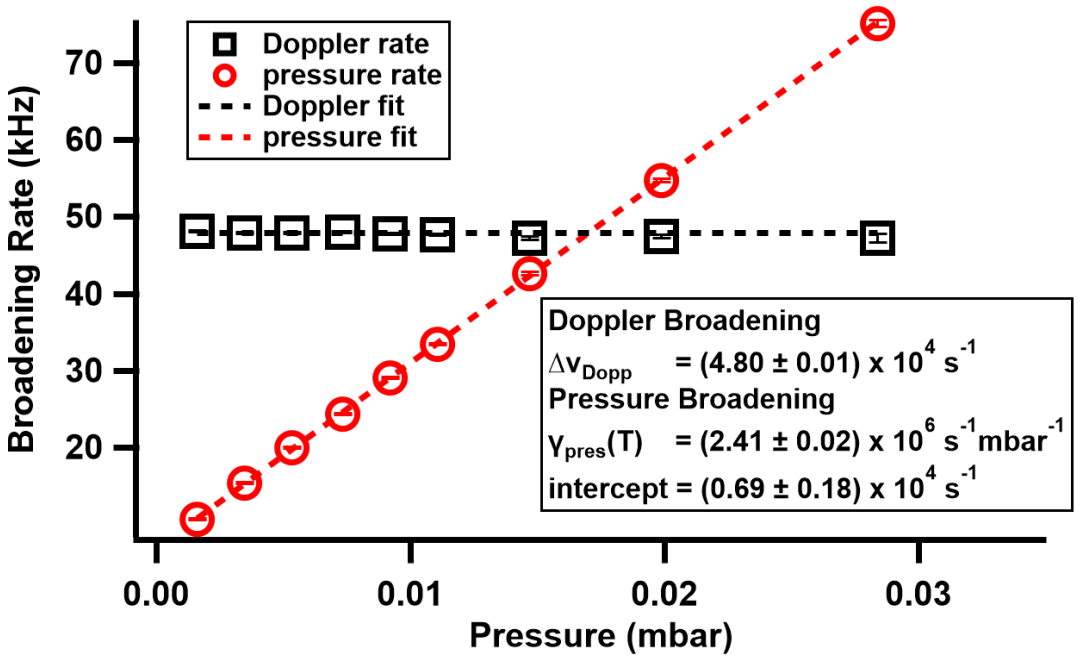

Figure 3.3: Low pressure fits of Doppler and pressure broadening for the J = 5–4 transition of OCS ($\sim 2.10^{-5}$ mbar) in He. The Doppler rate is constrained to zero slope, providing an average across the measured pressure range of (48.0 $\pm$0.01) kHz, while the pressure broadening rate is fit to a straight line whose slope yields the pressure broadening coefficient $\gamma_{Pres}(T)$. Uncertainties are quoted at the 95% confidence interval.

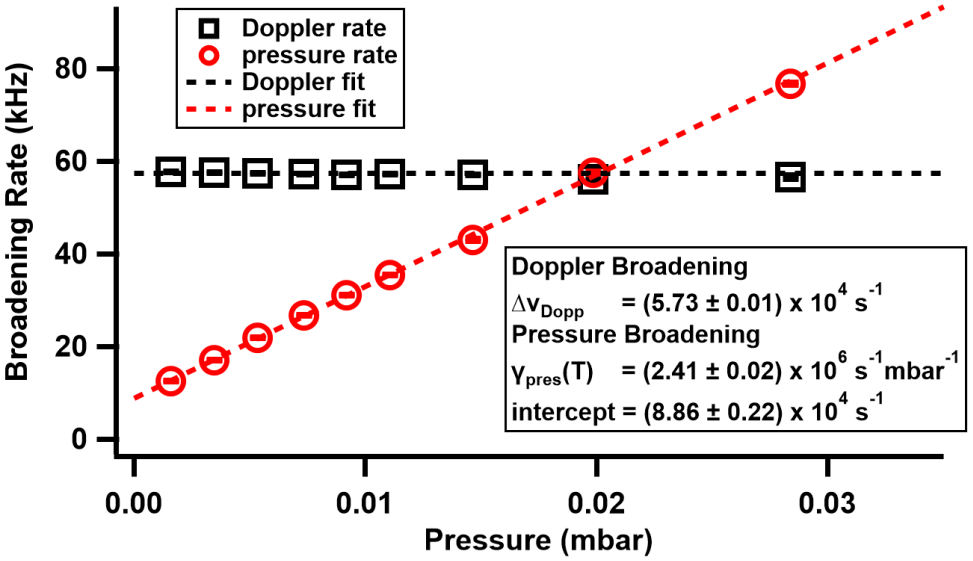

Figure 3.4: Low pressure fits of Doppler and pressure broadening for the J = 6–5 transition of OCS ($\sim 2.10^{-5}$ mbar) in He. The Doppler rate is constrained to zero slope, providing an average across the measured pressure range of (57.3 $\pm$0.01) kHz, while the pressure broadening rate is fit to a straight line whose slope yields the pressure broadening coefficient $\gamma_{Pres}(T)$. Uncertainties are quoted at the 95% confidence interval.

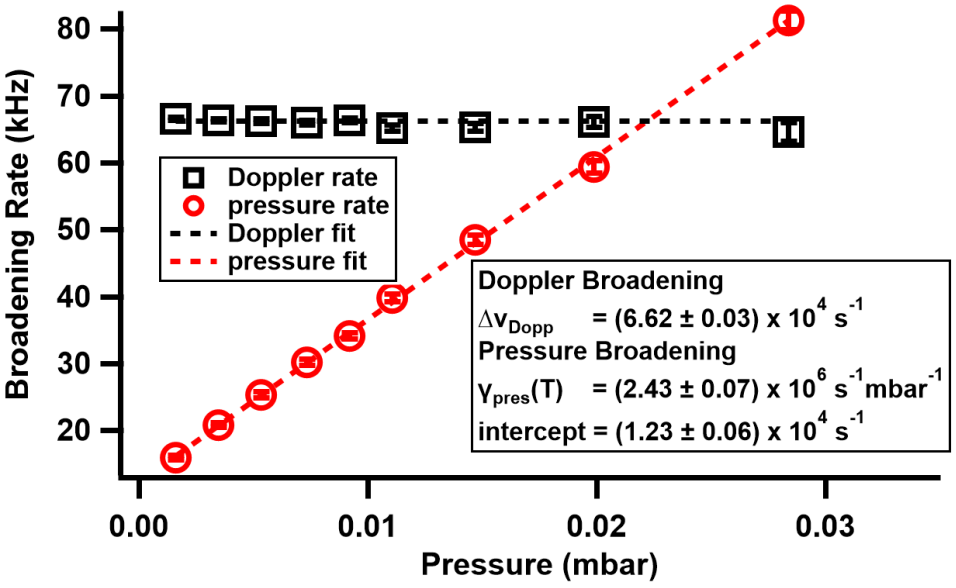

Figure 3.5: Low pressure fits of Doppler and pressure broadening for the J = 7–6 transition of OCS ($\sim 2.10^{-5}$ mbar) in He. The Doppler rate is constrained to zero slope, providing an average across the measured pressure range of (66.2 $\pm$0.03) kHz, while the pressure broadening rate is fit to a straight line whose slope yields the pressure broadening coefficient $\gamma_{Pres}(T)$. Uncertainties are quoted at the 95% confidence interval.

The results from higher pressure tests for the same transitions are shown in Figs. 3.6, 3.7 and 3.8, where exchanging the pumping group allowed the experiment to be performed at pressures up to 0.35 mbar. Noticeably, the pressure broadening rate was much faster at higher pressures than the Doppler broadening rate, which was constrained in Eq. 2.16 to 57.3 kHz, the value obtained from the low-pressure experiments. Fitting Eq. 2.16 at lower pressures produced well-constrained fitting parameters, while at higher pressures, especially above 0.25 mbar, the fit was found to be less robust due to the FID signal reducing towards the noise level in the time domain. At these high pressures, the decay has a time constant of around 200 ns, with very little data available for the fit. Except for pressures above 0.25 mbar, the pressure decay rates are well-represented by the linear fit. The pressure broadening coefficients of OCS in He at 295 K for each transition were found and all the measured coefficients are displayed in Table.3.1.

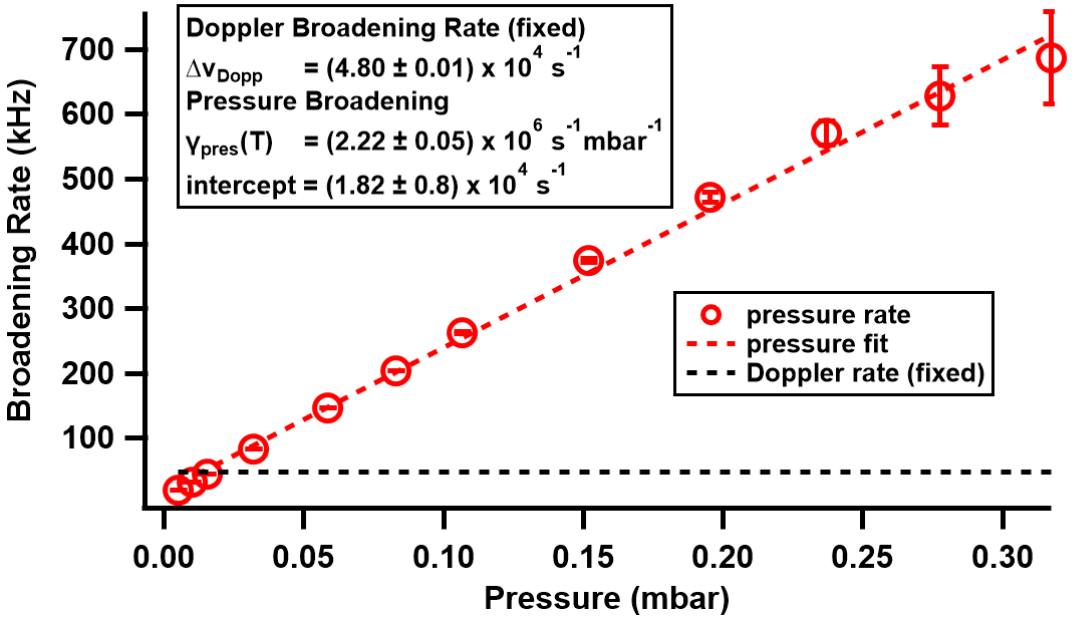

Figure 3.6: High pressure fits of pressure broadening for the J = 5-4 transition of OCS ($\sim 5.10^{-5}$ mbar) in He. The Doppler component was fixed to the value found in low pressure experiments. Uncertainties are quoted at the 95% confidence interval.

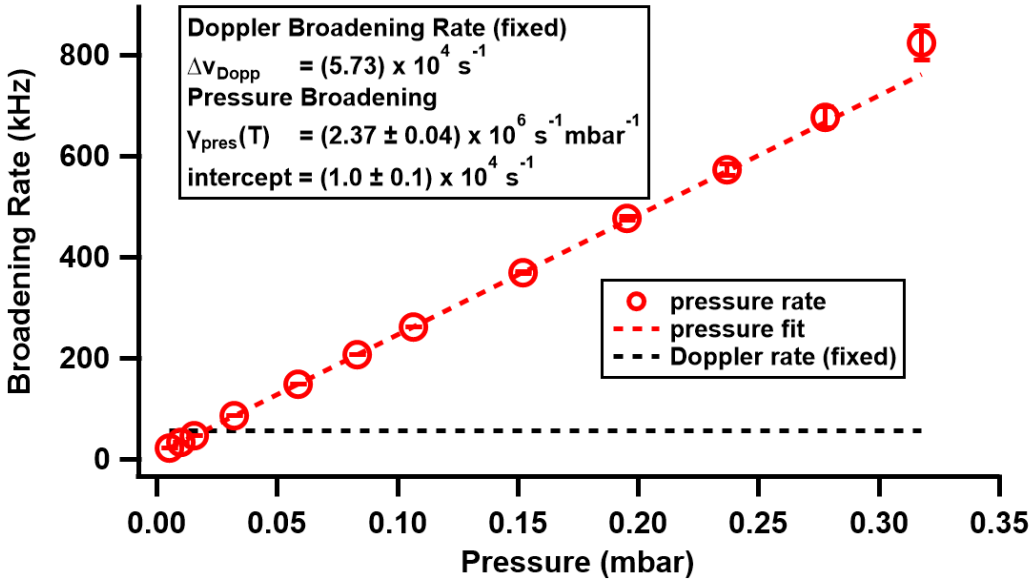

Figure 3.7: High pressure fits of pressure broadening for the J = 6–5 transition of OCS ($\sim 5.10^{-5}$ mbar) in He. The Doppler component was fixed to the value found in low pressure experiments. Uncertainties are quoted at the 95% confidence interval.

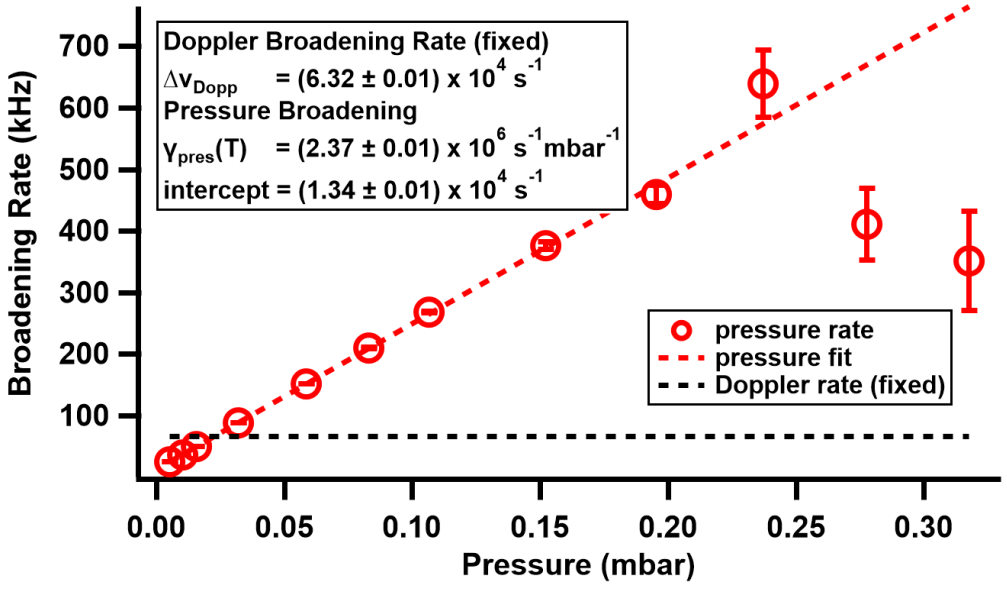

Figure 3.8: High pressure fits of pressure broadening for the J = 7-6 transition of OCS ($\sim 5.10^{-5}$ mbar) in He. The Doppler component was fixed to the value found in low pressure experiments. Uncertainties are quoted at the 95% confidence interval.

Transition	This experiment $\gamma_{Pres}(T)$ (MHz/mbar)	Previously published fits of $\gamma_{Pres}(T)$ (MHz/mbar)
HITRAN for unmeasured transitions		1.1[a]
J=1–0		2.45±0.04[b]
J=3–2		2.5±0.1[c]
J=5-6 (P branch,ν_3)		2.6±0.2[d]
J=11-10 (R branch,ν_3)		2.2±0.2[d]
J=5-4	2.39±0.01	
J=6-5	2.37±0.01	
J=7-6	2.38±0.01	

[a] Wilzewski JS, *et al.* [100]
[b] Mäder H, *et al.* [60] error 2σ.
[c] Story IC, *et al.* [98] error rms.
[d] Broquier M, *et al.* [99] error unknown.

Table 3.1: Measured OCS–He pressure broadening coefficients $\gamma_{Pres}(T)$ at 295 K with comparison to previous experiments and HITRAN. The uncertainties are quoted at the 95% confidence interval for the measurements reported here.

3.3 Discussion

The measured pressure broadening coefficients are compared against previously measured pressure broadening coefficients obtained using transient emission stark pulse spectroscopy [60], microwave spectroscopy [98], and infrared absorption spectroscopy [81] in Table.3.1. There is a transition with overlapping J levels between the infrared dataset and the current experiment, but from a P branch in an infrared band instead of a pure rotational transition, whose values should be similar. The difference between the previous experimental measurement of the J = 5–6 transition and the measurement presented here for J = 6–5 is just beyond the combined uncertainties of both experiments. The value in the HITRAN database is a factor of two lower than those found here and in previous experiments [100].

The theoretical data on the OCS + He collisional system are limited at room temperature. The theoretical pressure broadening cross-sections used in Broquier *et al.* [99] disagree dramatically from experimental values but agree qualitatively with the trend observed for different J levels of the OCS + He system. The theory predicted that the pressure broadening cross-section should be higher at low J levels but reduce slightly with increasing J levels before leveling off at higher J levels. The pressure broadening coefficients observed here are higher than those previously measured at high J levels but slightly lower than the previously observed J = 1–0 transition, which indicates that the

measured transitions are within the regime where pressure broadening depends upon J level. For a similar but more studied system, CO_2 + He, the trend of increasing pressure broadening coefficients with lower J was also observed [101]. The values reported here conform to the general trend predicted by theoretical pressure broadening cross-section calculations.

The residuals presented in Fig. 3.1 indicate that the time domain Voigt profile (Eq. 2.16) accounts for over 99% of the transition intensity. The remainder is expected to be due to small deviations in the profile caused by many possible effects, such as speed dependence of collisions [70], Dicke narrowing [102], or inhomogeneous fields [103]. This time-domain Voigt profile has been shown in a previous study to fit almost all of the FID from CH_3F in He, but not with heavier buffer gases [70]. The high signal-to-noise achieved in the spectra presented here shows that even small deviations in the line-shape can be observed in a relatively short time, and further experiments could be used to investigate more advanced effects on line-shape profiles. A preliminary analysis of the data indicates that these techniques could be used to determine line shift coefficients as well, but only within certain pressure ranges. No information on the line shift coefficients exist for the OCS + He system at room temperature, and so the initial results could not be compared against any previous work.

Fig. 3.9 shows FIDs from the J = 6–5 transition recorded at different pressures. The effects of pressure broadening are seen in the change in the shape of the decays from Doppler-dominated to pressure-dominated with the exponential decay apparent at higher pressures. The initial signal amplitude can also be seen to be strongly attenuated as the He pressure was raised. The reduction in initial signal intensity was likely an effect of collisions on the polarization induced from the single-frequency pulse, where the pulse time is longer than the T_2 time at higher pressures. As the pressure is raised in the experiment, the decay time becomes shorter than the pulse duration, with collisions disrupting the polarization of the sample. This effect is quite intense and means that at high pressures, even single frequency polarizing pulses can only effectively polarize for a limited amount of time. The reduction of the initial signal is particularly strong at low pressures, where there is a sharp loss of initial signal amplitude before leveling out at high pressures.

The decrease in FID amplitude is much larger than expected over the pressure range, with multiple effects likely contributing to this. Due to experimental constraints, namely reflections within the system, the FID was fit starting from 400 ns after the end of the excitation pulse. The FID decays rapidly during this time, reducing the available signal for fitting. As mentioned, the effective pulse length will shorten as T_2 starts to become

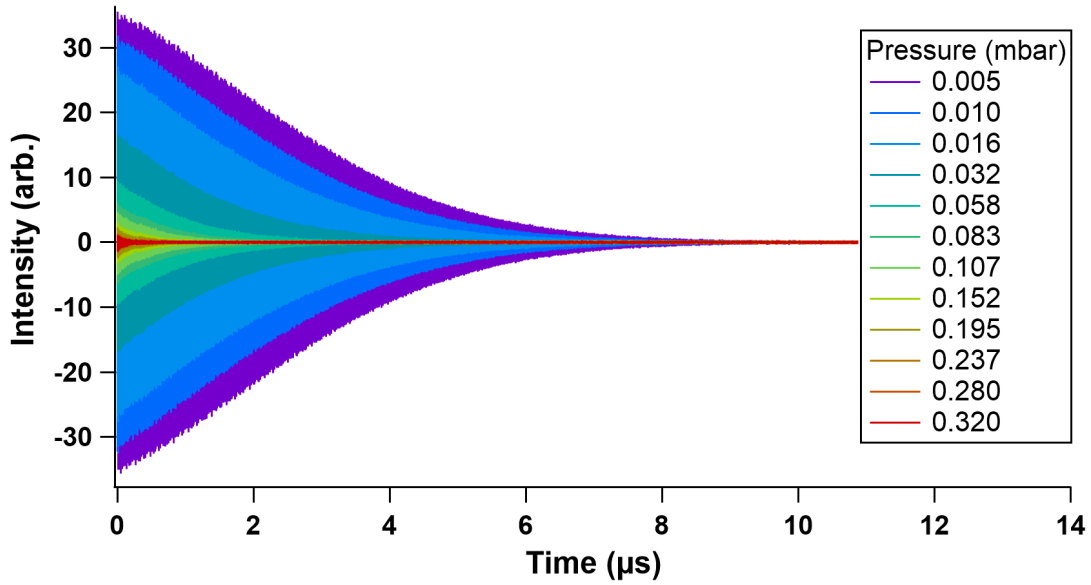

Figure 3.9: Experimental FIDs for the J = 6–5 transition over the experimental pressure range for a fixed partial pressure of OCS of $\sim 5.10^{-5}$ mbar in He buffer gas between 0.005–0.320 mbar.

the same magnitude or shorter than the pulse duration, reducing the polarization possible from a given pulse length. As the effective pulse becomes shorter, the frequency width of the pulse becomes greater, with less of the pulse overlapping with the frequency width of the transition. All of these effects will cause a reduction in initial FID amplitude, observed in these experiments, which makes excitation using single-frequency pulses difficult to model. This difficult modeling can be avoided by using chirped excitation in the linear fast passage regime, which has a fast polarization time per transition, in order to describe the relative intensities of the signal. However, in this regime there are other effects, dependent on pressure broadening, that must be accounted for such as decay within the chirp and the importance of transition position within the chirp [28, 92]. FID signals are inherently weaker in the linear fast passage regime compared to excitation via single-frequency pulses, even when $\pi/2$ pulse conditions cannot be attained, so the types of pulses used here are still effective for experiments.

Three OCS + He pressure broadening coefficients were determined in the range of the E-band CP-FTmmW spectrometer. A time-domain Voigt profile was employed to accurately represent the FID at both low and high pressures. The pressure broadening coefficients found here agree with previous work. The FID decays very rapidly at high pressures, which reduces the available signal for both time-domain fitting and Fourier transformation. Furthermore, the initial amplitude of the FID is affected by the pressure,

where the effective polarization of the polarizing pulse seems to be reduced as the pressure rises. The results presented in Fig. 3.9 guided the design of the helium nozzle specially fabricated for the CRESUCHIRP project, as the pressure in the CRESU chamber needs to be as small as possible to increase sensitivity. At this stage, only helium was considered as a buffer gas as argon and nitrogen are generally more effective colliders resulting in stronger quenching of the FIDs.

Chapter 4

Chirped Pulse in Uniform Flow (CPUF)

The main goal of the CRESUCHIRP project is to combine the CRESU technique with a detection system using CP-FTmmw spectroscopy in order to study reaction kinetics at low temperatures. In this context and after the preliminary demonstration of the spectrometer capability presented in the preceding chapters the new E-band spectrometer was coupled to the newly constructed CRESU chamber presented in section 2.7.1. This chapter presents results from the newly constructed experimental apparatus using the CPUF technique. It is divided into three parts, the first one describes the first CPUF experiments, which were used to benchmark the system, and the basis on which all of the technical developments presented in section 2.9 originated from. The second section presents the results of the measurements of the differences in collisional interactions between HCN + He and HNC + He. The third section presents the results of the application of the CPUF technique to low-temperature reaction dynamics.

The results presented in this chapter were taken using five different Laval nozzles (one used with two conditions leading to two temperatures). Three of these nozzles are designed using helium specifically for the CRESUCHIRP project by Omar Abdelkader Khedaoui (details will appear in his thesis). The other ones are previously made helium and argon nozzles. At the start of the project, only helium was considered as buffer gas for CPUF as from the three usual buffer gases used for the CRESU technique, helium, argon, and nitrogen, helium is the "best collider". Rohart *et al.* [104] measured the differences in the relaxation of $HC^{15}N$ J = 1-0 with different buffer gases, N_2, H_2, D_2, Ar, and He in function of the temperature down to 135 K using a low-temperature Stark cell. Fig. 4.1 presents their results, they showed that helium is the least efficient of the buffer gases used to relax $HC^{15}N$ compare to argon which is about 50% more efficient at room temperature and nitrogen about 350% more efficient. This implies that for the CPUF experiments, a Laval nozzle using helium as the buffer gas would have the least impact on the relaxation

of the FID which would lead to a stronger molecular signal compare to a nozzle with the same temperature and pressure but using argon or nitrogen. Helium is also the buffer gas that allows for the generation of the coolest CRESU flow which relates the most to the astrochemical environment. But helium nozzles have some practical limitations: they are the nozzle with the fastest flows (around 1700 m s^{-1} compare to around 500 m s^{-1} in argon nozzles); and the shortest length of uniformity (around 20 cm compared to more than 50 cm for argon and nitrogen nozzles) These two factors lead to helium uniform flows providing short hydrodynamic times (70-200 µs compared to a little more than 1 ms for argon nozzles). This short hydrodynamic time limits the systems that can be studied in these nozzles as processes can take longer than the hydrodynamic time to finish. Another limitation is that helium flows have smaller diameter isentropic cores than those from nitrogen or argon nozzles (0.5 cm compared to 1 to 2cm), leading to a factor of 4 to 16 in the number of molecules in the probing region when accounting for the number density. These limitations were only taken into account later in the project and at this stage, the argon nozzle was added to the list of nozzles used for these experiments as the gain in isentropic core size more than compensated for the increased collisional cross-section. Table 4.1 summarizes the conditions of the nozzles used. Pitot profiles can be found in the appendix.

Table 4.1: Summary of nozzle conditions used.

Nozzle name	Buffer gas	Temperature (K)	Density (cm^{-3})	hydrodynamic time (µs)
He10K	He	9.9	8.1×10^{16}	128
He20K	He	16.6	4.85×10^{16}	132
He20K	He	18.7	3.78×10^{16}	135
He35K	He	30.2	3×10^{16}	126
Ar50K0.3	He	71.6	6×10^{16}	163
Ar28K	Ar	30.5	1.9×10^{16}	1083

The data presented in this chapter represent the evolution of the molecular signal over time. The time dependence is acquired using the scheme presented in section 2.9, which relies on trains of frames being broadcast by the spectrometer. The frames are then analyzed individually or in packets to obtain the intensity of the molecular signal as a function of the time after the laser pulse. The type of analysis depends on the nature of the signal. For the molecular signal of stable molecules, which does not permit the removal of reflections, the intensity of the peak of the spectral line in the frequency domain is used to quantify the signal without any fitting. For laser-induced signals when the SNR

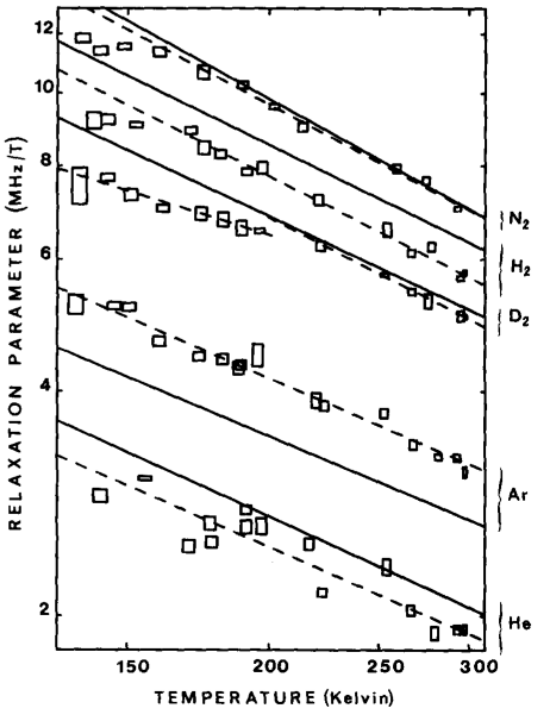

Figure 4.1: Figure and caption taken from Rohart *et al.* [104] to present the collisional cross-section variation in function of the buffer gas. "Foreign gas relaxation of the J = 1-0 line of $HC^{15}N$. Log-log plot of the relaxation parameters $C_{\omega}^{\mathrm{HCN}-b}$ vs the temperature T for the buffer gases b = N_2, H_2, D_2, Ar, and He. Reported uncertainties are one standard deviation for C_{ω} , and 2 K for temperatures (1 K at room temperature). The data are least-squares fitted according to Eq. (7) (dotted lines) and the ATC collision theory results are drawn in straight lines."

is sufficiently high, the amplitude of the FID in the time domain was fit using the model presented in section 2.4 to quantify the signal. In the case where the SNR is too small for the fit in the time domain to be reliable, the peak intensity of the spectral line in the frequency domain is used to quantify the signal in the same way it is done for a stable molecule without any fitting.

Tests were done in order to ensure that using only the peak intensity of a line is not introducing error or bias in the interpretation of the data, because of the finite resolution of the spectrometer which could miss the peak. An example of these tests is presented in Fig. 4.2 where it can be seen that comparing both the time domain fitting and the peak intensity of the spectral line in the frequency domain follow a similar shape and evolution. This demonstrates that the peak intensity still is a good approximation of the line intensity and that the fitting is not required to interpret the data. The time dependence presented in the chapter are analyzed using the time domain Voigt profile fitting when possible and the

intensity of the peak of the line is used when the fit cannot be used reliably. The methods used are detailed in the caption of the figure.

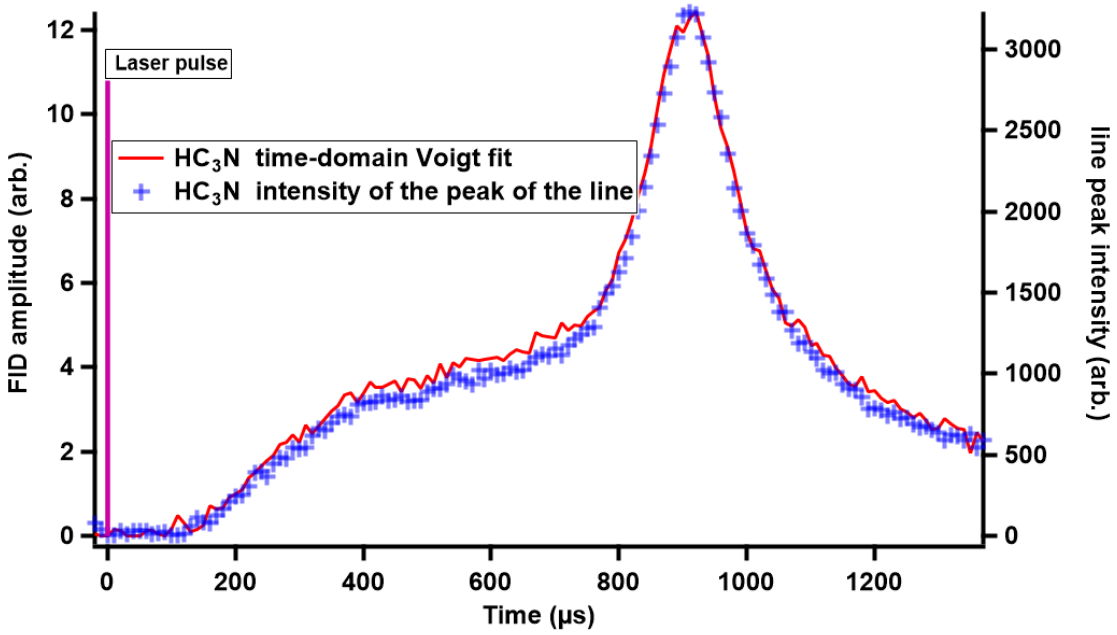

Figure 4.2: Comparison between analysis techniques on HC_3N J = 8-7 transition from photolysis of acrylonitrile (1.74×10^{12} cm^{-3}, fluence 2.3×10^{16}photons cm^{-2} per pulse) in an Ar 30 K CRESU flow 1.2×10^{5} avg per point. In red amplitude of the FID from the time-domain Voigt fit, in blue peak intensity of the line in the frequency domain.

4.1 Preliminary work on CPUF

As a proof of concept for the new experimental apparatus, the photodissociation of acrylonitrile (C_3H_3N, Sigma Aldrich $\geq$99%) was studied. Since acrylonitrile photolysis has already been studied with a similar spectrometer in a room temperature cell and a supersonic expansion, [78, 105] some of the results could be used to benchmark the time resolution and spectral performance of this apparatus. Acrylonitrile was chosen because its photolysis at 193 nm is well-studied [78, 105–107]. The photodissociation of acrylonitrile offers multiple advantages: it has a high absorption cross-section at 193 nm (2.85×10^{-17}cm^2) [108], and both acrylonitrile and several of the photolysis products possess readily accessible transitions within the frequency range of the spectrometer the photolysis products and acrylonitrile also have high dipole moments. As well, the photo fragments HCN and HNC are small linear molecules, possessing lower pressure broadening rates as compared to larger molecules.

The first experiments were focused on observing acrylonitrile as a stable product in the flow. The experiments were performed by flowing known quantities of acrylonitrile through the controlled evaporation and mixing system (CEM). A major advantage of using CP-FTmmW spectroscopy is its broadband capability, allowing for the detection of multiple transitions. Waveforms for the excitation pulse were generated according to the procedure presented in section 2.9.5. In the case of a stable product like acrylonitrile, which does not require a laser pulse to be generated, the scheme presented in section 2.9 cannot be used as it is impossible to define a background to be subtracted. Experiments were performed by measuring spectra, then stopping the flow of acrylonitrile and acquiring again a signal to generate a background of reflections to subtract from the spectra. However, this method of cleaning of the spectra is not reliable as the reflections evolve over time (probably with the mechanical vibration of the chamber) and good subtraction of the reflections can only be done when recorded at the same time as the molecular signal, which is only possible to do with laser experiment. In order to compensate for the reflections, the window of the Fourier transform was adjusted to start after the reflections have decayed. This leads to a greater reduction of the signal intensity as the reflection can last for a significant part of the FID. As well, they are more intense at the start of the FID when the signal is also most intense. The reflections in this case render the "best" part of the FID unusable and the only way to observe sufficient signal is to increase the amount of acrylonitrile in the flow. Fig. 4.3 presents the effect of the reflections on the spectrum. The blue trace shows the FFT being taken 40 ns after the pulse at the time the millimeter-wave switch stops attenuating the signal. At this time the spectra are covered by the reflections which affect the baseline and the lines. The red trace is the same signal but with the FFT taken 150 ns after the pulse. In this case, the reflections have decayed away and the spectral lines and can be seen with a flat baseline, which means that their shape is not affected by reflections.

When such spectra containing multiple transitions for a stable species can be measured, it is in theory possible to use the relative intensity of the lines to determine by spectroscopy the rotational temperature of the sample, as Abeysekera *et al.* [29] presented in a similar experiment. For this purpose, a spectrum of acrylonitrile was acquired using a chirped excitation, presented in Fig. 4.4. Multiple difficulties arise when trying to determine the temperature using this technique because of factors affecting the relative line intensity. First, the collisional environment being the principal quenching effect for the FID, the excitation pulse parameter needs to be decided carefully. The duration of the pulse has to be less or on the order of the decay rate of the FID, typically a few hundred

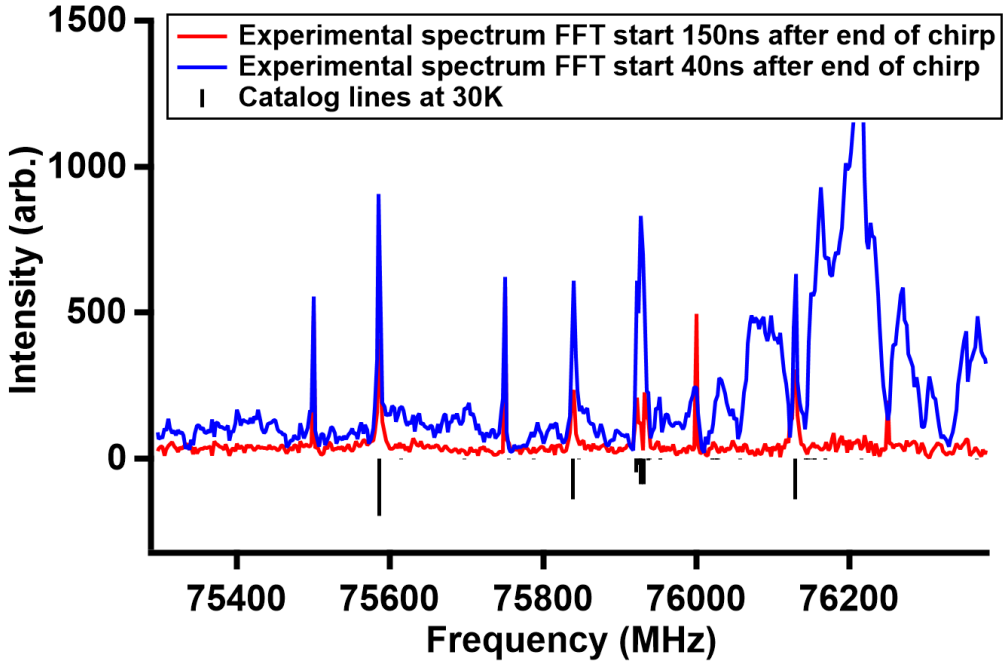

Figure 4.3: Acrylonitrile spectrum in an argon 30 K flow (density of acrylonitrile: 1.74×10^{12} cm^{-3}) using a 200 ns chirp from 74.835 to 76.95 GHz, 16×10^{6} averages. In blue Fourier transform of the acrylonitrile signal starting 40 after the excitation pulse end. In red Fourier transform of the acrylonitrile signal starting 150 ns after the excitation pulse end. In black and in reversed catalog transitions with intensity scaled at 30K.

nanoseconds. The bandwidth of the chirp needs to be wider than the separation between the farthest lines in order for the lines to be excited all in a relatively short time to avoid the first excited lines being affected significantly more by the collisional environment than the last ones. Having the line in the middle of the pulse and not at the end also mitigates the inherent effect of the exponential decay, after a few characteristic times, the variation of the amplitude becomes smaller as the time increases thus reducing this impact on the relative line intensities but at the cost of losing the more intense part of the FID [109]. Two scans with chirps going in the opposite direction (up or down in frequency) are also averaged in order to reduce this effect as presented in Abeysekera *et al.* [29]. Second, the reflections of the excitation pulse limit a possible optimization of the FFT window which could compensate for the effect described above. Third, the design of the experiment leads to the microwave "beam" probing perpendicularly the flow and thus exciting molecules from the residual gas in the chamber and the boundary layer. This affects the resulting relative line intensities as multiple samples of molecules with different temperatures are being probed at the same time. All of these effects do not permit reliable spectroscopic measurement of the temperature. There is in theory a possibility to mitigate all of the ef-

fects mentioned above except the one related to pressure broadening. If the sensitivity was sufficient it would be possible to use the excimer laser to photolyze acrylonitrile and then record a spectrum of it before and after the laser pulse. The subtraction of these two signals would allow the measurement of the spectrum of the acrylonitrile that was depleted. This signal would be free of reflections because of the background subtractions and would only come from the cold acrylonitrile of the CRESU flow as only these molecules would be photolyzed and the remaining contribution from the boundary layers and residual gas would be erased with background subtraction. Unfortunately, the detection is not yet sensitive enough to be able to perform this experiment. Temperatures of the flow are thus not characterized using a spectroscopic technique but using Pitot probe measurements as presented in section 2.1.

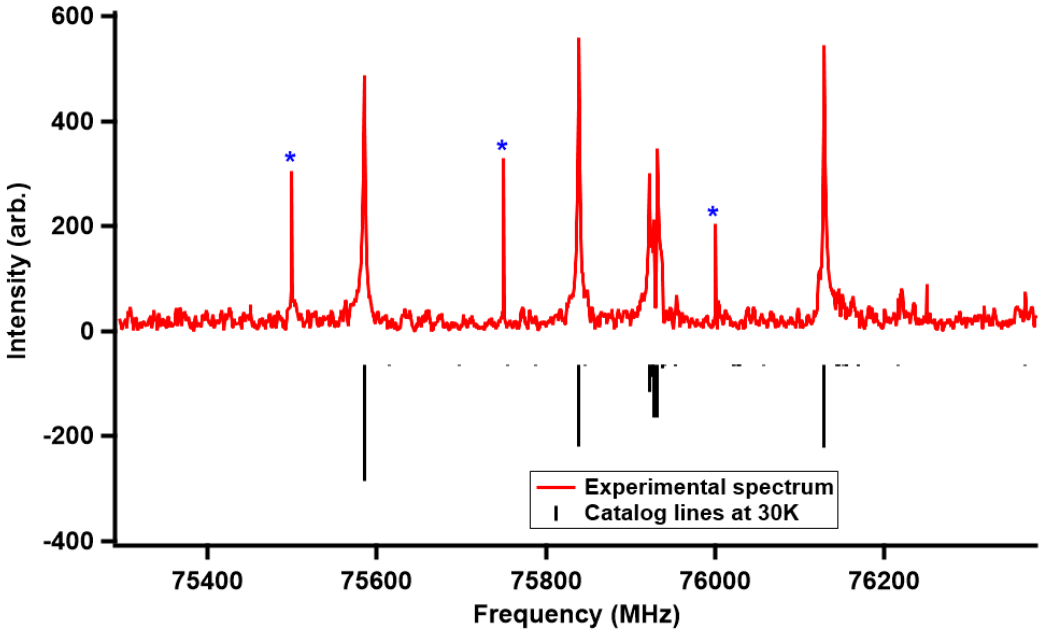

Figure 4.4: Acrylonitrile spectrum in an argon 30 K flow (density of acrylonitrile: 1.74×10^{12} cm^{-3}) using a 200 ns chirp from 74.835 to 76.95 GHz, 16×10^{6} averages. In red Fourier transform of the acrylonitrile signal. In black and in reversed catalog transitions with intensity scaled at 30K. Blue asterisks mark electronic spurs.

Acrylonitrile was then photolyzed at 193nm with a fluence of 2.3×10^{16}photons cm^{-2} per pulse, as measured on a power meter (Molectron) between experiments. Using the scheme presented in section 2.9, the time dependence of the acrylonitrile can be extracted as shown in Fig.4.5, where the depletion of one acrylonitrile line ($J_{Ka,Kc}$ = $8_{0,8}$-$7_{0,7}$ due to its photolysis in an argon flow at 30K is presented. The time trace displays the expected shape of the molecular signal in a CRESU flow. A flat region before the laser fires shows

the presence of acrylonitrile in the flow (region I). A sudden depletion occurs when the laser fires (0 µs) and the molecules are photodissociated. This is followed by another flat region with lower intensity than the first region (region II), this is the region that corresponds to the hydrodynamic time of the nozzle, where processes are observed. In the case of the photodissociation, the process is instantaneous for the time resolution of the spectrometer and thus region II is a stable plateau. The last part (region III) displays some structure, a larger depletion which is due to the gas that was photolyzed in the nozzle throat at the time of laser firing. At this point in the flow, the depletion is bigger due to two effects. First, the density at the throat is higher by orders of magnitudes which increase the depletion. Second, at this point the laser beam irradiates the whole flow cross-section, even the boundary layers compare to the other point in the flow where the laser only overlaps with only a part of the isentropic core thus reducing the quantity of molecule interaction with the laser beam. The signal from this region is not incorporated in the analysis of the results as it has come from a region where the conditions are non-uniform and unknown, though it is still used as a stronger signal to optimize the spectrometer parameters (length of the excitation pulse, LO position...). It can also be used to determine the end of the hydrodynamic time of the nozzle. The insets B) and C) of the figure present the spectrum of the transition before and after the laser pulse. It is clear that the lines are completely surrounded by significant reflections, which altered their shape. This is because the FFTs are taken only 22 ns after the excitation pulse, which is too close to the end of the excitation pulse to allow the reflection to decay. But since the reflections are constant on the timescale of one acquisition (a hypothesis which is validated by the total rejection of reflections when using the background subtraction scheme presented in section 2.9.2) they do not affect the shape of the signal but only add an offset on top of it.

These experiments were first used to try to estimate the quantity of acrylonitrile depleted to lead to an independent measurement of the fluence of the laser from those made by a laser power meter. However, two factors make it impossible to extract these two quantities. First is a geometric factor, the laser beam is adjusted to the size of the isentropic core and it is impossible to be certain that all the cold gas is illuminated by the laser or to estimate the contributions of the boundary layer on the molecular signal. These geometric effects make it difficult to quantify the proportion of the signal before the laser, which corresponds to the acrylonitrile present in the overlap between the laser beam and the isentropic core. The second factor related to the reflections will also have to be quantified as they affect the baseline and make it complicated to quantify any depletion signal.

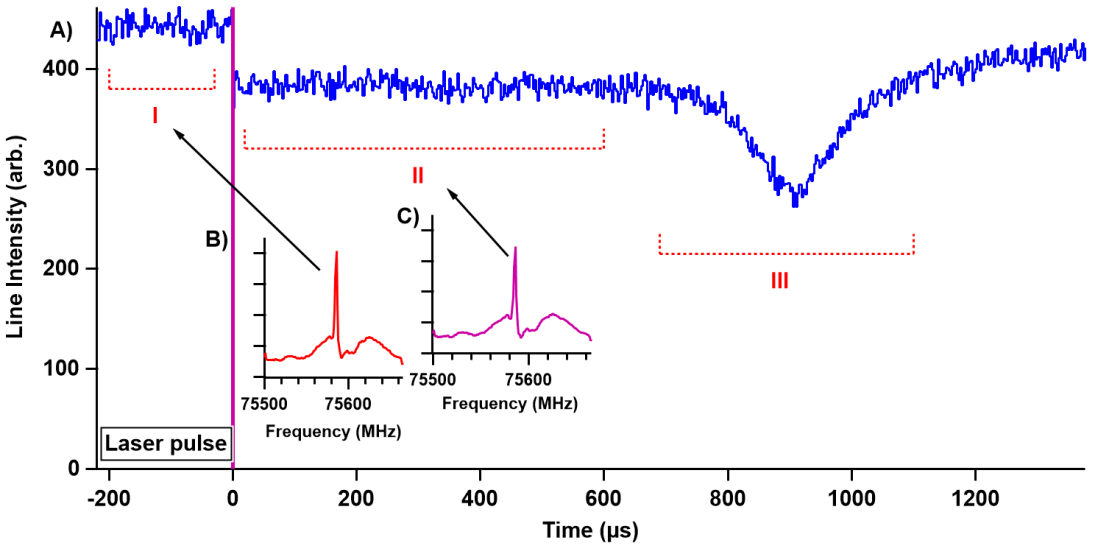

Figure 4.5: Acrylonitrile depletion 1.74×10^{12} cm^{-3}, fluence 2.3×10^{16}photons cm^{-2} per pulse in an argon 30 K flow. In blue line intensity of the $J_{Ka,Kc}$ = $8_{0,8}$-$7_{0,7}$ transition. 640 2.5 µs frames recorded at 1.25 GS/s, 10^4 averages, excitation: single frequency pulse of 200ns, inset show the FFT of the signal before and after the laser pulse.

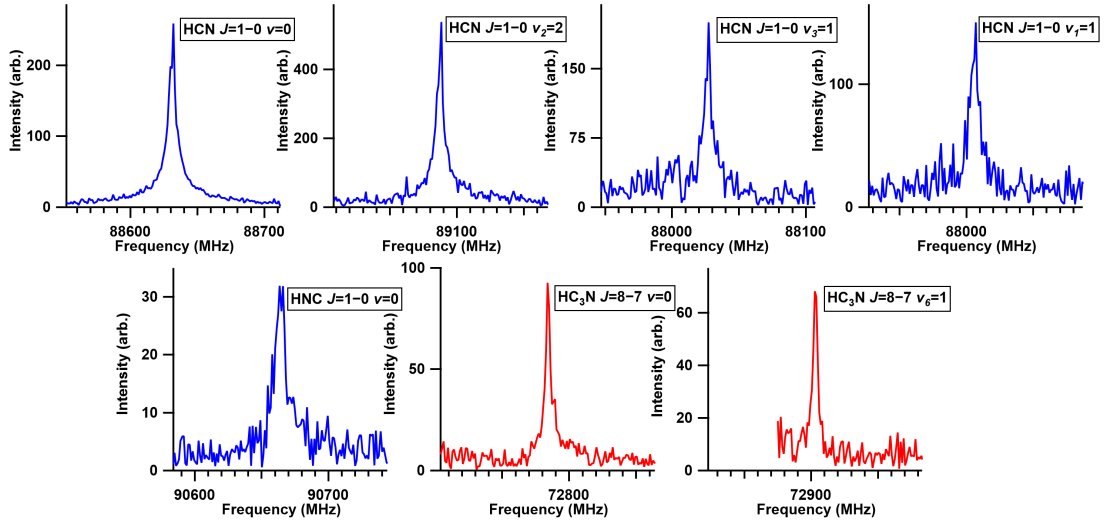

Figure 4.6: Acrylonitrile photodissociation products in a CRESU flow. In blue in a 10 K helium flow (density of acrylonitrile: 1.9×10^{13} cm^{-3}, fluence 3.4×10^{16} cm^{-2} photons per pulse, 2×10^5 avg) and in red in an argon 30 K flow (density of acrylonitrile: 1.8×10^{12} cm^{-3}, fluence 1.7×10^{16} cm^{-2} photons per pulses, 4×10^4 avg for HC_3N in its vibrational ground state and 2×10^5 avg for the vibrationally excited state)

Different products of the acrylonitrile photodissociation at 193 nm were detected and are presented in Fig. 4.6. In blue are detections made in the helium 10 K nozzle flow, HCN

J = 1–0, HNC J = 1–0 and some vibrationally excited transitions of HCN ($\nu_1 = 1$, $\nu_2 = 2$ and $\nu_3 = 1$) can be seen, resulting from the photolysis of 1.9×10^{13} cm^{-3} acrylonitrile density with a photon fluence of 3.4×10^{16} cm^{-2} per pulse. In red detections in the argon 30 K nozzle flow are shown with HC_3N J = 8–7 in its vibrational ground state as well as the vibrationally excited $\nu_6 = 1$ from the photolysis of 1.8×10^{12} cm^{-3} acrylonitrile density with a photon fluence of 1.7×10^{16} cm^{-2} per pulses The hyperfine splitting of HCN can be partially resolved, but not for HNC. The spectrometer in these conditions is sensitive enough to detect each of these species with enough SNR to allow for clear resolution of the line profile and intensity. The spectrometer was optimized for each of the vibrational ground state transitions. The duration of the single-frequency pulses used to excite the transitions was adjusted empirically to attain the maximum polarization possible, which in these pressure conditions differs from the $\pi/2$ pulse as the polarization decays too quickly due to the collisions. The local oscillator frequencies (LO) used to down-convert the frequency in the receiver were also empirically optimized by testing multiple LO frequencies. Table 4.2 summarized the parameters used for the probing of HCN, HNC, and HC_3N.

Table 4.2: Optimized spectrometer parameters for the detection of the acrylonitrile photoproduct in the helium 10 K flow for HCN and HNC and in the argon 30 K flow for HC_3N. The frequency of the lines are from CDMS and do not include hyperfine splitting.

Molecules	HCN	HNC	HC_3N
Transition quantum number	J = 1–0	J = 1–0	J = 8-7
Frequency of the line (MHz)	88631.602	90663.568	72783.822
Excitation pulse length (ns)	140	200	100
Local oscillator frequency (MHz)	87500	88400	73500

With the use of the acquisition scheme presented in section 2.9, the time dependence of the photoproduct signals can be extracted. Fig.4.7 presents the evolution of the HC_3N J = 8–7 from its vibrational ground state in the argon 30 K nozzle from photolysis. The different regions presented in Fig. 4.5 can be found in the time evolution of products with region I being present before the laser pulse for two points, region III with the signal from the nozzle is present after the dashed line signaling the end of the hydrodynamic time. Region II corresponds to the molecules formed in the cold isentropic core, where the time evolution of the HC_3N signal can be monitored under isentropic conditions. The evolution can be separated into three different regimes, first a delay $\sim$ 170 µs after the laser pulse before the appearance of the signal. An initial rise between $\sim$ 170 µs and

400 µs is followed by a change in the slope and a second rise between 400 µs and 700 µs. The two different slopes in the rise could arise from relaxation processes happening at different rates (rotation, vibration). In order to investigate these, the same experiment was repeated while searching for vibrationally excited states of HC_3N within the range of the spectrometer and catalog referenced in the CDMS database ; the J = 8–7 rotational level of the $v_2 = 1$, $v_3 = 1$, $v_4 = 1$, $v_5 = 1/v_7 = 3$, $v_6 = 1$, $v_6 = 2$, $v_7 = 1$, $v_7 = 2$, were investigated, photolyzing 1.8×10^{12} cm^{-3} acrylonitrile with a fluence of 1.1×10^{16} cm^{-2} per pulse) averaging 5 $\times 10^4$ time per scan. Only the $v_6 = 1$ transition could be detected in the cold part of the flow. The $v_7 = 1$ transition could be seen from the nozzle part of the flow. The vibrationally excited states could not be recorded with high SNR, it is difficult to evaluate if this is due to the sensitivity of the spectrometer or whether a specific level is not populated. Fig. 4.8 presents the time dependence of the $v_6 = 1$ transition on top of the ground state level. It is interesting to note that both present a similar structure, with a similar delay between the laser and the appearance of signal and a change in the slope of the evolution at a similar time. Both signals rise and reach a point where the evolution changes slope. The vibrationally excited state seems to stop rising halfway through the rise of the ground state. After this point, the signal of the vibrationally excited state decreases until the end of the hydrodynamic time while the ground state keeps rising. The second rise of the ground state could be explained by the relaxation of the vibrationally excited state to the ground state. But this cannot be the only effect as the change in slope does not happen at the same time for both signals. Other vibrationally excited states could be relaxing to the ground state and participate in the second rise of the signal. The delay before the start is difficult to explain but was also observed by Zaleski *et al.* [78] which they attributed to HC_3N forming via a sequential H loss mechanism. Another argon nozzle at 50 K was used in order to see if the delay would change under different conditions but the signal was too low in these experiments to draw some conclusions.

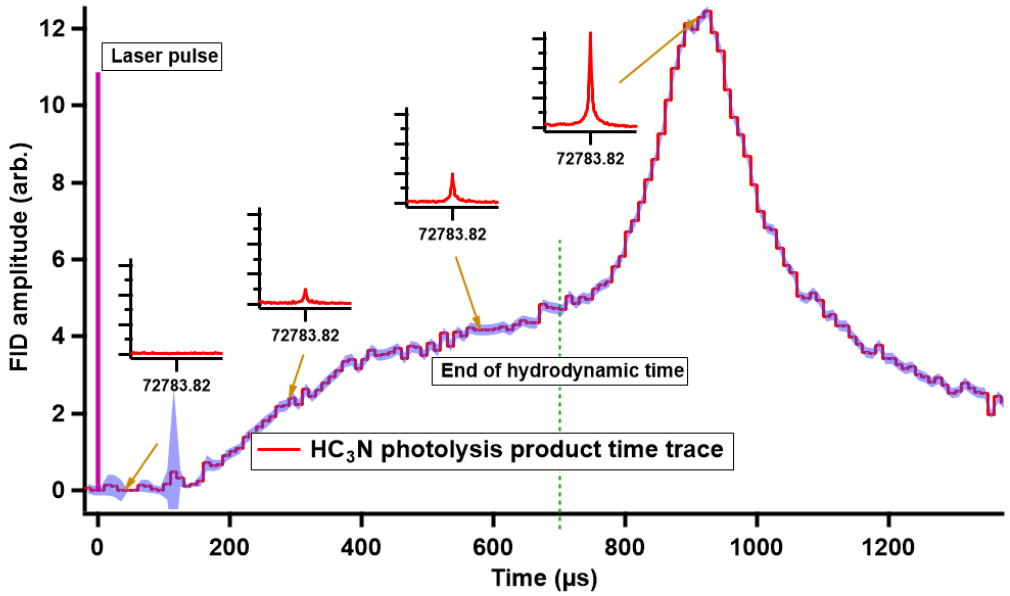

Figure 4.7: Time evolution of the FID amplitude of the HC_3N $J = 8$–7 vibrational ground state transition (1.8×10^{12} cm^{-3} acrylonitrile density, fluence 1.7×10^{16} cm^{-2} photons per pulse, 1.2×10^5 avg per point). Using the time domain Voigt fit. In shaded blue error on the amplitude 95% confidence. The insets show the FFT of the FID at different times.

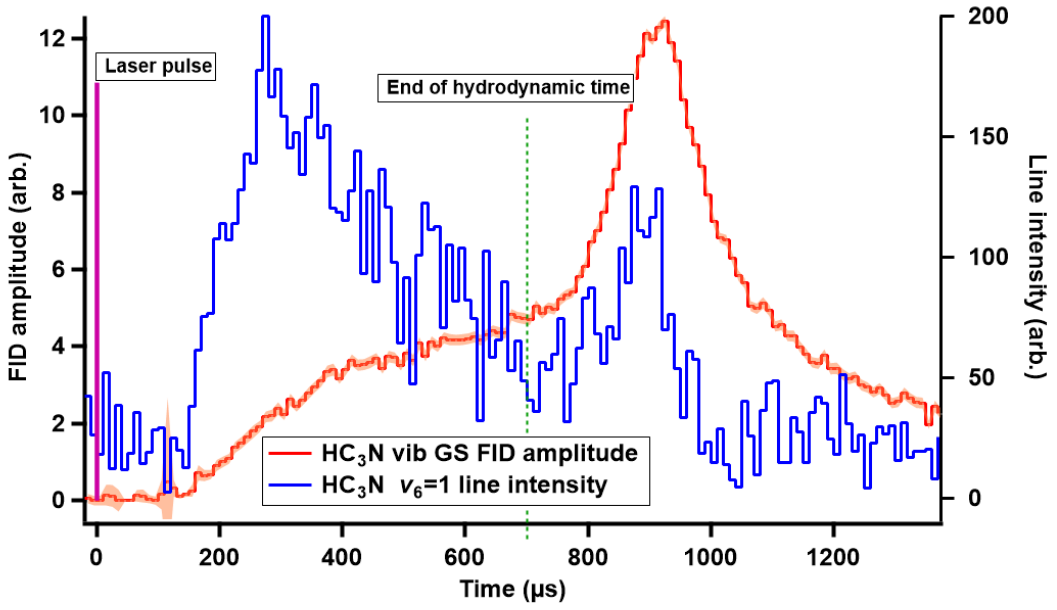

Figure 4.8: Ar 30 K time evolution of HC_3N $J = 8$–7 vibrational ground state transition in red (time domain Voigt fit) (1.8×10^{12} cm^{-3} acrylonitrile density, fluence 1.7×10^{16} cm^{-2} photons per pulse, 1.2×10^5) avg per point). In blue intensity of the $J = 8$–7 $\nu_6 = 1$ transition in the frequency domain with 2×10^5 avg per point.

Similar experiments were performed observing HCN as a product of the photodissociation of acrylonitrile at 193 nm in the helium 10 K nozzle. Fig. 4.9 presents the time dependence of the intensity of the J = 1–0 vibrational ground state transition of HCN. Compared to HC_3N the HCN signal appears directly after the laser pulse without any delay indicating a more direct mechanism for its formation during the photolysis. The signal then rises for 50 µs before stabilizing at a plateau until the end of the hydrodynamic time. The first rise could be attributed to rotational cooling as in past experiments [106, 107] it was found that HCN is generated with fairly high internal energy (~25 kcal mol^{-1}). Vibrationally excited states of HCN were probed to observed their evolution over time. The J = 1–0 transitions were probed and detected for $\nu_1 = 1$, $\nu_2 = 2$ and $\nu_3 = 1$ vibrational states, Fig. 4.10 presents their time evolution compared to the evolution of the vibrational ground state J = 1–0 transition. It can be noted that the vibrationally excited state signals appear at the same time as the vibrational ground state, just after the laser fires, and follows growth on a similar time scale as the vibrational ground state, except the $\nu_1 = 1$ signal, which presents too much variation from a low SNR to be able to draw conclusions. A notable difference is that the vibrationally excited state signals are not present with the characteristic rise of signal from the nozzle throat (region III of Fig.4.5) but on the contrary decrease. This is likely from faster relaxation rates in the conditions of the throat where the density and temperature are higher.

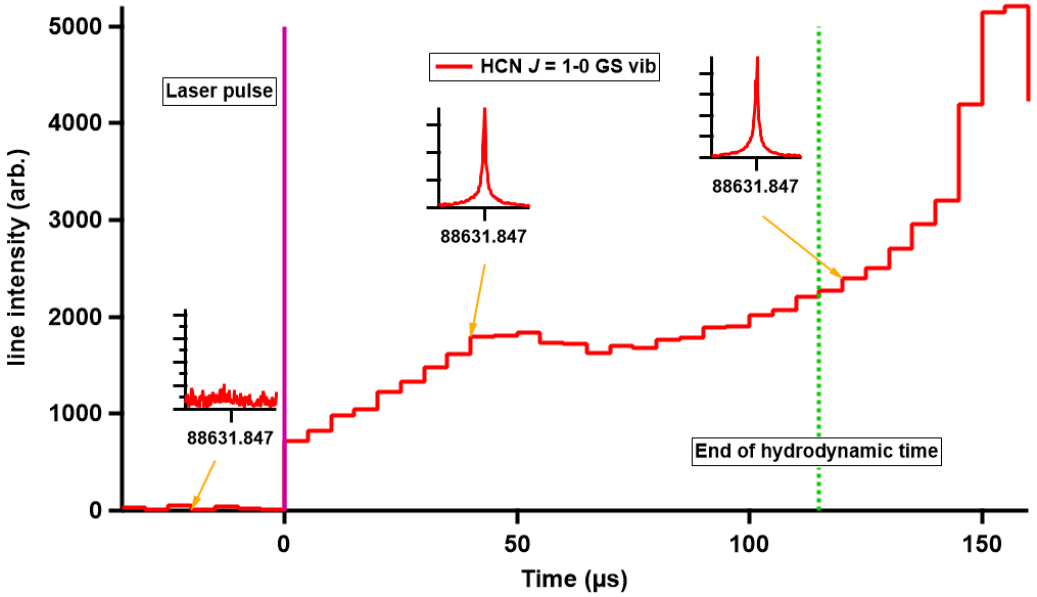

Figure 4.9: Line intensity of the J = 1–0 transition of HCN from the photolysis of 1.9×10^{13} cm^{-3} acrylonitrile with a fluence of 3.4×10^{16} cm^{-2} photons per pulse. 2×10^5 avg per point. The insets show the FFT of the FID at different times.

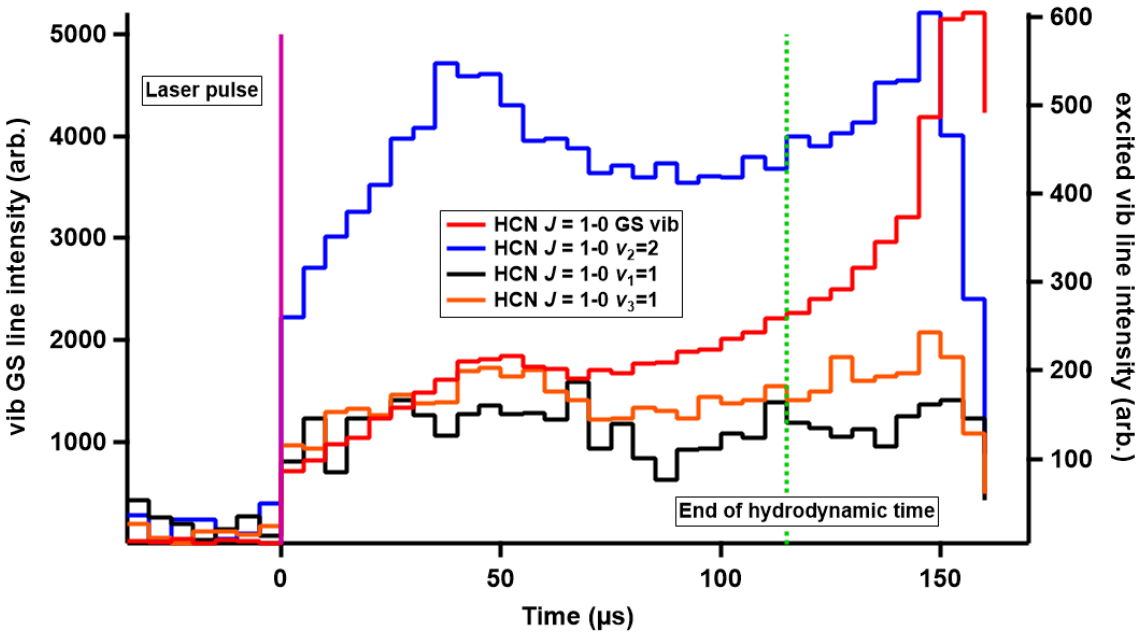

Figure 4.10: Line intensity of the J = 1–0 transition of HCN. In red the vibrational ground state, in blue $v_2 = 2$ vibrationally excited state, in black $v_1 = 1$ vibrationally excited state and in orange $v_3 = 1$ vibrationally excited state. From the photolysis of 1.9×10^{13} cm^{-3} acrylonitrile with a fluence of 3.4×10^{16} cm^{-2} photons per pulse.

A systematic study was then done in order to empirically compare the signal in the different cold temperature nozzles that were planned to be used to study reaction kinetics. The results of these tests are shown for HCN and HNC from cold helium nozzles in table 4.3, where the values presented are the amplitude of the FID's 100 µs after the laser pulse scaled by the density of acrylonitrile injected in the flow. The experiments were performed with the same laser fluence and similar iris size. The main uncertainty would come from differences in the overlap between the isentropic-core and the laser beam, which could come from inaccuracy in the alignment of the laser. One important hypothesis that could affect the results found in table 4.3 is that the photolysis branching fraction is assumed to be temperature independent.

HC_3N does not appear in this table as it was never detected in the cold CRESU flow of the helium nozzle. This can be explained by the delay observed in Fig.4.7 for the appearance of the HC_3N signal, which is longer than the hydrodynamic time of the helium nozzle used. HC_3N is only detected in the isentropic core of the Ar 30 K nozzle. This nozzle is not included in the table for HCN and HNC as its conditions are less favorable to detect these molecules. Between 30 and 10 K the partition function for HCN and HNC reduces the J = 1–0 transition intensity by an order of magnitude. Furthermore, the

hydrodynamic conditions of the argon 30 K nozzle do not allow for the injection of as much acrylonitrile as in the helium nozzle, further reducing their transition intensities.

Table 4.3

buffer gas and temperature (K)	He 10 K	He 16.6 K	He 18.7 K	He 30.2 K
HCN scaled FID amplitude (arb.)	2.15	0.98	0.57	0.28
HNC scaled FID amplitude (arb.)	0.41	0.23	0.18	0.13

It is interesting to note that the reduction of signal intensity as the temperature increases for HCN and HNC is different, HNC is less impacted by the increase of the temperature. Multiple factors lead to the variation of the signal strength in each nozzle, the different temperature of these nozzle affects the signal strength based on the partition function while the difference in chamber pressure affects the collisional broadening rate. These effects are molecule specific, even for isomers like HCN and HNC, and can affect the evolution of the signal between nozzle. The particular case of the evolution of the collision cross-section of HCN and HNC with helium as a function of the temperature is the subject of the study presented in the next section.

4.2 Measurements of the differences in collisional interactions between HCN + He and HNC + He

Work extracted and expanded from article under review *Brian M. Hays, Divita Gupta* ***Théo Guillaume****, Omar Abdelkader Khedaoui, Ilsa R. Cooke, Franck Thibault, François Lique and Ian R. Sims. Measuring the differences in collisional interactions of isomers at low temperatures: HCN and HNC with He.*

Contribution in the work in Methodology, Software, Validation, Formal analysis, Investigation, Resources, Writing - review and editing, Visualization.

Studying isomeric systems in space offers a tantalizing opportunity to investigate how extreme environments can affect chemically related species. HCN and HNC in the interstellar medium (ISM) are fascinating examples of this. HNC is the higher energy isomer by 62 kJ mol^{-1} with a large ca. 140 kJ mol^{-1} barrier to isomerization [110–112]. HCN is the dominant isomer on Earth, while HNC is only observed in the laboratory as a tran-

sient molecule or at very high temperatures [105, 113, 114]. In the rarefied environment of space, however, HNC is widely observed [115]. The ubiquity of these molecules and the temperature dependence of the HNC/HCN abundance ratio have been used as a tool to map the temperature of star-forming regions[116] and protoplanetary disks [117]. However, enigmatic observations from the 90's have found that despite being less stable than HCN, HNC can appear to be the more abundant isomer in very cold environments, by up to a factor of 5, an intriguing and non-intuitive result [118]. The kinetics that controls the HCN and HNC abundances in the ISM are thought to be dominated by highly exothermic reactions, such as the dissociative recombination of $HCNH^+$ and electrons, that form products with high internal energy, yielding both isomers with near unity ratio [114, 119, 120]. Destructive chemistry is then thought to preferentially deplete HNC as temperatures rise [121]. This simple model supports the use of the observed abundance ratio of these molecules as a thermometer [116], but is not sufficient to explain the enhanced abundance of HNC in certain environments. The determination of molecular abundances from observational spectra requires knowledge of the population of the rotational energy levels of the interstellar molecules. In the ISM, the density is generally not high enough to maintain local thermodynamic equilibrium conditions. As a consequence, the population of the molecular levels is controlled by the competition between collisional (de-)excitation and radiative processes. Given the similar dipole moments and rotational constants for HCN and HNC, it had been assumed that the excitation conditions (i.e. the populations of the rotational states) were almost identical [121], and these were computed on the basis of only HCN collisional rate coefficients. The HNC/HCN line intensity ratio then gives, as a first approximation, the HNC/HCN abundance ratio. Because the HNC lines are much stronger than those of HCN in the cold ISM, the HNC/HCN abundance ratio was found to be much greater than 1, in strong disagreement with existing astrochemical models [118]. To explain this, Lique and co-workers proposed that HCN and HNC do not undergo identical collisional excitation, contrary to what had been widely assumed [122, 123]. They obtained high-level ab initio potential energy surfaces (PESs) for HCN and HNC with both He and H_2, the dominant colliders in the cold ISM, [123–126] and performed close-coupling scattering calculations to generate collisional rate coefficients for rotational energy transfer (RET). They observed strong differences between the two isomers and attributed this to a change in anisotropy between the two potentials. When these newly calculated rate coefficients, now differing strongly between these two isomers, are used in conjunction with observational data, significantly lower abundance ratios are found ($\sim$1-2), compatible with the predictions of astrochemical models. However,

these calculations and their important astrochemical consequences have not yet been supported by any experimental measurements. While HCN and HNC are readily identified in the ISM, few laboratory experiments are available to confirm the theoretically supported kinetics or RET rates for these molecules. In fact, no experiments of this kind have been performed on HNC, presumably owing to its instability in the laboratory making it impossible to obtain pure samples. While vibrational spectroscopy has been used to examine these isomers in collisional or photodissociative environments [127, 128], only recently has rotational spectroscopy become sensitive enough to allow for the detection of these species through transient experiments [105, 129]. Here is described a new experiment to investigate the collisional properties of HCN and HNC with He at low temperatures, combining simultaneous in situ generation of HCN and HNC by laser photolysis in continuous uniform supersonic flows of cold He with time-resolved chirped-pulse Fourier transform millimeter-wave (CPFTmmW) spectroscopy [24, 54]. The pressure broadening cross sections for these two systems were measured down to 10 K and thereby verify the theoretically predicted difference in collisional excitation on an absolute scale.

Measurements were done in the helium nozzles presented at the start of the chapter. HCN and HNC were generated in the flow from the photolysis of acrylonitrile at 193 nm. The data were analyzed using the procedure presented in section 2.9 then the FIDs were fitted using the time domain Voigt profile model presented in section 2.4. The model was modified for the fitting of HCN data which present significant hyperfine splitting, equation 2.16 was changed to include the hyperfine components:

$$f(t) = exp\left(-2\pi\Delta\nu_{Pres}t - \frac{\pi^2\Delta\nu_{Dopp}^2 t^2}{ln(2)}\right) \times \sum_{n=1}^{N} A_n cos(2\pi\nu_n t + \theta_n) \tag{4.1}$$

Where A_n, ν_n, and θ_n are the amplitude, frequency, and phase for each hyperfine component, denominated by the n subscript. For the J = 1-0 transition of HCN or any other linear molecules with small hyperfine coupling, the pressure broadening and shifting parameters were found to be the same for each hyperfine component [130], greatly simplifying analysis. For both molecules, the Doppler component was constrained to the flow temperature, but this only has a minor contribution to the overall decay. This transition is much weaker at 70 K due to Boltzmann scaling. For the data taken at this temperature for HCN, the phase relationship between each hyperfine component was fixed to the values found from fitting the highest signal to noise FID within that dataset.

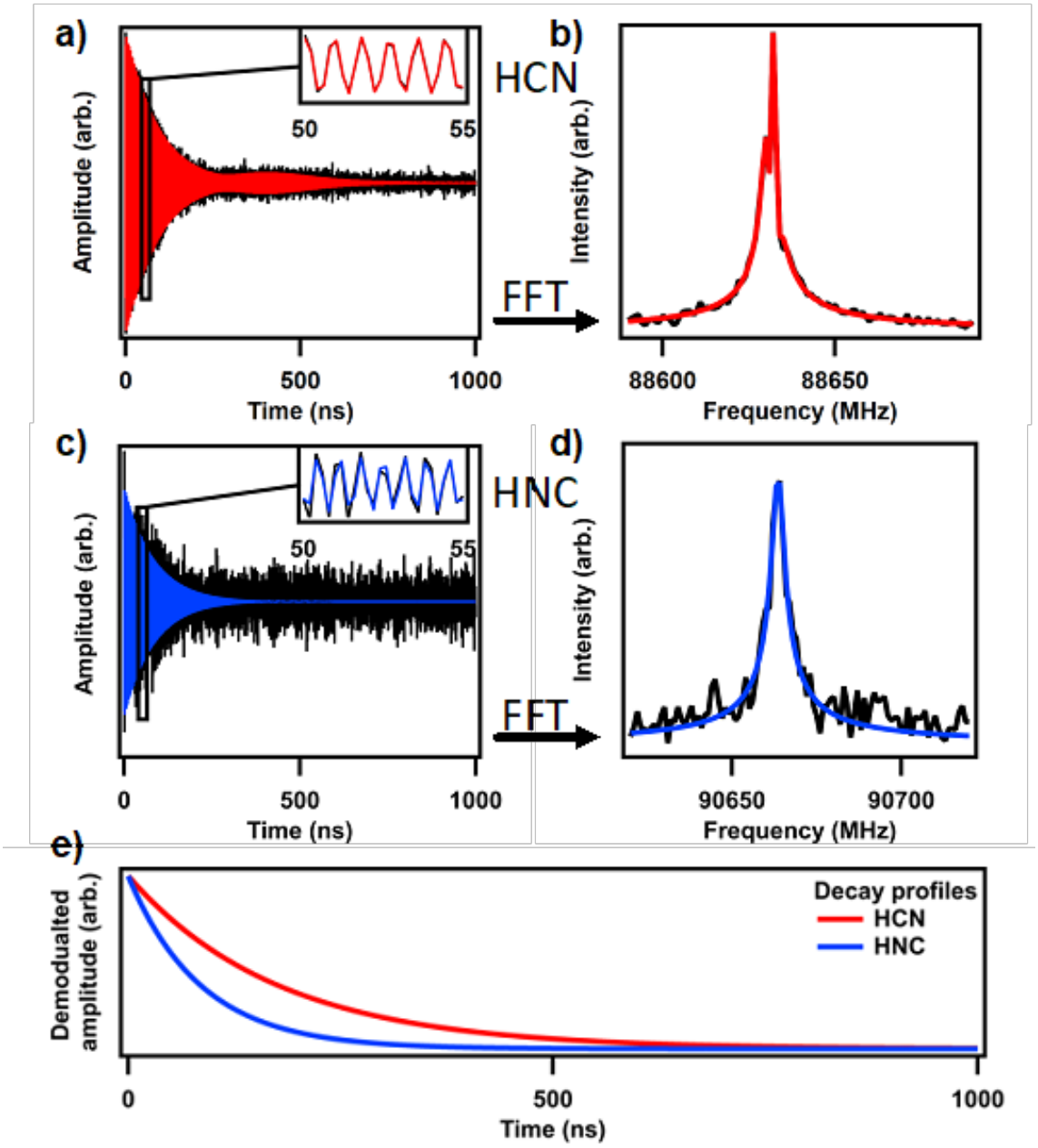

Figure 4.11: Examples of fits to FIDs for HCN and HNC in He at 16 K. a), Time domain data (black) and fit (red) using Equation 4.1 for HCN. b), FFT of data and fit for HCN. c), Time domain data (black) and fit (blue) for HNC using only one frequency. d), FFT of data and fit for HNC. e), demodulated decay profiles of fitted data for HCN (red) and HNC (blue).

The cross sections for the experimental data were found using equation 4.2:

$$\Re[\sigma(T)] = \frac{2\pi\Delta\nu_{pres}}{N\langle v\rangle} = \frac{1}{N\langle v\rangle T_2} \tag{4.2}$$

Where T_2 is the fitted decay time, $\sigma(T)$ is the pressure broadening cross-section, N is the total density in the flow, and $\langle v\rangle$ is the mean relative velocity of the colliding partners. The total density and the temperature are obtained from impact pressure measurements with Pitot tube, and the temperature is used to determine $\langle v\rangle$ in the probing region. Examples of fitted results for HCN and HNC in the helium nozzle at 16 K are presented in Fig.4.11. Panels b and d show the FFTs of both the data and the time domain fit, to show how well the FID decay is captured by the model. A time-domain Voigt model was used to fit this data, which also accounts for the hyperfine splitting of HCN that imposes a beat frequency along with the FID. The fitted exponential decays are shown in Fig. 2 panel e for HCN and HNC, without any frequency components. It is easily seen that the decay times T_2 for each of these molecules are different, despite being produced under the same conditions. This is entirely due to the difference in pressure broadening cross-section of these two molecules.

Data taken for each of the helium nozzles used were fitted to the time-domain Voigt profile to extract the T_2 time. Fig. 4.12 presents the T_2 time as a function of the time after the laser pulse for each of the nozzles used for HCN and HNC. In all of these, it can be seen that HNC shows shorter T_2 times than HCN. For all the nozzle conditions but at 70 K, some of the data are taken after the hydrodynamic time. It is interesting to point out that in this case, the T_2 values show an increase which is related to the gas photolyzed in the nozzle throat and from which a part ends up in the boundary layers in the probing region. The temperature is higher and the density smaller, the collision frequency decreases, and the T_2 increases.

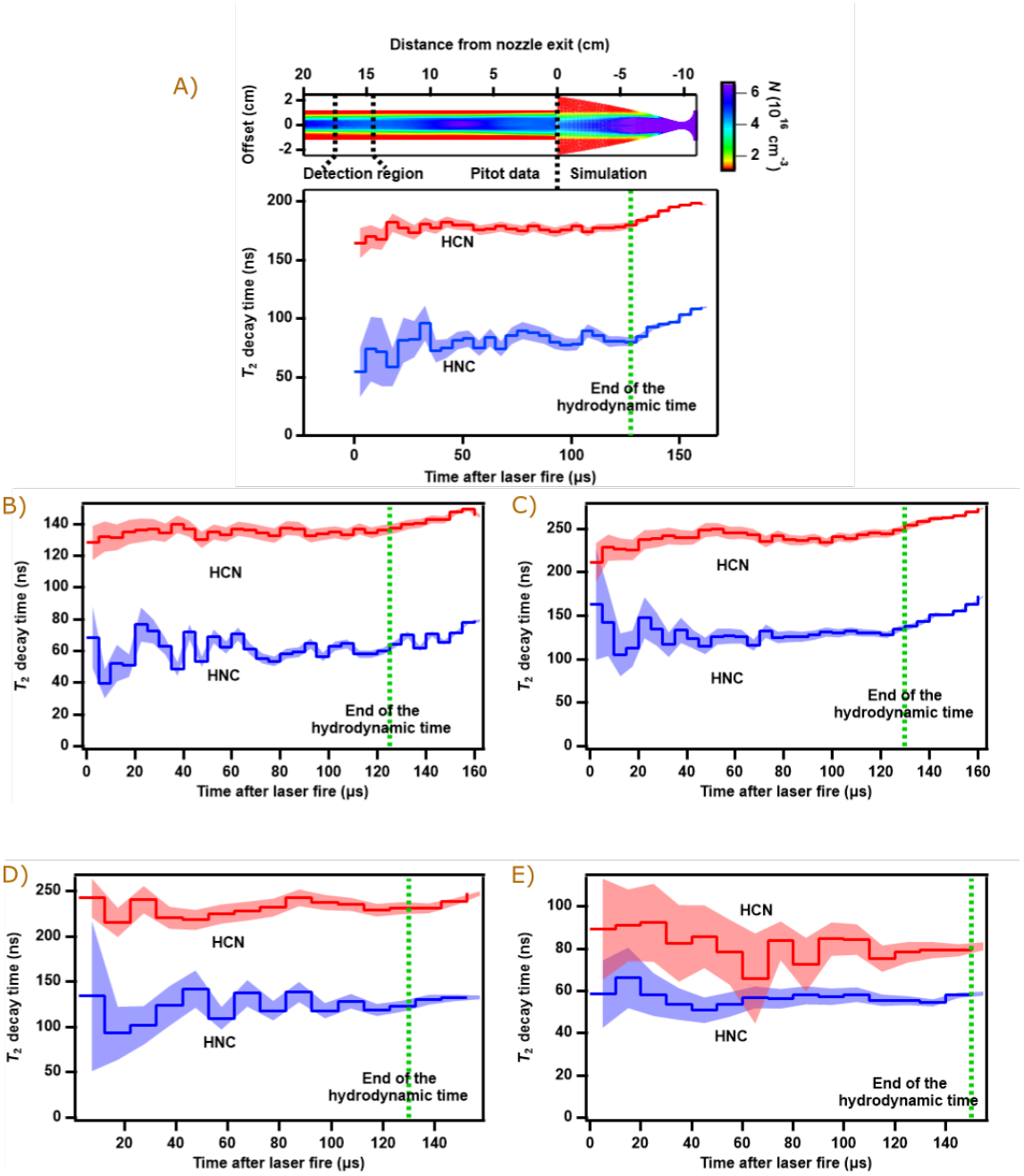

Figure 4.12: T_2 time for HCN (red) and HNC (blue) at five different temperature. A) T_2 time in the helium 16 K flow. The Pitot data and the nozzle simulation are presented on top of the graph at a position corresponding to the hydrodynamic time of the bottom graph. B) T_2 time in the helium 10 K flow. C) T_2 time in the helium 19 K flow. C) T_2 time in the helium 30 K flow. E) T_2 time in the helium 70 K flow. The shaded regions show the 95% confidence interval from the fit.

The T_2 measurements were averaged over the flow time then used to calculate the cross-section using equation 4.2. Fig 4.13 presents the experimental cross-sections as a

function of the temperature for HCN and HNC. The experimental data are compared with theoretical cross sections calculated by colleagues at the IPR, François Lique and Franck Thibault as well as with previous experimental data from Ronningen *et al.* [131] and Rohart *et al.* [132]. The use of very low densities of acrylonitrile precursor ($\sim$0.1% of the total density) ensured that pressure broadening from collision partners other than He could be ignored, as in previous work on rotational energy transfer in uniform supersonic flows [133, 134]. The possible effects of heating the uniform supersonic flow due to energy release from the acrylonitrile dissociation were investigated. However, these are very difficult to quantify owing to uncertainties in the quantum yields of the various channels after photon absorption. Furthermore, when such heating effects have been investigated using the VENOM (vibrationally excited NO monitoring) technique, simple calculations were found to significantly overestimate the actual observed temperature difference [135]. The effect was therefore investigated experimentally at the two lowest temperatures (where it would have the biggest impact) by doubling the acrylonitrile concentration. No difference was observed in the measured T_2 values outside of the quoted uncertainties, and so it is unlikely that significant heating is occurring.

The new experimental and theoretical pressure broadening cross sections are compared together and against previously available experimental data in Fig. 4.13. Importantly, these cross-sections are presented on an absolute scale, directly calibrating the magnitude of cross-sections used in these calculations. Table 4.4 summarizes the conditions of the experiments, details of the analysis and the result for each nozzle. The agreement between the new experimental data and the scattering calculations over the temperature range 10—70 K is very good. The J = 1-0 transition for HCN in He has been experimentally observed on several occasions above 130 K [132] and by Ronningen and de Lucia between 1.3 K and 6.2 K [131]. At higher temperatures, the new calculations agree very well with previous experiments. The highest temperature data from Ronningen and de Lucia are just below the lowest temperature at which the current experiments were performed (10 K). However, it can be seen from Fig. 4.13 that the calculations predict the cross-section to rise as the temperature drops and that this is confirmed by the current experiments down to 10 K. Other studies have called into question the absolute accuracy of the collisional cooling technique used by Ronningen and de Lucia especially at very low temperatures [131, 136]. It should be emphasized, though, that the temperature ranges of the two sets of measurements do not overlap. For the unstable HNC isomer, this is the first pressure broadening study to our knowledge, and so no data were available for comparison. The current experimental cross sections are in very good agreement with the

calculated values.

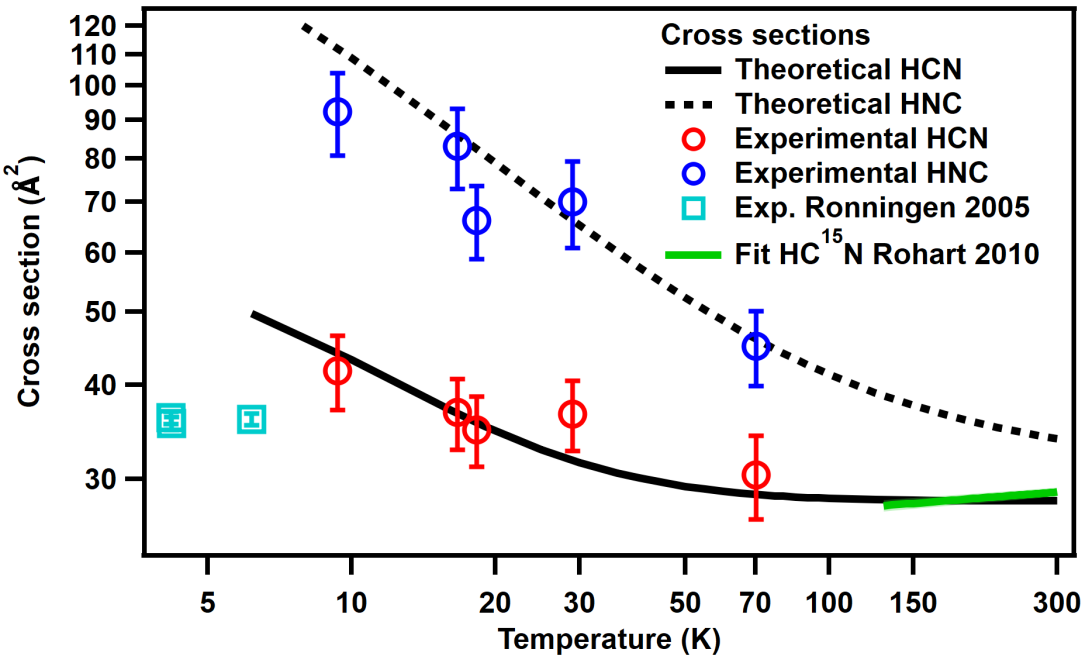

Figure 4.13: Theoretical and experimental pressure broadening cross sections for HCN and HNC with He. Results from this study are compared to those from other experiments, including empirical fits to $HC^{15}N$ data. Error bars for the current experiments correspond to 95% confidence intervals and include a contribution from estimated systematic error. Error bars from other work correspond to 2σ when available. Previous data for HCN is from Ronningen *et al.* [131] and Rohart *et al.* [132].

The predictions made from high-level scattering calculations are often compared against systems that are amenable for experimental measurement, usually employing laser excitation for detection, sometimes combined with velocity map imaging and other sophisticated techniques such as Stark deceleration [137]. While such experiments permit exquisite comparisons between theory and experiment, they are limited to a number of 'model' systems such as NO or OH with established laser detection schemes. The use of a chirped pulse spectrometer allows for a much wider variety of molecules to be probed. The cooling provided by the CRESU technique pushes the available energies into the regime where quantum effects are important, and the fact that the flow density and temperature are precisely known permits absolute measurements, further testing *ab initio* theories.

This study reports the first experiments to show that collisional excitation differs between structural isomers at interstellar temperatures. HCN and HNC have been formed together in situ in cold He supersonic flows, and a strong difference has been observed in

the pressure broadening cross sections for the two isomers, especially at the lowest temperatures. Theoretical calculations of the pressure broadening parameters for HCN and HNC with He have been made to compare against these results, and excellent agreement has been observed on an absolute scale. This is one of the few experiments to specifically address the HCN to HNC abundance in the interstellar medium, with a combination of new experimental techniques that allow for both isomers to be probed explicitly.

Table 4.4: Experimental conditions and results. The temperature and total density are derived from Pitot measurements and are subject to an estimated maximum uncertainty of 10%. The fractional number density of acrylonitrile is given in percent. The numbers of fitted FIDs and sequential averages taken along the uniform flow contributing to the final values are indicated, as well as the corresponding time range after the laser was fired. Uncertainties in the measured data are given in parentheses. For T_2 these are 95% confidence interval statistical errors from the fits, while for the cross sections these are combined with estimated systematic errors in the temperature and number density.

T(K)	N (10^{16} cm^{-3})	$f_{C_3H_3N}$ (%)	Number of FIDs (Hor avg)	Time range (μs)	T_2(ns) HCN	T_2(ns) HNC	σ(Å^2) HCN	σ(Å^2) HNC
70.3	6.07	0.12	13(4)	30-150	83(6)	56(3)	30(4)	45(5)
29.0	2.82	0.086	13(4)	10-130	231(6)	121(10)	37(4)	70(9)
18.3	3.60	0.11	24(2)	10-125	239(3)	126(4)	35(4)	66(7)
16.6	4.85	0.066	25(2)	5-125	176(2)	78(5)	37(4)	83(10)
9.4	7.43	0.029	20(2)	25-120	135(1)	61(4)	42(5)	92(12)

4.3 Low temperature reaction kinetics

From the acrylonitrile photodissociation experiments presented previously and the systematic study of sensitivity summarized in table 4.3, it was concluded that for the available conditions (nozzles) HCN at 10 K and HC_3N at 30 K were the best candidates to be studied as reaction products. Two reactions were then proposed to benchmark the experimental setup for the study of reaction products at cold temperature, CN + C_2H_6 which generate HCN and CN + C_2H_2 which produces HC_3N.

These reactions were among the first neutral-neutral reaction to be studied in a CRESU in the past, by Sims *et al.* [33] where their rate coefficients were measured down to 25 K using the PLP-LIF technique. Recently the reaction between CN + C_2H_2 was studied by Abeysekera *et al.* [29] in the first demonstration of the CPUF technique.

Reactions with the radical CN have a more direct impact on astronomical observations focusing on the discovery of PAHs in space. As some PAHs lack a dipole moment (benzene, naphthalene...) it is impossible to detect them with the use of radio telescope. But when "CN tagged", i.e. when a CN group is substituted for one of the hydrogen atoms in the molecule, these molecules acquire a dipole moment and become detectable by radio astronomy. Recently, multiple molecules containing CN groups have been detected in dense interstellar clouds [25, 138, 139]. These CN-tagged molecules could be used as a proxy (for example benzonitrile as a proxy for benzene), and the column density of the "pure molecule" could be derived from the measured column density of the CN tagged molecule. The accuracy of this calculation is highly dependent on the reaction network used and the parameters included in the reaction database. Particularly for the formation and destruction route from the "pure molecule" to the "CN tagged" analog. Direct reactions with the CN radical forming the "CN tagged" molecule or forming CN-containing molecule allowing for more formation routes to be open are important for the accuracy of these models. And parameters such as rate coefficients and branching fractions need to be measured at temperatures relevant for the interstellar environment where these molecules are found.

Both these exothermic reactions ($\Delta_r H$=-90 kJ mol^{-1} for CN + C_2H_2 and $\Delta_r H$=-92 kJ mol^{-1} for CN + C_2H_6) are expected to be single-channel at low temperatures. Huang *et al.* [140] calculated the Potential Energy Surface (PES) of the reaction between CN + C_2H_2 showing that only the HC_3N channel possesses no non-submerged barrier and should be open at low temperature. The case of CN + ethane is interesting as it is a seemingly simple reaction with only one apparent product channel, but experimental studies revealed that there is more to this reaction. The high-temperature rate coefficients for this reaction, which have been studied extensively [141, 142] indicated a slight positive temperature dependence indicative of a reaction barrier. However, some of the first measurements of neutral-neutral rate coefficients made with a CRESU apparatus by Sims *et al.* [33] revealed that the rate coefficient increases at low temperatures. High-level calculations by Georgievskii and Klippenstein [143] revealed that the barrier was just submerged and that entropic effects were responsible for the observed minimum in $k(T)$. Experimental confirmation that this reaction still proceeds to products at low temperatures has not been provided before, and this aspect of the reaction would validate the theoretical determination of this system.

As these reactions were expected to be single-channel, it was not possible to test the measurement of branching ratios using these systems. In order to benchmark the exper-

imental apparatus and quantify its sensitivity, a calibration procedure was explored. As already discussed with reference to LIF experiments [144], it is possible to measure the branching ratio of a reaction using an already known reaction as a calibration. A similar approach is proposed using CPUF to calibrate the two reactions proposed above using the photodissociation of acrylonitrile as the "calibration reaction".

The calibration consists of using the signal of the photoproduct to quantify the reaction product generated under similar conditions. First, the photoproduct signal is measured using the CPUF technique and then the reaction product is then acquired in similar conditions (same nozzle, same position in the flow, same laser parameters, same spectrometer parameters). The photoproduct signal is then quantified and compared to the reaction product to determine the density of the product generated.

To quantify the photoproduct, the amount of acrylonitrile depleted is calculated using the fluence of the laser (F in photons cm^{-2} per pulse), measured *in-situ* between scans using a power meter, the concentration of acrylonitrile injected in the flow $[C_3H_3N]_{flow}$ measured by the CEM system and the acrylonitrile absorption cross-section at 193 nm found in the literature $\sigma_{abs} = 2.85 \times 10^{-17} cm^2$ [108]. Assuming that the absorption cross-section does not vary with temperature the density of acrylonitrile depleted is then $[C_3H_3N]_{dep} = [C_3H_3N]_{flow} \times F \times \sigma_{abs}$ in the limit of weak absorption.

The photoproduct density can then be calculated using a photolysis branching ratio derived from literature values. In this case, the assumption is made that the dissociation only leads to three products HCN, HNC and HC_3N as presented by equation 4.3. Literature shows that an other pair of fragment as been detected CN + H_2CCH but most the literature agrees that this channel account for (at best) less than 1% of the total quantum yield [107, 145–148]. Zaleski *et al.* [78] measured the branching ratio between HCN and HC_3N in a room temperature cell and found it to be (1.72 ± 0.3). In their experiment, the calculation of the branching ratio was done after the complete isomerization of HNC, so this missing part of the ratio has to be taking into account. Wilhelm *et al.* [106] measured the branching ratio between HCN and HNC in a room temperature flow cell and found it to be (3.3 ± 0.1). From these two measurements and using equation 4.3 it is possible to calculate a branching fraction for each of the three considered products, error analysis allows for calculated uncertainties on these ratios propagating the experimental uncertainties from literature. This calculation leads to the three branching ratios presented in table 4.5.

$$[C_3H_3N]_{dep} = [HCN] + [HNC] + [HC_3N] \tag{4.3}$$

Table 4.5: Photolysis branching fractions derived from literature values errors are one sigma.

Photo product	Branching fraction
HCN	0.48±0.03
HNC	0.15±0.01
HC_3N	0.37±0.04

The product signals can then be directly compared (assuming that the quantum yield leading to the dissociation of BrCN to Br + CN is equal to the sum of the quantum yield leading to HCN, HNC and HC_3N in the photolysis of acrylonitrile) to quantify the amount of product generated by the reaction. An average of the signal is taken over the hydrodynamic time, the equivalent of region II in Fig. 4.5. The end of the hydrodynamic time is determined by Pitot measurements taken inside the nozzle and compared with the depletion signals. The experiments are conducted sequentially under similar conditions: first, the photodissociation experiment acquiring one scan for the photo product; then the reaction experiment measuring one scan for the reaction product. Where a scan corresponds to a set number of averages with a predetermined acquisition scheme. During the reaction scans, the concentration of BrCN is also monitored using the UV/Vis setup described in section 2.7.2. The concentration of CN generated can be calculated using the UV/Vis measurement of BrCN, the laser fluence and BrCN cross-section at 193 nm σ_{abs} =2.19×10^{-19} cm^{-2} measured by Felps *et al.* [77]. The reactions being single-channel and fast under the pseudo-first-order conditions employed, all the radicals are consumed during the measurement and so the density of the product should be equal to the density CN. Two independent ways of estimating the product density can then be compared.

The detection of the reaction products HCN and HC_3N from the reaction of CN with ethane and acetylene respectively and a tentative calibration using the acrylonitrile photodissociation at 193 nm are presented in the following paragraphs.

4.3.1 CN + C_2H_2 at 30 K

The reaction between the radical CN and acetylene producing HC_3N was studied in the argon nozzle at 30 K. Table 4.6 summarized the relevant conditions of these experiments. Fig. 4.14 presents the time evolution of the FID amplitude of the J = 8–7 transition of HC_3N. Similar to the photolysis signal, the reaction presents a delay before the appearance of HC_3N followed by a rise between 170 and 400 µs. The signal then reaches a plateau until the end of the hydrodynamic time. The rate of this reaction was measured by Sims *et al.* [33] in a CRESU and was found to be $(4.6 \pm 0.25)\times10^{-10}$ cm^3s^{-1} at 25 K. With the conditions presented in table 4.6 this would lead to a reaction half-life of 27 µs which is not consistent with the time it takes in this experiment for the signal of HC_3N to reach a plateau (about 10 characteristic times). This demonstrates one of the difficulties of studying the products of a reaction compares to the study of the reactant. The time evolution of the product is more complicated than the one of the reactants and thus harder to interpret, more details about the effect on the product will be discussed at the end of the chapter.

Table 4.6: Conditions of the experiment presented in Fig. 4.14 error one standard deviation.

quantity	value
Temperature (K)	29.6 ± 0.3
Total density (cm^{-3})	$(1.8 \pm 0.2)\times10^{16}$
BrCN density (cm^{-3})	$(1.65 \pm 0.2)\times10^{13}$
C_2H_2 density (cm^{-3})	$(5.6 \pm 0.6)\times10^{13}$
Fluence (photons cm^{-2} $pulse^{-1}$)	$(2.3 \pm 0.2)\times10^{16}$

Following the procedure presented above the reaction signal was calibrated. Fig. 4.15 presents the time evolution of the FID amplitude of the J = 8–7 transition of HC_3N as a photolysis and a reaction product under similar conditions. These amplitudes of the FIDs are average for both signals between 400 µs and 700 µs. This corresponds to the time when the reaction signal reaches a plateau and the end of the hydrodynamic time. During this time it is assumed that the reaction is complete and that HC_3N has rotationally and vibrationally relaxed though this assumption is clearly debatable, especially for the photoproduct. The standard deviation of the data during this time is used as an uncertainty for the calculation. Table 4.7 summarizes the relevant parameters of the calculation and presents the result of the calibration.

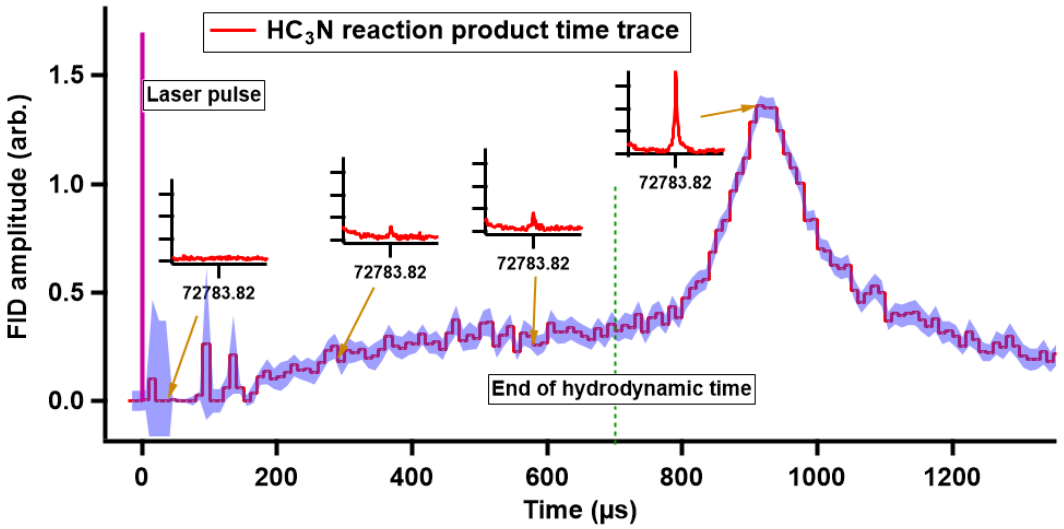

Figure 4.14: Time evolution of the recation product HC_3N J = 8–7 vibrational ground state transition (time-domain Voigt fit). 1.2×10^5 avg per point. In shaded blue the error on the amplitude 95% confidence. The inset presents the FFT of the data at different times.

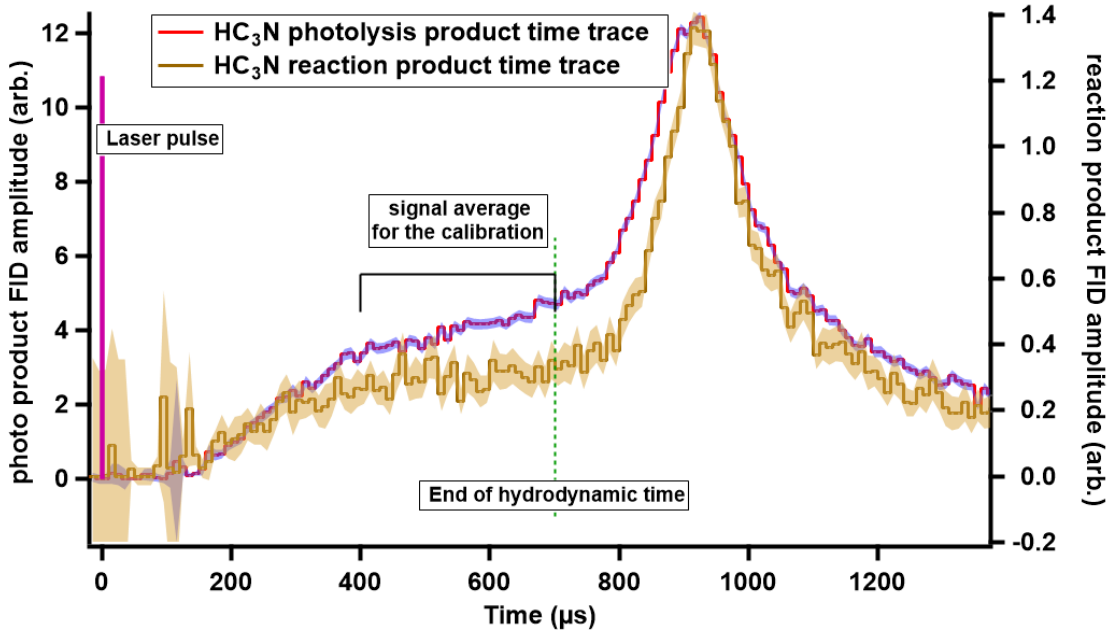

Figure 4.15: Time evolution of HC_3N J = 8–7 vibrational ground state transition (time-domain Voigt fit). 1.2×10^5 avg per point. In red for the photolysis product and in brown for the reaction product. In shaded error on the amplitude 95% confidence.

For the Ar 30 K data, the results of both calibration methods give a similar density of products generated with the BrCN calibration leading to a density about 1.5 times higher

Table 4.7: Summary of the calibration for the reaction between CN + C_2H_2 in argon at 30 K error are one standard deviation.

Quantities	Results
Acrylonitrile density (cm^{-3})	$(1.7 \pm 0.2)\times10^{12}$
Fluence (photons cm^{-2} $pulse^{-1}$)	$(2.3 \pm 0.2)\times10^{16}$
Product from photocalibration (cm^{-3})	$(3.0 \pm 0.7)\times10^{10}$
CN density (cm^{-3})	$(8 \pm 1)\times10^{10}$
Branching fraction %	37±10

than the calibration using the photoproduct. Several possibilities exist to explain this discrepancy, relating to the BrCN photolysis, the acrylonitrile photolysis, and vibrational relaxation of both HC_3N photoproduct and reaction product.

There exist some discrepancies in the literature regarding the BrCN photolysis cross-section. Felps *et al.* [77] reported a cross-section of σ_{abs} =2.19×10^{-19} cm^{-2} while Russell *et al.* [149] reported a value of σ_{abs} =3.75×10^{-19} cm^{-2}. This could be a contribution to the difference between the result of the two methods. Another possibility related to the BrCN is that its density in the flow is overestimated due to clustering. With an argon flow at this low temperature clustering is bound to be an issue if the concentration of the reactants is too high. The clustering limit for acrylonitrile and N_2O were measured by observing the variation of their signal intensity as a function of their calculated density in the flow. This was not done directly for BrCN as it is complicated to systematically vary the quantity of this species in the flow. Instead, acrylonitrile and N_2O were used as limits, N_2O is a small molecule less likely to cluster compare to acrylonitrile which also has a big dipole moment. It was found that the clustering limit for N_2O in these conditions is around 1.5 ×10^{14} cm^{-3} and for acrylonitrile around 1.0 ×10^{13} cm^{-3} (plots in appendix). In this experiment, the concentration of ethane and BrCN is around 7 ×10^{13} cm^{-3} which lies between the clustering limits of the two other molecules it is possible that the BrCN density used in the calculation is overestimated which would make the results of the two methods closer. BrCN photolysis is also known to generate rotationally hot CN radicals [150, 151] which could affect the time evolution of the signal but precedent study on rotational energy transfer [134] have shown that the CRESU technique is efficient at rotational cooling. The delay observed here is too long to be entirely caused by this relaxation.

More significant uncertainties may come from the acrylonitrile photolysis. While the 193 nm absorption cross-section is well established at room temperature, cooling of low-frequency vibrational modes might affect this cross-section at very low temperatures.

However, the main uncertainty regarding acrylonitrile photolysis relates to the overall quantum yield. The measurements of Zaleski *et al.* [78] and Wilhelm *et al.* [106] relate to branching fractions, but do not give absolute values for the quantum yields of the photoproducts, which could differ owing to unmeasured products or processes.

However, the calculation assumes that HC_3N, for both the photolysis and the reaction, has relaxed to the same equilibrium temperature T_{rot} and T_{vib}. This assumption is likely correct for the rotational temperature, as the CRESU conditions are efficient for rotationally cooling molecules in a few tens of μs [134]. Perhaps the greatest uncertainties arise from the possibility of incomplete vibrational relaxation of the HC_3N both as a photoproduct and as a reaction product. As shown for the photoproduct in Fig. 4.8, the vibrationally excited $\nu_6 = 1$ $J = 8$–7 transition of HC_3N does not completely relax in the hydrodynamic time of the nozzle. This implies that the signal used for the calibration from the ground state does not capture the full density of HC_3N. The same figure shows that the vibrational ground state never reaches a plateau in the same way as the reaction product appears to do. This for the calibration implies that the signal from the photoproduct is underestimated which would lead to an overestimation of the reaction product density using this method thereby increasing the difference between the results of the two calibration methods. Of course, the observed plateau in the HC_3N reaction product may be misleading and incomplete vibrational relaxation of the reaction product may also be influencing the result in the other direction.

As the signal of HC_3N as a reaction product was strong enough under these conditions, a titration experiment was performed varying the concentration of acetylene in the flow in order to observe the effect on the kinetics, the BrCN concentration was monitored and found to be stable within 10%. Fig. 4.16 present the results of this experiment. It can be seen that the reaction signal grows faster when the concentration of acetylene increases which is what is expected but the increase in growth rates is too small to be linked with the kinetics of the reaction and it is probably due to an increase in the relaxation rate due to the presence of more heavy colliders (ethane). The signal still shows the same delay before the appearance for all concentrations which is complicated to interpret especially if we assume the last sentence to be plausible. The two highest densities of acetylene show the same evolution which could be explained by a clustering effect that "saturated" the concentration of acetylene available for the reaction. This is also hinted at by the signal from the nozzle throat from these two scans which are smaller than from the other scan.

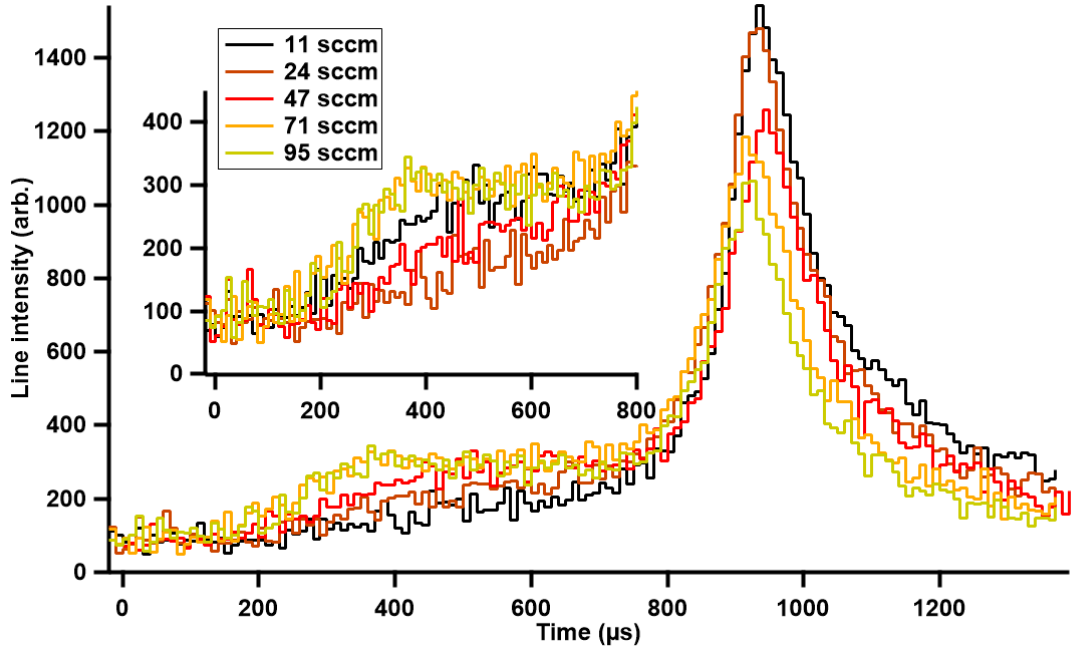

Figure 4.16: Line intensity of the J = 8–7 transition for HC_3N as a product from CN + acetylene varying the concentration of acetylene in the flow. The inset focuses on the part in the hydrodynamic time of the nozzle. 4×10^4 avg per point.

4.3.2 CN + C_2H_6 at 10 K

The reaction between the radical CN and ethane producing HCN was studied in the helium nozzle at 10 K. Table 4.8 summarizes the relevant conditions of the scan. Fig. 4.17 presents the time evolution of the transition intensity for the J = 1–0 transition. For this system, the signal of the reaction product is lower compared to the reaction given in the previous section, which makes interpretation of the results more difficult. It is less evident that the behavior extracted from this data still follows the trend seen in the photolysis data, with a first rise after the laser pulse until 50 μs followed by a more or less stable region from 50 to 75 μs ending with another rise till the end of the hydrodynamic flow. The data set presented here was acquired at a time where the BrCN measurement using the UV/Vis spectrometer was unavailable but later measurement showed that when using the same conditions in the BrCN vessel (flow and pressure) the concentration measured by the UV/Vis spectrometer was the about the same in every experiment with an estimated 20% variation. The value used for the result presented here was then extrapolated from these later experiments and the error used was the 20% variation found experimentally. This error accounts for a major part of all the errors of the quantities calculated from the BrCN concentration.

The rate of this reaction was measured by Sims *et al.* [33] in a CRESU and was found to be $(1.1 \pm 0.2)\times10^{-10}$ cm^{3}s^{-1} at 25 K. With the conditions presented in table 4.8 this would lead to a reaction half-life of 13 µs following the result of Sims *et al.* [33] at 25 K. However the rate coefficient is underestimated as the reaction keeps accelerating as the temperature goes down in Sims *et al.* [33] data. From the quality of the data and the consideration discussed earlier about the time evolution of the reaction product, it is difficult to relate the time dependence of fig. 4.17 to the reaction characteristic time.

Table 4.8: Conditions of the experiment presented in Fig. 4.17 error are one standar deviation

quantity	value
Temperature (K)	10±0.2
Total density (cm^{-3})	$(8.2 \pm 0.8)\times10^{16}$
BrCN density (cm^{-3})	$(3 \pm 1)\times10^{13}$
C_2H_6 density (cm^{-3})	$(5 \pm 0.5)\times10^{14}$
Fluence (photons cm^{-2} pulse^{-1})	$(2.3 \pm 0.2)\times10^{16}$

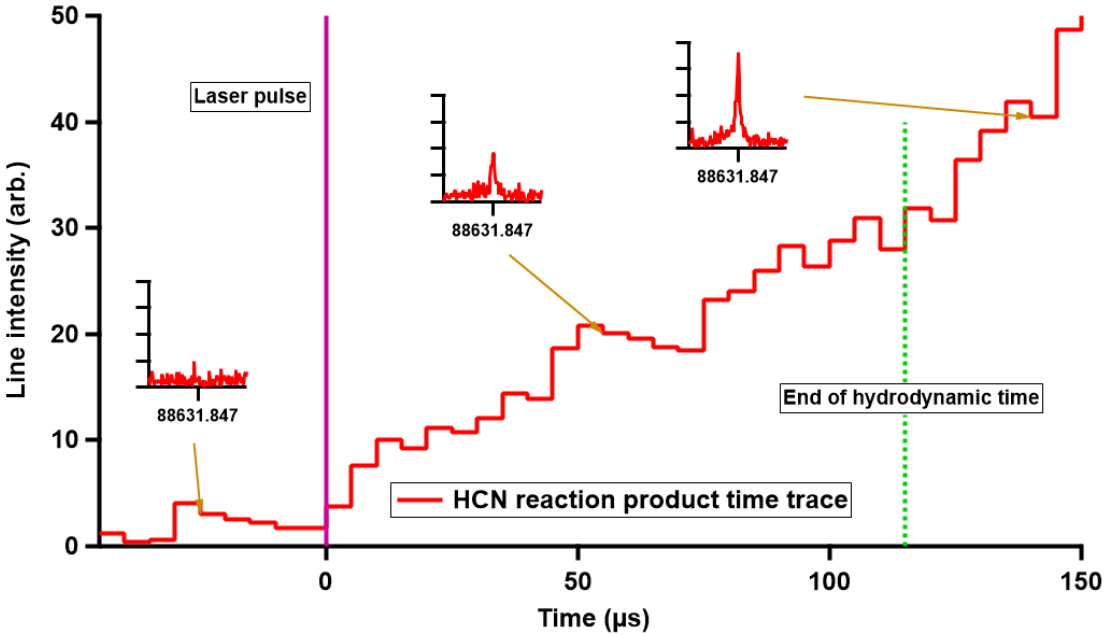

Figure 4.17: Line intensity of the J = 1–0 transition of HCN resulting from the reaction under the conditions given in table 4.8. 2×10^5 avg per point. The insets show the FFT of the FID at different times.

Following the procedure presented in section 4.3 the reaction signal was calibrated.

Fig. 4.18 presents the time evolution of the line intensity for the J = 1–0 transition of HCN as a photolysis and a reaction product under similar conditions. From this, the transition intensity was averaged between 50 and 115 µs. This corresponds to the time when the photolysis signal reaches a plateau and the end of the hydrodynamic time. The standard deviation of the data during this time is used as an uncertainty for the calculation. Table 4.9 summarizes the relevant parameters of the calculations and presents the results of the calibration.

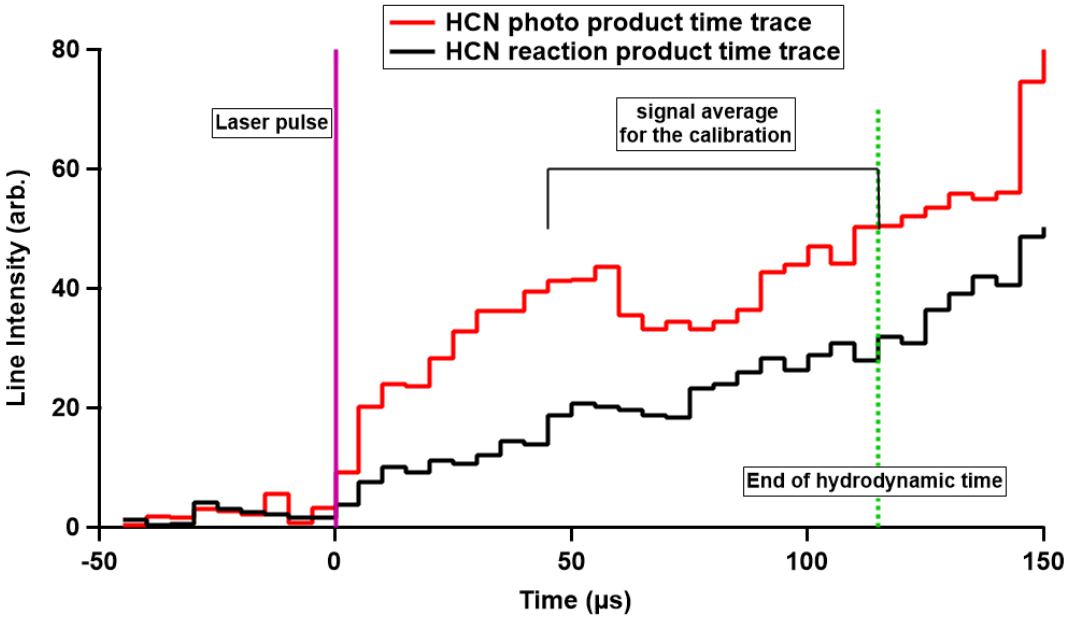

Figure 4.18: Line intensity of the J = 1–0 transition of HCN. 2×10^5 avg per point. In red for the photolysis product and in black for the reaction product.

Table 4.9: Summary of the calibration for the reaction between CN + C_2H_6 in helium at 10 K error are one standard deviation.

Quantities	Results
acrylonitrile density (cm^{-3})	$(5.9 \pm 0.6)\times10^{12}$
Fluence (photons cm^{-2} $pulse^{-1}$)	$2.3\pm0.2\times10^{16}$
Product from photocalibration (cm^{-3})	$8.19\pm2.1\times10^{11}$
CN density (cm^{-3})	$1.5\pm0.2\times10^{11}$
Branching fraction	540 ± 160

For the He 10 K data, the signal is much noisier and makes the analysis less reliable. But the two methods lead to different results. The calibration using the BrCN gives a value

about four times smaller than the calibration with the photoproduct. In this case, the ratio between the two methods is inverted compare to the Ar 30 K data. One explanation for this is that the photoproduct is generated vibrationally excited and does not relax in the time available which is shown fig. 4.10 this implies that the photolysis signal is underestimated and that the signal from the photo calibration is overestimated which would bring the two calibration methods results closer. This is also supported by preceding study on the vibrational distribution of HCN from this reaction by Bethardy *et al.* [152] who found that at room temperature. They found that HCN is generated in vibrationally excited state after the reaction and in there experiment the ground state is not populated at all. This could explain the slow rise of the signal observed in fig. 4.17. The HCN J = 1–0 $v_2 = 2$ transitions was probe during a reaction to observe if it was possible to detect HCN being formed vibratinally excited but the no signal was detected probing this level.

4.4 Conclusion on CPUF experiment

The capabilities of the CPUF instrument developed in Rennes have been presented. The preliminary photodissociation experiments showed that the instrument is capable of detecting multiple species and extracting their time dependence. From the study of the product of the photodissociation of acrylonitrile in different Laval nozzle flows the strong couplings between the conditions of the Laval nozzle and the molecular signal could be extrapolated and helped in understanding how the parts of the experiment interact and what are the important parameters to optimize. The first link with the Laval nozzle conditions is the size of the isentropic core. In order to optimize the generation of the products, the isentropic core needs to be at least the size of the laser beam to increase the interaction volumes. This is an important factor as it is the reason why it was possible to study HC_3N in the Ar 30 K nozzle despite the fact that argon is more efficient at quenching the FIDs as shown at the start of the chapter. The second factor that impacts the coupling of the spectrometer with the CRESU technique is the pressure of the flow. This is an important factor in the reduction of the sensitivity of the spectrometer and at this stage, a technical limit as the nozzles used for these experiments were designed to have the lowest pressure possible with the pumping capacity available. Comparing the T_2 time of HCN in the helium nozzle to the duration of the FIDs of OCS at room temperature from chapter 3 clearly shows the impact of the collision on the signal strength. The last factor related to the nozzle is the temperature of the jet. The intensities of rotational transitions are intrinsically related to the Boltzmann distribution of the population which is a limitation as it could limit the

temperature range available for certain molecules, for example, the J = 1-0 transition of HCN is 10 times weaker at 30 K compared to 10 K.

The variation of the signal between different nozzles is molecule dependent as not only the population distribution is molecule specific but the also collisional cross-section (pressure broadening) and it also evolves with the temperature as shown in section 4.2 on the difference in the collisional cross-section between HCN + He and HNC + He. In order to compare signals from two molecules, these differences need to be known.

The results from the reactions showed that studying the product of a reaction is more complex than looking at the reactant. When studying the reactant and assuming it is in local thermodynamic equilibrium, the only time dependence affecting the signal is the loss from the reaction which under pseudo-first-order conditions is exponential for the reactant. For the case of the products, the dependence can be much more complicated as on top of the exponential rise reflecting the loss of the reactant two effects add to the time evolution of the product signal. The first one is directly linked with the reaction itself and the different intermediate states required for the reactant to go to the product. Certain mechanisms occurring during this process may delay or alter the rate of the formation of the products. The second effect is related to which state distribution the products come out of the reaction. Usually, products are not formed directly at local thermodynamic equilibrium and undergo relaxation processes to reach that equilibrium. Spectroscopic techniques are sensitive to these intermolecular energy relaxations as it affects the distribution of population in the different state of the product which directly impacts the intensity of the signal. The rates of relaxation are thus added on top of the other time-dependent effects which can make the interpretation of the data more complicated. In theory, mass spectrometry is not so strongly affected by these relaxations as all the populations are detected together. CP-FTmmW spectroscopy could also with enough sensitivity go around the problem by probing multiple rotational transitions from different vibrational states, but in the work presented here, the sensitivity is too low to reliably allow such measurement. These effects underline the importance of having a long enough hydrodynamic time to allow for relaxation processes to happen or enough time-dependent signals to be recorded to interpret the results. This is a limitation of helium nozzles which only provide between 100 and 200 µs of hydrodynamic time which would explain why HC_3N was not detected in these nozzles.

The results of the calibration showed how difficult it can be to measure the absolute concentration of a single product. But it does show some potential especially if the sensitivity can be increased enough to allow the observation of multiple vibrational states

of the product and to quantify their contributions. Using the calibration on multiple systems and cross-calibrating would reduce the impact of wrong hypotheses (quantum yield) and errors in the parameters used to perform the calibration (branching fraction of the calibration system).

Despite these observed limitations, the experiences presented here represent sure of the first-ever direct detections of products of radical-molecule reaction at the low temperature of interstellar clouds and confirm the importance of such reactions for astrochemistry.

Chapter 5

Conclusion and perspectives

A new state-of-the-art chirped-pulse Fourier transform spectrometer in the E-band (60-90 GHz) has been designed and constructed. The spectrometer capabilities were demonstrated as a spectroscopic tool for room temperature measurement of the pressure broadening coefficient of the OCS + He system. The room temperature flow cell used for these measurements was designed with potential future extension to study spectroscopy at room temperature with the E-band spectrometer. A new CRESU chamber was designed and constructed, improving on the existing apparatus in Rennes. The chamber was coupled with the spectrometer in a first attempt in the Rennes lab at using the CPUF technique for the measurements of low-temperature collisional phenomenon. New experimental protocols and data analysis routines were developed to perform CPUF experiments with the new apparatus, improving on what was the state of the art at the start of the project. The apparatus capabilities were demonstrated with the study of the differences in collisional interactions of HCN and HNC with He at low temperatures. The CPUF technique was used to study two chemical systems at low-temperature: CN + ethane at 10 K and CN + acetylene at 30 K. A calibration protocol was proposed and tested revealing the limits of what is possible with the system for now.

5.1 Perspectives

For CPUF experiments the system is now limited by the CRESU environment impacting the sensitivity of the CP-FTmmW spectrometers via pressure broadening and by the concentration of radicals generated in the flow. In order to overcome the limitation related to the pressure broadening, two solutions were proposed and developed in parallel with the work presented here. The principle is to reduce the impact of collisions in the prob-

ing region by reducing the pressure. The first solution that is currently being tested is based on molecular beam sampling of the CRESU flow via a skimmer into a secondary chamber evacuated by a turbomolecular pump, in a similar way to that employed by Durif *et al.* [19] in the Rennes CRESUSOL instrument which couples the CRESU technique to synchrotron photoionization mass spectrometric detection. The impact of collisional dephasing of the FID is limited due to the reduction in collisions frequency in the secondary chamber. The addition of this chamber was done around the middle of the work described here and the details about the conception and characterization of this addition will be found in the thesis of Omar Abdelkader Khedaoui. Some of the technical demonstrations presented in chapter 2 were recorded using this modification of the experimental apparatus. Fig. 5.1 presents a comparison of spectra and an FID of acrylonitrile taken in the CRESU flow and in the skimmer chamber. It is clearly seen that there is a significant improvement in sensitivity when running with the skimmer apparatus also taking into account that the skimmer data in the figure were acquired in a tenth of the time taken for data in the CRESU flow.

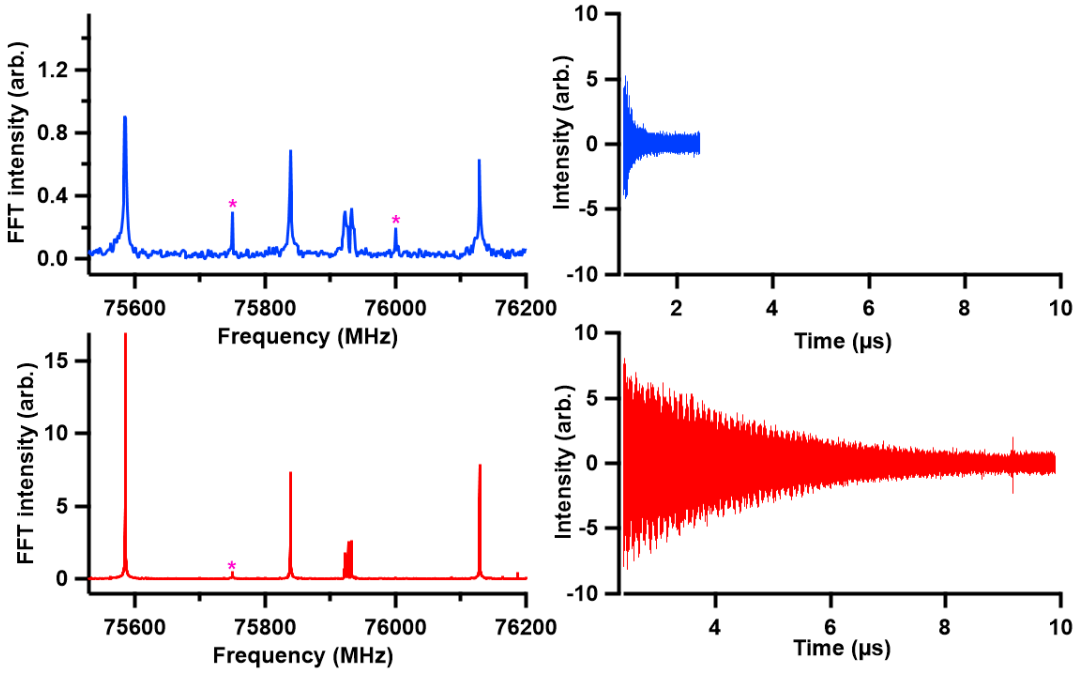

Figure 5.1: Comparison between an acrylonitrile chirp in the skimmer (red) 10^4 averages and in the continuous classic (blue) 10^5 averages density of acrylonitrile 1.8×10^{12} cm^{-3} in both cases. The first column shows the spectra and the second the time domain FID.

The second solution, also under development, is to switch from a continuous CRESU experiment to a pulsed CRESU design where the demands on the pumping group could

be much reduced and enabling a reduction in the pressure in the chamber. A prototype is currently in development and details will also be found in the thesis of Omar Abdelkader Khedaoui. It is a new version of a rotating disk chopper based on a design developed in the past in Rennes and with two versions currently used in Bordeaux (details can be found in the thesis of Sebastien Morales [153]) and in Ciudad Real [36]. This second solution is, in principle, better than the skimmer as it combines the best aspect of the "classic" continuous CPUF and the skimmer chamber. The pulsed system which is currently being developed would allow a reduction of the pressure in the probing region thus increasing the sensitivity of the CP-FTmmW spectrometer by reducing the impact of pressure broadening. The other improvement of the pulsed system is that it will enable the use of Laval nozzles with bigger isentropic cores. This means that the interaction volume (overlap between the core, the laser beam and the microwave beam) can be increased. For now, the laser beam size used has to be reduced to match the size of the existing nozzle isentropic core. If the whole laser beam output could be used this would lead to an increase of a factor of 12 due to change in interaction volume. As these nozzles are also designed with chamber pressures comparable to the skimmer chamber this geometrical factor of 12 would be added to the already increased signal presented in Fig. 5.1.

A potential way of increasing sensitivity especially for molecules with a high density of states could be to use a similar approach to a technique used for astronomical observation, the spectral stacking [154–156]. This technique is used on broadband observational data containing a lot of spectral lines to look at the signal from a molecule as one single line. Briefly, a catalog for the line position and intensities is calculated using SPFIT/SPCAT using the known physical conditions of the object observed. The catalog is then used to stack the signal at each line position of the catalog. This can achieve the detection of molecules for which the SNR is too low for each individual line but increased when the lines are stacked. A similar approach could be used in our experiment to increase the sensitivity, by chirping over a spectral range and then stacking the signal at each line frequency. Or even by using multicolor pulses on one species and stacking the resulting signal.

Another way to increase the sensitivity would be to increase the number of products generated by changing the source of radical. Even if CN is a good candidate for the high dipole moment of the products it generates and for its relevance to astrochemical problems, the precursor used for now BrCN and ICN are difficult to handle and to inject in the flow because they are solids. Changing the radical source to a gas or a liquid would allow more control on the density of precursor in the flow and the possibility to potentially

add more which would increase the amount of product generated thus increasing the signal of the product. Reactions with atomic oxygen could be good candidates as $O(^1D)$ can be generated by the photolysis of ozone at 248 nm and $O(^3P)$ can be generated by the photolysis of N_2O at 193 nm. Both precursors are gases, N_2O is easily available and to handle and a new ozone generator was recently installed on the system. This could allow increasing the quantity of radical and thus of product.

Combining the effect of the pulsed system and of a new radical source could potentially enable an increase in the signal of the skimmer (fig. 5.1 by two orders of magnitude to a point where it could be possible to detect multiple products at the same time. Reaching this point would make branching fraction measurements potentially possible but still not straightforward. Relating multiple spectral lines to lead to a branching ratio requires isolating every factor participating in the intensity of a spectral line. Enough information needs to be extracted from the data to generate an accurate population distribution for the product rotation and vibration. For the rotation the CRESU environment makes things simple as the high number of collisions allows for relaxation of the rotational population to the temperature of the flow which is easily measured by Pitot probe experiments. The vibration on the other hand is more complicated as in the typical hydrodynamic time vibrational relaxation may be incomplete, as demonstrated in chapter 4 section 4.1 for the photoproduct of the acrylonitrile photodissociation at 193 nm. In this case, it would be necessary to be able to understand how the population is distributed over the vibrational levels to account for this in the calculation of the branching ratio. Broadening effects also affect line intensity, in the case of the Doppler broadening the effect can be easily quantified as the parameters implied are easily measured. For pressure broadening however collisional cross-sections are molecules-specific and evolve with temperature. These are usually unknown at the temperature of interest. Fortunately as presented in chapter 4 section 4.2 the CRESUCHIRP experimental apparatus allows for the measurement of these parameters but the precise determination of these require enough SNR to be able to fit the FIDs with the adequate model. The spectrometer contribution also needs to be quantified. The response to excitation is also molecules-dependent through the transition dipole moment which then needs to be determined. For molecules for which the spectroscopic parameters are already known, this is an easy task but for some molecules, this would require spectroscopic work to be done. The spectrometer itself and its frequency calibration have been discussed in chapter 2 section 2.10, this must be taken into account when comparing two product signals. As presented in the same section this is a really tedious and long process.

All of these contributions would need to be taken into account in order to provide a rigorous determination of a branching fraction for a reaction. But for all of these contributions, a means to quantify their impact has already been theoretically provided in the preceding paragraph. From the conclusion of this work and work that was done in parallel and reported in the theses of fellow Ph.D. students Divita Gupta and Omar Abdelkader Khedaoui CPUF shows promises for further improvement and maybe to become a reference technique to measure branching ratio at low temperature.

Bibliography

[1] B. A. McGuire. “2018 census of interstellar, circumstellar, extragalactic, protoplanetary disk, and exoplanetary molecules”. *The Astrophysical Journal Supplement Series* 239.2 (2018), p. 17.

[2] I. W. M. Smith. “Reactions at very low temperatures: Gas kinetics at a new frontier”. *Angewandte Chemie-International Edition* 45.18 (2006), pp. 2842–2861. DOI: 10.1002/anie.200502747.

[3] I. W. M. Smith. “The temperature-dependence of elementary reaction rates: beyond Arrhenius”. en. *Chemical Society Reviews* 37.4 (Mar. 2008). Number: 4, pp. 812–826. DOI: 10.1039/B704257B.

[4] F. M. Flasar, R. K. Achterberg, B. J. Conrath, P. J. Gierasch, V. G. Kunde, C. A. Nixon, et al. “Titan’s Atmospheric Temperatures, Winds, and Composition”. en. *Science* 308.5724 (May 2005). Number: 5724, pp. 975–978. DOI: 10.1126/science.1111150.

[5] M. Agúndez and V. Wakelam. “Chemistry of Dark Clouds: Databases, Networks, and Models”. *Chemical Reviews* 113.12 (Dec. 2013). Number: 12, pp. 8710–8737. DOI: 10.1021/cr4001176.

[6] E. Herbst. “Chemistry of Star-Forming Regions”. *The Journal of Physical Chemistry A* 109.18 (2005). PMID: 16833724, pp. 4017–4029. DOI: 10.1021/jp050461c.

[7] M. Tizniti, S. D. Le Picard, F. Lique, C. Berteloite, A. Canosa, M. H. Alexander, and I. R. Sims. “The rate of the F + H_2 reaction at very low temperatures”. *Nature Chemistry* 6.2 (Jan. 2014), pp. 141–145. DOI: 10.1038/nchem.1835.

[8] P. W. Seakins. “Product branching ratios in simple gas phase reactions”. en. *Annual Reports Section ’C’ (Physical Chemistry)* 103.0 (June 2007). Number: 0, pp. 173–222. DOI: 10.1039/B605650B.

[9] I. R. Cooke and I. R. Sims. “Experimental Studies of Gas-Phase Reactivity in Relation to Complex Organic Molecules in Star-Forming Regions”. *ACS Earth and Space Chemistry* 3.7 (July 2019). Number: 7, pp. 1109–1134. DOI: 10.1021/acsearthspacechem.9b00064.

[10] M. A. Blitz and P. W. Seakins. “Laboratory studies of photochemistry and gas phase radical reaction kinetics relevant to planetary atmospheres”. *Chem. Soc. Rev.* 41 (19 2012), pp. 6318–6347. DOI: 10.1039/C2CS35204D.

[11] M. K. Sprague, L. A. Mertens, H. N. Widgren, M. Okumura, S. P. Sander, and A. B. McCoy. “Cavity Ringdown Spectroscopy of the Hydroxy-Methyl-Peroxy Radical”. *The Journal of Physical Chemistry A* 117.39 (2013). PMID: 23641685, pp. 10006–10017. DOI: 10.1021/jp400390y.

[12] S. S. Brown, A. R. Ravishankara, and H. Stark. “Simultaneous Kinetics and Ringdown: Rate Coefficients from Single Cavity Loss Temporal Profiles”. *The Journal of Physical Chemistry A* 104.30 (2000), pp. 7044–7052. DOI: 10.1021/jp0013715.

[13] J.-C. Loison and A. Bergeat. “Rate constants and the H atom branching ratio of the reactions of the methylidyne CH($X^2\Pi$) radical with C_2H_2, C_2H_4, C_3H_4 (methylacetylene and allene), C_3H_6 (propene) and C_4H_8 (*trans*-butene)”. *Phys. Chem. Chem. Phys.* 11 (4 2009), pp. 655–664. DOI: 10.1039/B812810C.

[14] S. E. Taylor, A. Goddard, M. A. Blitz, P. A. Cleary, and D. E. Heard. “Pulsed Laval nozzle study of the kinetics of OH with unsaturated hydrocarbons at very low temperatures”. *Phys. Chem. Chem. Phys.* 10 (3 2008), pp. 422–437. DOI: 10.1039/B711411G.

[15] D. L. Osborn, P. Zou, H. Johnsen, C. C. Hayden, C. A. Taatjes, V. D. Knyazev, S. W. North, D. S. Peterka, M. Ahmed, and S. R. Leone. “The multiplexed chemical kinetic photoionization mass spectrometer: A new approach to isomer-resolved chemical kinetics”. *Review of Scientific Instruments* 79.10 (Oct. 2008). Number: 10, p. 104103. DOI: 10.1063/1.3000004.

[16] J. F. Lockyear, M. Fournier, I. R. Sims, J.-C. Guillemin, C. A. Taatjes, D. L. Osborn, and S. R. Leone. “Formation of fulvene in the reaction of C_2H with 1,3-butadiene”. en. *International Journal of Mass Spectrometry*. SI: Bierbaum 65th Birthday 378 (Feb. 2015), pp. 232–245. DOI: 10.1016/j.ijms.2014.08.025.

[17] S. Soorkia, C.-L. Liu, J. D. Savee, S. J. Ferrell, S. R. Leone, and K. R. Wilson. "Airfoil sampling of a pulsed Laval beam with tunable vacuum ultraviolet synchrotron ionization quadrupole mass spectrometry: Application to low-temperature kinetics and product detection". *Review of Scientific Instruments* 82.12 (Dec. 2011). Number: 12, p. 124102. DOI: 10.1063/1.3669537.

[18] J. Bouwman, M. Fournier, I. R. Sims, S. R. Leone, and K. R. Wilson. "Reaction Rate and Isomer-Specific Product Branching Ratios of C_2H + C_4H_8: 1-Butene, *cis*-2-Butene, *trans*-2-Butene, and Isobutene at 79 K". *The Journal of Physical Chemistry A* 117.24 (June 2013). Number: 24, pp. 5093–5105. DOI: 10.1021/jp403637t.

[19] O. Durif, M. Capron, J. P. Messinger, A. Benidar, L. Biennier, J. Bourgalais, et al. "A new instrument for kinetics and branching ratio studies of gas phase collisional processes at very low temperatures". *Review of Scientific Instruments* 92.1 (2021), p. 014102. DOI: 10.1063/5.0029991.

[20] A. J. Fleisher, B. J. Bjork, T. Q. Bui, K. C. Cossel, M. Okumura, and J. Ye. "Mid-Infrared Time-Resolved Frequency Comb Spectroscopy of Transient Free Radicals". *The Journal of Physical Chemistry Letters* 5.13 (July 2014). Number: 13, pp. 2241–2246. DOI: 10.1021/jz5008559.

[21] B. J. Bjork, T. Q. Bui, O. H. Heckl, P. B. Changala, B. Spaun, P. Heu, et al. "Direct frequency comb measurement of OD + CO $\rightarrow$ DOCO kinetics". en. *Science* 354.6311 (Oct. 2016). Number: 6311, pp. 444–448. DOI: 10.1126/science.aag1862.

[22] F. C. Roberts, H. J. Lewandowski, B. F. Hobson, and J. H. Lehman. "A rapid, spatially dispersive frequency comb spectrograph aimed at gas phase chemical reaction kinetics". *Molecular Physics* 118.16 (2020), e1733116. DOI: 10.1080/00268976.2020.1733116.

[23] N. Suas-David, S. Thawoos, and A. G. Suits. "A uniform flow–cavity ring-down spectrometer (UF-CRDS): A new setup for spectroscopy and kinetics at low temperature". *The Journal of Chemical Physics* 151.24 (Dec. 2019). Number: 24, p. 244202. DOI: 10.1063/1.5125574.

[24] G. G. Brown, B. C. Dian, K. O. Douglass, S. M. Geyer, S. T. Shipman, and B. H. Pate. "A broadband Fourier transform microwave spectrometer based on chirped pulse excitation". *Review of Scientific Instruments* 79.5 (May 2008). Number: 5, p. 053103. DOI: 10.1063/1.2919120.

[25] B. A. McGuire, A. M. Burkhardt, S. Kalenskii, C. N. Shingledecker, A. J. Remijan, E. Herbst, and M. C. McCarthy. "Detection of the aromatic molecule benzonitrile (c-C_6H_5CN) in the interstellar medium". en. *Science* 359.6372 (Jan. 2018). Number: 6372, pp. 202–205. DOI: 10.1126/science.aao4890.

[26] M. C. McCarthy, K. L. K. Lee, R. A. Loomis, A. M. Burkhardt, C. N. Shingledecker, S. B. Charnley, et al. "Interstellar detection of the highly polar five-membered ring cyanocyclopentadiene". en. *Nature Astronomy* (Sept. 2020). Publisher: Nature Publishing Group, pp. 1–5. DOI: 10.1038/s41550-020-01213-y.

[27] K. L. K. Lee and M. McCarthy. "Study of Benzene Fragmentation, Isomerization, and Growth Using Microwave Spectroscopy". *The Journal of Physical Chemistry Letters* 10.10 (Apr. 2019), pp. 2408–2413. DOI: 10.1021/acs.jpclett.9b00586.

[28] J. M. Oldham, C. Abeysekera, B. Joalland, L. N. Zack, K. Prozument, I. R. Sims, G. B. Park, R. W. Field, and A. G. Suits. "A chirped-pulse Fourier-transform microwave/pulsed uniform flow spectrometer. I. The low-temperature flow system". *The Journal of Chemical Physics* 141.15 (2014), p. 154202. DOI: 10.1063/1.4897979.

[29] C. Abeysekera, L. N. Zack, G. B. Park, B. Joalland, J. M. Oldham, K. Prozument, N. M. Ariyasingha, I. R. Sims, R. W. Field, and A. G. Suits. "A chirped-pulse Fourier-transform microwave/pulsed uniform flow spectrometer. II. Performance and applications for reaction dynamics". *The Journal of Chemical Physics* 141.21 (Dec. 2014). Number: 21 Publisher: American Institute of Physics, p. 214203. DOI: 10.1063/1.4903253.

[30] C. Abeysekera, B. Joalland, N. Ariyasingha, L. N. Zack, I. R. Sims, R. W. Field, and A. G. Suits. "Product Branching in the Low Temperature Reaction of CN with Propyne by Chirped-Pulse Microwave Spectroscopy in a Uniform Supersonic Flow". *The Journal of Physical Chemistry Letters* 6.9 (May 2015). Number: 9, pp. 1599–1604. DOI: 10.1021/acs.jpclett.5b00519.

[31] C. Berteloite, M. Lara, A. Bergeat, S. D. Le Picard, F. Dayou, K. M. Hickson, et al. "Kinetics and Dynamics of the $S(^1D_2) + H_2 \rightarrow SH + H$ Reaction at Very Low Temperatures and Collision Energies". *Phys. Rev. Lett.* 105 (20 Nov. 2010), p. 203201. DOI: 10.1103/PhysRevLett.105.203201.

[32] G. Dupeyrat, J. B. Marquette, and B. R. Rowe. “Design and testing of axisymmetric nozzles for ion-molecule reaction studies between 20 K and 160 K”. *Physics of Fluids* (1985), pp. 1273–1279.

[33] I. R. Sims, J.-L. Queffelec, D. Travers, B. R. Rowe, L. B. Herbert, J. Karthäuser, and I. W. Smith. “Rate constants for the reactions of CN with hydrocarbons at low and ultra-low temperatures”. *Chemical Physics Letters* 211.4 (1993), pp. 461–468. DOI: https://doi.org/10.1016/0009-2614(93)87091-G.

[34] E. Dudas, N. Suas-David, S. Brahmachary, V. Kulkarni, A. Benidar, S. Kassi, C. Charles, and R. Georges. “High-temperature hypersonic Laval nozzle for non-LTE cavity ringdown spectroscopy”. *The Journal of Chemical Physics* 152.13 (2020), p. 134201. DOI: 10.1063/5.0003886.

[35] N. Daugey, P. Caubet, B. Retail, M. Costes, A. Bergeat, and G. Dorthe. “Kinetic measurements on methylidyne radical reactions with several hydrocarbons at low temperatures”. *Phys. Chem. Chem. Phys.* 7 (15 2005), pp. 2921–2927. DOI: 10.1039/B506096F.

[36] E. Jiménez, B. Ballesteros, A. Canosa, T. M. Townsend, F. J. Maigler, V. Napal, B. R. Rowe, and J. Albaladejo. “Development of a pulsed uniform supersonic gas expansion system based on an aerodynamic chopper for gas phase reaction kinetic studies at ultra-low temperatures”. *Review of Scientific Instruments* 86.4 (Apr. 2015). Publisher: American Institute of Physics, p. 045108. DOI: 10.1063/1.4918529.

[37] J. E. Wollrab. *Rotational Spectra and Molecular Structure*. Academic, 1967.

[38] C. Townes and A. Schawlow. *Microwave Spectroscopy*. Dover books on physics. Dover Publications, 2013.

[39] W. Gordy and R. L. Cook. *Microwave Molecular Spectra*. 3rd. New York: John Wiley & Sons, Inc., 1984.

[40] Müller, H. S. P., Thorwirth, S., Roth, D. A., and Winnewisser, G. “The Cologne Database for Molecular Spectroscopy, CDMS”. *A&A* 370.3 (2001), pp. L49–L52. DOI: 10.1051/0004-6361:20010367.

[41] H. S. Müller, F. Schlöder, J. Stutzki, and G. Winnewisser. “The Cologne Database for Molecular Spectroscopy, CDMS: a useful tool for astronomers and spectroscopists”. *Journal of Molecular Structure* 742.1 (2005). MOLECULAR SPECTROSCOPY AND STRUCTURE, pp. 215–227. DOI: https://doi.org/10.1016/j.molstruc.2005.01.027.

[42] C. P. Endres, S. Schlemmer, P. Schilke, J. Stutzki, and H. S. P. Müller. "The Cologne Database for Molecular Spectroscopy, CDMS, in the Virtual Atomic and Molecular Data Centre, VAMDC". *Journal of Molecular Spectroscopy*. New Visions of Spectroscopic Databases, Volume II 327 (Sept. 2016), pp. 95–104. DOI: 10.1016/j.jms.2016.03.005.

[43] H. Pickett, R. Poynter, E. Cohen, M. Delitsky, J. Pearson, and H. Muller. "Submillimeter, millimeter, and microwave spectral catalog". *Journal of Quantitative Spectroscopy and Radiative Transfer* 60.5 (1998), pp. 883–890. DOI: https://doi.org/10.1016/S0022-4073(98)00091-0.

[44] T. J. Balle and W. H. Flygare. "Fabry–Perot cavity pulsed Fourier transform microwave spectrometer with a pulsed nozzle particle source". *Review of Scientific Instruments* 52.1 (Jan. 1981). Number: 1, pp. 33–45. DOI: 10.1063/1.1136443.

[45] J. C. McGurk, T. G. Schmalz, and W. H. Flygare. "Fast passage in rotational spectroscopy: Theory and experiment". *The Journal of Chemical Physics* 60.11 (June 1974). Number: 11 Publisher: American Institute of Physics, pp. 4181–4188. DOI: 10.1063/1.1680886.

[46] B. C. Dian, G. G. Brown, K. O. Douglass, and B. H. Pate. "Measuring Picosecond Isomerization Kinetics via Broadband Microwave Spectroscopy". en. *Science* 320.5878 (May 2008). Number: 5878, pp. 924–928. DOI: 10.1126/science.1155736.

[47] J. L. Neill, A. L. Steber, M. T. Muckle, D. P. Zaleski, V. Lattanzi, S. Spezzano, et al. "Spatial Distributions and Interstellar Reaction Processes". *The Journal of Physical Chemistry A* 115.24 (June 2011). Number: 24, pp. 6472–6480. DOI: 10.1021/jp200539b.

[48] D. P. Zaleski, J. L. Neill, M. T. Muckle, N. A. Seifert, P. Brandon Carroll, S. L. Widicus Weaver, and B. H. Pate. "A Ka-band chirped-pulse Fourier transform microwave spectrometer". *Journal of Molecular Spectroscopy*. Broadband Rotational Spectroscopy 280 (Oct. 2012), pp. 68–76. DOI: 10.1016/j.jms.2012.07.014.

[49] A. L. Steber, B. J. Harris, J. L. Neill, and B. H. Pate. "An arbitrary waveform generator based chirped pulse Fourier transform spectrometer operating from 260 to 295 GHz". *Journal of Molecular Spectroscopy*. Broadband Rotational Spectroscopy 280 (Oct. 2012), pp. 3–10. DOI: 10.1016/j.jms.2012.07.015.

[50] J. L. Neill, B. J. Harris, A. L. Steber, K. O. Douglass, D. F. Plusquellic, and B. H. Pate. "Segmented chirped-pulse Fourier transform submillimeter spectroscopy for broadband gas analysis". EN. *Optics Express* 21.17 (Aug. 2013). Number: 17, pp. 19743–19749. DOI: 10.1364/OE.21.019743.

[51] L. Allen and J. H. Eberly. *Optical Resonance and Two-Level Atoms*. New York: Dover Publications, Inc., 1987.

[52] J.-U. Grabow. "Fourier Transform Microwave Spectroscopy Measurement and Instrumentation". en. *Handbook of High-resolution Spectroscopy*. Ed. by M. Quack and F. Merkt. John Wiley & Sons, Ltd, 2011. DOI: 10.1002/9780470749593.hrs037.

[53] F. Wolf. "Fast sweep experiments in microwave spectroscopy". en. *Journal of Physics D: Applied Physics* 27.8 (Aug. 1994). Number: 8, pp. 1774–1780. DOI: 10.1088/0022-3727/27/8/029.

[54] G. B. Park, A. H. Steeves, K. Kuyanov-Prozument, J. L. Neill, and R. W. Field. "Design and evaluation of a pulsed-jet chirped-pulse millimeter-wave spectrometer for the 70–102 GHz region". *The Journal of Chemical Physics* 135.2 (July 2011). Number: 2 Publisher: American Institute of Physics, p. 024202. DOI: 10.1063/1.3597774.

[55] J. C. McGurk, H. Mäder, R. T. Hofmann, T. G. Schmalz, and W. H. Flygare. "Transient emission, off-resonant transient absorption, and Fourier transform microwave spectroscopy". *The Journal of Chemical Physics* 61.9 (Nov. 1974). Number: 9, pp. 3759–3767. DOI: 10.1063/1.1682562.

[56] R. H. Schwendeman. "Transient Effects in Microwave Spectroscopy". *Annual Review of Physical Chemistry* 29.1 (1978). Number: 1, pp. 537–558. DOI: 10.1146/annurev.pc.29.100178.002541.

[57] H. Mäder. "Microwave fourier transform spectroscopy: Linewidth effects in the low pressure limit". *Journal of Quantitative Spectroscopy and Radiative Transfer* 32.2 (Aug. 1984). Number: 2, pp. 129–140. DOI: 10.1016/0022-4073(84)90077-3.

[58] J. C. McGurk, R. T. Hofmann, and W. H. Flygare. "Transient absorption and emission and the measurement of T_1 and T_2 in the J 0→1 rotational transition in OCS". *The Journal of Chemical Physics* 60.7 (Apr. 1974). Number: 7, pp. 2922–2928. DOI: 10.1063/1.1681462.

[59] W. E. Hoke, D. R. Bauer, J. Ekkers, and W. H. Flygare. “The measurement and interpretation of T_1 and T_2 in the inversion doublets of $^{15}NH_3$ and the rotational transitions in OCS”. *The Journal of Chemical Physics* 64.12 (June 1976). Number: 12, pp. 5276–5282. DOI: 10.1063/1.432156.

[60] H. Mäder, J. Ekkers, W. Hoke, and W. H. Flygare. “A π, τ, $\pi/2$ type pulse sequence method for the determination of T_1 in rotational transitions”. *The Journal of Chemical Physics* 62.11 (June 1975). Number: 11, pp. 4380–4387. DOI: 10.1063/1.430338.

[61] H. Mäder, W. Lalowski, and R. Schwarz. “Investigation of T_1 and T_2 Relaxation for Ethylene Oxide Rotational Transitions”. *Zeitschrift für Naturforschung A* 34.10 (1979). Number: 10, pp. 1181–1184. DOI: 10.1515/zna-1979-1006.

[62] H. Mäder, H. Bomsdorf, and U. Andresen. “The Measurement of Rotational Relaxation Time T_2 for $CH_3C^{15}N$ Self-and Foreign Gas Collisions”. *Zeitschrift für Naturforschung A* 34.7 (1979). Number: 7, pp. 850–857. DOI: 10.1515/zna-1979-0709.

[63] S. C. Mehrotra, G. Bestmann, H. Dreizler, and H. Mäder. “A Contribution to the Investigation of T_2-Relaxation: Rotational Transitions of OCS and SO_2”. *Zeitschrift für Naturforschung A* 39.7 (1984). Number: 7, pp. 633–636. DOI: 10.1515/zna-1984-0707.

[64] S. C. Mehrotra, H. Dreizler, and H. Mäder. “J-Dependence of T_2-Parameters for Rotational Transitions of SO_2 and CH_3OH in K-Band”. *Zeitschrift für Naturforschung A* 40.7 (1985). Number: 7, pp. 683–685. DOI: 10.1515/zna-1985-0705.

[65] S. C. Mehrotra, H. Dreizler, and H. Mäder. “Investigations of self-, H_2- and He-broadening for rotational transitions of $HCCC^{15}N$, CF_3D and CF_3CCH by the microwave transient emmission technique”. *Journal of Quantitative Spectroscopy and Radiative Transfer* 34.3 (Sept. 1985). Number: 3, pp. 229–231. DOI: 10.1016/0022-4073(85)90003-2.

[66] S. C. Mehrotra and H. Mäder. “Study of T_1-and T_2-Relaxation by Microwave Pulse Techniques: Rotational Transition J=0-1 of HCCF,J-Dependence of Rotational Transitions of $S0_2$,and l-Type Doublet Transitions of $HC^{15}N$ Perturbed by Self, H_2, D_2, and He”. *Zeitschrift für Naturforschung A* 43.5 (1988). Number: 5, pp. 454–468. DOI: 10.1515/zna-1988-0510.

[67] J. Haekel and H. Mäder. “Determination of Spectral Parameters in Microwave Fouriertransform Spectroscopy by Analysis of Time-Domain Signals”. *Zeitschrift für Naturforschung A* 43.3 (1988). Number: 3, pp. 203–206. DOI: 10.1515/zna-1988-0304.

[68] S. L. Coy. “Speed dependence of microwave rotational relaxation rates”. *The Journal of Chemical Physics* 73.11 (Dec. 1980). Number: 11, pp. 5531–5555. DOI: 10.1063/1.440073.

[69] J. Haekel and H. Mäder. “Speed-dependent T_2-relaxation rates of microwave emission signals”. *Journal of Quantitative Spectroscopy and Radiative Transfer* 46.1 (July 1991). Number: 1, pp. 21–30. DOI: 10.1016/0022-4073(91)90063-V.

[70] F. Rohart, H. Mäder, and H.-W. Nicolaisen. “Speed dependence of rotational relaxation induced by foreign gas collisions: Studies on CH_3F by millimeter wave coherent transients”. *The Journal of Chemical Physics* 101.8 (Oct. 1994). Number: 8, pp. 6475–6486. DOI: 10.1063/1.468342.

[71] J. He and C. Zhang. “The accurate calculation of the Fourier transform of the pure Voigt function”. en. *Journal of Optics A: Pure and Applied Optics* 7.10 (Sept. 2005). Number: 10, pp. 613–616. DOI: 10.1088/1464-4258/7/10/014.

[72] D. W. Marquardt. “An Algorithm for Least-Squares Estimation of Nonlinear Parameters”. *Journal of the Society for Industrial and Applied Mathematics* 11.2 (June 1963). Number: 2, pp. 431–441. DOI: 10.1137/0111030.

[73] V. Wakelam, E. Herbst, J.-C. Loison, I. W. M. Smith, V. Chandrasekaran, B. Pavone, et al. “A KINETIC DATABASE FOR ASTROCHEMISTRY (KIDA)”. *The Astrophysical Journal Supplement Series* 199.1 (Mar. 2012), p. 21. DOI: 10.1088/0067-0049/199/1/21.

[74] I. R. Sims, I. W. M. Smith, D. C. Clary, P. Bocherel, and B. R. Rowe. “Ultra-low temperature kinetics of neutral–neutral reactions: New experimental and theoretical results for OH + HBr between 295 and 23 K”. *The Journal of Chemical Physics* 101.2 (1994), pp. 1748–1751. DOI: 10.1063/1.467733.

[75] P. L. James, I. R. Sims, I. W. M. Smith, M. H. Alexander, and M. Yang. “A combined experimental and theoretical study of rotational energy transfer in collisions between NO($X^2\Pi_{1/2}$, v=3,J) and He, Ar and N_2 at temperatures down to 7 K”. *The Journal of Chemical Physics* 109.10 (1998), pp. 3882–3897. DOI: 10.1063/1.476517.

[76] D. Gupta, S. Cheikh Sid Ely, I. R. Cooke, T. Guillaume, O. Abdelkader Khedaoui, T. S. Hearne, B. M. Hays, and I. R. Sims. "Low Temperature Kinetics of the Reaction Between Methanol and the CN Radical". *The Journal of Physical Chemistry A* 123.46 (2019). PMID: 31647680, pp. 9995–10003. DOI: 10.1021/acs.jpca.9b08472.

[77] W. S. Felps, K. Rupnik, and S. P. McGlynn. "Electronic spectroscopy of the cyanogen halides". *The Journal of Physical Chemistry* 95.2 (1991), pp. 639–656. DOI: 10.1021/j100155a028.

[78] D. P. Zaleski, L. B. Harding, S. J. Klippenstein, B. Ruscic, and K. Prozument. "Time-Resolved Kinetic Chirped-Pulse Rotational Spectroscopy in a Room-Temperature Flow Reactor". *The Journal of Physical Chemistry Letters* 8.24 (Dec. 2017). Number: 24 Publisher: American Chemical Society, pp. 6180–6188. DOI: 10.1021/acs.jpclett.7b02864.

[79] B. E. Arenas, S. Gruet, A. L. Steber, B. M. Giuliano, and M. Schnell. "Chirped-pulse Fourier transform millimeter-wave spectroscopy of ten vibrationally excited states of i-propyl cyanide: exploring the far-infrared region". en. *Physical Chemistry Chemical Physics* 19.3 (Jan. 2017). Number: 3, pp. 1751–1756. DOI: 10.1039/C6CP06297K.

[80] D. P. Zaleski, C. Duan, M. Carvajal, I. Kleiner, and K. Prozument. "The broadband rotational spectrum of fully deuterated acetaldehyde (CD_3CDO) in a CW supersonic expansion". *Journal of Molecular Spectroscopy*. Spectroscopy of Large Amplitude Vibrational Motions, on the Occasion of Jon Hougen's 80th Birthday - Part I 342 (Dec. 2017), pp. 17–24. DOI: 10.1016/j.jms.2017.01.010.

[81] B. Harris. "A Chirped Pulse Fourier Transform Millimeter Wave Spectrometer for Room Temperature, Gas Mixture Analysis". PhD thesis. University of Virginia, Apr. 2014. DOI: 10.18130/v3vj8m.

[82] N. Wehres, B. Heyne, F. Lewen, M. Hermanns, B. Schmidt, C. Endres, U. U. Graf, D. R. Higgins, and S. Schlemmer. "100 GHz Room-Temperature Laboratory Emission Spectrometer". en. *Proceedings of the International Astronomical Union* 13.S332 (Mar. 2017). Number: S332, pp. 332–345. DOI: 10.1017/S1743921317007803.

[83] N. Wehres, J. Maßen, K. Borisov, B. Schmidt, F. Lewen, U. U. Graf, C. E. Honingh, D. R. Higgins, and S. Schlemmer. "A laboratory heterodyne emission spec-

trometer at submillimeter wavelengths". en. *Physical Chemistry Chemical Physics* 20.8 (2018). Number: 8, pp. 5530–5544. DOI: 10.1039/C7CP06394F.

[84] G. A. Ediss, N. Horner, F. Johnson, D. Koller, and A. R. Kerr. "WR-10 Waveguide Vacuum Feedthrough for the ALMA Band-6 Cartridge". *ALMA Memo 536* (2005).

[85] K. Prozument, G. Barratt Park, R. G. Shaver, A. K. Vasiliou, J. M. Oldham, D. E. David, et al. "Chirped-pulse millimeter-wave spectroscopy for dynamics and kinetics studies of pyrolysis reactions". *Phys. Chem. Chem. Phys.* 16 (30 2014), pp. 15739–15751. DOI: 10.1039/C3CP55352C.

[86] A. O. Hernandez-Castillo, C. Abeysekera, B. M. Hays, and T. S. Zwier. "Broadband multi-resonant strong field coherence breaking as a tool for single isomer microwave spectroscopy". *The Journal of Chemical Physics* 145.11 (Sept. 2016). Number: 11, p. 114203. DOI: 10.1063/1.4962505.

[87] B. M. Broderick, N. Suas-David, N. Dias, and A. G. Suits. "Isomer-specific detection in the UV photodissociation of the propargyl radical by chirped-pulse mm-wave spectroscopy in a pulsed quasi-uniform flow". *Phys. Chem. Chem. Phys.* 20 (8 2018), pp. 5517–5529. DOI: 10.1039/C7CP06211G.

[88] B. M. Hays, T. Guillaume, T. S. Hearne, I. R. Cooke, D. Gupta, O. A. Khedaoui, S. D. L. Picard, and I. R. Sims. "Design and performance of an E-band chirped pulse spectrometer for kinetics applications: OCS – He pressure broadening". *Journal of Quantitative Spectroscopy and Radiative Transfer* 250 (July 2020), p. 107001. DOI: 10.1016/j.jqsrt.2020.107001.

[89] G. B. Park and R. W. Field. "Perspective: The first ten years of broadband chirped pulse Fourier transform microwave spectroscopy". *The Journal of Chemical Physics* 144.20 (May 2016). Number: 20, p. 200901. DOI: 10.1063/1.4952762.

[90] D. Patterson and J. M. Doyle. "Cooling molecules in a cell for FTMW spectroscopy". *Molecular Physics* 110.15-16 (Aug. 2012). Number: 15-16, pp. 1757–1766. DOI: 10.1080/00268976.2012.679632.

[91] B. J. Harris, A. L. Steber, K. K. Lehmann, and B. H. Pate. "Gas Analysis by Fourier Transform mm-wave Spectroscopy". Columbus, OH, June 2013.

[92] F. Hindle, C. Bray, K. Hickson, D. Fontanari, M. Mouelhi, A. Cuisset, G. Mouret, and R. Bocquet. “Chirped Pulse Spectrometer Operating at 200 GHz”. en. *Journal of Infrared, Millimeter, and Terahertz Waves* 39.1 (Jan. 2018). Number: 1, pp. 105–119. DOI: 10.1007/s10762-017-0445-3.

[93] C. P. Endres, P. Caselli, and S. Schlemmer. “State-to-State Rate Coefficients for NH_3–NH_3 Collisions from Pump–Probe Chirped Pulse Experiments”. *The Journal of Physical Chemistry Letters* 10.17 (Sept. 2019). Number: 17, pp. 4836–4841. DOI: 10.1021/acs.jpclett.9b01653.

[94] F. A. Liuima, A. V. Bushkovitch, and A. G. Rouse. “Pressure Broadening of OCS in Foreign Gas Mixtures”. *Physical Review* 96.2 (Oct. 1954). Number: 2, pp. 434–435. DOI: 10.1103/PhysRev.96.434.

[95] M. J. Burns and S. L. Coy. “Rotational relaxation rates for the OCS J=0–1 pure rotational transition broadened by argon and helium”. *The Journal of Chemical Physics* 80.8 (Apr. 1984). Number: 8, pp. 3544–3551. DOI: 10.1063/1.447199.

[96] K. A. Ross and D. R. Willey. “Low temperature pressure broadening of OCS by He”. *The Journal of Chemical Physics* 122.20 (May 2005). Number: 20, p. 204308. DOI: 10.1063/1.1901659.

[97] K. H. Casleton, K. .-R. Chien, P. B. Foreman, and S. G. Kukolich. “Rotational relaxation measurements on OCS using a beam maser”. *Chemical Physics Letters* 36.3 (Nov. 1975). Number: 3, pp. 308–311. DOI: 10.1016/0009-2614(75)80243-0.

[98] I. C. Story, V. I. Metchnik, and R. W. Parsons. “The measurement of the widths and pressure-induced shifts of microwave spectra lines”. en. *Journal of Physics B: Atomic and Molecular Physics* 4.4 (Apr. 1971). Number: 4, pp. 593–608. DOI: 10.1088/0022-3700/4/4/023.

[99] M. Broquier, A. Picard-Bersellini, B. J. Whitaker, and S. Green. “Rotational inelastic cross sections for OCS–Ar, OCS–He, OCS–H_2 collisions: A comparison between theory and experiment”. *The Journal of Chemical Physics* 84.4 (Feb. 1986). Number: 4, pp. 2104–2107. DOI: 10.1063/1.450421.

[100] J. S. Wilzewski, I. E. Gordon, R. V. Kochanov, C. Hill, and L. S. Rothman. “H2, He, and CO_2 line-broadening coefficients, pressure shifts and temperature-dependence exponents for the HITRAN database. Part 1: SO_2, NH_3, HF, HCl, OCS and C_2H_2”. *Journal of Quantitative Spectroscopy and Radiative Transfer* 168 (Jan. 2016), pp. 193–206. DOI: 10.1016/j.jqsrt.2015.09.003.

[101] J. Boissoles, F. Thibault, R. L. Doucen, V. Menoux, and C. Boulet. “Line mixing effects in the 00°3–00°0 band of CO_2 in helium. II. Theoretical analysis”. *The Journal of Chemical Physics* 100.1 (Jan. 1994). Number: 1, pp. 215–223. DOI: 10.1063/1.466989.

[102] F. Rohart, P. Glorieux, and B. Macke. “’Rotary’ single photon echoes”. en. *Journal of Physics B: Atomic and Molecular Physics* 10.18 (Dec. 1977). Number: 18, pp. 3835–3848. DOI: 10.1088/0022-3700/10/18/035.

[103] T. Köhler and H. Mäder. “Measurement of speed dependent rotational relaxation rates using a microwave spectrometer with a circular waveguide”. *Molecular Physics* 86.2 (Oct. 1995). Number: 2, pp. 287–300. DOI: 10.1080/00268979500102021.

[104] F. Rohart, D. Derozier, and J. Legrand. “Foreign gas relaxation of the J=0→1 transition of $HC^{15}N$. A study of the temperature dependence by coherent transients”. en. *The Journal of Chemical Physics* 87.10 (Nov. 1987). Number: 10, pp. 5794–5803. DOI: 10.1063/1.453503.

[105] K. Prozument, J. H. Baraban, P. B. Changala, G. B. Park, R. G. Shaver, J. S. Muenter, S. J. Klippenstein, V. Y. Chernyak, and R. W. Field. “Photodissociation transition states characterized by chirped pulse millimeter wave spectroscopy”. *Proceedings of the National Academy of Sciences* 117.1 (2020), pp. 146–151. DOI: 10.1073/pnas.1911326116.

[106] M. J. Wilhelm, M. Nikow, L. Letendre, and H.-L. Dai. “Photodissociation of vinyl cyanide at 193 nm: Nascent product distributions of the molecular elimination channels”. *The Journal of Chemical Physics* 130.4 (Jan. 2009). Number: 4 Publisher: American Institute of Physics, p. 044307. DOI: 10.1063/1.3065986.

[107] D. A. Blank, A. G. Suits, Y. T. Lee, S. W. North, and G. E. Hall. “Photodissociation of acrylonitrile at 193 nm: A photofragment translational spectroscopy study using synchrotron radiation for product photoionization”. *The Journal of Chemical Physics* 108.14 (1998), pp. 5784–5794. DOI: 10.1063/1.475989.

[108] S. Eden, P. Limão-Vieira, P. Kendall, N. J. Mason, S. V. Hoffmann, and S. M. Spyrou. “High resolution photo-absorption studies of acrylonitrile, C_2H_3CN, and acetonitrile, CH_3CN”. *The European Physical Journal D - Atomic, Molecular, Optical and Plasma Physics* 26.2 (2003), pp. 201–210. DOI: 10.1140/epjd/e2003-00223-5.

[109] D. Fontanari, C. Bray, G. Dhont, G. Mouret, A. Cuisset, F. Hindle, R. Bocquet, and K. M. Hickson. "Molecules probed with a slow chirped-pulse excitation: Analytical model of the free-induction-decay signal". *Phys. Rev. A* 100 (4 Oct. 2019), p. 043407. DOI: 10.1103/PhysRevA.100.043407.

[110] T. L. Nguyen, J. H. Baraban, B. Ruscic, and J. F. Stanton. "On the HCN – HNC Energy Difference". *The Journal of Physical Chemistry A* 119.44 (Nov. 2015). Publisher: American Chemical Society, pp. 10929–10934. DOI: 10.1021/acs.jpca.5b08406.

[111] J. H. Baraban, P. B. Changala, G. C. Mellau, J. F. Stanton, A. J. Merer, and R. W. Field. "Spectroscopic characterization of isomerization transition states". en. *Science* 350.6266 (Dec. 2015). Publisher: American Association for the Advancement of Science Section: Research Article, pp. 1338–1342. DOI: 10.1126/science.aac9668.

[112] V. Y. Makhnev, A. A. Kyuberis, N. F. Zobov, L. Lodi, J. Tennyson, and O. L. Polyansky. "High Accuracy ab Initio Calculations of Rotational–Vibrational Levels of the HCN/HNC System". *The Journal of Physical Chemistry A* 122.5 (Feb. 2018). Publisher: American Chemical Society, pp. 1326–1343. DOI: 10.1021/acs.jpca.7b10483.

[113] A. G. Maki and R. L. Sams. "High temperature, high resolution infrared spectral measurements on the HNC–HCN equilibrium system". *The Journal of Chemical Physics* 75.9 (Nov. 1981). Publisher: American Institute of Physics, pp. 4178–4182. DOI: 10.1063/1.442645.

[114] M. B. Mendes, H. Buhr, M. H. Berg, M. Froese, M. Grieser, O. Heber, et al. "Cold Electron Reactions Producing the Energetic Isomer of Hydrogen Cyanide in Interstellar Clouds". en. *The Astrophysical Journal* 746.1 (Jan. 2012). Publisher: IOP Publishing, p. L8. DOI: 10.1088/2041-8205/746/1/L8.

[115] J.-C. Loison, V. Wakelam, and K. M. Hickson. "The interstellar gas-phase chemistry of HCN and HNC". en. *Monthly Notices of the Royal Astronomical Society* 443.1 (Sept. 2014). Publisher: Oxford Academic, pp. 398–410. DOI: 10.1093/mnras/stu1089.

[116] A. Hacar, A. D. Bosman, and E. F. van Dishoeck. "HCN-to-HNC intensity ratio: a new chemical thermometer for the molecular ISM". en. *Astronomy & Astrophysics* 635 (Mar. 2020), A4. DOI: 10.1051/0004-6361/201936516.

[117] Long, Feng, Bosman, Arthur D., Cazzoletti, Paolo, van Dishoeck, Ewine F., Öberg, Karin I., Facchini, Stefano, Tazzari, Marco, Guzmán, Viviana V., and Testi, Leonardo. "Exploring HNC and HCN line emission as probes of the protoplanetary disk temperature". *A&A* 647 (2021), A118. DOI: 10.1051/0004-6361/202039336.

[118] T. Hirota, S. Yamamoto, H. Mikami, and M. Ohishi. "Abundances of HCN and HNC in Dark Cloud Cores". en. *The Astrophysical Journal* 503.2 (Aug. 1998). Number: 2, pp. 717–728. DOI: 10.1086/306032.

[119] T. Barger, A. M. Wodtke, and J. M. Bowman. "Radiative Relaxation and Isomeric Branching of Highly Excited H/C/N: The Importance of Delocalized Vibrational States". en. *The Astrophysical Journal* 587.2 (Apr. 2003). Publisher: IOP Publishing, p. 841. DOI: 10.1086/368254.

[120] E. Herbst, R. Terzieva, and D. Talbi. "Calculations on the rates, mechanisms, and interstellar importance of the reactions between C and NH_2 and between N and CH_2". en. *Monthly Notices of the Royal Astronomical Society* 311.4 (Feb. 2000). Number: 4, pp. 869–876. DOI: 10.1046/j.1365-8711.2000.03103.x.

[121] D. M. Graninger, E. Herbst, K. I. Öberg, and A. I. Vasyunin. "The HNC/HCN Ratio in Star-forming Regions". en. *The Astrophysical Journal* 787.1 (May 2014). Publisher: IOP Publishing, p. 74. DOI: 10.1088/0004-637X/787/1/74.

[122] M. Hernández Vera, F. Lique, F. Dumouchel, P. Hily-Blant, and A. Faure. "The rotational excitation of the HCN and HNC molecules by H_2 revisited". en. *Monthly Notices of the Royal Astronomical Society* 468.1 (June 2017). Number: 1, pp. 1084–1091. DOI: 10.1093/mnras/stx422.

[123] E. Sarrasin, D. B. Abdallah, M. Wernli, A. Faure, J. Cernicharo, and F. Lique. "The rotational excitation of HCN and HNC by He: new insights on the HCN/HNC abundance ratio in molecular clouds". en. *Monthly Notices of the Royal Astronomical Society* 404.1 (May 2010). Number: 1, pp. 518–526. DOI: 10.1111/j.1365-2966.2010.16312.x.

[124] O. Denis-Alpizar, Y. Kalugina, T. Stoecklin, M. H. Vera, and F. Lique. "A new ab initio potential energy surface for the collisional excitation of HCN by para- and ortho-H_2". *The Journal of Chemical Physics* 139.22 (Dec. 2013). Publisher: American Institute of Physics, p. 224301. DOI: 10.1063/1.4833676.

[125] F. Dumouchel, A. Faure, and F. Lique. “The rotational excitation of HCN and HNC by He: temperature dependence of the collisional rate coefficients”. en. *Monthly Notices of the Royal Astronomical Society* 406.4 (Aug. 2010). Number: 4 Publisher: Oxford Academic, pp. 2488–2492. DOI: 10.1111/j.1365-2966.2010.16826.x.

[126] F. Dumouchel, J. Kłos, and F. Lique. “The rotational excitation of the interstellar HNC by para- and ortho-H_2”. en. *Physical Chemistry Chemical Physics* 13.18 (Apr. 2011). Publisher: The Royal Society of Chemistry, pp. 8204–8212. DOI: 10.1039/C0CP02436H.

[127] M. J. Wilhelm, E. Martínez-Núñez, J. González-Vázquez, S. A. Vázquez, J. M. Smith, and H.-L. Dai. “Is Photolytic Production a Viable Source of HCN and HNC in Astrophysical Environments? A Laboratory-based Feasibility Study of Methyl Cyanoformate”. en. *The Astrophysical Journal* 849.1 (Oct. 2017). Publisher: American Astronomical Society, p. 15. DOI: 10.3847/1538-4357/aa8ea7.

[128] M. J. Wilhelm and H.-L. Dai. “Collisional Energy Transfer from Vibrationally Excited Hydrogen Isocyanide”. *The Journal of Physical Chemistry A* 123.32 (Aug. 2019). Publisher: American Chemical Society, pp. 6927–6936. DOI: 10.1021/acs.jpca.9b07041.

[129] K. Prozument, R. G. Shaver, M. A. Ciuba, J. S. Muenter, G. B. Park, J. F. Stanton, H. Guo, B. M. Wong, D. S. Perry, and R. W. Field. “A new approach toward transition state spectroscopy”. en. *Faraday Discussions* 163.0 (July 2013). Number: 0, pp. 33–57. DOI: 10.1039/C3FD20160K.

[130] S. Green. “Effect of nuclear hyperfine structure on microwave spectral pressure broadening”. *The Journal of Chemical Physics* 88.12 (June 1988). Number: 12, pp. 7331–7336. DOI: 10.1063/1.454344.

[131] T. J. Ronningen and F. C. De Lucia. “Helium induced pressure broadening and shifting of HCN hyperfine transitions between 1.3 and 20 K”. *The Journal of Chemical Physics* 122.18 (May 2005). Number: 18, p. 184319. DOI: 10.1063/1.1895905.

[132] F. Rohart and F. Kaghat. “HCN absorption line shapes studied by millimeter wave coherent transients: speed dependent effects and collision interaction potential”. en. Ed. by J. Lewis and A. Predoi-Cross. St. John’s, (Canada), 2010, pp. 209–213. DOI: 10.1063/1.3517557.

[133] D. Carty, A. Goddard, I. R. Sims, and I. W. M. Smith. “Rotational energy transfer in collisions between CO(X $^1\Sigma^+$, v=2, J=0, 1, 4, and 6) and He at temperatures from 294 to 15 K”. en. *The Journal of Chemical Physics* 121.10 (Sept. 2004). Number: 10, pp. 4671–4683. DOI: 10.1063/1.1780163.

[134] L. A. Mertens, H. Labiad, O. Denis-Alpizar, M. Fournier, D. Carty, S. D. Le Picard, T. Stoecklin, and I. R. Sims. “Rotational energy transfer in collisions between CO and Ar at temperatures from 293 to 30K”. en. *Chemical Physics Letters*. Ahmed Zewail (1946-2016) Commemoration Issue of Chemical Physics Letters 683 (Sept. 2017), pp. 521–528. DOI: 10.1016/j.cplett.2017.05.052.

[135] R. Sánchez-González, R. D. W. Bowersox, and S. W. North. “Simultaneous velocity and temperature measurements in gaseous flowfields using the vibrationally excited nitric oxide monitoring technique: a comprehensive study”. *Appl. Opt.* 51.9 (Mar. 2012), pp. 1216–1228. DOI: 10.1364/AO.51.001216.

[136] M. Thachuk, C. E. Chuaqui, and R. J. Le Roy. “Linewidths and shifts of very low temperature CO in He: A challenge for theory or experiment?” *The Journal of Chemical Physics* 105.10 (1996), pp. 4005–4014. DOI: 10.1063/1.472274.

[137] T. de Jongh, M. Besemer, Q. Shuai, T. Karman, A. van der Avoird, G. C. Groenenboom, and S. Y. T. van de Meerakker. “Imaging the onset of the resonance regime in low-energy NO-He collisions”. *Science* 368.6491 (2020), pp. 626–630. DOI: 10.1126/science.aba3990.

[138] B. A. McGuire, R. A. Loomis, A. M. Burkhardt, K. L. K. Lee, C. N. Shingledecker, S. B. Charnley, et al. “Detection of two interstellar polycyclic aromatic hydrocarbons via spectral matched filtering”. *Science* 371.6535 (2021), pp. 1265–1269. DOI: 10.1126/science.abb7535.

[139] M. C. McCarthy, K. L. K. Lee, R. A. Loomis, A. M. Burkhardt, C. N. Shingledecker, S. B. Charnley, et al. “Interstellar detection of the highly polar five-membered ring cyanocyclopentadiene”. *Nature Astronomy* 5.2 (2021), pp. 176–180. DOI: 10.1038/s41550-020-01213-y.

[140] L. C. L. Huang, O. Asvany, A. H. H. Chang, N. Balucani, S. H. Lin, Y. T. Lee, R. I. Kaiser, and Y. Osamura. “Crossed beam reaction of cyano radicals with hydrocarbon molecules. IV. Chemical dynamics of cyanoacetylene (HCCCN; $X^1\Sigma^+$) formation from reaction of CN($X^2\Sigma^+$) with acetylene, $C_2H_2(X^1\Sigma^{g+})$”. *The Journal of Chemical Physics* 113.19 (2000), pp. 8656–8666. DOI: 10.1063/1.1289530.

[141] R. J. Balla, K. H. Casleton, J. S. Adams, and L. Pasternack. "Absolute rate constants for the reaction of cyanogen with methane, ethane, and propane from 292 to 1500 K using high-temperature photochemistry and diode laser absorption". *The Journal of Physical Chemistry* 95.22 (1991), pp. 8694–8701. DOI: 10.1021/j100175a051.

[142] G. Saidani, Y. Kalugina, A. Gardez, L. Biennier, R. Georges, and F. Lique. "High temperature reaction kinetics of CN(v = 0) with C_2H_4 and C_2H_6 and vibrational relaxation of CN(v = 1) with Ar and He". *The Journal of Chemical Physics* 138.12 (Mar. 2013). Number: 12, p. 124308. DOI: 10.1063/1.4795206.

[143] Y. Georgievskii and S. J. Klippenstein. "Strange Kinetics of the C_2H_6 + CN Reaction Explained". *The Journal of Physical Chemistry A* 111.19 (May 2007). Number: 19, pp. 3802–3811. DOI: 10.1021/jp068430k.

[144] K. L. Gannon, D. R. Glowacki, M. A. Blitz, K. J. Hughes, M. J. Pilling, and P. W. Seakins. "H Atom Yields from the Reactions of CN Radicals with C_2H_2, C_2H_4, C_3H_6, *trans*-2-C_4H_8, and iso-C_4H_8". *The Journal of Physical Chemistry A* 111.29 (July 2007). Publisher: American Chemical Society, pp. 6679–6692. DOI: 10.1021/jp0689520.

[145] A. Fahr and A. H. Laufer. "The 1,1-elimination of hydrogen cyanide and formation of triplet vinylidene from the photolysis of acrylonitrile". *The Journal of Physical Chemistry* 96.11 (1992), pp. 4217–4219. DOI: 10.1021/j100190a022.

[146] S. W. North and G. E. Hall. "The radical photodissociation channel of acrylonitrile". *Chemical Physics Letters* 263.1 (1996), pp. 148–153. DOI: https://doi.org/10.1016/S0009-2614(96)01191-8.

[147] C. A. Bird and D. Donaldson. "Photodissociation of acrylonitrile at 193 nm: the CN-producing channel". *Chemical Physics Letters* 249.1 (1996), pp. 40–45. DOI: https://doi.org/10.1016/0009-2614(95)01336-9.

[148] A. Derecskei-Kovacs and S. W. North. "The unimolecular dissociation of vinylcyanide: A theoretical investigation of a complex multichannel reaction". *The Journal of Chemical Physics* 110.6 (1999), pp. 2862–2871. DOI: 10.1063/1.477929.

[149] J. A. Russell, I. A. McLaren, W. M. Jackson, and J. B. Halpern. "Photolysis of cyanogen bromide between 193 and 266 nm". *The Journal of Physical Chemistry* 91.12 (1987), pp. 3248–3253. DOI: 10.1021/j100296a029.

[150] R. Lu, J. Halpern, and W. Jackson. “Photodissociation of C_2N_2, chlorine cyanide (ClCN), and bromine cyanide (BrCN) in a pulsed molecular beam”. *The Journal of Physical Chemistry* 88.16 (1984), pp. 3419–3425.

[151] J. B. Halpern and W. M. Jackson. “Partitioning of excess energy in the photolysis of cyanogen chloride and cyanogen bromide at 193 nm”. *The Journal of Physical Chemistry* 86.18 (1982), pp. 3528–3533. DOI: 10.1021/j100215a009.

[152] G. A. Bethardy, F. J. Northrup, and R. G. Macdonald. “The initial vibrational state distribution of HCN $\tilde{X}^1\Sigma^+$(v1,0,v3) from the reaction $CN(^2\Sigma^+)+C_2H_6 \rightarrow HCN+C_2H_5$”. *The Journal of Chemical Physics* 102.20 (1995), pp. 7966–7982. DOI: 10.1063/1.468995.

[153] S. Morales. “Le hacheur aérodynamique : un nouvel instrument dédié aux processus réactionnels à ultra-basse température”. PhD thesis. Université de Rennes 1, 2009.

[154] G. Langston and B. Turner. “Detection of^{13}C Isotopomers of the Molecule HC_7N”. *The Astrophysical Journal* 658.1 (Mar. 2007), pp. 455–461. DOI: 10.1086/511332.

[155] C. Walsh, R. A. Loomis, K. I. Öberg, M. Kama, M. L. R. van ’t Hoff, T. J. Millar, Y. Aikawa, E. Herbst, S. L. W. Weaver, and H. Nomura. “FIRST DETECTION OF GAS-PHASE METHANOL IN A PROTOPLANETARY DISK”. *The Astrophysical Journal* 823.1 (May 2016), p. L10. DOI: 10.3847/2041-8205/823/1/l10.

[156] R. A. Loomis, C. N. Shingledecker, G. Langston, B. A. McGuire, N. M. Dollhopf, A. M. Burkhardt, et al. “Non-detection of HC11N towards TMC-1: constraining the chemistry of large carbon-chain molecules”. *Monthly Notices of the Royal Astronomical Society* 463.4 (Sept. 2016), pp. 4175–4183. DOI: 10.1093/mnras/stw2302.

Appendices

.1 Résumé substanciel en français

L'avènement de la radio-astronomie dans les années 70 et son utilisation qui continue aujourd'hui, ont montré que, contrairement à ce que l'on pouvait penser au premier abord, la chimie dans l'espace est très riche. Plus de 200 molécules ont été découvertes dans des environnements variés. Cette richesse a vu la naissance de son propre domaine de recherche: l' astrochimie, à la croisée de la chimie, de l'astronomie et de la physique. L'astro-chimie est un domaine interdisciplinaire qui progresse sur plusieurs fronts reposant les uns sur les autres. Les observations astronomiques permettent d'identifier les molécules et les conditions dans lequelles elles sont formées en observant la lumière qui nous parvient de ces environments lointains. La modélisation a pour but de comprendre les observations en simulant les phénomènes qui se produisent dans les conditions observées; l'objectif étant de faire correspondre les résultats de la simulation avec les observations en introduisant des paramètres physico-chimiques. Les expériences de laboratoire ont alors pour but de décortiquer le problème en phénomènes élementaires et de déterminer expérimentalement les paramètres introduits dans les modèles dans les conditions observées. Une catégorie de paramètres nécessaires pour améliorer la présion des modèles est directement reliée à la chimie qui prend place dans les différents environnements dans lesquels les molécules sont observées. La cinétique des réactions à basse température, en particulier celle des réactions qui forment et transforment les molécules qui sont détectées, est en grande partie toujours inconnue et difficile à prédire de façon théorique et pour cela des mesures en laboratoire sont donc nécessaires.

Ce manque de données a poussé la recherche sur la détermination des coefficients de vitesse de réaction pour des réactions élémentaires à basse température pendant les dernières décennies. La plupart des réactions voit

leur coefficient de vitesse devenir négligeable à basse température dû à la présence de barrières d'énergie le long de leur surface d'énergie potentielle. Mais certaines réactions, dont un grand nombre faisant intervenir des radicaux, ne possèdent pas de barrière le long de leur canal de moindre énergie et voient donc leur taux augmenter à basse température. Ces réactions sans barrière restent efficaces ou deviennent même plus rapides lorsque la température diminue et ce jusqu'aux basses températures recontrées dans les atmosphères extraterrestres comme celle de Titan (70-150 K) ou celles des nuages interstellaires (10-100 K). De grandes campagnes de mesure ont été menées et ont enrichi notre connaissance sur le taux de réaction à basse température pour les réactions qui sont présumées participer à la chimie du milieu interstellaire. Mais ces mesures ne sont pas suffisantes pour comprendre entièrement les mécanismes de physico-chimie menant à la richesse des ces milieux. Une seconde catégorie de paramètres doit être étudiée afin d'améliorer la précision des modèles. En effet, il est important de connaître les produits formés par les réactions chimiques dans ces environnements et dans le cas de réaction à plusieurs canaux, il est essentiel de connaître les rapports de branchements entre chacun de ces canaux pour comprendre l'impact d'une réaction sur le milieu interstellaire.

La mesure de ces rapports de branchement à basse température reste à ce jour un problème complexe. De nombreuses techniques expérimentales présentent des possibilités prometeuses. La LIF (Laser Induced Fluorescence) qui possède l'avantage d'une excellente sensibilité et qui a montré son potentiel pour la détermination de constantes de vitesse de réaction à basse température depuis plusieurs décennies, est en revanche limitée par les difficultés liées à la comparaison quantitative de différents signaux moléculaire nécessaires à la mesure de rapport de branchement. La spectrométrie de masse qui a l'avantage d'être une technique de détection universelle a été employée pour la détermination de rapport de branchement

à température ambiante, mais les difficultés techniques liées aux mesures à basse température et à l'identification de différents isomères sont encore un frein à son utilisation routinière pour la mesure de rapport de branchement. Les techniques d'absorption infrarouge CRDS (cavity ring down spectroscopy) et peigne de fréquence possède l'avantage d'utiliser l'absorption directe, qui rend la mesure de concentration absolue possible et donc simplifie la détermination de rapport de branchement. Elles bénéficient aussi d'une large gamme spectrale et de très bonne sensibilité due au couplage avec une cavité. Plusieurs instruments sont en court de développement ou ont déjà montré d'intéressants résultats pour leurs applications à la cinétique de réaction à basse température. La spectroscopie rotationelle présente des possibilités prometeuses aussi notamment grâce au développement de la spectroscopie large bande à onde "chirpée" CP-FTMW (chirped pulse Fourier transforme microwave spectroscopy). La spectroscopie roatationelle est une technique quasi universelle qui nécessite un moment dipolaire non nul chez la molécule, et qui permet l'identification précise des molécules y compris de différents isomères. Récemment, cette technique a été couplée à un réacteur CRESU (cinétique de réaction en écoulement supersonique uniforme) permettant la génération de jet supersonique à basse température aux caractéristiques propices à l'étude de la cinétique de réaction. La technique résultante CPUF (chirped pulse in uniform flow) a pu démontrer que la détection de produit de réaction à basse température dans des conditions propices à la mesure de rapport de branchement est possible. C'est cette technique qui a été choisie pour le project CRESUCHIRP dans lequel cette thèse intervient, avec pour objectif la construction d'un nouvel instrument CPUF au niveau de l'état de l'art des deux techniques dont il est composé ainsi que son utilisation pour la mesure de rapport de branchement à basse température pour des réactions d'intérêt astronomique.

Cette thèse présente dans son chapitre deux, le développement et la construction de l'instrument de CPUF de l'Institut de Physique de Rennes (IPR). Le design du nouveau réacteur CRESU est détaillé ainsi que les innovations liées à son couplage au nouveau spectromètre à onde "chirpé" en bande E (60-90 GHz). De nombreuses procédures expérimentales et de traitement des données ont été developpées autour de cette nouvelle technique dans le but d'optimiser la prise de mesure et de palier aux différentes limites rencontrées au court du développement. Ce travail présente ces procédures et leur intérêt pour différentes applications: amélioration de la sensibilité, réjection du bruit et optimisation du cycle de fonctionement. Des exemples concrets de situations rencontrées au court du développement de l'instrument illustrent l'intérêt de ces procédures.

Le chapitre trois présente les capacités du nouveau spectromètre en bande E, au travers de la mesure de l'élargissement spéctrale de la molécule OCS avec l'hélium à température ambiante. Cette étude fournit de nouvelles données expérimentales sur ce système et est utilisée pour valider les outils développés pour l'analyse des données moléculaires en comparant les résultats avec des données de la littérature. Cette étude sert aussi d'illustration des performances du spectromètre dans les conditions du réacteur CRESU.

Le chapitre quatre présente l'application de ces développements à plusieurs systèmes à basse température au travers de la technique CPUF. Tout d'abord, la photodissociation de l'acrylonitrile à 193 nm est utilisé pour présenter les caratéristiques large bande de l'instrument ainsi que son potentiel pour l'observation de l'évolution de différents produits et de leur distribution ro-vibrationelle à basse température. La détection des produits de la photodissociation HCN HNC et HC_3N est présentée à différentes températures pour leurs états vibrationels fondamentaux et certains états vibrationellement excités. L'évolution de la relaxation ro-vibrationelle des

produits est présentée et discutée, éclairant sur les difficultés de l'étude de produit de photodissociation. La production à basse température des isomères HCN et HNC au travers de cette photodissociation permet une étude originale sur la mesure des différences de section efficace de collision entre les isomères et l' hélium à différentes températures. Cette étude est comparée aux résultats de calcul théorique des membres du département de physique moléculaire de l'IPR. Les résultats de cette étude originale sont rendus possibles par le développement de ce nouvel instrument et leurs impacts sur les observations astronomiques sont discutés. Cette étude présente la versatilité de l'instrument développé et son potentiel qui va au-delà de l'objectif original de la mesure de rapport de branchement à basse température.

L'étude de deux systèmes réactionels à basse température est presentée : la réaction entre le radical CN et l'acétylène qui forme le produit HC_3N à 30 K ainsi que la réaction entre le radical CN et l'éthane qui forme le produit HCN à 10 K. La détection des deux produits ainsi que l'évolution de leur signal au cours de la cinétique de la réaction sont présentées et discutées. Une tentative de calibration du signal réactionel est expliquée et présentée dans le but d'établir une limite de sensibilité de l'instrument. L'étude de ces résultats et leur discussion détaillent les avantages et les limitations de l'instrument. Une discussion sur la complexité de l'étude des produits comparés aux réactifs ainsi que les dificultés liées à la comparaison quantitative de différents produits concluent sur le potentiel de l'instrument.

En conclusion, plusieurs pistes d'améliorations sont proposées pour circonvenir aux limitations actuelles de l'instrument. De futurs améliorations techniques sont développées avec des résultats préliminaires ainsi qu'une discussion sur la procédure de détermination d'un rapport de branchement à partir des données du spectromètre.

Enfin, cette thèse s'inscrit dans un projet qui va au-delà du travail présenté ici. L'ensemble des résultats du projet est retranscrit dans trois thèses interconnectées. Celle-ci, la thèse de Omar Abdelkader Khedaoui qui présente le deuxième spectromètre développé dans le cadre du projet ainsi que les améliorations techniques décrites en conclusion de ce travail et l'autre, la thèse de Divita Gupta qui présente l'application de l'ensemble des développements techniques sur un système réactionnel à plusieurs canaux.

.2 Pitot profile of the nozzle used

.2.1 Ar 30 K

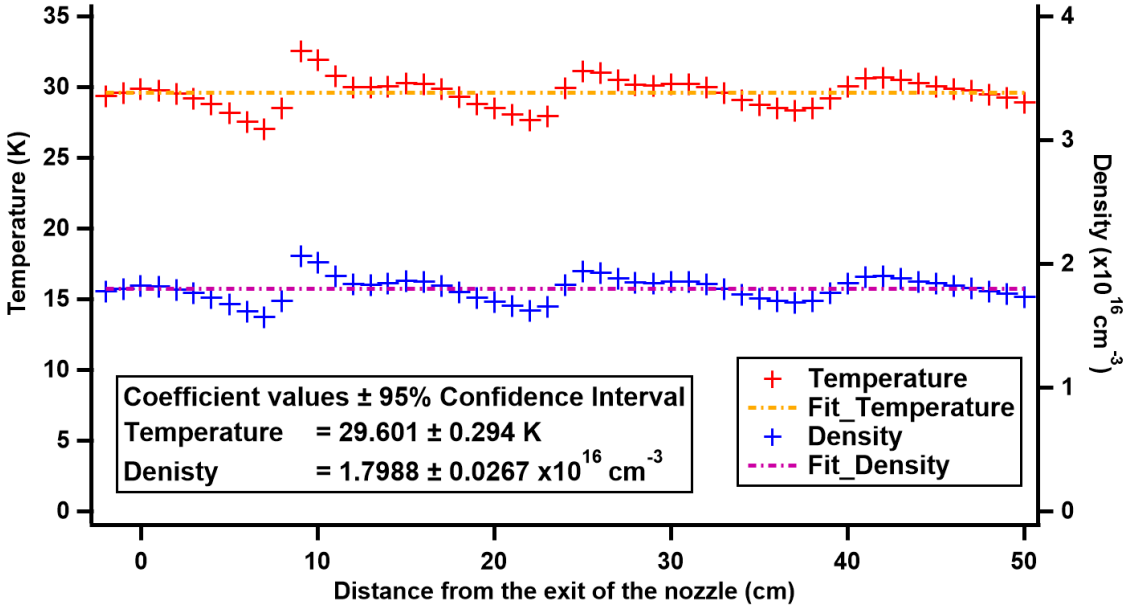

Figure 2: 1-D Pitot measurement of the Ar 30 K nozzle

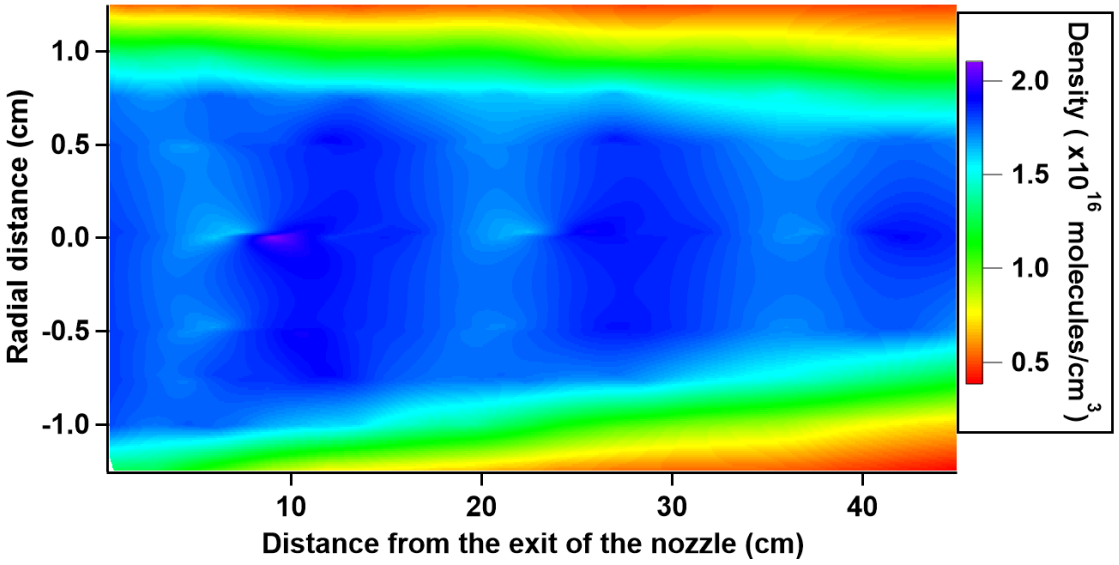

Figure 3: 2-D Pitot measurement of the Ar 30 K nozzle

.2.2 He 10 K

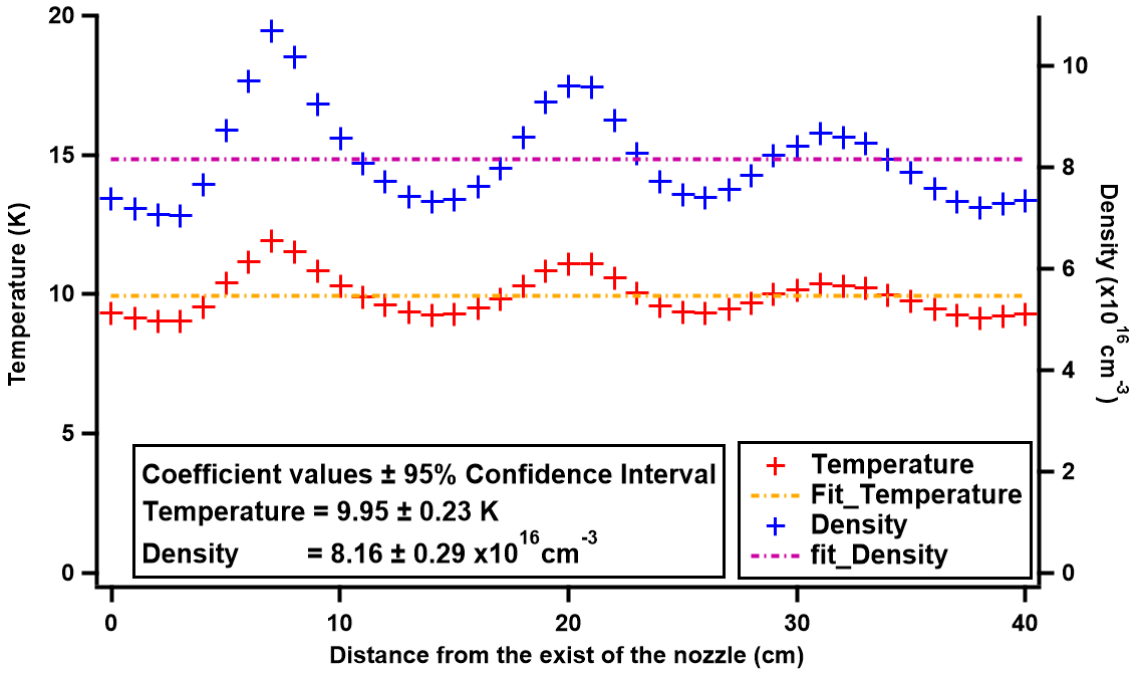

Figure 4: 1-D Pitot measurement of the He 10 K nozzle

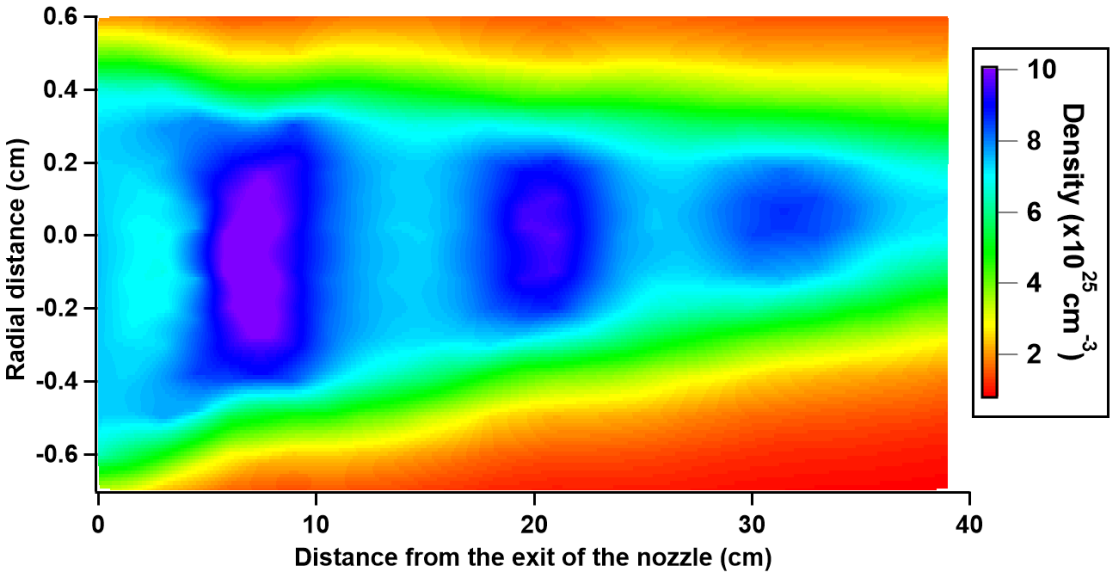

Figure 5: 2-D Pitot measurement of the He 10 K nozzle

.2.3 He 16 K

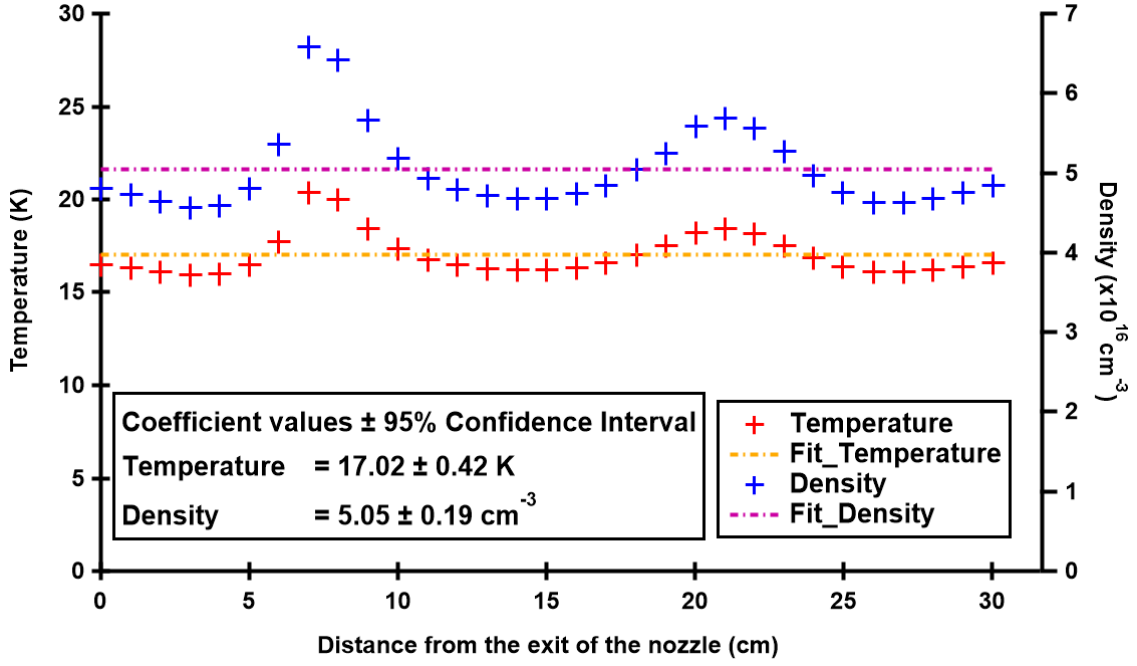

Figure 6: 1-D Pitot measurement of the He 16 K nozzle

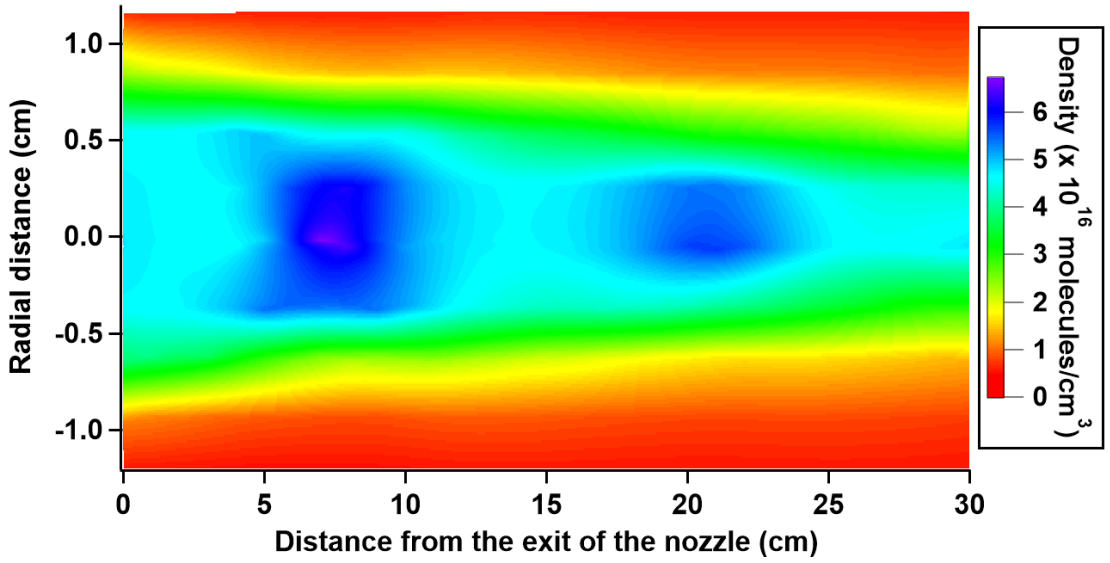

Figure 7: 2-D Pitot measurement of the He 16 K nozzle

.2.4 He 19 K

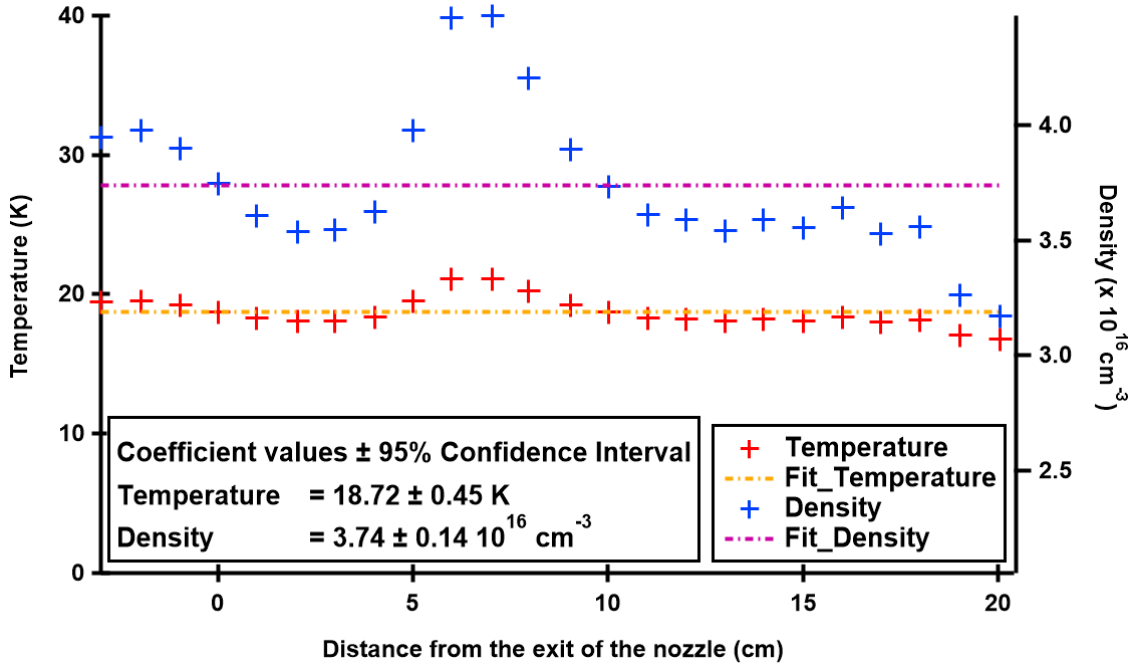

Figure 8: 1-D Pitot measurement of the He 19 K nozzle

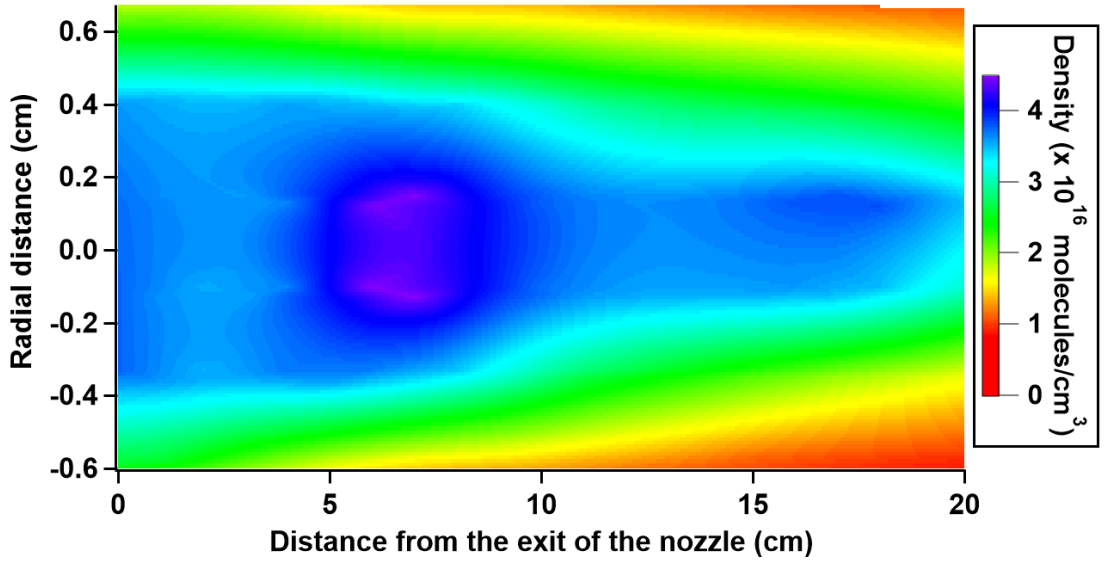

Figure 9: 2-D Pitot measurement of the He 19 K nozzle

.2.5 He 30 K

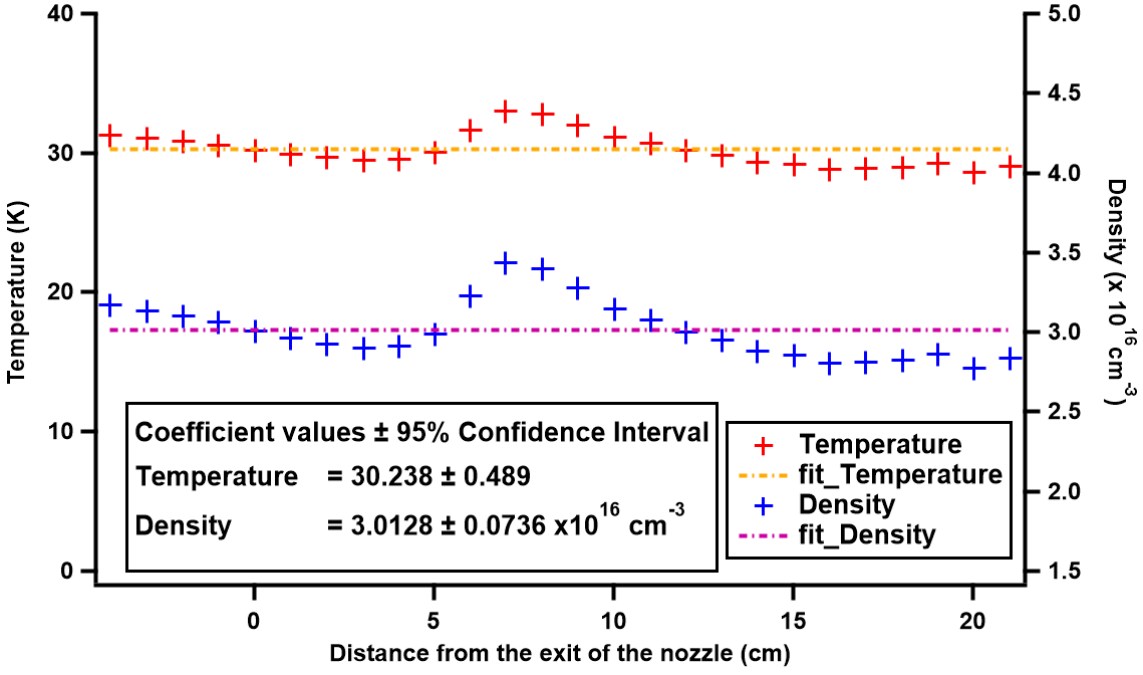

Figure 10: 1-D Pitot measurement of the He 30 K nozzle

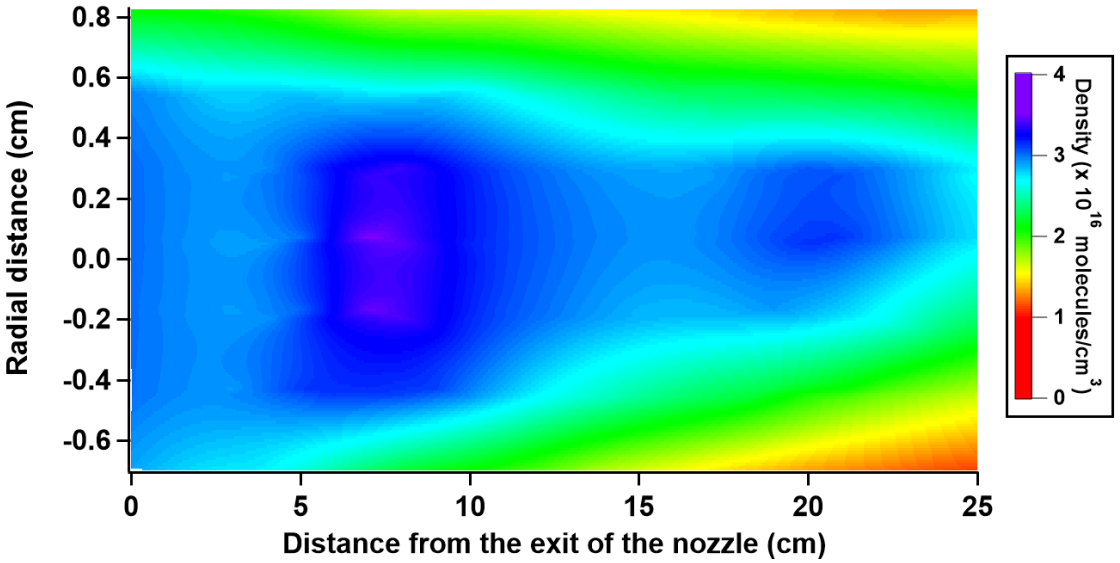

Figure 11: 2-D Pitot measurement of the He 30 K nozzle

.3 Analysis program on Igor Pro (version 8, Wavemetrics)

.3.1 Pattern filter

This code is use to apply the pattern filter presented in section 2.9

```
function patternfilter(inputwave,patternsize,startpattern,
switchoffset,outputtargetwave)
// called in other analysis functions

//  outputtargetwave: 1=output with "_TLF" added, other
//values output the same as input
//      startpattern : starting point of the pattern for
//the patternfilter
//      switchoffset : ending point of the pattern for the
//patternfilter (If the switch closein the next
//frame then put swtichofset=sizeofframe-1)
//      patternisize : size in sample of the pattern
//for the patternfilter

wave inputwave
```

```
variable patternsize,switchoffset,startpattern,outputtargetwave
wave TLFwave
variable i,j,numpatavg,numpatinframe,remains

numpatavg=floor((switchoffset-startpattern)/patternsize)
numpatinframe=floor(switchoffset/patternsize)
remains=switchoffset-(numpatinframe*patternsize)
Make/N=(switchoffset)/D patternframe
Make/N=(patternsize)/D pattern
duplicate /o inputwave,TLFwave

//FIR adjusting depending on the transition

        //FilterFIR/LO={0.43763,0.45,101}/HI={0.01405,0.0198,
        ///NMF={0.5,0.05,9.09495e-13,2}TLFwave       //HCN
        FilterFIR/HI={0.01405,0.0198,101}TLFwave      //HNC


//making the pattern wave

        pattern=0
        for (i=1; i<numpatavg; i+=1)
                for (j=0; j<patternsize; j+=1)
                        pattern[patternsize-1-j]=
                        pattern[patternsize-1-j]+
                        TLFwave[switchoffset-
                        patternsize*i-j-1]
                endfor
        endfor

        pattern=pattern/numpatavg
        patternframe=0

//making a wave the size of the frame with the pattern
```

```
        for (i=numpatinframe; i>0; i-=1)
                if(i>0)
                        for (j=0; j<patternsize; j+=1)
                                patternframe[i*patternsize+
                                remains-1-j]=pattern
                                [patternsize-1-j]
                        endfor
                else
                        for (j=0; j<remains; j+=1)
                                patternframe[remains-1-j]=
                                pattern[patternsize-j]
                        endfor
                endif
        endfor

        Redimension/N=(numpnts(inputwave)) patternframe
        for (i=(switchoffset); i<numpnts(inputwave); i+=1)
        patternframe[i]=0
        endfor

//subtracting the pattern

        TLFwave=TLFwave-patternframe

//control for the output wave name
        //change, 1=output the targetwave as "targetwave"_TLF
        //other values output as the same as the input
        string s1, s2
        s1=NameofWave(inputwave)
        if(outputtargetwave==1)
                s2=s1+"_TLF"
                Duplicate/O TLFwave $s2
        else
                inputwave=TLFwave
        endif
```

```
killwaves pattern,patternframe,TLFwave

end
```

.3.2 Segmented averaging and analysis using "scheme"

This is the most used version of the function used to analyse raw data outputted by the digitizer. An example of it does on the data is presented in section 2.9. It is used for laser induced product.

```
function cutavgfilpieceLaser(rawData,sizeofframe,sampleskip,
numoframetot,numofcut,BGendframe,A,B,startpattern,
switchoffset,patternsize)
//this function as for goal to extract the information from
//a raw scan of the acquisition card. It does background
//subtract and thus should be use to analyse laser scans


//      parameters description:
//              UD= userdefined can be adjust to adjust
//the result of the analysis
//              SD= scandefined is set by the parameter
//of the scan (in the summary file)

//      rawData = SD: name of the wave in igor
//      sizeofframe = SD: size in sample of the frame
//use, depend on the sampleskip factor and the
//file loaded in th AWG can be calculated =2000000/numoframe
//      sampleskip =SD: sampleskip factor used in the scan
// numoframetot = SD: total number of frame in the scan
//      numofcut = UD: number of cut for horizontal averaging
//numofcut=numoframe/horizontal_averaging
//      BGendframe = UD: number of frame to use to generate
//the background
//      A = UD: starting point of the FFT
//      B = UD: ending point of the FFT
```

```
//        startpattern = UD: starting point of the pattern
//for the patternfilter
//        switchoffset = UD: ending point of the pattern
//for the patternfilter
//        patternisize = UD: size in sample of the pattern
//for the patternfilter for E band spectrometer it
//should be at least 800point at 10GS/s to get good rejection

        // some general example !


// example for sample skip 2/ 2.5 micro s frame laser fire
//at the 87 frame horizontal averaging every 4 frames
//        cutavgfilpieceLaser(run1,12500,2,160,40,80,3550,
//8000,8000,12400,800)

// example for sample skip 4/ 2.5 micro s frame laser
//fire at the 87 frame horizontal averaging every 4 frames
//        cutavgfilpieceLaser(run1,6250,4,320,70,80,1740,
//4000,4000,6200,800)

// example for sample skip 8/ 2.5 micro s frame laser
//fire at the 87 frame horizontal averaging every 4 frames
//        cutavgfilpieceLaser(run1,3125,8,640,140,80,870,
//2000,2000,3100,800)

// example for sample skip 2/ 10 micro s frame laser
//fire at the 7 frame no horizontal averaging
//        cutavgfilpieceLaserx(run1,50000,2,40,34,6,12000,
//35000,35000,49500,800)

// example for sample skip 4/ 10 micro s frame laser
//fire at the 7 frame no horizontal averaging
//        cutavgfilpieceLaser(run1,25000,4,80,74,6,6000,
//18000,18000,24900,800)
```

```
// example for sample skip 8/ 10 micro s frame laser
//fire at the 7 frame no horizontal averaging
//       cutavgfilpieceLaser(run1,12500,8,160,154,6,3000,
//8000,8000,12400,800)


wave rawdata
variable sizeofframe,sampleskip,numoframetot,numofcut,
BGendframe,A,B,switchoffset,startpattern,patternsize
string outputwave,outputFFT,outputfreq
wave rawdatasig,rawdataBG
variable N,i,j,k,numpatavg,numpatinframe,remains,
numframeincut,remains2,avg,BGcut,numofsigframe

avg=100000
//calculation on horizontal averaging
numofsigframe=numoframetot-BGendframe
numframeincut=floor(numofsigframe/numofcut)
remains2=numofsigframe-(numframeincut*numofcut)


Make/N=(sizeofframe)/D tempw
Make/N=(sizeofframe)/D w,wBG
duplicate rawdata,rawdatasig
duplicate rawdata,rawdataBG
rawdatasig=rawdatasig/avg
rawdataBG=rawdataBG/avg
//prepargin for BG substraction
BGcut=sizeofframe*BGendframe

deletepoints 0,BGcut,rawdatasig
deletepoints BGcut,2000000-BGcut,rawdataBG

//creating BG frame
```

```
w=0
tempw=0
for (i=0; i<(BGendframe); i+=1)
                    for (j=0; j<sizeofframe; j+=1)
                                        tempw[j]=rawdataBG[j+i*
                                        sizeofframe+k*numframeincut
                                        *sizeofframe]
                                endfor
                    w=w+tempw
                    endfor
w=w/BGendframe
//Filtering BGframe
wBG=w
patternfilter(wBG, patternsize , startpattern , switchoffset ,0)

////cutting and filtering the time domain data according

for(k=0; k<(numofcut); k+=1)
          w=0
          tempw=0
          if(k==numofcut-1)
                    for (i=0; i<(numframeincut+remains2); i+=1)
                    for (j=0; j<sizeofframe; j+=1)
                                        tempw[j]=rawdatasig[j+i*
                                        sizeofframe+k*numframeincut
                                        *sizeofframe]
                                endfor
                    w=w+tempw
                    endfor
          w=w/(numframeincut+remains2)
          else
                    for (i=0; i<(numframeincut); i+=1)
                    for (j=0; j<sizeofframe; j+=1)
                                        tempw[j]=rawdatasig[j+i*
                                        sizeofframe+k*numframeincut*
```

```
                                        sizeofframe]
                                endfor
                        w=w+tempw
                        endfor
                w=w/numframeincut
                endif
//Filtering signalframe

                patternfilter(w,patternsize,startpattern,switchoffset,0)
                w=w-wBG
//naming the cut
                outputwave=nameofwave(rawdata)+"avgandfilcut"+num2str(k+1)
                duplicate/O w,$outputwave

                if (k==0)                                               //display
                        display $outputwave
                else
                appendtograph $outputwave
                endif
                setcolor()//automatic assignement of color

endfor

//FFT
for(k=0; k<(numofcut); k+=1)
                outputwave=nameofwave(rawdata)+"avgandfilcut"
                +num2str(k+1)
outputFFT=outputwave+"_FFT"
outputfreq=outputwave+"_FFTfreq"
FixedFFT($outputwave,10/sampleskip,A,B,""// FFT function
//with real frequencies
if (k==0)                                                               //display
        display $outputFFT vs $outputfreq
        else
        appendtograph  $outputFFT vs $outputfreq
```

```
        endif
setcolor()//automatic assignement of color
endfor

//deleting temporary waves
killwaves w,tempw,rawdatasig,wBG,rawdataBG
end
```

An other version of the same function used for non laser induced signal, which can not be background subtracted.

```
function cutavgfilpiecenoBG(rawData,sizeofframe,sampleskip
,numofframe,numofcut,A,B,startpattern,switchoffset,patternsize)
//this function as for goal to exctract the information
//from a raw scan of the aqcuisition card it doesnt do any
//background substraction. ex use to look at a non
//laser generated product like VCN


//      parameters description:
//              UD= userdefined can be adjust to adjust
//the result of the analysis
//              SD= scandefined is set by the parameter
//of the scan (in the sumary file)

//      rawData = SD: name of the wave in igor
//      sizeofframe = SD: size in sample of the frame
//use, depend on the sampleskip factor and the
//file loaded in th AWG can be calculated =2000000/numoframe
//      sampleskip =SD: sampleskip factor used in the scan
// numofframe = SD: total number of frame in the scan
//      numofcut = UD: number of cut for horizontal averaging
//numofcut=numofframe/horizontal_averaging
//      A = UD: starting point of the FFT
//      B = UD: ending point of the FFT
//      startpattern = UD: starting point of the pattern
```

```
//for the patternfilter
//        switchoffset = UD: ending point of the pattern
//for the patternfilter
//        patternisize = UD: size in sample of the pattern
for the patternfilter for E band spectrometer
should be at least 800point at 10GS/s to get good rejection


// example for sample skip 2/ 2.5 micro s all frame average
//        cutavgfilpiecenoBG(run1,12500,2,160,1,3550,
//8000,8000,12400,800)

// example for sample skip 4/ 2.5 micro s all frame average
//        cutavgfilpiecenoBG(run1,6250,4,320,1,1740,
//4000,4000,6200,800)

// example for sample skip 8/ 2.5 micro s all frame average
//        cutavgfilpiecenoBG(run1,3125,8,640,1,870,
//2000,2000,3100,800)

// example for sample skip 2/ 10 micro s all frame average
//        cutavgfilpiecenoBG(run1,50000,2,40,1,12000,
//35000,35000,49500,800)

// example for sample skip 4/ 10 micro s all frame average
//        cutavgfilpiecenoBG(run1,25000,4,80,1,6000,
//18000,18000,24900,800)

// example for sample skip 8/ 10 micro s all frame average
//        cutavgfilpiecenoBG(run1,12500,8,160,1,3000,
//8000,8000,12400,800)
```

```
wave rawdata
variable sizeofframe,sampleskip,numofframe,numofcut
//,A,B,startpattern,switchoffset,patternsize
string outputwave,outputFFT,outputfreq
wave rawdatatemp
variable N,i,j,k,numpatavg,chirpend,numpatinframe,
//remains,numframeincut,remains2,avg

avg=100000

//calculation on horizontal averaging
numframeincut=floor(numofframe/numofcut)
remains2=numofframe-(numframeincut*numofcut)


Make/N=(sizeofframe)/D tempw
Make/N=(sizeofframe)/D w
duplicate rawdata,rawdatatemp
rawdatatemp=rawdatatemp/avg

//cuting and filtering the time domain data according

for(k=0; k<(numofcut); k+=1)
        w=0
        tempw=0
        if(k==numofcut-1)
                for (i=0; i<(numframeincut+remains2); i+=1)
                for (j=0; j<sizeofframe; j+=1)
                                tempw[j]=rawdatatemp[j+i*
                                sizeofframe+k*numframeincut*
                                sizeofframe]
                        endfor
                w=w+tempw
                endfor
        w=w/(numframeincut+remains2)
```

```
        else
                for (i=0; i<(numframeincut); i+=1)
                for (j=0; j<sizeofframe; j+=1)
                                tempw[j]=rawdatatemp[j+i*
                                sizeofframe+k*numframeincut*
                                sizeofframe]
                        endfor
                w=w+tempw
                endfor
        w=w/numframeincut
        endif

        //filtering using pattern filter
        patternfilter(w,patternsize,startpattern,switchoffset,0)
        //Sometime a second run on specificly the 5GHz
        //clock clean it more
        patternfilter(w,4,startpattern,switchoffset,0)

        //naming the cut
        outputwave=nameofwave(rawdata)+"avgandfilcut"+num2str(k+1)
        duplicate/O w,$outputwave

        if (k==0)
                display $outputwave
        else
        appendtograph $outputwave
        endif
        setcolor()

endfor

//FFT

for(k=0; k<(numofcut); k+=1)
        outputwave=nameofwave(rawdata)+"avgandfilcut"+num2str(k+1)
```

```
outputFFT=outputwave+"_FFT"
outputfreq=outputwave+"_FFTfreq"
FixedFFT($outputwave,10/sampleskip,A,B,"")
if (k==0)
        display $outputFFT vs $outputfreq
        else
        appendtograph  $outputFFT vs $outputfreq
        endif
setcolor()
endfor

//deleting temporary waves
killwaves w,tempw,rawdatatemp

end
```

The last version of the same function which correct for potential phase variation in the train of pulse.

```
function cutavgfilpieceLaser_phase(rawData,sizeofframe,sampleskip,
numofframetot,numofcut,BGendframe,A,B,startpattern,
switchoffset,patternsize)
//this function as for goal to exctract the information from
//a raw scan of the aqcuisition card. It does background
//subtract and thus should be use to analyse laser scans
//it also correct for a potential phase shift between
//the frames and could improve the look of the data.
//with the new aquisition card it doesnt seems to be a
//big problem. Should probably be use only to provide paper results
//does not use FixedFFT, instead does FFT within the function
//has two options for choosing the theta for the phase shift


//      parameters description:
//              UD= userdefined can be adjust to adjus
//t the result of the analysis
//              SD= scandefined is set by the parameter
```

```
//of the scan (in the sumary file)

//       rawData = SD: name of the wave in igor
//       sizeofframe = SD: size in sample of the frame
//use, depend on the sampleskip factor and the
//file loaded in the AWG can be calculated =2000000/numoframe
//       sampleskip =SD: sampleskip factor used in the scan
// numoframetot = SD: total number of frame in the scan
//       numofcut = UD: number of cut for horizontal averaging
//numofcut=numofframe/horizontal_averaging
//       BGendframe = UD: number of frame to use to generate
//the background
//       A = UD: starting point of the FFT
//       B = UD: ending point of the FFT
//       startpattern = UD: starting point of the pattern
//for the patternfilter
//       switchoffset = UD: ending point of the pattern
for the patternfilter
//       patternisize = UD: size in sample of the pattern
//for the patternfilter for E band spectrometer
//should be at least 800point at 10GS/s to get good rejection

// some general example ! A and B could need to be adjusted


// example for sample skip 2/ 2.5 micro s frame laser
//fire at the 87 frame horizontal averaging every 4 frames
//       cutavgfilpieceLaser_phase(run1,12500,2,160,40,80,
//3550,8000,8000,12400,800)

// example for sample skip 4/ 2.5 micro s frame laser fire
//at the 87 frame horizontal averaging every 4 frames
//       cutavgfilpieceLaser_phase(run1,6250,4,320,70,80,
//1740,4000,4000,6200,800)
```

```
// example for sample skip 8/ 2.5 micro s frame laser fire
//at the 87 frame horizontal averaging every 4 frames
//       cutavgfilpieceLaser_phase(run1,3125,8,640,140,80,
//870,2000,2000,3100,800)

// example for sample skip 2/ 10 micro s frame laser fire
//at the 7 frame no horizontal averaging
//       cutavgfilpieceLaser_phase(run1,50000,2,40,34,
//6,12000,35000,35000,49500,800)

// example for sample skip 4/ 10 micro s frame laser fire
//at the 7 frame no horizontal averaging
//       cutavgfilpieceLaser_phase(run1,25000,4,80,74,6,
//6000,18000,18000,24900,800)

// example for sample skip 8/ 10 micros frame laser fire
//at the 7 frame no horizontal averaging
//       cutavgfilpieceLaser_phase(run1,12500,8,160,154,
//6,3000,8000,8000,12400,800)


wave rawdata
variable sizeofframe,sampleskip,numoframetot,numofcut
//,BGendframe,A,B,switchoffset,startpattern,patternsize
string outputwave,outputFFT,outputfreq
wave rawdatasig,rawdataBG
variable N,i,j,k,numpatavg,numpatinframe,remains,
//numframeincut,remains2,avg,BGcut,numofsigframe

avg=100000
numofsigframe=numoframetot-BGendframe
numframeincut=floor(numofsigframe/numofcut)
remains2=numofsigframe-(numframeincut*numofcut)
```

```
Make/N=(sizeofframe)/D tempw
Make/N=(sizeofframe)/D w,wBG, wsig
duplicate rawdata ,rawdatasig
duplicate rawdata ,rawdataBG
rawdatasig=rawdatasig/avg
rawdataBG=rawdataBG/avg

BGcut=sizeofframe*BGendframe

deletepoints 0,BGcut,rawdatasig
deletepoints BGcut,2000000-BGcut,rawdataBG


//cutting BG frames

w=0

for (i=0; i<(BGendframe); i+=1)

                string outputBG=nameofwave(rawdata)+
                "BGcut"+num2str(i+1)
                make/n=(sizeofframe) $outputBG
                wave outBG=$outputBG

        outBG=0
        for (j=0; j<sizeofframe; j+=1)
                        outBG[j]=rawdataBG[j+i*
                        sizeofframe+k*numframeincut*
                        sizeofframe]
                endfor

                wave outBG=$outputBG
```

```
//take phase from first BG

        if (i==0)

                make/n=(sizeofframe/2+1)/d w0BG_FFTX


                patternfilter(outBG,patternsize,startpattern,switchof

                FixedFFT_select(outBG,0,sizeofframe-1,"w0BG_FFTX",3)

                //display w0BG_FFTX

                Extract/INDX w0BG_FFTX, ind, w0BG_FFTX==
                wavemax(w0BG_FFTX)
                //takes the index for which the magnitude
                FFT is the maximum

                make/o/n=(sizeofframe/2+1)/d BGphase

                FixedFFT_select(outBG,0,sizeofframe-1,"BGphase",5)

                variable theta_BG

                theta_BG=BGphase[ind[0]] //takes the phase
                //of the first BG cut at the index
                //where the magnitude was the maximum
                print ind[0]

                //duplicate/o outBG, BGcut1

                killwaves w0BG_FFTX, BGphase
                print theta_BG

        endif
```

```
//phaseturnFFT for all BG; this has to be done in the
//(complex FFT)frequency domain


        wave outp
        make/n=(sizeofframe/2+1) outp

        FixedFFT_select($outputBG,0,sizeofframe-1,"outp",5)

        string outputBGphase= nameofwave(rawdata)+
        "BGphasecut"+num2str(i+1)

        Duplicate/o outp, $outputBGphase

        wave/c outF
        make/c/n=(sizeofframe/2+1) outF

        FixedFFT_select($outputBG,0,sizeofframe-1,"outF",1)

        string outputBGFFT= nameofwave(rawdata)+
        "BGFFTcut"+num2str(i+1)

        Duplicate/o/c outF, $outputBGFFT

        wave g,h
        make /n=(numpnts($outputBGFFT)) g
        make /n=(numpnts($outputBGFFT)) h

        variable theta_b

        theta_b=outp[ind[0]] //takes the phase at the
        //same index (where the magnitude was found to
        //be maximum for BGcut1) for all the BG cuts
```

```
//        g =  cos(-theta_b+theta_BG)*Real(outF) +
sin(-theta_b+theta_BG)*Imag(outF)
//shifts the real part of our new phase shifted
//FFT using the difference between the phases
//for BGcut1 and every BGcut after
//        h = -sin(-theta_b+theta_BG)*Real(outF) +
cos(-theta_b+theta_BG)*Imag(outF)
//shifts the imaginary part of our new phase shifted
//FFT using the difference between the phases
//for BGcut1 and every BGcut after

        g =  cos(theta_b-theta_BG)*Real(outF) +
        sin(theta_b-theta_BG)*Imag(outF)
        //shifts the real part of our new phase shifted
        //FFT using the difference between the phases
        //for BGcut1 and every BGcut after
        h = -sin(theta_b-theta_BG)*Real(outF) +
        cos(theta_b-theta_BG)*Imag(outF)
        //shifts the imaginary part of our new phase
        //shifted FFT using the difference between the phases
        //for BGcut1 and every BGcut after

        string outputBGshift, outputBGFFTshift

        outputBGshift= nameofwave(rawdata)+
        "BGshcut"+num2str(i+1)
        outputBGFFTshift= nameofwave(rawdata)+
        "BGFFTshcut"+num2str(i+1)

        make/c/n=(numpnts($outputBGFFT)) $outputBGFFTshift
        make/n=(sizeofframe)/d $outputBGshift

        wave/c wc= $outputBGFFTshift
        wave wo= $outputBGshift
```

```
        wc= cmplx(g,h) //creates a new wave using
        //the real and imaginary parts as calculated above

        IFFT/DEST=wo wc //take Inverse FFT to get
        //the new phase shifted data in time domain
        SetScale/P x 0,1,"",wo

        killwaves g,h,outBG,outp,outF


//creating BG frame

    w=w+wo //add all the BGcuts together

    killwaves wc,wo
    killwaves/Z $outputBG, $outputBGphase,
    $outputBGshift, $outputBGFFTshift, $outputBGFFT

endfor

wBG=w/BGendframe //taking the average of the BGcuts

//Filtering BGframe

patternfilter(wBG,patternsize,startpattern,switchoffset,0)
patternfilter(wBG,4,startpattern,switchoffset,0)
patternfilter(wBG,2,startpattern,switchoffset,0)

killwaves w

//Cuting signal frames

for(k=0; k<(numofcut); k+=1)
        wsig=0
```

```
tempw=0

if(k==numofcut-1)
        for (i=0; i<(numframeincut+remains2); i+=1)
        for (j=0; j<sizeofframe; j+=1)
                        tempw[j]=rawdatasig[j+i*
                        sizeofframe+k*numframeincut*
                        sizeofframe]
                endfor
        wsig=wsig+tempw
        endfor
wsig=wsig/(numframeincut+remains2)
else
        for (i=0; i<(numframeincut); i+=1)
        for (j=0; j<sizeofframe; j+=1)
                        tempw[j]=rawdatasig[j+i*
                        sizeofframe+k*numframeincut*
                        sizeofframe]
                endfor
                wsig=wsig+tempw
endfor
wsig=wsig/numframeincut
endif

patternfilter(wsig,patternsize,startpattern,switchoffset,0)
patternfilter(wsig,4,startpattern,switchoffset,0)

wave osphase
make/n=(sizeofframe/2+1) osphase

FixedFFT_select(wsig,0,sizeofframe-1,"osphase",5)

string outputsigphase= nameofwave(rawdata)+
"phcut"+num2str(k+1)
```

```
        Duplicate/o osphase,$outputsigphase

        wave/c osigFFT
        make/c/n=(sizeofframe/2+1) osigFFT

        FixedFFT_select(wsig,0,sizeofframe-1,"osigFFT",1)

        string outputsigFFT= nameofwave(rawdata)+
        "FFTcut"+num2str(k+1)

        Duplicate/o/c osigFFT,$outputsigFFT

        wave g,h
        make /n=(numpnts($outputsigFFT)) g
        make /n=(numpnts($outputsigFFT)) h

        variable theta_sig

        theta_sig=osphase[ind[0]] //takes the phase at
        the same index (where the magnitude was found to
        //be maximum for BGcut1) for all the signal cuts

//      g = cos(theta_BG-theta_sig)*Real(osigFFT) + sin
(theta_BG-theta_sig)*Imag(osigFFT)
//shifts the real part of our new phase shifted
//FFT using the difference between the phases
//for BGcut1 and every signal cut
//      h = -sin(theta_BG-theta_sig)*Real(osigFFT) +
cos(theta_BG-theta_sig)*Imag(osigFFT)
//shifts the imaginary part of our new phase shifted
//FFT using the difference between the phases
//for BGcut1 and every signal cut

        g = cos(-theta_BG+theta_sig)*Real(osigFFT) +
        sin(-theta_BG+theta_sig)*Imag(osigFFT)
```

```
        //shifts the real part of our new phase shifted
        //FFT using the difference between the phases
        //for BGcut1 and every signal cut
        h = -sin(-theta_BG+theta_sig)*Real(osigFFT) +
        cos(-theta_BG+theta_sig)*Imag(osigFFT)
        //shifts the imaginary part of our new phase
        //shifted FFT using the difference between
        //the phases for BGcut1 and every signal cut

        string outputsigshift, outputsigFFTshift

        outputsigshift= nameofwave(rawdata)+"shcut"+num2str(k+1)
        outputsigFFTshift= nameofwave(rawdata)+"FFTshcut"+num2str(k+1

        make/c/n=(numpnts($outputsigFFT))/d $outputsigFFTshift
        make/n=(sizeofframe)/d $outputsigshift

        wave/c wcs= $outputsigFFTshift
        wave wos= $outputsigshift

        wcs = cmplx(g,h) //creates a new wave using
        //the real and imaginary parts as calculated above

        IFFT/z/DEST=wos wcs //take Inverse FFT to get
        //the new phase shifted data in time domain
        SetScale/P x 0,1,"time",wos


        killwaves g,h,osphase,osigFFT,wcs
        killwaves/Z $outputsigphase, $outputsigFFT


//Filtering signalframe
        patternfilter(wos,patternsize,startpattern,switchoffset,0)
        patternfilter(wos,4,startpattern,switchoffset,0)
```

```
        wos=wos-wBG //taking the difference between the
        //filtered and phase shifted time domain data for
        //the signal and the averaged BG which was
        //also filtered and phase shifted

        outputwave=nameofwave(rawdata)+"avgshfilcut"+num2str(k+1)

        duplicate/O wos,$outputwave

        killwaves wos

        if (k==0)                //display phase shifted
        //time domain signal cuts
        display $outputwave
        else
        appendtograph $outputwave
    endif
        setcolor()


endfor



        //does taking and displaying FFT


for(k=0; k<(numofcut); k+=1)
        outputwave=nameofwave(rawdata)+"avgshfilcut"+num2str(k+1)
        outputFFT=outputwave+"_FFT"
        outputfreq=outputwave+"_FFTfreq"
        FixedFFT($outputwave,10/sampleskip,A,B,"")

        if (k==0)
        display $outputFFT vs $outputfreq
```

```
        else
        appendtograph  $outputFFT vs $outputfreq
    endif
setcolor()
killwaves/Z $outputsigshift, $outputsigFFTshift,
$outputsigFFT, $outputsigphase
endfor

killwaves ind,w,tempw,rawdatasig,rawdataBG,wBG,wsig
end
```

.4 LabVIEW program presentation

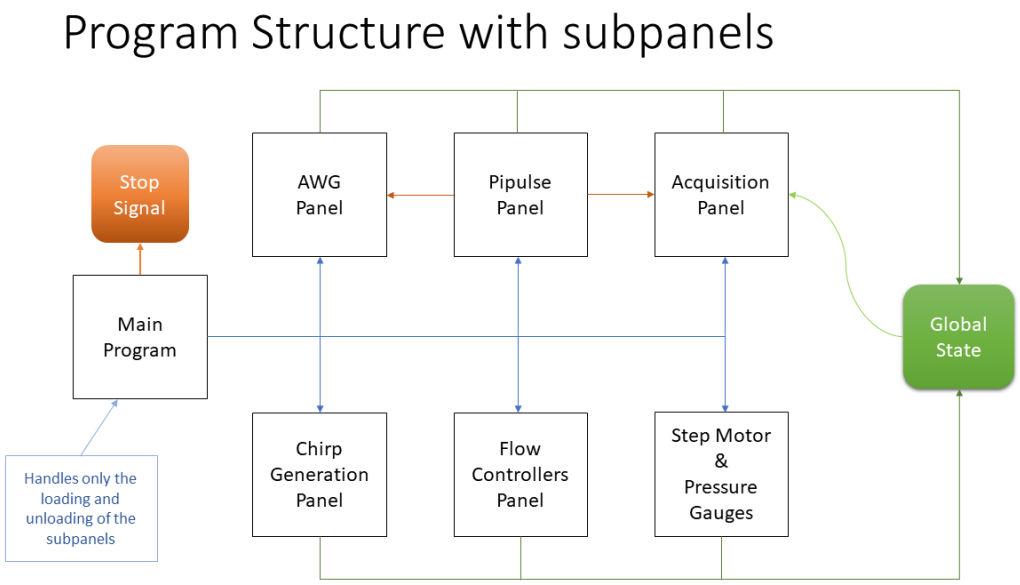

Figure 12: Presentation of the program structure with sub-panel credit: Luc Briand

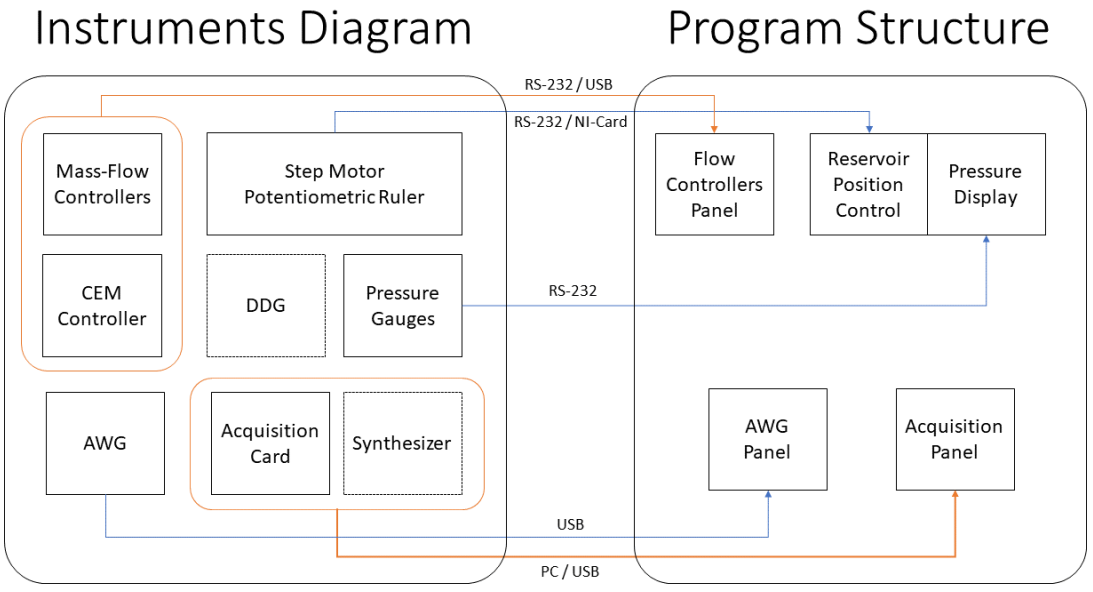

Figure 13: Presentation of the program interface with the instrument credit: Luc Briand

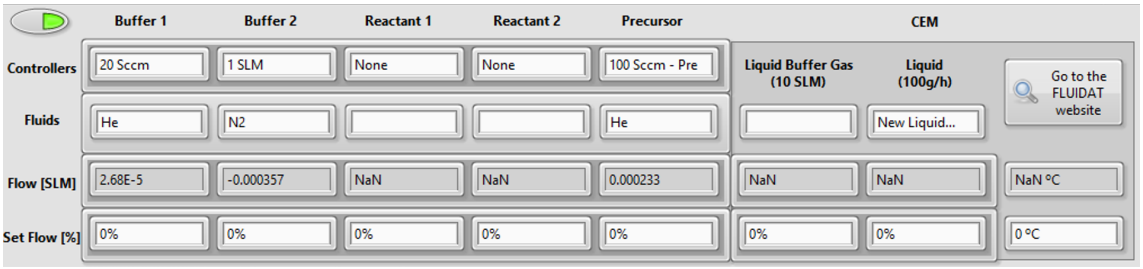

Figure 14: Presentation of the flow controller panel

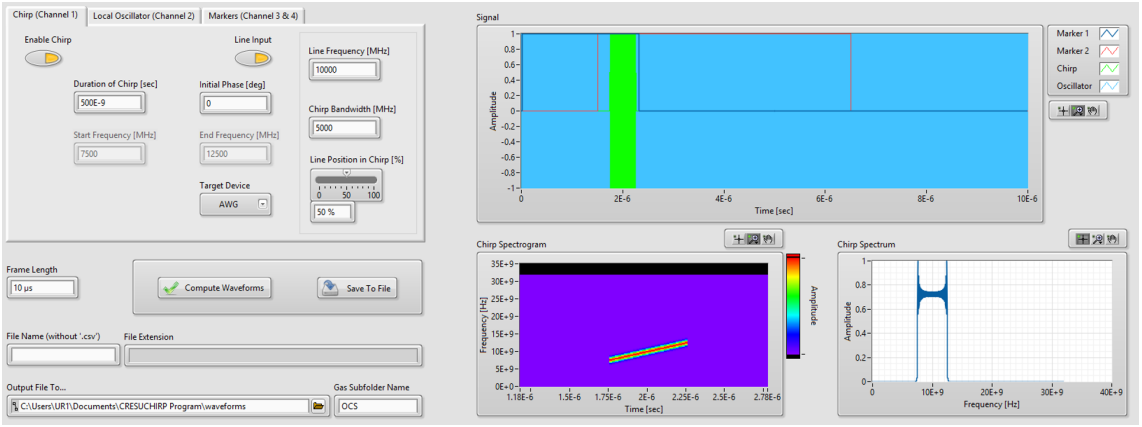

Figure 15: Presentation of the waveform generation panel

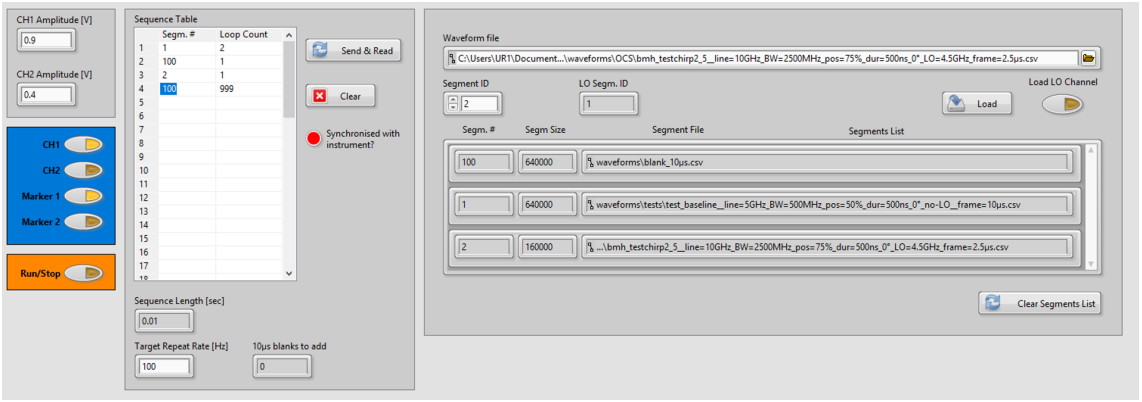

Figure 16: Presentation of the Arbitrary waveform generator panel

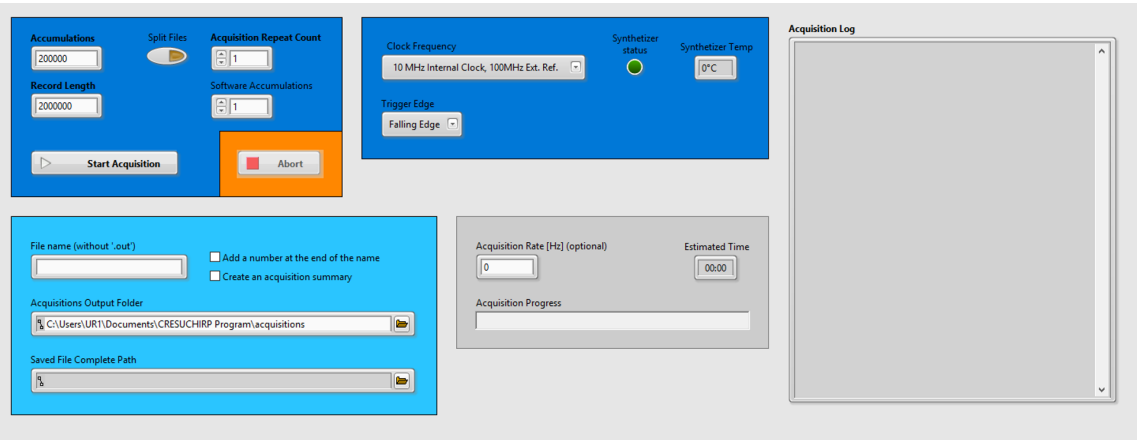

Figure 17: Presentation of the digitizer panel

.5 Clustering experiment in the Ar 30 K nozzle

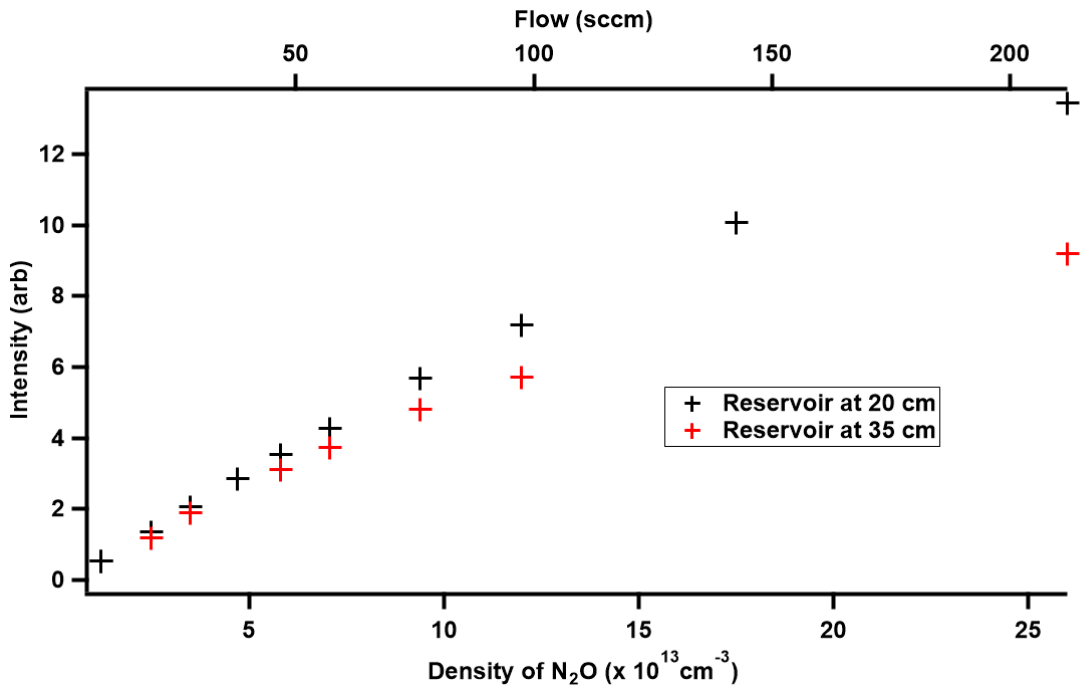

Figure 18: Clustering test in the Ar 30 K nozzle using N_2O J = 3-0 transition.

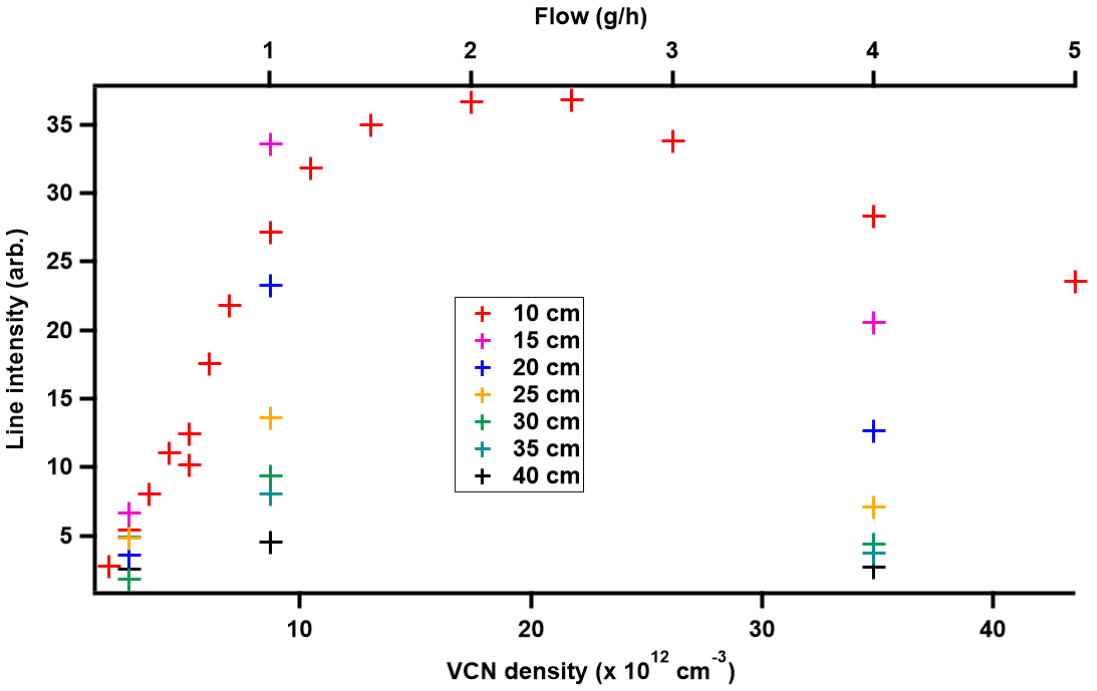

Figure 19: Clustering test in the Ar 30 K nozzle using acrylonitrile $J_{Ka,Kc}$ = $8_{0,8}$-$7_{0,8}$ transition

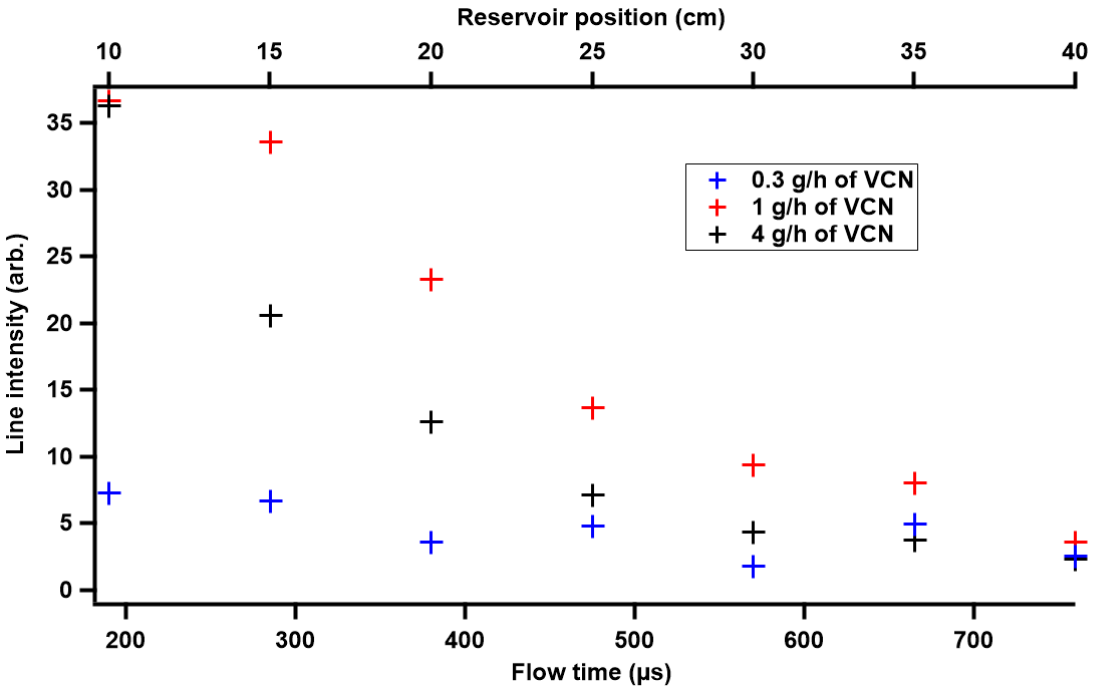

Figure 20: Clustering test in the Ar 30 K nozzle using acrylonitrile $J_{Ka,Kc}$ = $8_{0,8}$-$7_{0,8}$ transition changing the position of the reservoir at constant flow of acrylonitrile

.6 BrCN UV/Vis measurement

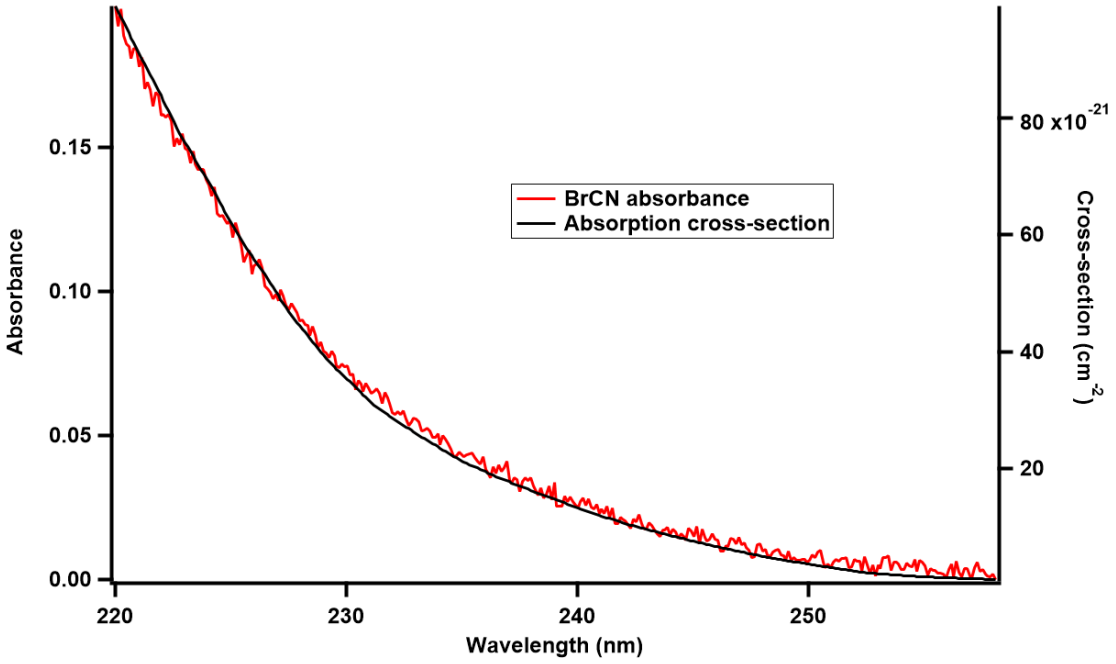

Figure 21: Example of the absorbance of BrCN measured on the UV/Vis spectrometer credit: Divita Gupta.